

Department of Civil and Environmental Engineering  
University of Strathclyde

HOW DO PLATE BOUNDARY  
FAULT CORES EVOLVE AND WHY?  
A CASE STUDY OF THE HIGHLAND  
BOUNDARY FAULT, SCOTLAND

By

Lucy McKay

MGeol (University of St Andrews)

Thesis submitted in fulfilment of the requirement of the degree of  
'DOCTOR OF PHILOSOPHY'

# Declaration

This thesis is the result of the author's original research. It has been composed by the author and has not been previously submitted for examination which has led to the award of a degree.

The copyright of this thesis belongs to the author under the terms of the United Kingdom Copyright Acts as qualified by University of Strathclyde Regulation 3.50. Due acknowledgement must always be made of the use of any material contained in, or derived from, this thesis.



May 2021

# Abstract

Understanding the internal structure (i.e., fault core composition, thickness and geometry) of large faults is crucial because their fault structure and properties control how and where earthquakes occur. Compilations of data from multiple fault studies show that fault cores get thicker on average with increasing total displacement (and hence slip events). However, the majority of faults in these datasets are from intraplate settings (faults within the interior of tectonic plates). Plate boundary faults have largely been excluded. As such there are no studies that systematically compare the two fault systems.

This study aims to address this knowledge gap: compiling and harmonising a global dataset of intraplate and plate boundary fault core thickness and total displacement data in order to examine whether these fault systems evolve in a similar way with repeated slip events. The Highland Boundary fault (HBF), an ancient plate boundary fault in Scotland, is used as a field site to provide a case study for examining the internal structure and inferring the evolution of a plate boundary fault core.

Detailed field, laboratory and mineralogical work reveal that the HBF core consists of four distinct units that remain unmixed. Not every unit is continuous along-strike and each unit varies in thickness (between 2.95 and 10.7 m). The units remain distinct as they formed at different stages of faulting and by different mechanisms affecting the faults ability to host earthquakes through time.

For the first time, this work discovers quantitatively that plate boundary fault cores are narrower than predicted by the trend for intraplate faults and highlights that, for this reason, plate boundary faults do not dissipate as much energy as intraplate faults during earthquakes. These results are crucial for understanding the internal structure and evolution of plate boundary fault cores and have implications for understanding how earthquakes behave.

# Table of Contents

Declaration .....	ii
Abstract .....	iii
Table of Contents .....	iv
List of Figures .....	viii
List of Tables .....	xi
Acknowledgements .....	xii
<b>Chapter 1 – Introduction.....</b>	<b>1</b>
1.1. Introduction .....	1
1.2. Aims and Research Questions.....	2
1.3. Thesis Outline and Style .....	4
<b>Chapter 2 – Literature Review .....</b>	<b>7</b>
2.1. Structural Geological Constraints on Earthquakes .....	7
2.2. What do Earthquakes Teach us about the Internal Structure of Faults? ....	15
2.3.1. Plate Boundary Fault Growth.....	21
2.4. The Highland Boundary Fault.....	23
2.5. Summary .....	24
<b>Chapter 3 – The Internal Structure of a Plate Boundary Fault. How Thick is the Highland Boundary Fault Core and How Variable is it?.....</b>	<b>26</b>
Abstract .....	26
3.1. Introduction .....	27
3.2. Geological Setting: The Highland Boundary Fault.....	28
3.3. Structural Framework.....	33
3.4. Methods.....	34
3.5. Structure of the HBF Fault Zone.....	37

3.6. Fault Core Lithologies.....	40
3.7. Fault Core Variability .....	47
3.8. Mineralogy .....	49
3.9. Discussion .....	53
3.9.1. Origin of the Clay-rich Fault Core .....	53
3.9.2. How Representative is the HBF of Active Plate Boundary Faults? .....	56
3.9.3. Along-Strike Variability and Its Implication for Rupture Propagation.....	57
3.10. Conclusion.....	58
<b>Chapter 4 - Do Plate Boundary and Intraplate Fault Systems Evolve in a Similar Way with Repeated Slip Events? .....</b>	<b>60</b>
Abstract .....	60
4.1. Introduction .....	61
4.2. Methods.....	63
4.3. Comparing Fault Core Thickness and Total Displacement for Plate Boundary and Intraplate Faults .....	66
4.4. Plate Boundary Fault Structure and Composition.....	72
4.5. Comparing Plate Boundary and Intraplate Fault Earthquake Events.....	76
4.6. Discussion .....	82
4.7. Conclusion.....	85
<b>Chapter 5 – The Temporal Evolution of a Plate Boundary Fault Core: A Case Study of the Highland Boundary Fault at Stonehaven.....</b>	<b>87</b>
Abstract .....	87
5.1. Introduction .....	88
5.2. Geological Setting: The Highland Boundary Fault.....	90
5.3. Methods.....	94
5.3.1. Microstructural Analysis .....	94
5.3.2. XRD Analysis.....	96
5.4. Microstructural Observations of the Highland Boundary Fault Core.....	97

5.4.1. Green Gouge.....	97
5.4.2. Blue Gouge .....	98
5.4.3. Contact between the Blue Gouge and Red Foliated Chaotic Breccia .....	103
5.4.5. Red Foliated Chaotic Breccia .....	106
5.4.5. Clasts within the Fault Core .....	109
5.5. Mineralogy .....	112
5.6. Synthesis of Key Results.....	114
5.7. Discussion .....	115
5.7.1. A Model of Fault Core Evolution.....	115
5.7.2. Impact on Fault Strength and Ability to Host Earthquakes Through Time.....	123
5.8. Conclusion.....	124
<b>Chapter 6 – Discussion and Conclusion .....</b>	<b>125</b>
6.1. Understanding the Evolution of the Highland Boundary Fault .....	125
6.1.1. Evidence of Slip Weakening Mechanisms .....	125
6.1.2. Evolution of the Damage Zone.....	127
6.1.3. The Evolution of the Highland Boundary Fault System (Fault Core + Damage Zone)..	133
6.2. Why are Plate Boundary Fault Cores Narrow?.....	137
6.3. Conclusions .....	143
<b>Chapter 7 – Future Work.....</b>	<b>146</b>
1. 3D Microstructural Studies .....	146
2. Argon Radiometric Dating .....	147
3. Oxygen and Hydrogen Isotopes .....	148
4. Experimental Deformation Experiments.....	148
5. 2D and 3D Microstructural Studies of the Damage Zone/Host Rock.....	149
6. Carbonate Clumped Isotope Thermometry on the Highland Border Ophiolite (Footwall Damage Zone) .....	150
7. Calcite Dating of the Highland Border Ophiolite .....	151
8. Detailed Field Mapping of the Dalradian Damage Zone .....	152
9. Field Mapping of Other Locations Along the HBF .....	152

10. A Comparison of Plate Boundary Fault and Intraplate Fault Geometry...	152
<b>References .....</b>	<b>154</b>
<b>Appendix 1 – Published Paper Chapter 3.....</b>	<b>193</b>
<b>Appendix 2 – Geoscientist Magazine Chapter 3.....</b>	<b>206</b>
<b>Appendix 3 – Published Paper Chapter 4.....</b>	<b>212</b>
<b>Appendix 4 – Details of the Compiled Fault Core Thickness – Displacement Dataset in Chapter 4 .....</b>	<b>220</b>

# List of Figures

<b>Fig. 2.1.</b> Relationship between geometrical discontinuities/complexities in fault surface traces of strike-slip faults to the endpoints of historical earthquake ruptures..	9
<b>Fig. 2.2.</b> Conceptualised illustration of a typical fault zone and its different elements (i.e., internal structure) .....	10
<b>Fig. 2.3.</b> Scaling relations between fault displacement/offset and fault core thickness and geometric complexity (defined as steps per unit length).....	12
<b>Fig. 2.4.</b> A graphical representation of the slip weakening model relating the partitioning of energy between fracture energy ( $E_G$ ), frictional energy ( $E_F$ ) and radiated energy ( $E_R$ ) to the shear stress acting on the fault ( $\tau$ ) .....	19
<b>Fig. 2.5.</b> Evolution of the San Andreas Fault System.....	22
<b>Fig. 2.6.</b> Location of the Highland Boundary fault (HBF) and field site near Stonehaven on the northeast coast of Scotland .....	24
<b>Fig. 3.1.</b> Block diagram illustrating the tectonic setting of the Highland Boundary Fault.....	30
<b>Fig. 3.2.</b> Our geological map of the Highland Boundary fault (HBF) near Stonehaven, NE Scotland.....	31
<b>Fig. 3.3.</b> Damage zone deformation of the HBF .....	34
<b>Fig. 3.4.</b> The University of Strathclyde’s Fault and Fluid Flow research group ‘digging’ for the Highland Boundary fault near Stonehaven. ....	35
<b>Fig. 3.5.</b> Exposing the clay within the Highland Boundary fault core.....	36
<b>Fig. 3.6.</b> Summarised fault zone structure .....	38
<b>Fig. 3.7.</b> Multiphase carbonate vein in ophicarbonite. ....	39
<b>Fig. 3.8.</b> Modelling a fish in the field out of the blue clay.....	41
<b>Fig. 3.9.</b> Field exposure of the blue gouge from Log 4 .....	43
<b>Fig. 3.10.</b> Centimetre-scale variations in the FC units.....	44
<b>Fig. 3.11.</b> Photographs and detailed sketches of the fault core units .....	45
<b>Fig. 3.12.</b> Field photograph of the red foliated chaotic breccia from Log 4.....	46
<b>Fig. 3.13.</b> Structural logs highlighting the along-strike variability in the thickness of the HBF FC units over the well-exposed 560 m Stonehaven section .....	47



<b>Fig. 3.14.</b> Smaller-scale structural logs at Garron Point highlighting the along-strike, metre-scale variability of the HBF fault core over a 50 m section .....	48
<b>Fig. 3.15.</b> Summary schematic log of the HBF architecture with associated mineralogy determined via x-ray diffraction (XRD) analysis .....	51
<b>Fig. 3.16.</b> XRD diffractograms for <b>(a)</b> the whole (bulk) rock and <b>(b)</b> <2 $\mu\text{m}$ size fractions of the three clay-rich FC domains of the HBF .....	52
<b>Fig. 3.17.</b> Fault zone palaeontology: shallow-marine microfossils in the blue gouge .....	53
<b>Fig. 4.1.</b> Schematic diagram defining the terms used in this chapter .....	62
<b>Fig. 4.2.</b> Log-log plot of fault core thickness and total displacement for <b>(a)</b> intraplate faults and <b>(b)</b> plate boundary (colour) faults vs. intraplate (greyscale) faults .....	71
<b>Fig. 4.3.</b> Schematic structural logs illustrating fault core thickness and composition for plate boundary faults. ....	73
<b>Fig. 4.4.</b> Log-log plot of total displacement and fault complexity (defined as steps per km) for plate boundary (blue squares) and intraplate (pink circles) strike-slip fault systems.....	76
<b>Fig. 4.5.</b> Comparing intraplate and plate boundary fault earthquake events. ....	82
<b>Fig. 5.1.</b> The Highland Boundary Fault .....	92
<b>Fig. 5.2.</b> Simplified, schematic 3D block diagram of the HBF at Stonehaven.....	93
<b>Fig. 5.3.</b> Thin section of green gouge (Log4-0.1m).....	98
<b>Fig. 5.4.</b> Thin section of blue gouge (Log4-0.32m).....	100
<b>Fig. 5.5.</b> Thin section of blue gouge (Log5-2.25m).....	101
<b>Fig. 5.6.</b> Photomicrographs of the blue gouge all aligned in the same relative orientation to the HBF.....	102
<b>Fig. 5.7.</b> Localised section of microfossils within the blue gouge.....	103
<b>Fig. 5.8.</b> Contact between the blue gouge and red foliated chaotic breccia at Log5, 2.6m from the PSS of the HBF .....	104
<b>Fig. 5.9.</b> Thin section of the contact between the blue gouge and red foliated chaotic breccia (Log5-2.6m).....	105
<b>Fig. 5.10.</b> Photomicrographs of the red foliated chaotic breccia all aligned in the same relative orientation to the HBF.. ....	107
<b>Fig. 5.11.</b> Thin section of red foliated chaotic breccia (Log6-1m).....	108

<b>Fig. 5.12.</b> Clast aspect ratio plotted against clast long axis length across all fault core units. ....	110
<b>Fig. 5.13.</b> Conceptual model of the Highland Boundary fault core evolution based on field, microstructural and XRD observations.....	122
<b>Fig. 6.1</b> Preliminary hydraulic conductivity measurements of the blue gouge and red foliated chaotic breccia of the HBF fault core. ....	127
<b>Fig. 6.2.</b> Photographs of carbonate units within the Highland Border Ophiolite (footwall damage zone).....	128
<b>Fig. 6.3.</b> Map of the HBF showing sample locations.....	129
<b>Fig. 6.4.</b> Conventional $\delta^{13}\text{C}$ and $\delta^{18}\text{O}$ isotope data determined via mass spectrometry .....	131
<b>Fig. 6.5.</b> Measured $\delta^{18}\text{O}$ versus temperature for measured $\delta^{18}\text{O}$ isotope values in calcite and dolomite .....	133
<b>Fig. 6.6.</b> Schematic tectonic evolution model for the Highland Boundary fault system (fault core + damage zone).....	136
<b>Fig. 6.7.</b> Field photograph of the ophicarbonates and carbonated serpentinite units of the Highland Border Ophiolite (footwall damage zone).....	137
<b>Fig. 7.1</b> Example of 3D reconstructions of FIB slices from the San Andreas fault gouge .....	146
<b>Fig. 7.2.</b> Thin section showing the multiphase carbonate vein in ophicarbonate. ...	150

# List of Tables

<b>Table 2.1.</b> Compilation of faults studied in Chapter 4 showing the number of fault studies decreasing when the displacement of the fault increases.....	14
<b>Table 3.1.</b> XRD results of the whole (bulk) rock fraction (5-10 $\mu$ m) from three clay-rich fault core units of the HBF.....	50
<b>Table 3.2.</b> XRD results of the fine-grained <2 $\mu$ m fraction from three clay-rich fault core units of the HBF .....	50
<b>Table 4.1.</b> Compiled dataset of fault core thickness and total displacement observations for intraplate faults.....	67
<b>Table 4.2.</b> Compiled dataset of fault core thickness and total displacement observations for plate boundary faults .....	70
<b>Table 4.3.</b> Compiled dataset of fault geometries (steps per unit length) for plate boundary and intraplate strike-slip faults.....	76
<b>Table 4.4.</b> Compiled dataset of plate boundary fault earthquake events.....	79
<b>Table 4.5.</b> Compiled dataset of intraplate fault earthquake events.....	81
<b>Table 5.1.</b> Summary of clast area, length of long axis, aspect ratio and circularity for each sample in this study.....	111
<b>Table 5.2.</b> Summary of clast area, length of long axis, aspect ratio and circularity by fault core unit .....	111
<b>Table 5.3.</b> XRD results of the semi-quantitative mineralogical composition (wt.%) of the recovered size fractions.....	113
<b>Table 5.4.</b> XRD results showing the relative percentages of clay minerals in the various clay fractions as determined from oriented specimens. ....	113
<b>Table 5.5.</b> Synthesis of key results for each fault core unit.....	114
<b>Table 6.1.</b> Synthesis of the major findings of this thesis.....	142

# Acknowledgements

There are so many to acknowledge and thank both professionally and personally. First, I would like to thank my supervisors Prof. Zoe Shipton, Prof. Rebecca Lunn, Prof. Adrian Boyce and Dr. Tim Raub for constantly reminding me of my own abilities and their knowledge and unfaltering support over the past four years. Zoe, despite having rather a large number of other tasks to perform as head of department (and take care of two children), thank you for finding me a PhD, always having the time to meet regularly, discuss new ideas, edit manuscripts and grant applications and spend time in the field digging clay. Even through the Covid-19 global pandemic you still managed to provide valuable support while managing a virtual department! Becky, similarly, thank you for regularly attending meetings, discussing new ideas, editing manuscripts, spending time in the field and most importantly keeping the geologists on track. Adrian and Tim, thank you for your laboratory guidance and support, and providing access to facilities not available at Strathclyde.

I would like to acknowledge the funding acquired for this project from the Environmental and Physical Science Research Council (EPSRC) – thank you very much for your support over the last four years. Laboratory work was also funded by a Geological Society of London Research Grant from the William George Fearnside's fund. Laboratory work and analysis was also made possible by staff at the Advanced Materials Research laboratory (AMRL) at the University of Strathclyde, the James Hutton Institute, Spectrum Petrographics, the Scottish Universities Environmental Research Centre (SUERC) and X-ray Minerals Ltd.

Thank you also to the Scottish Natural Heritage (SNH) and associated landowners for permission to sample the Highland Boundary fault at Craigeven Bay, without which this research would not have been possible. Also, to the team of diggers who helped discover, expose and sample the clays that form the backbone of this project – Zoe Shipton, Rebecca Lunn, Billy Andrews, Izabella Otalega, Lisa Millar, Carla Romano, Yannick Kremer and Bruno Thomas.

No one understands the challenging environment and stress of doing a PhD better than another PhD student. So, thank you to the fellow FAFF'ers for your support and help with the PhD at some point or other – Izabella Otalega, Jen Roberts, Yannick Kremer, Mark Stillings, Lisa Millar, Carla Romano, Mike Schiltz, Gareth Johnson and Chris McMahon. A special thanks must go to Billy Andrews for his invaluable field assistance and friendship.

I'd also like to say a very special thank you to my family and friends for being such a huge source of support and love for me during this PhD, especially Mum and Dad who have made everything possible. A special thanks must also go to John who moved to Scotland to be by my side throughout this PhD and for your incredible support and belief in me. And finally, to Hugo for being such a good baby, making it possible and giving me the motivation to complete what I started.

# Chapter 1 – Introduction

## 1.1. Introduction

Major earthquakes can occur on any large fault, but 90% are associated with plate boundary faults (USGS 2016). Understanding the internal structure (e.g., fault core composition, thickness and geometry) of large faults is crucial, because their fault structure and properties control how and where earthquakes rupture, nucleate and propagate (Aydin & Du 1995; Barka 1996; Caine *et al.* 1996; Andrews 2005; Wesnousky 2006; Wibberley *et al.* 2008; Faulkner *et al.* 2010; Kirkpatrick *et al.* 2018). This in turn limits the size of the earthquake (Cohee & Beroza 1994; Kirkpatrick *et al.* 2008) or the amount of radiated seismic energy (Heermance *et al.* 2003; Ma *et al.* 2003; Madariaga *et al.* 2006) and consequently surface severity and damage (Lin *et al.* 2001; Heermance *et al.* 2003; Ma *et al.* 2003). For example, the 1999 magnitude 7.7 earthquake along the Chelungpu plate boundary fault – the second deadliest earthquake in Taiwan’s recorded history – saw significant variations in slip and ground motion at different locations along the fault which resulted in large local variations in casualties and damage (Ma *et al.* 2001). Subsequent field investigation related these changes to variations in the fault’s structure (i.e., thickness of clay-rich fault zone and geometry of juxtaposed beds on either side of the fault), which in turn controlled how the fault moved (Heermance *et al.* 2003). Therefore, understanding the internal structure of plate boundary faults is crucial if we are to better understand and mitigate damage (i.e., build disaster resilient infrastructure) from future natural disasters.

Despite the fact that 90% of global seismicity occurs at plate boundary faults, our knowledge of their internal structure is lacking as opportunities to directly study the internal structure of large (in terms of length and displacement) plate boundary faults are few. This, in part, is because field studies are biased towards features that are both exposed and visible at a scale that humans can realistically observe and measure (Shipton *et al.* 2019). This biases study towards faults with smaller displacements. For example, compilations of data from multiple fault studies show that faults get thicker on average with increasing total displacement (and hence slip events) (e.g., Childs *et*

al., 2009; Shipton et al., 2006b; Torabi et al., 2019; Van Der Zee et al., 2008; Wibberley et al., 2008), albeit with a large range in magnitude of thickness for a given displacement (Shipton et al 2006b). However, the vast majority of the faults in these datasets are from intraplate settings (faults within the interior of tectonic plates and not the boundary of such plates). Plate boundary faults, with larger displacements, have largely been excluded. As such there are no studies that systematically compare the observations between the two fault systems.

This thesis aims to address these knowledge gaps: compiling and harmonising a global dataset of intraplate and plate boundary fault core thickness and total displacement data in order to examine whether these fault systems evolve in a similar way with repeated slip events. The Highland Boundary fault (HBF), a past plate boundary fault in Scotland, is used as a field site in order to provide a case study for examining the internal structure and inferring the evolution of a plate boundary fault core. Data from the HBF is then added to the global dataset.

## 1.2. Aims and Research Questions

This study aims to advance our understanding of the internal structure and evolution of plate boundary faults, with particular focus on their fault core as that is where the majority of earthquake slip is accommodated. Primary data are from the Highland Boundary fault and includes field mapping, structural analysis, mineralogical analysis and microscopic investigation. These data were then compared with data from the peer-reviewed scientific literature. First, data were compiled on the internal structure (e.g. fault core composition, fault core thickness, total displacement) of both active and ancient plate boundary faults. This compilation was then compared to intraplate faults in order to examine whether the two fault systems evolve in a similar way with repeated slip events. Finally, data were compiled on the seismic moment (a measure of the ‘size of’ or ‘work done by’ an earthquake) to compare estimates of radiated seismic energy for intraplate and plate boundary fault events.

Principal aims of the study are to:

- Map the internal structure of the Stonehaven section of the HBF, describe the fault rock lithologies and assess the spatial and temporal evolution of the fault core (in present space and through time);
- Compare the internal structure of the HBF to other plate boundary faults;
- Compile and harmonise a global dataset of intraplate and plate boundary fault core thickness and total displacement data to examine whether these fault systems evolve in a similar way with repeated slip events;
- Examine the scaling relations between seismic moment, average displacement and surface rupture length to examine if plate boundary faults and intraplate faults radiate energy and process intact rocks in the same ratio during seismic events.

Research questions include:

- RQ1: What is the internal structure of the HBF in terms of fault core and damage zone and what fault rock lithologies are present?
- RQ2: How does the internal structure of the HBF vary spatially (in present space) and temporally (through time)? What implications did this have on the mechanical properties of the fault and its ability to host earthquakes through time?
- RQ3: How comparable is the internal structure of the HBF to other plate boundary faults?
- RQ4: Do plate boundary and intraplate faults evolve similarly with repeated slip events (and hence earthquakes)?
- RQ5: Do plate boundary faults and intraplate faults radiate energy and process intact rocks in the same way during seismic events?
- RQ6: How do plate boundary fault cores evolve and why?



### 1.3. Thesis Outline and Style

Chapter 2 of this thesis reviews the literature and gives an introduction of the field site. Chapters 3-5 have each been written as a standalone manuscript, and each has been published in or is in preparation to be submitted to a peer-reviewed scientific journal. As such, each chapter contains a separate abstract and introduction, and separate sections dealing with the geological setting, discussion of data, and conclusions. Inevitably some overlap will exist between the chapters. Because the chapters are published or intended for publication, they are written in the first-person plural. However, I am the primary author for each paper and responsible for over 90% of the data collection, data interpretation and paper writing. Co-authors provided scientific advice and discussion, assistance with data collection and normal levels of editorial guidance. Chapter 6 discusses and summarises the major findings of the thesis, while Chapter 7 provides some suggestions for future work.

**Chapter 3** – This chapter was published in the Journal of the Geological Society. Published article included in Appendix 1. A sub-set of the information from this journal paper was also published as the feature article in the Geological Society’s fellowship magazine, *Geoscientist*. The published magazine article is included in Appendix 2. Note, following the Viva examination and recommendations from the examiners, minor additions and modifications have been made to this chapter that are not included in the published article.

Published as: McKay, L., Shipton, Z.K., Lunn, R.J., Andrews, B., Raub, T.D., Boyce, A.J., 2020. Detailed Internal Structure and Along-Strike Variability of the Core of a Plate Boundary Fault: The Highland Boundary Fault, Scotland. *Journal of the Geological Society*, 177, 283-296. doi: 10.1144/jgs2018-226

Published as the feature article of *Geoscientist* as: McKay, L., 2020. Core surprise: What's inside a plate boundary? *Geoscientist*, 30 (6), 11-15. doi: 10.1144/geosci2020-092

This chapter describes new and detailed field, structural and mineralogical observations of the HBF internal structure. It focusses primarily on the fault core. Detailed field mapping and structural analyses reveal a remarkable sequence of clay and microfossils within the core of this ancient plate boundary. Structural logs are used to demonstrate the variability in fault core thickness and composition at different locations along the fault. The thickness of the fault varies but the structure does not. The observations and conclusions presented in this chapter are used as a framework for subsequent chapters.

**Chapter 4** – This chapter was published in *Earth and Planetary Science Letters*. Published article included in Appendix 3. Note, following the Viva examination and recommendations from the examiners, minor additions and modifications have been made to this chapter that are not included in the published article.

Published as: McKay, L., Lunn, R.J., Shipton, Z.K., Pytharouli, S., Roberts, J.J., 2021. Do intraplate and plate boundary fault systems evolve in a similar way with repeated slip events? *Earth and Planetary Science Letters*, 559, 1-18. doi: 10.1016/j.epsl.2021.116757

This chapter compiles and compares observations of the HBF fault core, outlined in Chapter 3, with other plate boundary faults. It focusses primarily on fault core thickness and total displacement data. The data for plate boundary faults (including the HBF) is then compared with intraplate faults to examine if these fault systems break down rock, and hence evolve in the same way during earthquakes. The results presented in this chapter suggest plate boundary faults and intraplate faults do not evolve in a similar way with increasing displacement and hence repeated slip events. Observations are then used to infer how fault zone processes could cause the systematic differences observed between these two fault systems including differences on how seismic energy is partitioned.

**Chapter 5** – This chapter is in preparation to be submitted to the Journal of Structural Geology. Co-authors include Shipton, Z.K., Lunn, R.J., and Andrews B.

By examining the internal structure of a seismogenic fault we are looking at the frozen-in finite record of multiple earthquakes on a fault. To understand the processes during earthquakes we must peel away the record of the processes that occurred as the fault was exhumed. This chapter presents the first detailed field, microstructural and x-ray diffraction (XRD) observations of the HBF in order to comment on how strain is localised and the processes leading to the genesis of the multiple fault rocks found within its core. In an attempt to unravel the evolution of this plate boundary fault, the observations are used to suggest likely mechanisms by which the fault core evolved through time and propose an evidenced-based six-stage evolutionary model. The multi-event evolution caused the mechanical properties of the fault core to vary through time, impacting the fault's ability to host earthquakes through time.

## Chapter 2 – Literature Review

This chapter reviews the interdependence between fault structure and earthquake processes and provides an introduction to the field site for the thesis.

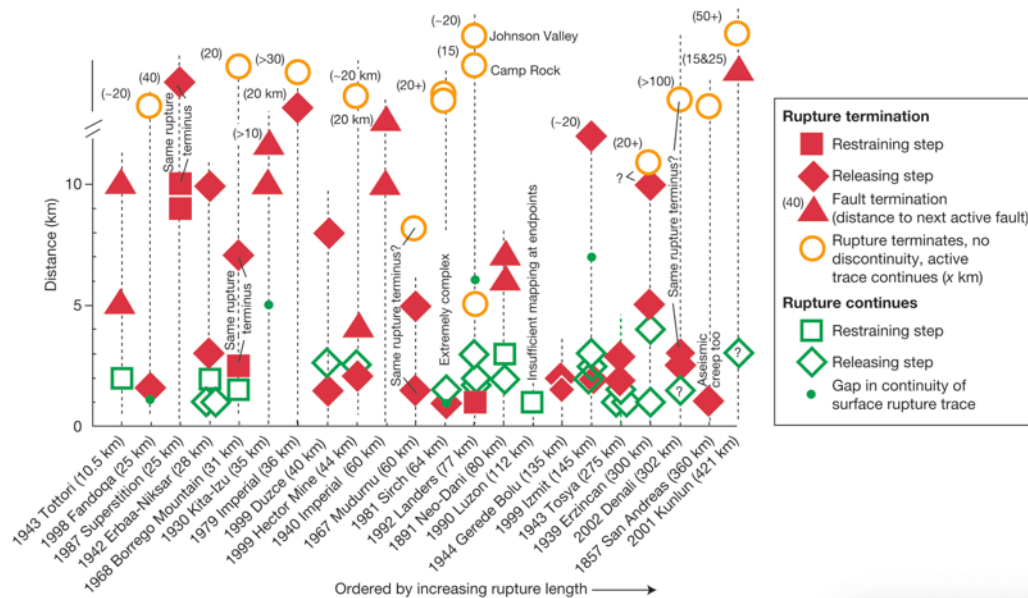
### 2.1. Structural Geological Constraints on Earthquakes

Faults, defined as structural discontinuities in the Earth's crust, form in response to plate tectonic forces and result in crustal deformation and displacement. In the upper ~10 km of the crust, rocks are deformed within the brittle (or frictional) regime through brittle deformation mechanisms such as frictional sliding along grain boundaries, grain rotation and/or grain fracturing (Sibson 1977; Fossen 2010). Associated deformation results in characteristic fault rocks in which fracturing and cataclasis fragments the host rock minerals, and typically reduces grain size with progressive deformation (Sibson 1977). For this reason, fault rocks are typically poorly preserved in the rock record.

As first demonstrated by Gilbert (1883) most of the relative displacement of actively deforming crust occurs when an earthquake ruptures a geological fault (Sibson 1989). Earthquakes can happen on faults, but not all fault slip generates seismically released energy. For instance, stick-slip displacement on a fault (the fast movement that occurs when the two sides of the fault become unstuck) radiates energy in the form of seismic waves manifested as earthquakes. However, fault creep, defined as the slow continuous movement on a fault in response to tectonic forces, does not tend to generate earthquakes (Fossen 2010; Fagereng & Toy 2011 and references therein).

The response of a fault to slip is dependent on its internal structure and physical properties (Chester *et al.* 2005; Wibberley & Shimamoto 2005; Wesnousky 2006; Kirkpatrick & Shipton 2009; Fagereng & Toy 2011; Kirkpatrick *et al.* 2018). Field observations of surface ruptures demonstrate that two thirds of earthquakes on strike-slip faults terminate at geometric complexities in fault traces (**Fig. 2.1**; Wesnousky

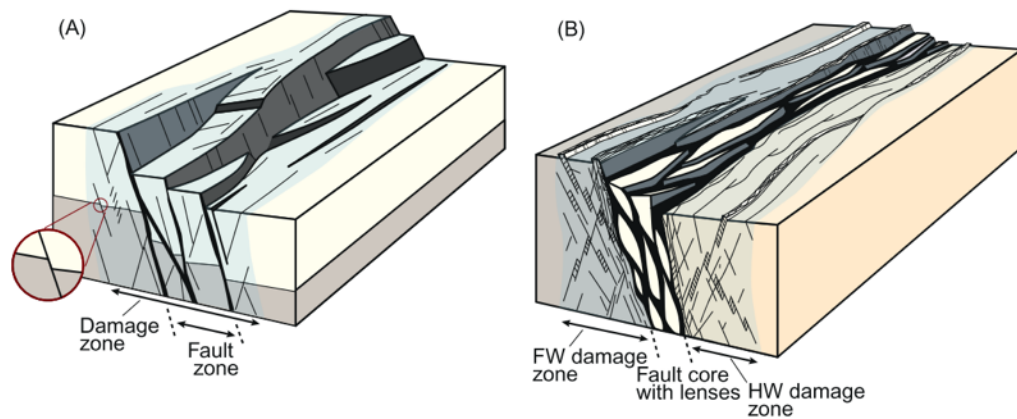
2006). Ruptures also decelerate in areas of structural complexity (Barka & Kadinsky-Cade 1988; Aydin & Du 1995; Barka 1996; Andrews 2005). For an earthquake to occur, the frictional strength of the fault must decrease with increasing slip or slip rate (Rice 2006). Several slip weakening mechanisms have been proposed to achieve a dynamic reduction in the strength of a fault (e.g., Sibson 1973; Lachenbruch 1980; Hirose & Shimamoto 2005; DiToro *et al.* 2006, 2011; Rempel & Rice 2006; Rice 2006; Goldsby & Tullis 2011; Kirkpatrick *et al.* 2013; Brantut & Platt 2017). However, such slip weakening mechanisms depend on the physical properties of fault rock assemblage such as mineralogy (e.g., clay content) which in turn controls the frictional strength (e.g., Smith & Faulkner 2010; Ikari *et al.* 2011; Behnsen & Faulkner 2012; Boulton *et al.* 2014), structure of the fault zone including thickness (Kirkpatrick *et al.* 2018), fault growth (Perrin *et al.* 2016) and/or the presence and geochemistry of the fluids (Rice 2006). As such, the composition and properties of the material in the slipping zone must control the rupture process to a large extent (Chester *et al.* 2005; Wibberley & Shimamoto 2005; Kirkpatrick & Shipton 2009; Fagereng & Toy 2011; Kirkpatrick *et al.* 2018).



**Fig. 2.1.** Relationship between geometrical discontinuities/complexities in fault surface traces of strike-slip faults to the endpoints of historical earthquake ruptures. These geometrical discontinuities/complexities may slow or stop rupture propagation and hence play a controlling part in limiting the size of the earthquake rupture. Figure from Wesnousky (2006).

Faults are not just a line on a map, or a plane within an interpreted 3D seismic volume, they are a zone of variably deformed fault rock that forms through a complex interaction of mechanical, hydraulic and/or chemical processes (Fossen, 2020 and references therein). Studies of the internal structure of a fault, or fault zone, advanced over the past ~30 years from Chester and Logan (1986), show that variably deformed fault rock consequently leads to variable mechanical and hydraulic properties that control the frictional and hydraulic behavior of the resulting fault zone. Caine *et al.* (1996), splits the fault zone into a simplified three-component model: (1) host rock (type of rock being faulted); (2) fault core (the zone which accommodates the maximum displacement); and (3) the bounding fracture-dominated damage zone (Fig. 2.2) although not all of these components exist in every fault zone (Wibberley *et al.* 2008). The fault core, which ranges from a few centimetres up to tens of metres wide, accommodates most of the fault slip. It consists of localised slip zones containing cataclastically deformed fault rocks such as clay-rich gouge, breccia and/or cataclasites (see Woodcock and Mort, 2008 for fault rock classification terminology). The damage zone, which can reach several hundred metres wide, may include

fractured host rocks, subsidiary faults, small-displacement subsidiary slip surfaces, veins and folding at all scales (Faulkner *et al.*, 2010). The critical distinction between fault core and fault damage zone is that the latter does not accommodate significant shear displacement (Sutherland *et al.* 2012).



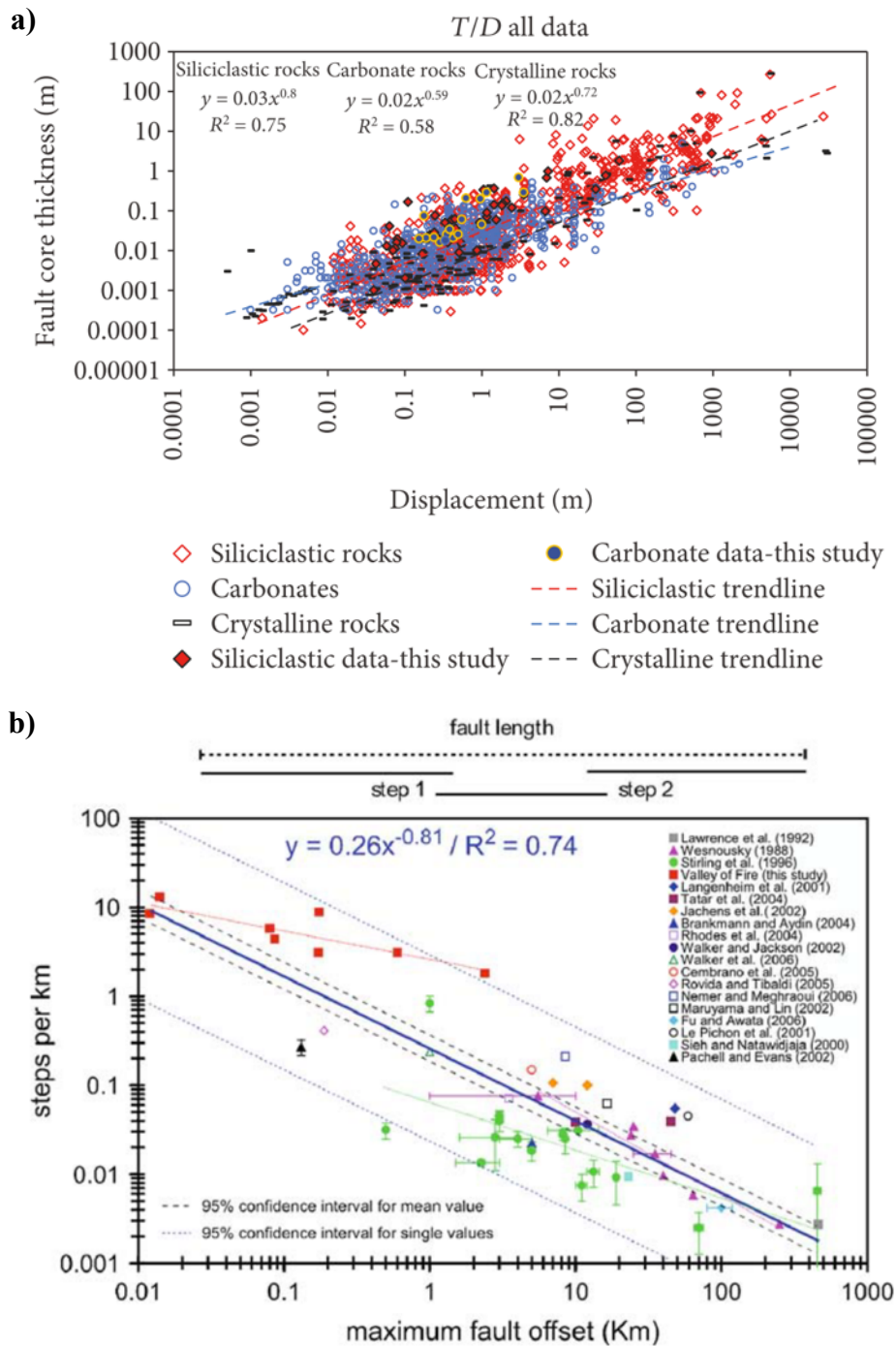
**Fig. 2.2.** Conceptualised illustration of a typical fault zone and its different elements (i.e., internal structure). a) Low displacement fault showing early fault growth. Slip is localised on one or more narrow high-strain fault cores (shown in black) surrounded by a low-strain damage zone. A subsidiary footwall shear fracture (i.e., a small-scale fault) is highlighted within the circle inset. b) High displacement fault showing the evolution, linkage and increased complexity of a fault zone over time. FW, footwall; HW, hangingwall. Figure from Fossen (2020).

Faults (in terms of structure and behaviour) rarely adhere to a simple conceptual model: instead, they are highly variable in space and time. Geologists studying faults exhumed from depth have demonstrated that faults are variable along-strike and down-dip at a variety of scales ranging from small (in terms of length or displacement) (Kirkpatrick *et al.* 2008, 2018; Lawther *et al.* 2016; Sosio De Rosa *et al.* 2018) to large faults (Faulkner *et al.* 2003; Heermance *et al.* 2003; Barth *et al.* 2013). For instance the fault core thickness, described as the thickness of the fault rocks situated within the fault core, can vary in thickness by a full order of magnitude over short distances along the fault (Shipton *et al.* 2006a; Kirkpatrick *et al.* 2018). This spatial variability in fault properties is the result of macroscale discontinuities such as bends and step overs (e.g., Wesnousky 2006), juxtaposition of different rock types along-strike (e.g., Dor *et al.* 2006), displaying different internal structures along-strike (Faulkner *et al.*

2003) and/or different fault rocks of different chemical and mechanical properties along-strike (i.e., gouge or cataclasite) (e.g., Evans 1990; Van Der Zee *et al.* 2008). They can also be temporally variable as a result of the effects of previous deformation events, variations in strain-rate over the course of the seismic cycle (e.g., DiToro *et al.* 2011 and references therein), ruptures opening up flow networks allowing transient high permeabilities (e.g., Lawther *et al.* 2016; Faulkner *et al.* 2010) and due to the progressive accumulation of fault core thickness as the fault grows and accumulates displacement through time (e.g., Childs *et al.* 2009). The Alpine fault in New Zealand is just one example of a fault that is both spatially and temporally variable (Barth *et al.* 2013; Schleicher *et al.* 2015; Toy *et al.* 2015; Williams *et al.* 2017).

Properties and thickness of both the fault core and damage zone are mechanically related to the mechanism by which the fault grows through time (during rupture and between rupture events), and hence evolves with increasing total displacement (Sibson 1977). Compilations of data from multiple fault studies (intraplate faults only) show that, on average, faults get thicker as total displacement increases through time (e.g., Childs *et al.*, 2009; Shipton *et al.*, 2006b; Torabi *et al.*, 2019; Van Der Zee *et al.*, 2008; Wibberley *et al.*, 2008) (**Fig. 2.3a**), albeit with a large range in magnitude of thickness for a given displacement (Shipton *et al.* 2006b). This is true regardless of fault type (Childs *et al.* 2009) or the type of rock being faulted (**Fig. 2.3b**) (Shipton *et al.* 2006b; Torabi *et al.* 2019). This displacement-thickness scaling relationship represents a growth trend where low displacement faults represent a stage of early growth and are narrow (**Fig. 2.2a**) but on average they evolve into thicker, longer and more complex faults zones over time with increasing displacement (**Fig. 2.2b**) (Wesnousky 1988; Childs *et al.* 1996, 2009; Wibberley *et al.* 2008; Fossen 2020 and references therein).





**Fig. 2.3.** Scaling relations between fault displacement/offset and fault core thickness and geometric complexity (defined as steps per unit length). a) Fault core thickness increases with increasing displacement regardless of rock type. Figure from Torabi et al. (2019). b) Steps per unit kilometre decrease with increasing displacement suggest faults become smoother and straighter the more displacement they accumulate. Figure from de Joussineau & Aydin (2009).

Faults typically initiate as opening-mode cracks with discrete tips/ends and grow through lateral tip-processing (Cowie & Scholz 1992; Vermilye & Scholz 1998) and/or the linkage of structures to form a continuous through-going fault plane (Segall & Pollard 1980; Peacock 1991; Trudgill & Cartwright 1994; Zhang *et al.* 1999; Walsh *et al.* 2003; Childs *et al.* 2009). Low displacement faults are typically composed of kinematically-related, irregular and segmented surfaces separated by geometrical discontinuities such as steps. With increasing displacement, the steps are breached and adjacent fault segments coalesce to form a long, smoothed and straightened, through-going fault trace where large-scale motion is localised (Wesnousky 1988; Stirling *et al.* 1996; de Joussineau & Aydin 2009; Brodsky *et al.* 2011). As a result of the irregularities being sheared off, lenses of fault-bounded rocks, including the former high-strain stepped zone between the segments, can enter the fault zone (Childs *et al.* 2009). With further displacement, these lenses become comminuted to fault rock, permitting an increased thickness of the fault core (Childs *et al.* 2009). Several studies have demonstrated that the number of fault steps per unit length decreases as a function of increasing total displacement (**Fig. 2.3b**) (Wesnousky 1988; Stirling *et al.* 1996; de Joussineau & Aydin 2009). This suggest large displacement, crustal-scale faults should be expected to have thicker fault cores with a smooth and straight geometry

However, there are few studies on large (in terms of length and displacement) faults. This in part is because field studies are biased towards features that are both exposed and visible at a scale that humans can realistically observe and measure (Shipton *et al.* 2019). The larger the fault the more difficult it is (or the larger the job it is) to untangle the story of how the fault grew. For a small fault entirely contained within a cliff section with clear offset markers and where you can see both tips/ends, and ideally some slip vectors, you can capture the entire geometry and kinematics. If there are subsidiary structures and the fault occurs in a basin with a relatively well understood basin history, you can start to infer the mechanics. If the mineralisation is datable, and if you can demonstrate from cross-cutting that it is fault related, you may be able to date the fault activity. All of this gets harder with large faults – you may not be able to trace offset markers to get displacement; there may be multiple episodes of slip,

making the kinematics difficult to disentangle; there may be evidence of activity at varying depths making the mechanics complex. This bias in studying smaller faults is evident from the compilation of data presented in Chapter 4, where out of the 1,298 faults studied, 41% have small displacements ranging from 0 to 1 m while only 2% have large displacements greater than 100,000 m (**Table 2.1**).

Fault Displacement	Count	%
0 – 1 m	528	41
1 – 10 m	348	27
10 – 100 m	281	22
100 – 1,000 m	66	5
1,000 – 10,000 m	20	2
10,000 – 100,000	24	2
100,000+ m	31	2

**Table 2.1.** Compilation of faults studied in Chapter 4 showing the number of fault studies decreasing when the displacement of the fault increases.

This bias, in part, is due to the scale of human mapping i.e. measuring the fault and what we see of earthquake ruptures at the surface. However, what we see at the surface is different to what we see at depth. Earthquake hypocentre data show that the majority of continental earthquakes nucleate at depths of approximately 5-15 km (Scholz 1988), or 10-40 km in the case of subduction zone earthquakes (Byrne *et al.* 1988; Hyndman *et al.* 1997). Slip will not be the same at depth as it is at the surface. Dolan & Haravitch (2014) demonstrated that for six large ( $M_w > 7.1$ ) strike-slip earthquakes the degree to how much slip varies between the surface and depth depends on the structural complexity of the fault. Low displacement ( $\leq 25$  km) faults with complex geometries manifest only ~50-60% of total slip on narrow fault surface traces. Whereas, high displacement ( $\geq 85$  km) faults with smooth and straightened geometries manifest ~85-95% of total slip to thicker fault surface traces (Dolan & Haravitch 2014). These results imply that geologic measurements of surface slip along structurally immature faults are likely to significantly underestimate the true slip at depth in large earthquakes (Dolan & Haravitch 2014).

Major advances in sensor technology and data processing have revolutionised the amount of information we can get from depth, however, these techniques are too

coarse a scale to understand the metre-scale processes within an earthquake. To understand the physical processes that go on during an earthquake means that we have to look at the evidence preserved from faults exhumed from seismogenic depths including fault structure, geometry, thickness and composition. Even then we are looking at the frozen-in finite record of multiple earthquakes on a fault and have to peel away the record of the processes that occurred as the fault was exhumed. Recent studies involving high-velocity rock friction experiments are reviewed in DiToro *et al.* (2011), suffer from the limitations that they cannot constrain the full range of boundary conditions found at depth (in situ stress, temperature, pore pressure etc).

## 2.2. What do Earthquakes Teach us about the Internal Structure of Faults?

By examining classic fault mechanics laboratory data, Byerlee (1978) found that for crustal depths where brittle deformation dominates (upper ~10 km), most rocks have a friction coefficient ( $\mu$ ) in the range of 0.6-0.8. The coefficient of friction is expressed as equation (2.1):

$$\mu = \tau / (\sigma_n - p_f), \quad (\text{eq. 2.1})$$

where  $\tau$  is the fault-parallel shear stress,  $\sigma_n$  is the effective normal stress and  $p_f$  is the pore fluid pressure. However, these experiments neglect fundamental mechanisms that control friction at the scale of large faults (d'Alessio *et al.* 2003). To match observations of earthquake propagation, there has to be some dynamic weakening process that reduces friction from static values 0.6-0.8 to dynamic values of 0.2 (Scholz 2002). This can be confined to a single rupture patch that is susceptible to earthquake nucleation owing to its rate-weakening properties at low slip rates (Scholz 2002). Alternatively, sufficiently energetic ruptures may be able to propagate through stronger fault patches or fault patches that have not have accumulated stress or load (Sutherland *et al.* 2007; Noda & Lapusta 2013). This can activate coseismic weakening in creeping fault segments essentially changing the patch from being (interseismically) stable to (coseismically) unstable (Noda & Lapusta 2013).

Many investigations into potential processes responsible for dynamic friction drops, implicitly assume it is a single process. However, the frictional response of a fault to slip must be dependent on the properties of faults and given the variability of most mapped fault zones, the coexistence of multiple dynamic weakening mechanisms in a single earthquake is likely to be common (Kirkpatrick & Shipton 2009). Field observations suggest multiple slip weakening mechanisms are active at different scales during faulting resulting in spatially and temporally variable earthquake slip distributions and coseismic processes during a single rupture (Cohee & Beroza 1994; Ma *et al.* 2001; Mai & Beroza 2002; Kirkpatrick & Shipton 2009; Perrin *et al.* 2016).

Dynamic weakening during earthquake slip must be influenced by processes that operate along the principal slip surface within the fault core. Previous research has highlighted several mechanisms for which the dynamic reduction in frictional strength may be attained. These include thermally-driven processes such as thermal pressurisation (e.g., Sibson, 1973; Lachenbruch, 1980), flash heating (Rice, 2006; Goldsby and Tullis, 2011) and melt lubrication (Hirose and Shimamoto, 2005; Di Toro *et al.*, 2006; Di Toro *et al.*, 2011). These thermally-driven processes are activated by frictional heating during slip. Thermal pressurisation involves the thermal expansion of the pore fluid within the slip zone (e.g., Sibson, 1973; Lachenbruch, 1980). If the permeability is low and the fluid cannot escape, the pore fluid pressure increases, decreasing the effective normal stress and therefore the shear strength across the slip zone. Analyses of the fluid transport properties of exhumed faults, which generally present relatively low values of permeability, demonstrate that thermal pressurisation is likely to occur during large earthquakes (Wibberley & Shimamoto 2005; Mizoguchi *et al.* 2008). Flash heating involves heat generation at microscale to nanoscale asperity contacts across a sliding surface during rapid slip (Rice, 2006; Goldsby and Tullis, 2011). At larger values of slip, melt lubrication (Hirose and Shimamoto, 2005; Di Toro *et al.*, 2006; Di Toro *et al.*, 2011), or gel formation in silica-rich lithologies (Goldsby and Tullis, 2002; Di Toro *et al.*, 2004; Kirkpatrick *et al.*, 2013), may be the dominant weakening mechanisms. If frictional sliding generates sufficient heat, a continuous layer of melt can form, which due to its lower viscosity, will lubricate the slip surface

(Hirose & Shimamoto 2005). Pseudotachylytes, despite being rarely observed in the rock record due to their vulnerability to destruction (Sibson & Toy 2006; Kirkpatrick *et al.* 2009), are a product of melt lubrication during past seismic events (Sibson 1975). In all of these mechanisms, the rate of heating will depend on the properties (e.g. conductivity, heat capacity) and mineralogy of the rock being heated and on the thickness of the unit being heated – thinner layers heat faster than thicker layers. Thus, if the fault core has variable thickness, then the heating and consequently lubrication effect will also be variable (Kirkpatrick *et al.* 2018).

Other potential weakening mechanisms, such as elastohydrodynamic lubrication (Brodsky & Kanamori 2001) and acoustic fluidisation (Melosh 1996; Giacco *et al.* 2015), are less sensitive to temperature but are dependent on the permeability of fault rocks in and around the slip zone, the presence or absence of fluids and variable slip zone thickness (Rice 2006). Elastohydrodynamic lubrication involves the presence of a trapped, pressurised pore fluid in a narrow (1-5 mm thick) and slightly rough slip zone (Brodsky & Kanamori 2001). Analogous to lubricated bearings used in industrial applications, the trapped fluid lubricates the solid-solid interfaces as the viscous shear resistance of the fluid is lower than the friction between solids. During an earthquake, the energy released is partly absorbed by the fault and partly radiated to the surface as seismic waves (Kanamori & Rivera 2006). Acoustic fluidisation is the process by which radiated seismic waves are energetic enough to elastically deform the wall rock in the direction perpendicular to rupture propagation, which temporarily reduces the effective normal stress, facilitating fault slip at low shear stresses (Melosh 1996). However, as is the problem with many seismic models, both of these weakening processes are modelled on a variety of assumptions of a simplified fault zone and it remains unclear if they can occur in naturally variable fault zones.

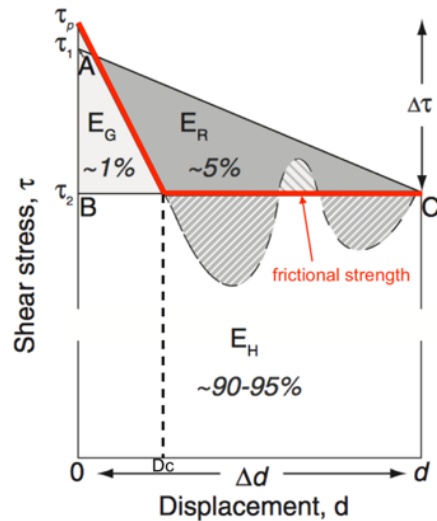
In naturally variable fault zones not only can the slip weakening mechanism vary along-strike as a result of varying fault properties (Kirkpatrick & Shipton 2009), seismic energy release and coseismic slip also varies (Wald & Heaton 1994; Ma *et al.* 2001; Mai & Beroza 2002; Perrin *et al.* 2016). For instance, due to variable fault zone

properties, seismic and rupture characteristics of the 1999 earthquake along the Chelungpu plate boundary in Taiwan varied along-strike (Heermance *et al.* 2003; Heermance & Evans 2006). The northern end of the fault saw high displacement (~11 m) and slip values, and consequently the greatest surface damage and casualties. However, despite having the greatest amount of high-frequency ground acceleration, the southern end of the fault near the epicenter had low displacement (~2 m) and slip values, and the resulting surface damage was minimal (Ma *et al.* 2001; Heermance *et al.* 2003). Thus, changes to variations in the fault's structure (i.e., fault type, clay thickness and geometry) controlled how the fault slipped (Heermance *et al.* 2003). This in turn limited the amount of radiated seismic energy and consequently surface severity and damage.

The seismic energy balance as defined by Kanamori & Anderson (1975; see also Kanamori & Brodsky, 2001 and references therein) states that the total energy released during an earthquake is partly absorbed on the fault plane by fracturing and frictional dissipation and partly radiated out of the source as seismic waves. This can be expressed simply as equation (2.2):

$$E_T = (E_G + E_F) + E_R \quad (\text{eq. 2.2})$$

where  $E_T$  is the total energy released,  $E_G$  is the fracture energy needed to create a new rupture surface,  $E_F$  is the frictional energy required to slide along that surface and  $E_R$  is radiated energy. This can be represented graphically as in **Fig. 2.4**.



**Fig. 2.4.** A graphical representation of the slip weakening model relating the partitioning of energy between fracture energy ( $E_G$ ), frictional energy ( $E_F$ ) and radiated energy ( $E_R$ ) to the shear stress acting on the fault ( $\tau$ ). Figure from Fulton et al. (2011).

Seismologically  $E_G$  and  $E_F$  are defined as separate terms. However, from a geological perspective, when considering the processes active along faults during slip events,  $E_G$  and  $E_F$  cannot be separated (Shipton et al., 2006a). This is because there are several physical processes that occur near the rupture front and in the surrounding damage zone that involve frictional and/or fracture energy (Shipton et al., 2006a). These include gouge production, cataclasis, fracturing in the damage zone, the dissolution and growth of minerals and the various slip weakening mechanisms discussed above. All of these consume energy, preventing it radiating to the surface. Together, they are referred to as the dissipative energy ( $E_G + E_F$ ). During repeated slip events, energy will continue to be dissipated by these processes in the fault zone (both in the fault core and damage zone).

The proportion of energy consumed by the fault compared to that radiated to surface as seismic waves depends on the structure of the fault (e.g., Kirkpatrick & Shipton 2009). For instance, the more complex the fault geometry, the more energy has to be consumed at depth during an earthquake and the less energy reaches the surface. As demonstrated by Wesnousky (2006), earthquake ruptures can jump across fault



segments, providing the fault step length is less than 3-4 km (**Fig. 2.1**). This was evident in the 1992 Landers earthquake where the rupture started on one fault segment and jumped across two steps to create a magnitude 7.2 earthquake (Wald & Heaton 1994). Extra energy will be consumed by the fault in order to hop over segments, allowing less energy to be radiated to the surface, manifested as lower magnitude earthquakes. In comparison, if the fault was smooth with less segments for the rupture to jump over, then less energy will be required by the fault, allowing more energy to be radiated to the surface. Fault zone geometry, composition, and physical properties are therefore integral to fault strength, stability, and dynamic processes during earthquakes.

### 2.3. Plate Boundary Faults

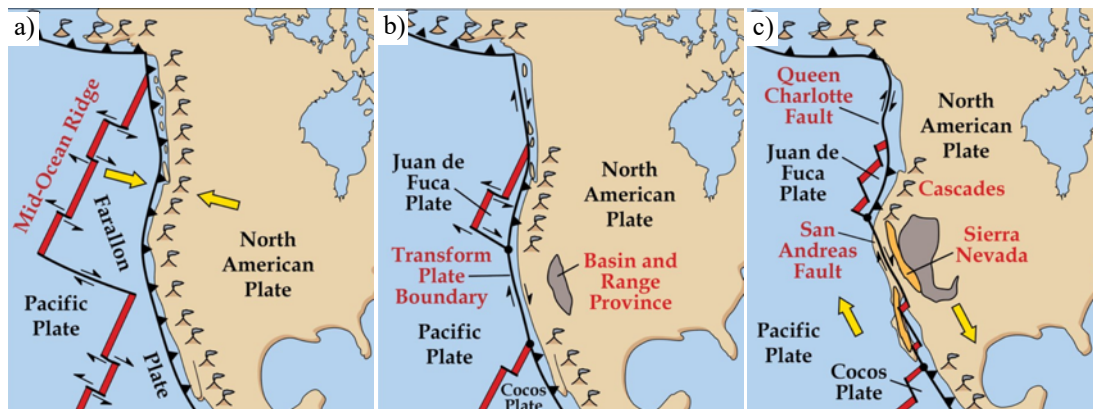
Despite the internal structure and physical properties of faults being integral to the dynamic processes that occur during earthquakes, knowledge of the internal structure of plate boundary faults is lacking (in part because they are difficult to study, see above). Plate boundary faults are those found at the intersection between two tectonic plates. The movement of the plates relative to each other distorts the crust in the region of the boundaries creating systems of faults capable of generating large magnitude earthquakes. As such, there is no standard definition of a plate boundary fault and it is unclear if these faults within plate boundary fault systems, or branches off the main fault trace, should be classed as a plate boundary fault. The main trace of the plate boundary can also shift through time as the plates constantly move relative to each other. For instance, today the Punchbowl and San Gabriel faults are dextral strike-slip faults that are part of the San Andreas fault system. However, during the Miocene and Pliocene epochs they likely represented the main trace of the plate boundary fault before being abandoned in favour of displacement along the present-day plate boundary fault known as the San Andreas fault (Chester & Logan 1986; Chester *et al.* 1993).

Recently several expensive drilling projects have been undertaken at active plate boundary faults in order to explore their internal structure and evolution at depth (e.g., the San Andreas fault in California [Bradbury *et al.* 2011], the Alpine fault in New

Zealand [Toy *et al.* 2015] and the Japan Trench [Kirkpatrick *et al.* 2015]). Yet given the high project costs and difficulty of studying large faults, opportunities like this are few. They are also limited in what they can tell us, effectively sampling only spatially limited '1D' transects across a fault, which limits the ability to capture the variability in the internal structure at different locations along the fault. Further, despite the fact that 90% of global seismicity (USGS 2016) occurs at plate boundary faults, there are no studies that comment on the earthquake energy balance and how plate boundary faults grow with repeated slip events. For instance, intraplate faults get thicker and smoother with increasing displacement (hence slip events) (**Fig. 2.3**). But do plate boundary faults show the same relationships? To answer this question, the growth of plate boundary faults must be considered.

### *2.3.1. Plate Boundary Fault Growth*

Plate boundary faults, found at the intersection between two tectonic plates, do not grow in the same way as intraplate faults. Tectonic plates are continually moving, albeit very slowly at a rate between 2.5 to 15 cm per year (USGS 2014) and are constantly rearranging themselves in response to each other. For instance, the boundary between the North American and Pacific Plate has evolved and grown through time from a subduction boundary to the present-day San Andreas transform fault (**Fig. 2.5**; Marshak 2001). 40 million years ago the Farallon plate, situated between the Pacific and North American plate, subducted beneath the North American plate forming a line of volcanoes (**Fig. 2.5a**). Beginning about 30 million years ago, when the mid-ocean ridge separating the Farallon and Pacific Plates entered the subduction zone, the Farallon Plate separated into the Juan de Fuca and Cocos Plates. When the Pacific and North American Plates were in contact a transform fault formed. To the east, the North American Plate began to rift forming the Basin and Range Province (**Fig. 2.5b**). Today, the Juan de Fuca Plate continues to be subducted beneath the North American Plate forming the Cascades and dextral strike-slip motion occurs along the San Andreas and Queen Charlotte Fault as the Pacific Plate moves northward past the North American Plate (**Fig. 2.5c**).



**Fig. 2.5.** Evolution of the San Andreas Fault System. a) 40 million years ago: subduction of the Farallon Plate beneath the North American Plate. b) 20 million years ago: mid ocean ridge separating the Farallon and Pacific Plates entered the subduction zone and formation of a transform plate boundary. c) Today: Continued subduction of the Juan de Fuca Plate beneath the North American Plate and dextral strike-slip motion between the North American and Pacific Plate along the San Andreas and Queen Charlotte Faults. Figure modified from Marshak (2001).

Plate boundary faults therefore start as pre-existing, inherited structures on regional-scale zones of weakness. As such, their tips do not terminate within intact rock - they terminate at triple junctions where three plate boundaries meet (McKenzie & Morgan 1969). Today off the west coast of America, triple junctions exist between the North American, Pacific and Juan de Fuca Plates and the North American, Pacific and Cocos Plates (Fig. 2.5c). As a result, while plate boundary faults still grow and evolve through time as triple junctions and plates move apart relative to each other, they are not required to grow in length either by damaging intact rock at their tips or by linking with other pre-existing structures (as shown for intraplate faults in Fig. 2.2). Their internal structure and evolution with repeated slip events would therefore be expected to be different to the more widely studied and thus understood intraplate faults.

Motivated by the need to advance our understanding of the internal structure and evolution of plate boundary faults, the purpose of this study is to examine the internal structure, fault core thickness and variability (both spatial and temporal) of an iconic past plate boundary fault in Scotland – the Highland Boundary fault. These observations are then be compared with observations from the peer-reviewed literature

to determine if plate boundary and intraplate fault evolve in the same way during repeated slip events.

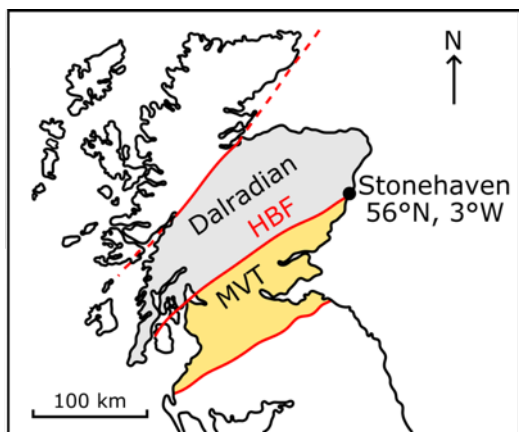
## 2.4. The Highland Boundary Fault

The Highland Boundary fault (HBF) is an important past plate boundary fault in the UK which has been the subject of many regional tectonic studies (e.g., Bluck, 1985; Cawood et al., 2012; Chew, 2003; Chew et al., 2010; Dewey and Strachan, 2003; Tanner, 2008; Tanner and Sutherland, 2007). While the HBF is well-characterised in terms of regional tectonic importance, the only studies discussing mineralisation of the fault focus on the wall rocks (on both sides), and do not address the internal fault zone structure.

The HBF is thought to have been active during two events of the Caledonian Orogeny: the early Ordovician Grampian Orogeny (480-460 Ma) and the mid-Devonian Acadian Orogeny (420-390 Ma) (Chew & Strachan 2014). Like the San Andreas fault system (**Fig. 2.5**), the HBF has grown and evolved through time. Early fault motion during the Grampian Orogeny was reverse before being reactivated in sinistral strike-slip during the Acadian Orogeny (Chew *et al.* 2010; Chew & Strachan 2014). The magnitude of sinistral strike-slip offset is debated (Dewey & Strachan 2003; Cawood *et al.* 2012). Like other terrane-bounding, crustal-scale Caledonian faults in Scotland it would not be surprising if the HBF accommodated minor motion more recently, associated with late Acadian orogenic collapse (Chew & Stillman 2009), Carboniferous extension (Kemp *et al.* 2019), North Sea extension (Fossen *et al.* 2016) or North Atlantic opening (Le Breton *et al.* 2013).

The remarkably straight fault trace extends for over 240 km NE to SW across Scotland and separates the Scottish Highlands (composed of the Dalradian Supergroup) from the Midland Valley (**Fig. 2.6**). It is exceptionally well-exposed along a coastal section ~1 km north of Stonehaven. Adjacent to the HBF near Stonehaven and at other locations along the fault (e.g., Comrie, Loch Ard forest, Cowal & Rosneath peninsulas and the Isle of Arran), intermittent serpentinite exposures with impersistent low-

alteration zones represent the dismembered Highland Border Ophiolite (see Leslie, 2009; Henderson *et al.*, 2009 for detailed reviews). Near Stonehaven the HBF juxtaposes distinct terranes: oceanic serpentinite of the Highland Border Ophiolite and quartzo-feldspathic crustal rocks of the Dalradian group. Such juxtaposition of quartzo-feldspathic crustal rocks with a serpentinite zone has been observed along active plate boundary faults (e.g., sections of the San Andreas fault in California [Moore & Rymer 2012] and the Alpine fault in New Zealand [Barth *et al.* 2013]) making the HBF a potential field analogue for the internal structure of these fault zones.



**Fig. 2.6.** Location of the Highland Boundary fault (HBF) and field site near Stonehaven on the northeast coast of Scotland. MVT: Midland Valley Terrane.

## 2.5. Summary

While a lot of work exists around the internal structure, evolution and mechanics of faults, for reasons stated above, most of this work is on small (in terms of length and displacement) intraplate faults. As field studies are biased towards features that are both exposed and visible at a scale that humans can realistically observe and measure (Shipton *et al.* 2019), there are few studies on large plate boundary faults. However, of the data that does exist, a compilation and comparison of the data between the two categories of fault systems has not previously been presented in the literature.

By using the HBF as a case example, this study, for the first time, provides insight into the internal structure of the HBF and compiles and compares data from plate boundary and intraplate fault systems. The results in the subsequent chapters provide geological

insights in the internal structure of plate boundary faults, the structural differences between plate boundary and intraplate faults and the implications for earthquakes.

# Chapter 3 – The Internal Structure of a Plate Boundary Fault. How Thick is the Highland Boundary Fault Core and How Variable is it?

*This chapter was published as: McKay, L., Shipton, Z.K., Lunn, R.J., Andrews, B., Raub, T.D., Boyce, A.J., 2020. Detailed Internal Structure and Along-Strike Variability of the Core of a Plate Boundary Fault: The Highland Boundary Fault, Scotland. Journal of the Geological Society, 177, 283-296. doi: 10.1144/jgs2018-226*

*A subset of this chapter was also published as the feature article in the Geological Society of London's fellowship magazine as: McKay, L., 2020. Core surprise: What's inside a plate boundary? Geoscientist, 30 (6), 11-15. doi: 10.1144/geosci2020-092*

*Note, following the Viva examination and recommendations from the examiners, minor additions and modifications have been made to this chapter that are not included in the published article (Appendix 1).*

## *Abstract*

The Highland Boundary fault near Stonehaven, NE Scotland, provides a rare opportunity to study the internal fault structure of a well-exposed, along-strike section of an ancient plate boundary fault. As in many plate boundaries, serpentinite juxtaposes quartzo-feldspathic crustal rocks of distinct terranes. We report, for the first time, the complex internal structure of the Highland Boundary fault core, composed of four structurally and chemically distinct clay-rich units that remain unmixed. Despite the evidence for internal strain, relatively intact clasts of wall rock and microfossils are preserved within the clay. The fault core clay mineralogy is consistent with a shallow, low-temperature authigenesis derived from shear-enhanced chemical reactions between wall rocks of contrasting chemistry during sinistral strike-slip. The observed structure is comparable to those of other major weak-cored plate boundaries (e.g. the San Andreas fault). Through detailed mapping, we demonstrate that the internal structure of a plate boundary fault core can vary in thickness and composition along-strike over centimetre- to metre- length scales. Earthquake rupture mechanics critically depend on the physical properties of fault rock assemblages. Therefore, models that investigate rupture propagation at active plate boundaries should incorporate, or else assess tolerance and sensitivity to, variable fault core thickness and composition.

### 3.1. Introduction

Understanding the internal structure of large faults is crucial because the chemical and mechanical properties of faults control how earthquakes rupture, nucleate and propagate (e.g., Caine *et al.* 1996; Wibberley *et al.* 2008; Faulkner *et al.* 2010). Geologists studying faults exhumed from depth have shown that they are heterogeneous along-strike and down-dip at a variety of scales (Faulkner *et al.* 2003; Heermance *et al.* 2003; Wibberley & Shimamoto 2003; Kirkpatrick *et al.* 2008, 2018; Barth *et al.* 2013; Lawther *et al.* 2016; Sosio De Rosa *et al.* 2018b). Such internal variations in properties can influence how readily a rupture begins and terminates (Kirkpatrick & Shipton 2009), limiting the size of an earthquake (Cohee & Beroza 1994; Kirkpatrick *et al.* 2008) or the frequency of the radiated seismic energy (Ma *et al.* 2003; Madariaga *et al.* 2006) and consequently surface severity and damage (Lin *et al.* 2001; Heermance *et al.* 2003; Ma *et al.* 2003). Knowledge of the internal structure and rheology of seismogenic plate boundary faults is lacking as they are normally poorly exposed at the surface.

Recently, several drilling projects have been undertaken to explore how the internal structure of active plate boundary fault zones at-depth influences slip behaviour (e.g., at the San Andreas fault in California, Bradbury *et al.*, 2011; the Alpine fault in New Zealand, Toy *et al.* 2015; the Japan Trench, Kirkpatrick *et al.* 2015; the Nankai Trough offshore Japan, Ujiie & Kimura 2014; and the Chelungpu fault in Taiwan, Yeh *et al.* 2007). Scientific findings for each of these projects highlight the presence and importance of clay-rich fault rocks for influencing slip behaviour. However, drilling projects are expensive (e.g., \$25M for SAFOD at the San Andreas; Winchester 2006) and effectively sample only one or two transects across a fault, limiting the ability to capture along-strike variability in fault zone properties.

In contrast, the Highland Boundary fault (HBF), NE Scotland, provides a rare opportunity to study the internal fault structure of a well-exposed, along-strike section of a major plate boundary fault. The HBF extends for >240 km along-strike separating Dalradian meta-sediments to the north from late Silurian to Early Carboniferous



volcanics and siliciclastics to the southeast (Tanner 2008; Fig. 1). This paper uses a field-based approach to characterise the along-strike variability in the internal structure of the HBF using an exceptional 560 m along-strike exposure of the fault near Stonehaven, NE Scotland. While the HBF is well-characterised in terms of its regional tectonic importance (e.g., Tanner 2008), the only studies discussing mineralisation of the fault zone focus on the wall rocks on both sides of the fault (e.g., Parnell *et al.* 2000; Elmore *et al.* 2002) and do not address the internal fault zone structure.

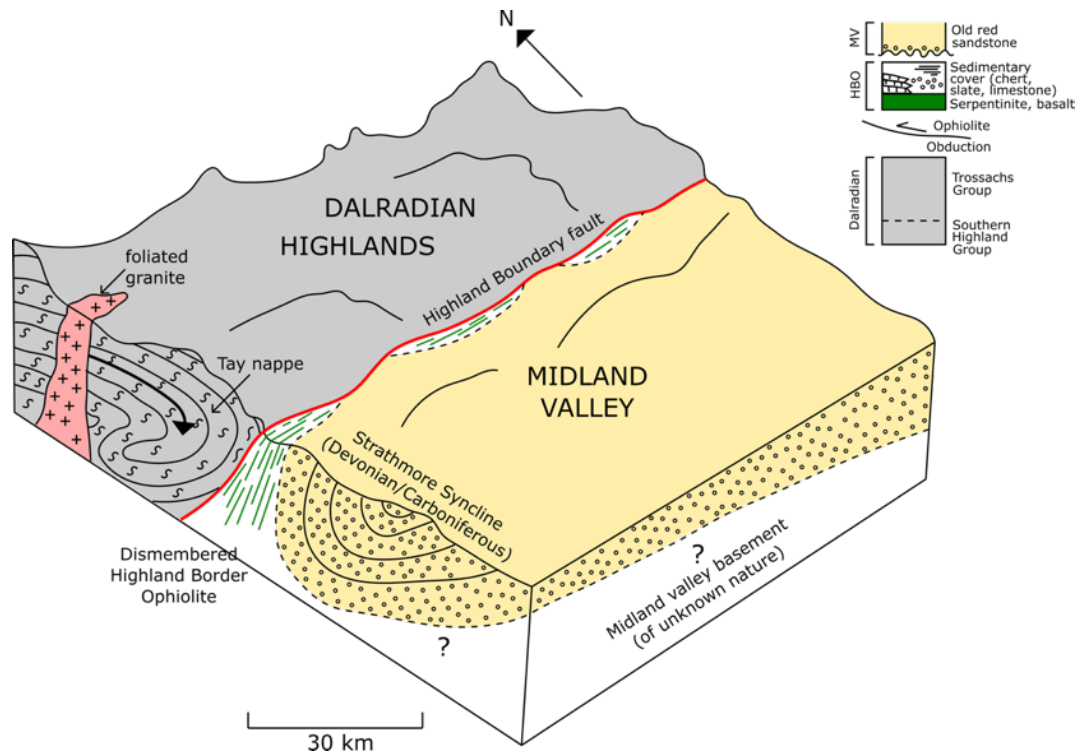
In this paper the first field observations of the internal structure and fault rock lithologies of the HBF are presented, and they are comparable to other plate boundary faults such as the San Andreas fault in California. By dissecting the modern-day physical and chemical properties of the fault (e.g., thickness, fault structures and mineralogy) we demonstrate the Stonehaven section of the Highland Boundary fault core is internally composed of four distinct structurally and mineralogically variable clay-rich units that vary in thickness along-strike over different length scales. As well as contributing to the understanding of the sequence of events at the Highland Boundary fault system, these observations of variable along-strike fault core internal structure, composition and thickness have implications for modelling earthquake ruptures at active plate boundaries.

### 3.2. Geological Setting: The Highland Boundary Fault

The HBF is a mature, ancient plate boundary fault with a long and complex history. Today, the remarkably straight surface trace extends for over 240 km NE to SW across Scotland, with possible along-strike extension into western Ireland (Chew 2003; Tanner 2008). The fault separates two distinct geological terranes: the Neoproterozoic to Cambrian, crustal, quartzo-feldspathic metasedimentary rocks (Dalradian Supergroup) of the Grampian terrane to the north from Lower Devonian/Carboniferous, volcano-sedimentary rocks of the Midland Valley terrane (e.g., Stonehaven Group) to the south (**Fig. 3.1**).

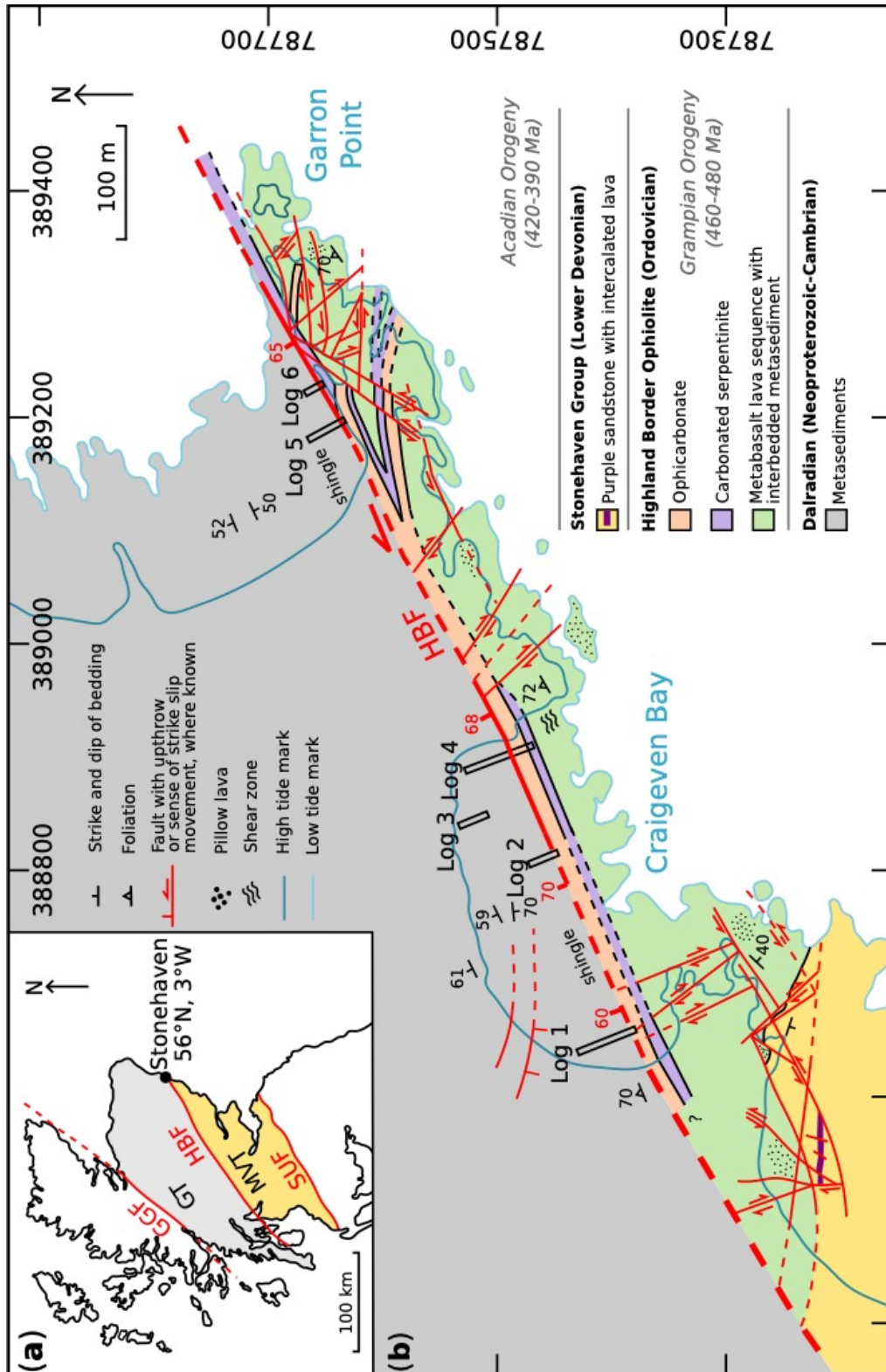
The Dalradian Supergroup is a sequence of metasedimentary rocks (primarily turbidite facies psammitic and pelitic sediments) with rare sedimentary carbonate beds and intermittent mafic volcanic rocks that were all deformed and metamorphosed during the Grampian Orogeny (Stephenson *et al.*, 2013, and references therein). The Grampian Orogeny (480-460 Ma) controlled the overall stratigraphy of the Dalradian leading to the development of major nappe structures as shown in **Fig. 3.1**, minor folding and locally developed fabrics (Harte *et al.* 1984; Stephenson *et al.* 2013). Deformation occurred during regional Barrovian metamorphism (Harte *et al.* 1984). Metamorphic grade increases from chlorite-biotite grade greenschist facies near the HBF through the north-eastern extension of Barrow's chlorite, biotite, garnet, staurolite zones to amphibolite facies north of the fault (Masters *et al.* 2000). The easternmost exposures of the Dalradian near Stonehaven experienced low pressure chlorite-grade, greenschist facies metamorphism (0.4 to 0.55 GPa) with peak temperatures of c. 375 °C (Vorhies & Ague 2011). The maximum burial depth of the Stonehaven group was 3-5 km as determined from vitrinite reflectance (Monaghan 2014).

The Midland Valley terrane is a fault-bounded, WSW–ENE trending Late Palaeozoic sedimentary basin, bounded by the HBF to the north and the Southern Upland Fault to the south (**Fig. 3.2a**) (Monaghan 2014). It consists of an internally complex arrangement of Carboniferous sedimentary basins and Carboniferous volcanic rocks overlying Lower Palaeozoic strata (Monaghan 2014).



**Fig. 3.1.** Block diagram illustrating the tectonic setting of the Highland Boundary Fault. The diagram is a composite, incorporating information from a number of outcrops across Scotland. The orientation of the faulted contact between the Dalradian Supergroup and the Highland Border Ophiolite (HBO) is variable across Scotland, and other local variations in HBO geology have not been incorporated in this stylised summary of HBO relationships and internal structure. Figure modified from Curry (1986) and stratigraphy from Tanner & Sutherland (2007).

Adjacent to the HBF near Stonehaven and at other locations along the fault (e.g., Comrie, Loch Ard forest, Cowal & Rosneath peninsulas and the Isle of Arran), intermittent serpentinite exposures with impersistent low-alteration zones represent the dismembered Highland Border Ophiolite (see Leslie, 2009; Henderson *et al.*, 2009 for detailed reviews) (**Fig. 3.1**, **Fig. 3.2**). An ophiolite is an assemblage of rocks commonly associated with plate boundary faults (e.g. the well-studied Troodos ophiolite in Cyprus or Semail ophiolite in Oman). Such juxtaposition of quartzofeldspathic crustal rocks with a serpentinite zone has been observed along active plate boundary faults (e.g., sections of the San Andreas fault in California [Moore & Rymer 2012] and the Alpine fault in New Zealand [Barth *et al.* 2013]) making the HBF a potential field analogue for the internal structure of these plate boundaries.



**Fig. 3.2.** Our geological map of the Highland Boundary fault (HBF) near Stonehaven, NE Scotland. (a) Simplified geological map of Scotland indicating the location of the study site near Stonehaven. GT, Grampian Terrane; MVT, Midland Valley Terrane; GGF, Great Glen fault; SUF, Southern Uplands fault. (b) The HBF along the coastal section c. 1 km north of Stonehaven. The location of the six structural logs are indicated by the black rectangles.

The HBF is considered to have been active during two events of the Caledonian Orogeny: the early Ordovician Grampian Orogeny (480 to 460 Ma) responsible for the associated deformation and metamorphism in the Dalradian, and the mid-Devonian Acadian Orogeny (420 to 390 Ma) (Chew & Strachan 2014). Early fault motion was believed to be reverse, inheriting the subduction interface and emplacing the Highland Border Ophiolite 490 Ma, immediately prior to the Grampian Orogeny (Ramsay 1962; Chew *et al.* 2010). The Highland Border Ophiolite is a mixture of both collisional (Penrose) type sequences (Chew *et al.* 2010) and Ligurian-type ophiolites, including seafloor supporting latest stages of Dalradian sedimentation in an extensional ocean–continent transition environment (Henderson *et al.* 2009; Leslie 2009; Dilek & Furnes 2014). It probably also incorporates more allochthonous ocean crust, especially proximal to the HBF zone (Chew *et al.* 2010; Chew & Strachan 2014). Tanner & Sutherland (2007), suggest the HBO lies in stratigraphy continuity with the Dalradian. Therefore, the HBO also experienced overprinting by Grampian metamorphism and deformation ca. 465 to 461 Ma (Viète *et al.* 2013).

Following the Grampian Orogeny, the continental collision of Laurentia with Avalonia was accommodated by partitioned transpressive, sinistral strike-slip movement on the HBF and related faults (McCarthy *et al.* 2015) during the Acadian Orogeny ca. 420 Ma (Chew & Strachan 2014). Tanner (2008), suggests the formation of the Strathmore Syncline, a primary fold in the Midland Valley terrane (**Fig. 3.1**), formed in conjunction with this sinistral strike-slip motion. The axial trace of the Strathmore Syncline runs parallel to the HBF for >200 km and its axial plane has a dip similar to that of the fault (Tanner 2008).

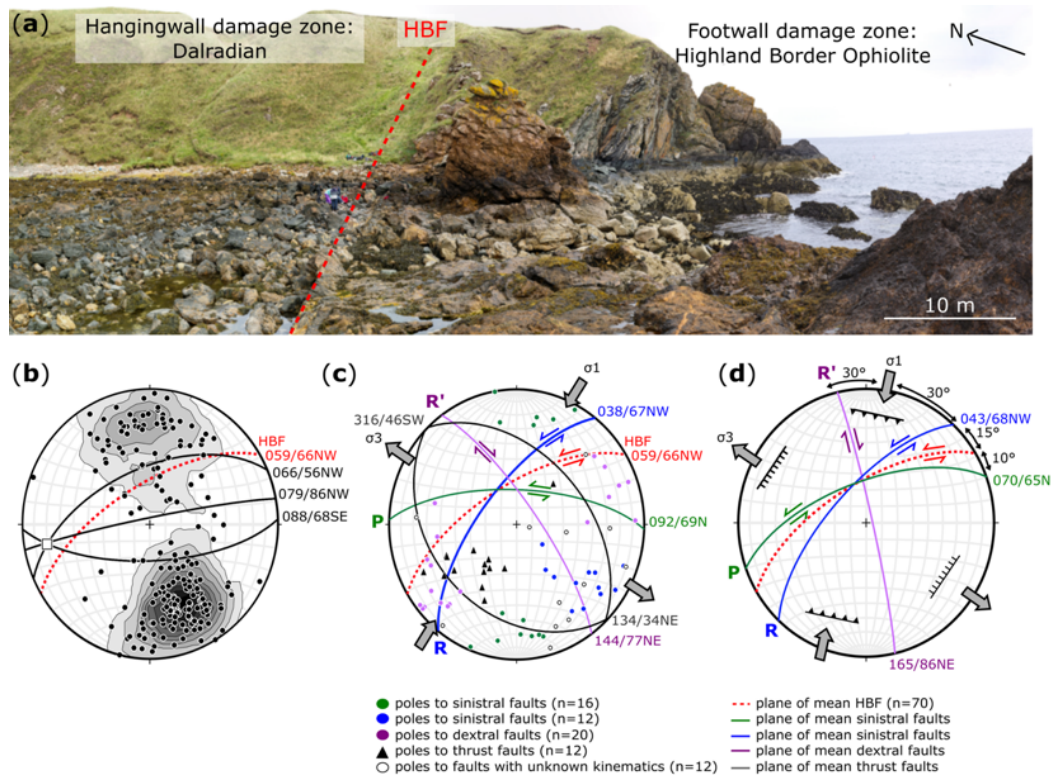
The magnitude of strike-slip displacement on the HBF is debated. Based on palaeogeographical reconstructions and detrital zircon data from both the hangingwall and footwall of the fault, Dewey & Strachan (2003) and Cawood *et al.* (2012) support significant sinistral offset of up to several hundreds of kilometres; whereas, Tanner (2008) compiles the case for an alternative minimum offset of <30 km.

The HBF was probably reactivated during late Acadian orogenic collapse as a result of regional crustal extension (Chew & Stillman 2009; Mendum & Noble 2010). Other terrane-bounding, crustal-scale Caledonian faults in Scotland were reactivated with sinistral displacement during Carboniferous extension (Kemp *et al.* 2019), dextral and normal offset in the Mesozoic during North Sea extension and in the Cenozoic as Scotland exhumed regionally on the flanks of North Atlantic opening (e.g., Le Breton *et al.* 2013). It would not be surprising if the HBF accommodated minor motion at these younger ages.

### 3.3. Structural Framework

Our field observations suggest the HBF near Stonehaven is marked by a relatively straight, steep (dip:  $66 \pm 7^\circ$ ;  $n=70$ ), north-west dipping contact (strike:  $059 \pm 8^\circ$ ;  $n=70$ ) between the fault core and Highland Border Ophiolite (footwall damage zone) (**Fig. 3.3a**). A major splay of unknown offset, and with no development of clay gouge, is observed trending east to west towards Garron Point (**Fig. 3.2b**). New mapping as part of this study highlights numerous small offset ( $\sim 5$ -10 m), sinistral and dextral strike-slip faults within the Highland Border Ophiolite (footwall damage zone) towards Garron Point (**Fig. 3.2b**). Kinematic markers, primarily slickenfibres recorded on calcite mineralised slip surfaces enable these faults to be grouped into one dextral and two sinistral sets that are subdivided based on orientation with respect to the mean HBF (**Fig. 3.3c**). The dextral set has a mean strike of  $144 \pm 18^\circ$  ( $n=20$ ) and a north-easterly dip of  $77 \pm 11^\circ$  ( $n=20$ ) developing  $\sim 80^\circ$  anticlockwise from the mean HBF. The first sinistral set has a mean strike of  $038 \pm 11^\circ$  ( $n=12$ ) and a north-westerly dip of  $67 \pm 19^\circ$  ( $n=12$ ) developing  $\sim 19^\circ$  anticlockwise from the mean HBF. The second sinistral set has a mean strike of  $92 \pm 24^\circ$  ( $n=16$ ) and a northerly dip of  $69 \pm 14^\circ$  ( $n=18$ ) developing  $\sim 30^\circ$  clockwise from the mean HBF. Several small-scale ( $<1$  m offset) thrust faults are also observed below the scale of mapping. In places, these thrust faults sole onto strike-slip faults. No consistent cross-cutting relationships are observed, suggesting they all formed concurrently. If these faults represent Reidel shears to the main fault, they fit with sinistral strike-slip motion on the HBF (**Fig. 3.3d**).

We see no field-scale evidence for late-stage dextral or normal offset that would be consistent with Mesozoic and Cenozoic reactivation.



**Fig. 3.3.** Damage zone deformation of the HBF. **(a)** Field photograph of the HBF at the northern end of Craigeven Bay looking NE [grid reference NO 8870 8740]. **(b)** Stereographic projection of poles to Dalradian bedding showing the mean bedding planes and the interpreted fold axis (Kamb contours of interval  $2\sigma$  and confidence level 3). **(c)** Stereographic projection of field data on small faults associated with the HBF consistent with strike-slip faulting. Poles to all faults in the Highland Border Ophiolite and the mean planes of sinistral, dextral and thrust faults can be interpreted within the framework of a strike-slip strain ellipse for sinistral motion of the HBF (separated based on kinematic markers in the field). Mean planes were determined from contour maps. There are numerous faults where the sense of motion cannot be determined (unfilled); however, they are not outliers and can be grouped into one of the three sets. The principal stress axes are inferred from kinematic data. **(d)** Ideal strike-slip strain ellipse for comparison, assuming symmetry of the Reidel shears around a fault with pure strike-slip. All stereonet plots were created using Stereonet 10 software.

### 3.4. Methods

To characterise the internal structure of the HBF and its along-strike variability, we applied for, and were granted permission from the Scottish Natural Heritage to scrape

back the shingle below the high tide mark. Six across-fault transects (structural logs) were collected perpendicular to the fault plane (**Fig. 3.2b**). All logs except Log 3 mapped the fault core. Log 3 investigated the folding and maximum extent of the Dalradian damage zone. To expose the fault core for mapping and sampling, we gathered a group of geologists from the University of Strathclyde's Faults and Fluid Flow research group and travelled from Glasgow to Stonehaven in order to 'dig' out the fault (**Fig. 3.4**).



**Fig. 3.4.** *The University of Strathclyde's Fault and Fluid Flow research group 'digging' for the Highland Boundary fault near Stonehaven.*

The shingle below the high tide mark was scraped back using spades and trowels along as linear a transect as possible (**Fig. 3.5**). This was easier said than done as in places the shingle layer was very deep and we had to avoid some very large boulders. Several measurements were made in the field including clast size (the length of both the long and short axis), clast orientation (the orientation of the long axis) and fabric orientation. Clast shape was assessed visually and not calculated.



After mapping and sample collection, the shingle was replaced to maximise conservation before tide covered the study area. The site is an important Site of Special Scientific Interest and we wished to ensure that the work left no permanent mark. We returned after six weeks to confirm that the area that we had excavated was indistinguishable. On a separate trip, and with further permission from the Scottish Natural Heritage, a series of eighteen logs 1 m apart were also collected between Logs 5 and 6 to capture the smaller, metre-scale variability of the fault core. In this study and throughout the thesis, we describe the fault breccias following the classification of Woodcock & Mort (2008).



**Fig. 3.5.** *Exposing the clay within the Highland Boundary fault core.*

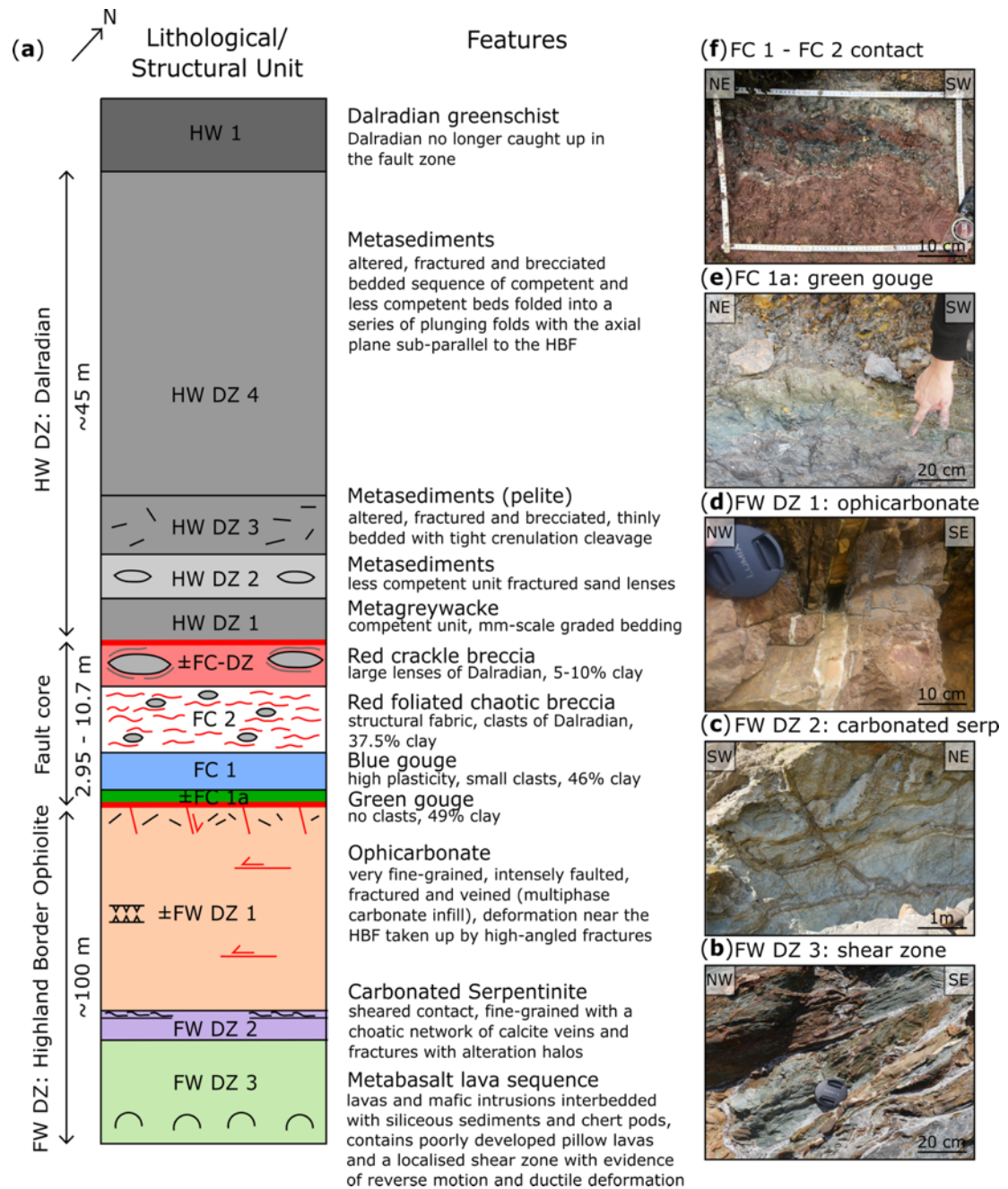
Twelve samples from Log 4 [grid reference NO 388914 787493] were analysed by X-ray diffraction (XRD). These include one representative sample from each of the three fault core units, two samples of the clasts within the red foliated chaotic breccia, six damage zone samples from the Highland Border Ophiolite and Dalradian and one from the Dalradian host rock. ~10 g of each sample was oven dried before grinding to a fine powder with a mean particle diameter of 5 to 10 microns before analysis. Randomly oriented samples were analysed for whole-rock mineralogy. Highland Border Ophiolite and Dalradian powders were analysed using a Bruker D8 Advance Diffractometer, scanning from 5° to 60° at 0.02° 2 $\theta$  step-size intervals at 40 kV and 40 mA (Cu-K $\alpha$  radiation). Clay powders were analysed by X-Ray Minerals Ltd. using a PANalytical X'Pert3 Diffractometer and scanned from 4.5° to 75° at 0.013° 2 $\theta$  step-

size intervals at 40 kV and 40 mA (Cu-K $\alpha$  radiation). An intensity-based quantification analysis was performed where the maximum intensity of each mineral identified was measured and compared to a standard intensity for a pure sample of that mineral. The results were normalised to 100% based on the assumption that the complete mineral content of the sample is accounted for in the diffractogram.

Additionally, the <2  $\mu\text{m}$  fraction was separated, to identify clay mineral phases following Moore & Reynolds (1997). Samples were placed on orientated mounts and analysed before and after treatment with ethylene glycol and heating to 380°C and 550°C using a Philips PW1730 Generator Diffractometer. Air-dried and glycolated samples were scanned from 3° to 35° at 0.05° 2 $\Theta$  step-size intervals at 40 kV and 40 mA (Cu-K $\alpha$  radiation). The untreated sample was also analysed between 24 to 27° at 0.02° 2 $\Theta$  step-size intervals to further define kaolinite and chlorite peaks. Chlorite, illite, and mixed-layer illite-smectite determination was based on the comparison between air-dried and glycolated samples and a peak intensity quantification process. Specific peak thicknesses indicate clay crystallinity. Relative intensities of the chlorite 001 and 003 peaks determined Fe occupancy in the six octahedral sites.

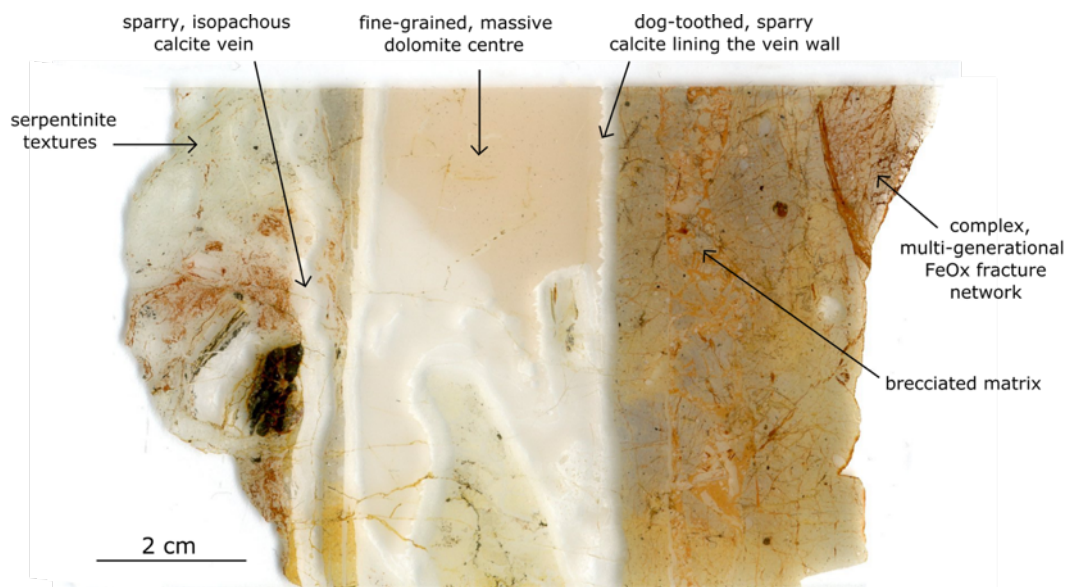
### 3.5. Structure of the HBF Fault Zone

The internal structure of the HBF can be described as a single high-strain fault core bounded by damage zones of contrasting lithology. From south to north in an across-fault transect, the HBF consists of: (1) a footwall damage zone (FW DZ) comprising faulted and veined metabasalt and serpentinite sequences of the Highland Border Ophiolite; (2) a structurally and lithologically variable fault core (FC) comprising four distinct units, and; (3) a hangingwall damage zone (HW DZ) developed in chlorite- to biotite-grade Dalradian metasedimentary rocks (**Fig. 3.6**).



**Fig. 3.6.** Summarised fault zone structure. (a) Schematic structural log illustrating the units within the fault core (FC) and footwall and hanging-wall damage zones (footwall damage zone and hangingwall damage zone, respectively) of the HBF. The structural log schematically highlights the typical fabrics in each unit. The tick marks and other ornamentation within the units correspond to foliations. The ± symbol indicates that the unit may or may not be present in all structural logs. (b) Shear zone in metabasalt lava sequence (footwall damage zone 3) [grid reference NO 388953 787474]. (c) Fractures with alteration halos in carbonated serpentinite (footwall damage zone 2) [grid reference NO 388939 787494]. (d) Multiphase carbonate veining in ophicarbonite (footwall damage zone 1) [grid reference NO 388931 787496]. (e) Green gouge (FC 1a) between ophicarbonite wall rock to the SE and the blue gouge unit to the NW (Log 4 only) [grid reference NO 388914 787493]. (f) The contact between the blue gouge (FC 1) and the red foliated chaotic breccia (FC 2) indicating localized mixing [grid reference NO 389201 787640].

The footwall damage zone of the Highland Border Ophiolite is characterised by three distinct units. In logs 1-5 the footwall damage zone adjacent to the fault core (footwall damage zone 1) is characterised by an intensely faulted, fractured and veined, buff coloured dolomitised serpentinite properly termed ophicarbonates. Veins in this unit are ~2 to 10 cm thick and are filled by multiphase carbonate including very fine-grained, massive dolomite in the centre with isopachous, sparry calcite lining the vein wall (**Fig. 3.6d, Fig. 3.7**). The calcite displays a dog-toothed epitaxial texture, indicative of crack-seal growth and extensional opening mode fractures. The veins are typically aligned sub-parallel to the HBF but can be split into two distinct sets based on dip and cross-cutting relationships (set 1: 062/67NW, n=67, crosscut by set 2: 111/21NE, n=11).



**Fig. 3.7.** *Multiphase carbonate vein in ophicarbonates.*

The second unit (footwall damage zone 2), adjacent to the HBF in Log 6, is a carbonated serpentinite displaying a chaotic network of cross-cutting calcite veins. This unit is cut by localised, sub-horizontal fractures with an alteration halo (**Fig. 3.6c**). The fractures have an anastomosing, conjugate geometry composed of curvy, cross-cutting, brittle cracks. Orange to brown, calcitic alteration halos extend ~3 cm either side of the fractures, where the alteration is symmetrical around the aperture. The alteration follows the same geometry as the fractures and can be traced into the

ophicarbonatite unit. The third unit (footwall damage zone 3) is a fractured metabasalt lava sequence with interbedded ferruginous chert and siliceous siltstone/shale, sporadic pillow lavas and a localised shear zone with evidence of reverse motion and ductile deformation (**Fig. 3.6b**). Damage zone alteration decreases away from the HBF with the ophicarbonatite unit displaying the most fault-related deformation (i.e., subsidiary faulting, fractures and veining).

The Dalradian north of the HBF is composed of a succession of competent (e.g., metagreywacke) and less competent (e.g., pelite) beds. Beds within the hangingwall damage zone are folded into a series of open, plunging folds (wavelength ~5 m) with the axial plane sub-parallel to the HBF (079/86NW; **Fig. 3.3b**), and display evidence of fault-related deformation such as alteration, subsidiary fractures and brecciation. Fault-related deformation is absent beyond approximately 45 m. We consider this the extent of the hangingwall damage zone.

### 3.6. Fault Core Lithologies

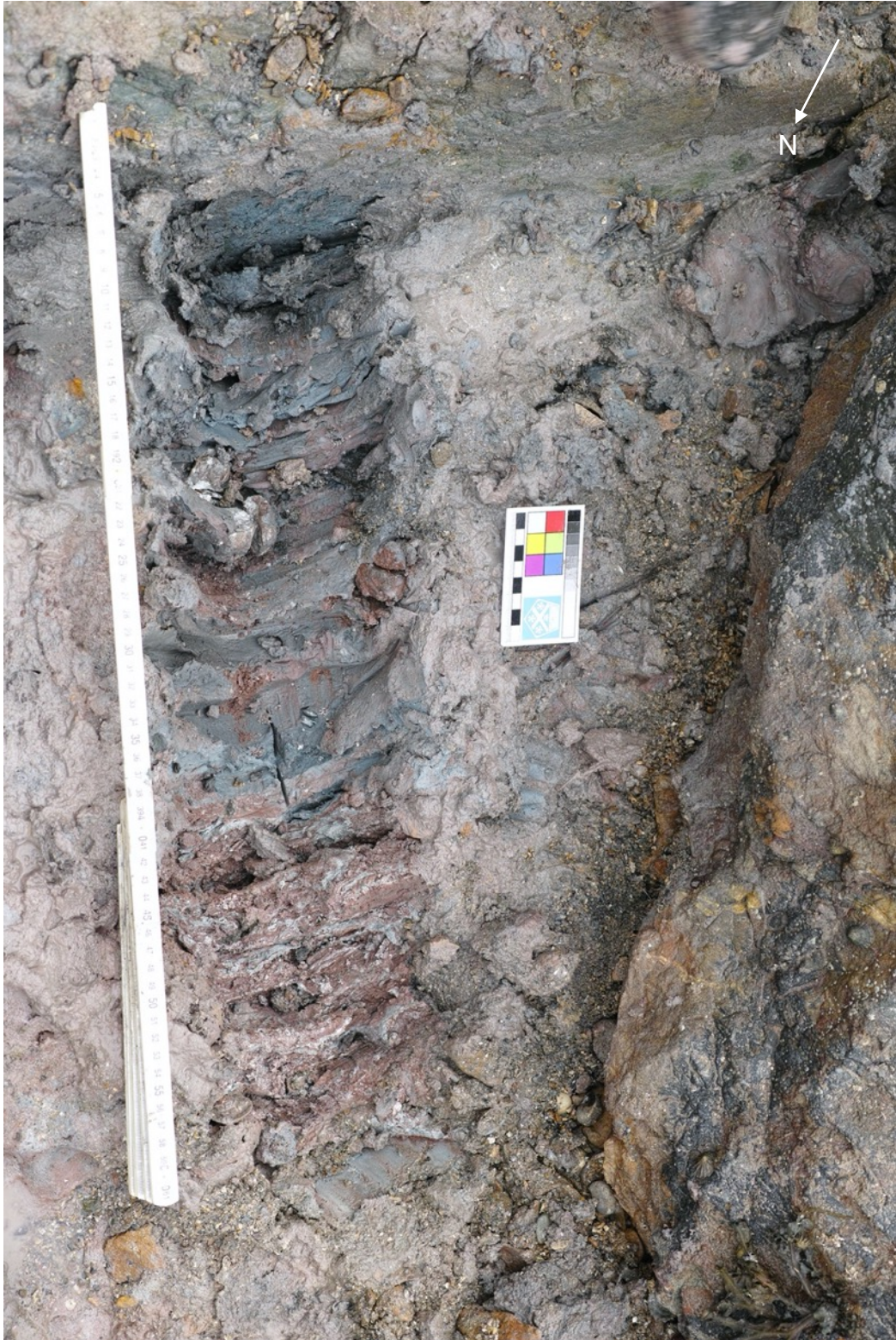
The fault core, which is between 2.95 (Log 4) and 10.7 m (Log 5) thick, comprises four structurally and chemically distinct units with sharp, fault-parallel contacts. Adjacent to the HBF, observed at Log 4 only, is a zone of green foliated gouge (fault core 1a) that is relatively homogenous and free of obvious clasts (**Fig. 3.6e**). This is in sharp contact with a zone of a blue gouge (fault core 1) of high plasticity that was exactly like modelling clay (**Fig. 3.8, Fig. 3.9**). In fact, a member of our team even managed to model a fish out of the clay in the field (**Fig. 3.8**), which demonstrates the nature of the clay (i.e., plasticity and impermeability). In places this blue gouge unit is internally foliated, the foliations being sub-parallel to the HBF ( $070 \pm 15^\circ$ ;  $n=17$ ) (**Fig. 3.10b**). Small (typically <5 cm diameter), sub-rounded clasts of wall rock are observed within this unit altered to a bleached white colour. Occasionally larger, fragmented, altered clasts are observed (**Fig. 3.11a**).



**Fig. 3.8.** *Modelling a fish in the field out of the blue clay.*

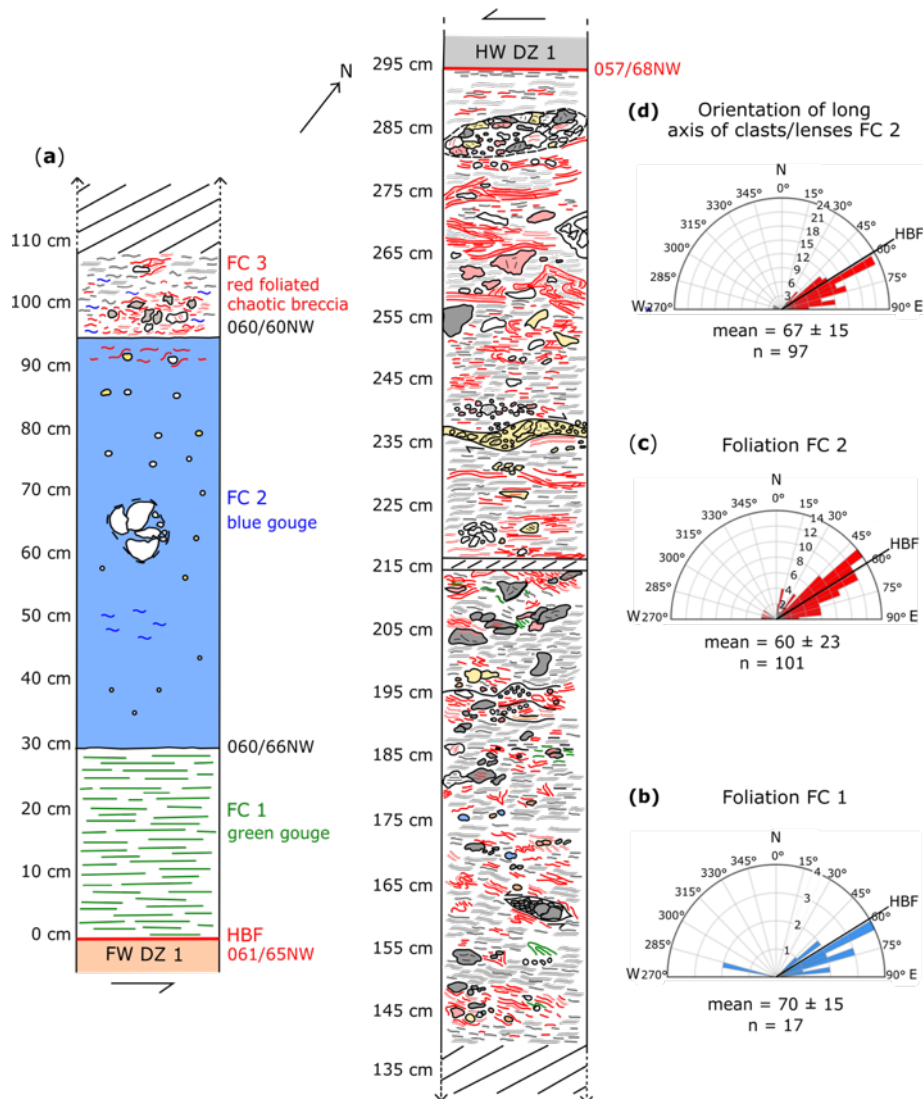
Towards the hangingwall damage zone the blue gouge has a distinct fault-parallel contact with a red foliated chaotic breccia unit (fault core 2) (**Fig. 3.9**, **Fig. 3.10a**). A localised zone of mixing (10 to 50 cm thick) is observed against the sharp contact, where the zone of mixing extends into both units either side of the contact (**Fig. 3.6f**, **Fig. 3.11a**). This zone consists of distinct patches and stripes of red and blue clay. The foliated chaotic breccia unit has a grey silty texture with red, hematitic foliations that define a clear structural fabric (**Fig. 3.12**). The compositional (colour) foliations are generally aligned parallel to the HBF with a mean orientation of  $060 \pm 23^\circ$  ( $n=101$ ) (**Fig. 3.10c**) but anastomose and wrap around variably altered, sub-angular, centimetre-scale, metasedimentary clasts of the Dalradian. In places the foliation is internally folded (**Fig. 3.11b**). Clast size, aspect ratio and abundance increase towards the hangingwall (**Fig. 3.10a**). For example, clasts within the blue gouge have a mean long axis of 1 cm ( $n=8$ ) and a mean aspect ratio of 1.7 ( $n=8$ ). Within the red foliated chaotic breccia, the clasts have a mean long axis of 19 cm ( $n=65$ ) elongate parallel to the HBF and a mean aspect ratio of 2.8 ( $n=65$ ). Several clasts can be described as lens-shaped boudins with the long axis (orientation  $076^\circ$ ) parallel to the HBF, indicating asymmetric shear fractures parallel to the HBF (**Fig. 3.10a**).

At Logs 5 and 6, the transition zone between the fault core and hangingwall damage zone comprises a red crackle breccia with large, fragmented, metasedimentary lenses of Dalradian up to 2.3 m long. Thin (< 5 cm and typically < 1 cm) zones of foliated clay (clay content 5 to 10%) are observed between, and wrapping around the lenses (**Fig. 3.11c**). The lenses have a mean long axis of 81 cm (n=32) and a mean aspect ratio of 3.3 (n=32). All clasts and lenses within the fault core have a preferred orientation and are elongate in the direction parallel to the HBF with a mean apparent long axis orientation of  $067 \pm 15^\circ$  (n=97) on a sub-horizontal exposure (**Fig. 3.10d**), and clasts observe to be dipping parallel to the dip of the footwall damage zone contact. The clay content generally decreases away from the HBF with a concomitant increase in size and angularity of clasts/lenses.

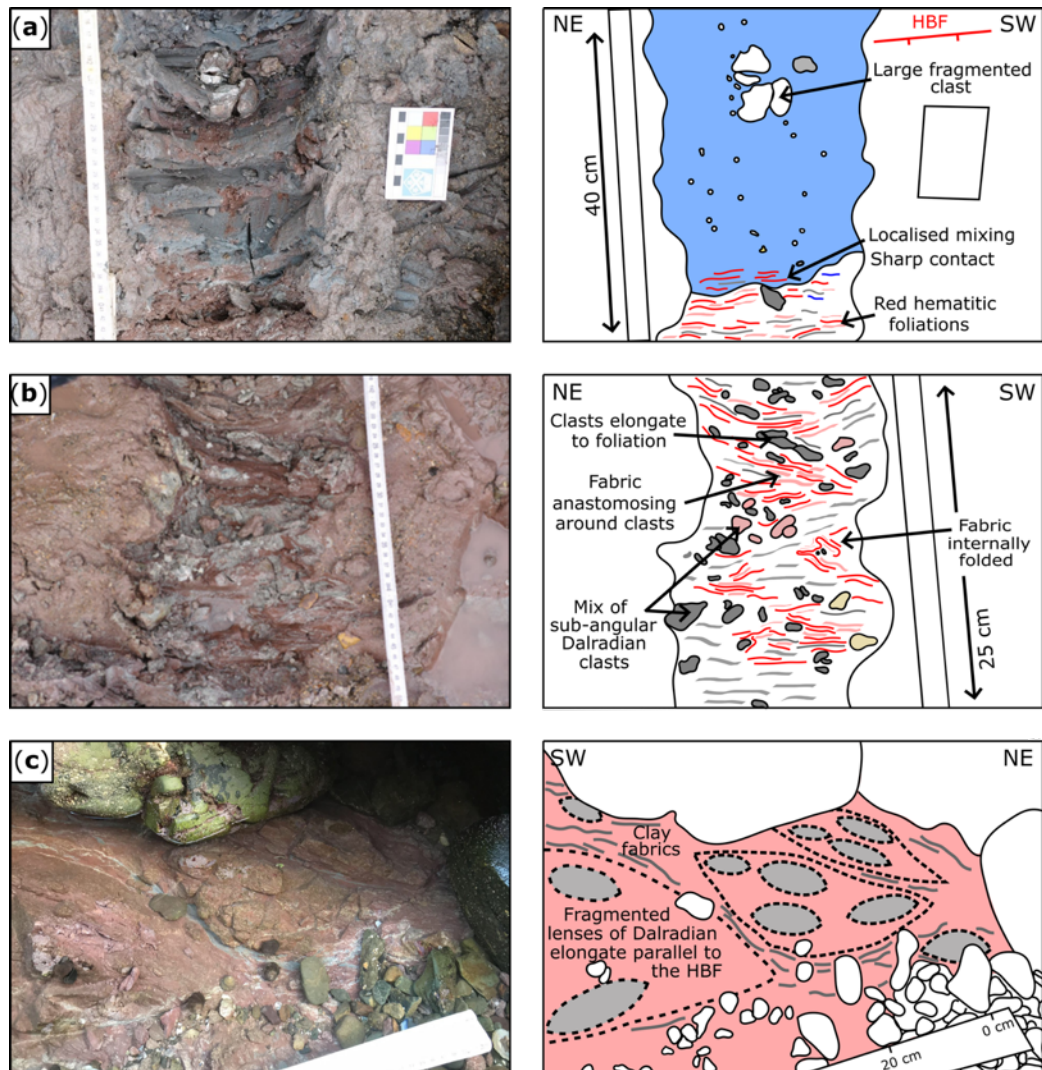


**Fig. 3.9.** Field exposure of the blue gouge from Log 4 [grid reference NO 388914 787493]. Note the sharp contact between the blue gouge and red foliated chaotic breccia. The indents are spade marks from digging.





**Fig. 3.10.** Centimetre-scale variations in the FC units. (a) Detailed sketch of the FC from Log 4. Clast sizes and foliation thicknesses are exaggerated ( $\times 2$ ) for illustration purposes. The variation in clast composition (colour) is also shown with sandier wall rock clasts depicted in yellow. (b) Rose diagram of the foliations from the blue gouge (FC 1) (all logs). (c) Rose diagram of the foliations from the red foliated chaotic breccia (FC 2) (all logs). (d) Rose diagram of the orientation of the long axis of the clasts and lenses from both the red foliated chaotic breccia (FC 2) and the red crackle breccia from the fault core–hangingwall damage zone transition (all logs).



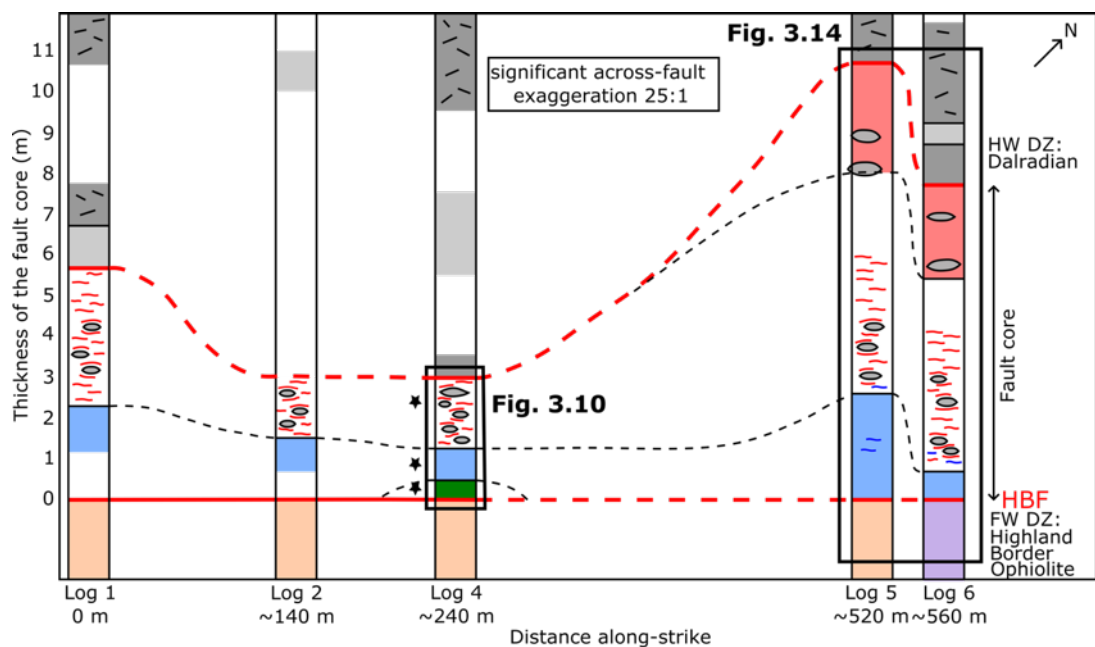
**Fig. 3.11.** Photographs and detailed sketches of the fault core units. The fault core clays were wet and sticky meaning that attempts to clean the outcrop resulted in smearing of the clays across the surface. The internal structure was therefore exposed by lifting out sections of the clay with a shovel-tip. This left an irregular surface that did not photograph well, but which could be logged and sampled in the field. **(a)** Blue gouge (FC 1). The indents in the photograph represent the spade marks from digging [grid reference NO 388914 787494]. **(b)** Red foliated chaotic breccia with clear structural fabrics (FC 2) [grid reference NO 388914 787495]. **(c)** Red crackle breccia with large, fragmented lenses of Dalradian in the fault core–hangingwall damage zone transition zone [grid reference NO 389238 787664]. The ‘clasts’ that are white are shingle.



**Fig. 3.12.** Field photograph of the red foliated chaotic breccia from Log 4[grid reference NO 388914 787493].

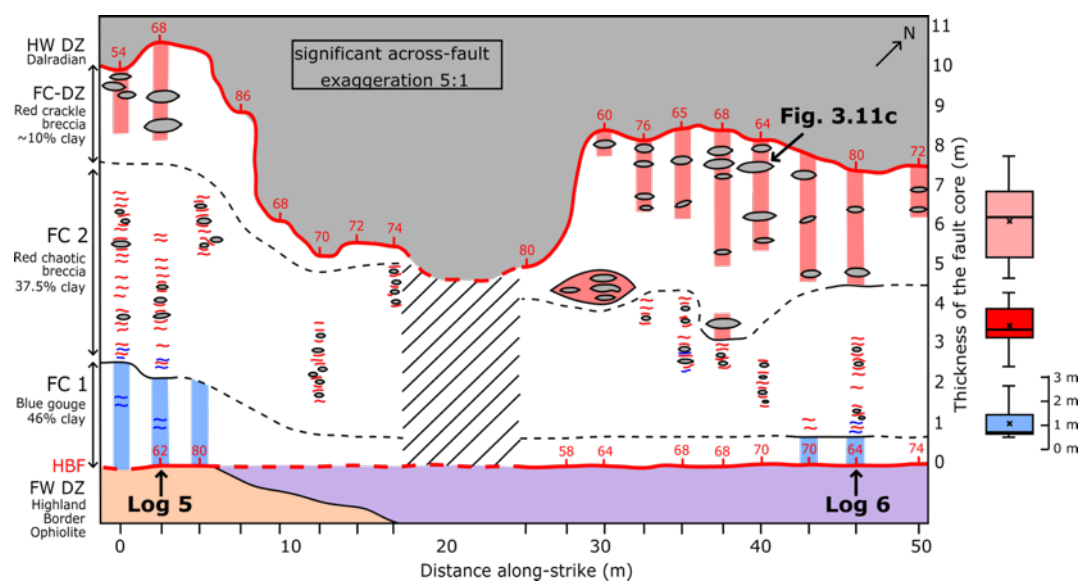
### 3.7. Fault Core Variability

Not every unit is laterally continuous along-strike, and each fault core unit varies in thickness over different length scales (**Fig. 3.13**, **Fig. 3.14**). Observations from the six structural logs reveal the total thickness of the fault core varies from 2.95 to 10.7 m over an along-strike distance of 560 m (**Fig. 3.13**). Every unit is internally variable. For example, the green gouge is only observed in Log 4 and is 0.3 m wide. The blue gouge is continuous along-strike and varies from 0.65 to 2.65 m thick over 560 m. The red foliated chaotic breccia is continuous along-strike and varies from ~1.5 to 5.4 m thick. The red crackle breccia is only present between Logs 5 and 6 so varies in thickness from 0 to 4.65 m.



**Fig. 3.13.** Structural logs highlighting the along-strike variability in the thickness of the HBF FC units over the well-exposed 560 m Stonehaven section (refer **Fig. 3.2b**) for the location of each log). The thickness of the FC units is to the same scale (that on the left), whereas the horizontal axis is only schematically to scale to indicate the approximate position along-strike of the structural logs beginning at 0 m for Log 1 (significant across-fault exaggeration 25:1). Each log mapped a patchy shoreline with large boulders in places, thus the contacts between each unit are inferred by the dashed line. The Dalradian is a mix of polyphase metamorphic- and fault-related folding so the units are not correlated along-strike. Key as in **Fig. 3.6**. The stars in Log 4 represent the location of the FC samples used for XRD analysis (**Table 3.1**, **Table 3.2**). Green gouge [grid reference NO 388914 787493]; blue gouge [grid reference NO 388914 787494]; red foliated chaotic breccia [grid reference NO 388914 787495].

Mapping of the fault core at Garron Point between Logs 5 and 6 reveals the smaller, metre-scale variability over an along-strike section of 50 m (Fig. 3.14). Over this 50 m section, the blue gouge varies from 0.7 to 2.6 m thick with a mean of  $1.1 \pm 0.7$  m ( $n = 20$ ). The red foliated chaotic breccia varies from 2.3 to 5.4 m thick with a mean of  $4.1 \pm 0.8$  m ( $n = 20$ ). The red crackle breccia varies from 0.35 to 4.65 m thick with a mean of  $2.6 \pm 1.5$  m ( $n = 20$ ). These observations demonstrate that, in addition to the smaller, centimetre-scale variability in each unit (Fig. 3.10) the total thickness of the fault core, and each unit within the fault core, can vary considerably over relatively short distances of 50 m.



**Fig. 3.14.** Smaller-scale structural logs at Garron Point highlighting the along-strike, metre-scale variability of the HBF fault core over a 50 m section (refer to Fig. 3.2b, Fig. 3.13 for location). The horizontal and vertical axes are not to the same scale with significant across-fault exaggeration (5:1). The tick marks on the horizontal axis shows the density of mapping. Each log mapped a patchily exposed shoreline, thus the contacts between each unit are inferred by the dashed line. We have only mapped the exposure, thus the units between the logs are not inferred. Key as in Fig. 3.6 (the lithological variations in the Dalradian hangingwall are not shown). The red numbers refer to the dip of the faults bounding the fault core, while the grey 'lentils' represent the size and orientation of the Dalradian clasts/lenses. The clast size generally decreases away from the Dalradian with a concomitant increase in clay content. Boxplots highlight that each unit within the fault core varies in thickness over the 50 m section. The thick black line represents the median, while the cross represents the mean. The same length scale applies to all three boxplots.

### 3.8. Mineralogy

XRD results are summarised in **Fig. 3.15**. Surrounding the fault core are damage zones of contrasting mineralogy: the Fe-, Mg- and Ca-rich ferromagnesian serpentinites of the Highland Border Ophiolite to the south from K- and Al-rich quartzo-feldspathic crustal rocks of the Dalradian to the north. The Highland Border Ophiolite in the footwall damage zone is characterised by two mineralogically-distinct units. Ophicarbonates (footwall damage zone 1) is characterised by serpentinite (lizardite polymorph), carbonate (primarily dolomite) and quartz, despite serpentinite and quartz not commonly co-existing (although see Streit *et al.*, 2012). Carbonated serpentinite (footwall damage zone 2) is composed of serpentinite (lizardite polymorph), calcite, dolomite, and silicates such as chlorite, prehnite, wollastonite, tremolite, talc and diopside (see Frost & Beard, 2007). The hangingwall damage zone units are characterised by quartz and K- and Al-rich felsic minerals such as white mica and feldspar, presumably derived from the Dalradian. Chlorite and biotite are also present indicative of low-grade, greenschist facies metamorphism supporting previous studies on the Dalradian (e.g., Vorhies and Ague, 2011).

The whole rock (**Fig. 3.16a**) and the fine grained (<2  $\mu\text{m}$  fraction; **Fig. 3.16a**) mineral assemblages of the three fault core units demonstrate variable clay content as summarised in **Table 3.1** and **Table 3.2**. Bulk mineralogy of the green gouge (FC 1a) comprises 48.8 weight % (wt%) clay (24.3 wt% illite + mica, 1.4 wt% mixed layer illite-smectite (I-S) and 23.1% chlorite), with additional quartz, dolomite and anatase. The mixed layer illite-smectite and chlorite clays expand whereas illite does not. The <2  $\mu\text{m}$  fraction suggests the clay minerals are poorly to moderately crystallised and Fe-rich (**Table 3.2**). Similarly, the blue gouge (FC 1) comprises 45.3 wt% clay (15.6 wt% illite + mica, 6.1 wt% I-S and 23.6% chlorite), with additional quartz, dolomite and anatase. Despite comparable mineralogy, subtle differences exist between the green and blue gouge units. For example, the blue gouge is finer-grained with a higher % of the <2  $\mu\text{m}$  fraction and contains more mixed layer illite-smectite and dolomite.

Sample	Illite/ Smectite (I-S)	Illite + Mica	Kaolinite	Chlorite	Qtz	K Feldspar	Plagioclase	Dolomite	Anatase	Hematite
FC 1a	1.4	24.3	0	23.1	44.6	TR	0	3.3	3.3	0
FC 1	6.1	15.6	0	23.6	41.4	TR	0	11.2	2.1	TR
FC 2	5.6	23.8	8.1	0	57.7	TR	TR	1.7	0.4	2.7

**Table 3.1.** XRD results of the whole (bulk) rock fraction (5-10 $\mu$ m) from three clay-rich fault core units of the HBF (FC1a: green gouge; FC1: blue gouge; FC 2: red foliated chaotic breccia). See **Fig. 3.13** for sample locations. Modal % was determined via peak intensity quantification.

Sample	Wt. % <2 $\mu$ m	Illite/smectite			Illite		Kaolinite		Chlorite			Qtz	Dol
		%	Order*	% illite	%	Crys $\dagger$	%	Crys $\dagger$	%	Crys $\dagger$	Y $\ddagger$	%	%
FC 1a	12.5	11.6	O	70-80	25.2	P	0		45.4	M	2	17.8	0
FC 1	51.1	11.9	O	70-80	19.9	P	0		46.1	M	2	13.5	8.5
FC 2	19.6	28.7	O	70-80	39	H	21.2	M	0		-	11.1	0

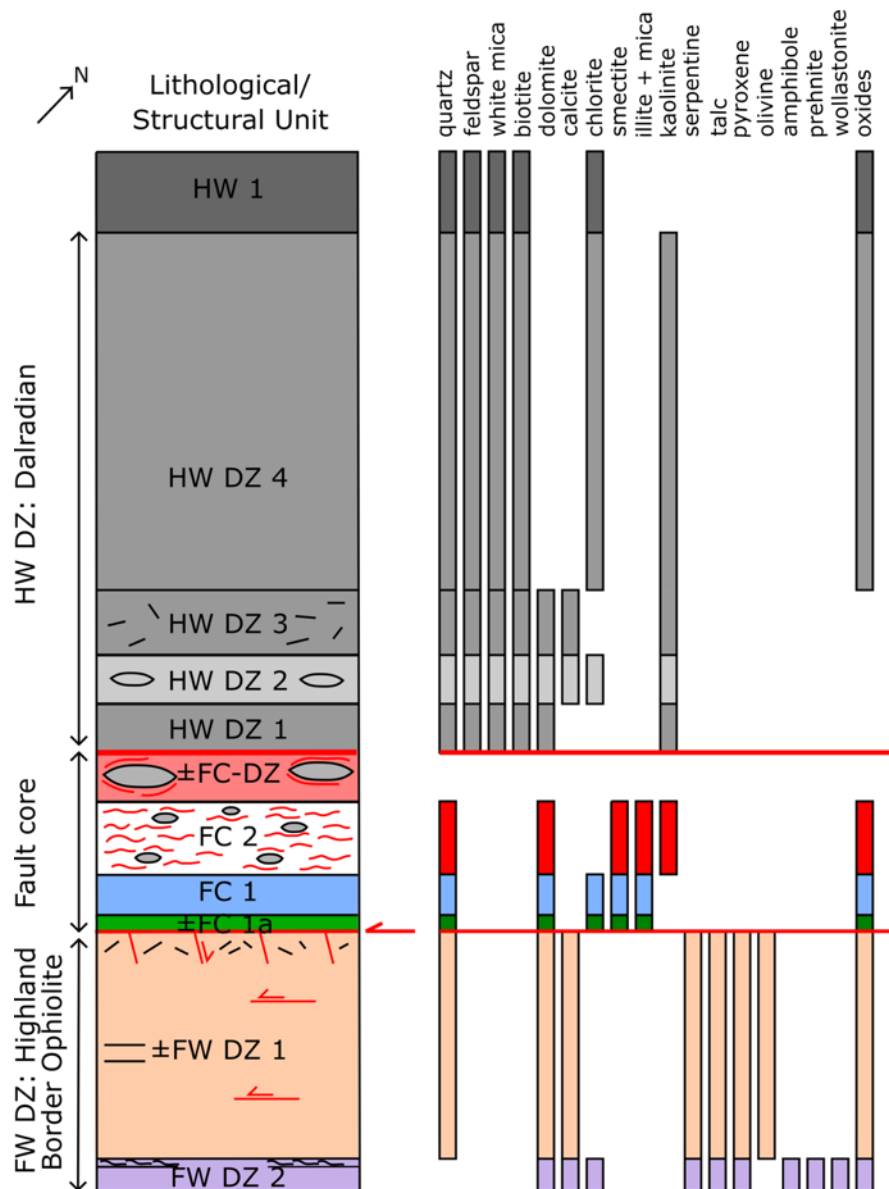
\* Order: O = ordered interstratification

$\dagger$  Clay crystallinity: H = highly crystalline; M = moderately crystalline; P = poorly crystalline

$\ddagger$  Y = number of Fe atoms in six octahedral sites

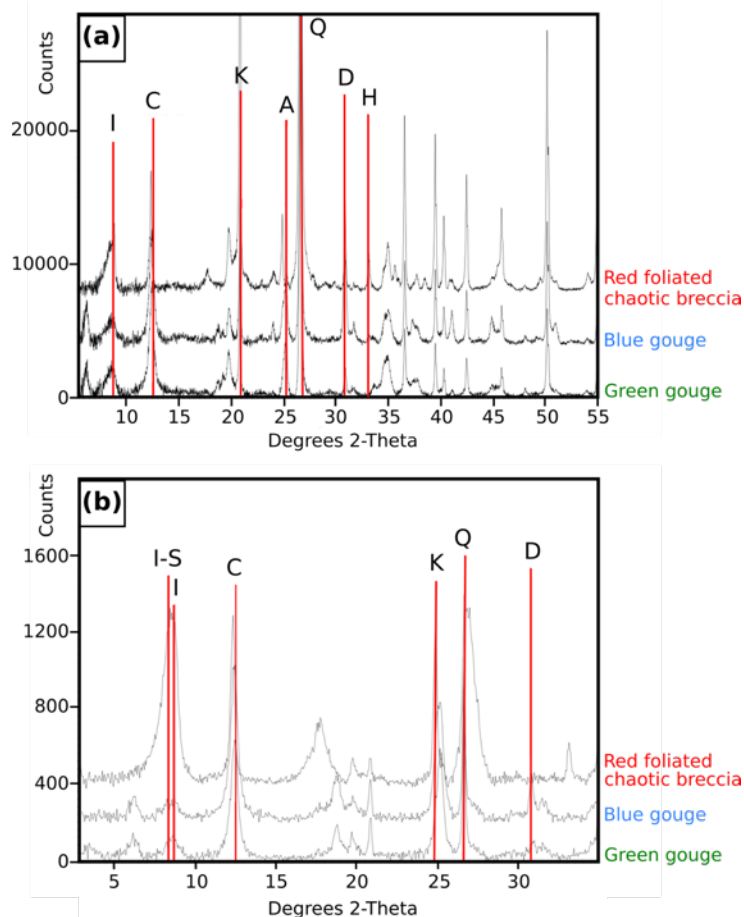
**Table 3.2.** XRD results of the fine-grained <2  $\mu$ m fraction from three clay-rich fault core units of the HBF (FC1a: green gouge; FC1: blue gouge; FC 2: red foliated chaotic breccia). See **Fig. 3.13** for sample locations. Modal % was determined via peak intensity quantification.

The red foliated chaotic breccia (FC 2) comprises 37.5 wt% clay (23.6 wt% illite + mica, 5.6 wt% I-S and 8.1% kaolinite), with additional phases of quartz, dolomite, hematite and anatase. Compared to the blue gouge, the red foliated chaotic breccia contains non-swelling clays such as kaolinite and illite, chlorite is absent and has a higher percentage of quartz. The <2  $\mu$ m fraction suggests the clay minerals within the red foliated chaotic breccia are moderately to well-crystallised (**Table 3.2**). In addition to a change in colour and structure, a distinct mineralogical change therefore occurs between the blue gouge and red foliated chaotic breccia. In the <2  $\mu$ m fraction (**Table 3.2**), the green and blue gouge primarily comprise chlorite, which is Fe- and Mg-rich. Conversely, the red foliated chaotic breccia comprises primarily kaolinite and illite assemblages, which are K- and Al-rich.



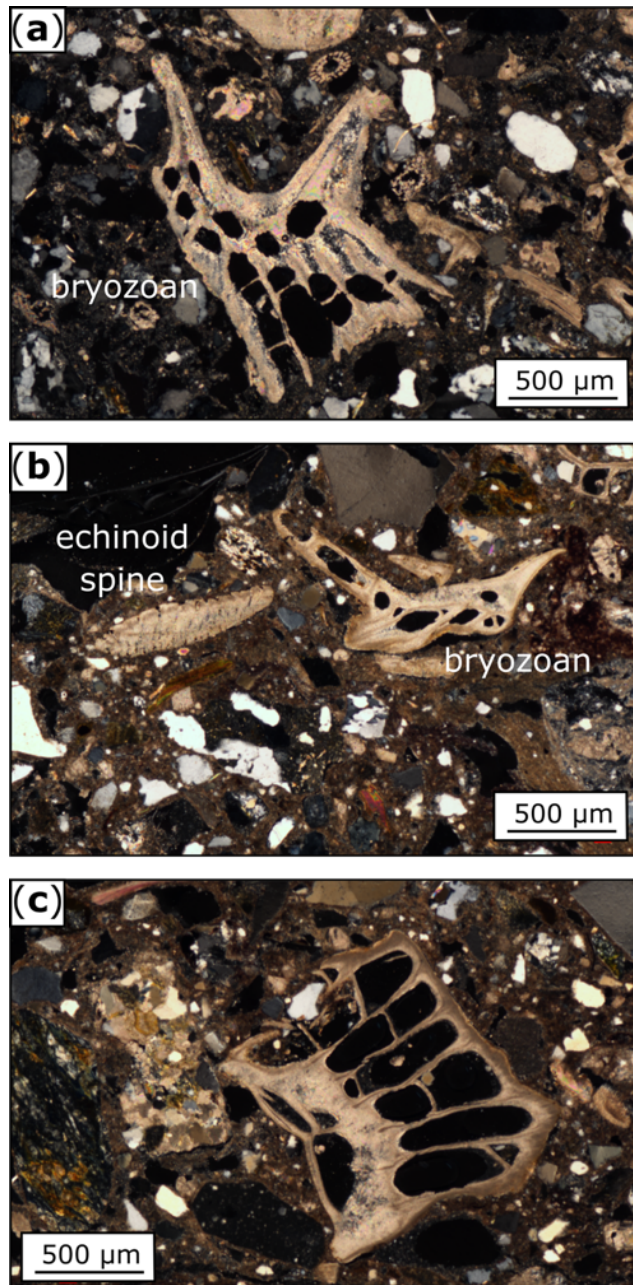
**Fig. 3.15.** Summary schematic log of the HBF architecture with associated mineralogy determined via x-ray diffraction (XRD) analysis. The samples used for analysis were from Log 4 only [grid reference NO 388914 787493]. The  $\pm$  symbol indicates that the unit may or may not be present depending on the location of structural log. For the mineralogy of the metabasalt lava sequence (footwall damage zone 3) refer to Ikin (1983).





**Fig. 3.16.** XRD diffractograms for (a) the whole (bulk) rock and (b) <2 μm size fractions of the three clay-rich FC domains of the HBF. I, illite; I-S, illite-smectite; C, chlorite; K, kaolinite; A, anatase; Q, quartz; D, dolomite; H, hematite. For the <2 μm size fraction, the diffractograms for the four clay treatments are overlain to identify the clay mineral assemblages present.

Optical microscopy reveals the presence of microfossils within the clay-rich fault core (Fig. 3.17). These include relatively intact fragments of ancient bryozoans, possibly belonging to the order Fenestrata (as identified by P. D. Taylor, pers. comm. 2018) (Fig. 3.17a, c), brachiopods and an echinoid spine (Fig. 3.17b). Both primary fabrics and secondary recrystallisation/growth textures are observed. Despite the fossils being preserved within a high-strain fault gouge, there is no evidence of internal strain (e.g., microfracturing or shear indicators) within the fossil fragments.



**Fig. 3.17.** Fault zone palaeontology: shallow-marine microfossils in the blue gouge. **(a)** Fan-shaped bryozoan, possibly of the Fenestrata order, displaying both primary and secondary recrystallization textures. **(b)** A bryozoan and echinoid spine. **(c)** Fan-shaped bryozoan, possibly of the Fenestrata order. All images are in cross-polarized light.

### 3.9. Discussion

#### 3.9.1. Origin of the Clay-rich Fault Core

The mineralogical composition of the fault core matches the wall rocks. From the distinct chemical change between the blue gouge and red foliated chaotic breccia, it can be assumed the Mg- and Fe-rich green and blue gouges are chemically derived

from the Mg- and Fe-rich Highland Border Ophiolite serpentinite wall rocks (footwall damage zone 1 and 2). In contrast, the K- and Al-rich red foliated chaotic breccia is chemically derived from the quartzo-feldspathic Dalradian wall rocks. These units remain surprisingly unmixed: there are a limited number of clasts of weathered host rock within the clay units, but there are no clasts of one clay unit within another that would be indicative of mixing. Similarly to other plate boundary settings where serpentinite and quartzo-feldspathic wall rocks juxtapose (e.g., Moore and Rymer, 2012), the HBF clay likely formed through fluid-assisted, shear-enhanced chemical reactions between wall rocks of contrasting chemistry (the serpentinite of the Highland Border Ophiolite provides the Mg and Fe, while the Dalradian provides K, Al and some of the Si). The green gouge is only observed at one location (**Fig. 3.10**, **Fig. 3.13**) so could either represent a zone of localised alteration, or a remnant fragment of a reworked, previously extensive, fault core lithology. The blue gouge and red foliated chaotic breccia are continuous along-strike, albeit varying in thickness, suggesting that for this 560 m along-strike section, there has been continuous processing of both wall rocks. It remains unclear why the red crackle breccia is not laterally continuous along-strike. However, this may be controlled by the rheological variation within the Dalradian or by stress heterogeneities along the fault.

The mineralogical composition of the clays provides constraints on the temperature of clay authigenesis. With increasing temperatures, smectite transforms to illite. The reaction is complete by ~120-150°C, which suggests an increasing proportion of illite within mixed layer illite-smectite with increasing temperature and depth (e.g., Hower *et al.* 1976; Vrolijk 1990). Hower *et al.* (1976), show that the degree of smectite transformation to illite can be used to gauge temperature. In all observed HBF fault core units, the smectite to illite reaction has progressed to 70-80% illite (**Table 3.2**) equating to a reaction temperature of 100 and 110°C, corresponding to <3 km depth (<1 kbar) assuming a high geothermal gradient setting. Mineral assemblages of chlorite, illite, smectite, kaolinite, as well as serpentinite and talc have been associated with fluid flow and brittle deformation under low temperature conditions (~100°C) at other plate boundary settings where the clays have formed through strike-slip

deformation (e.g., the San Andreas fault; Moore and Rymer, 2007; Schleicher *et al.*, 2009).

Fault rocks exhumed at Earth's surface, particularly on faults with a dip slip kinematic component, develop through progressive deformation at a range of crustal conditions. The exhumed product is thus complicated by overprinting. The low temperatures of formation of the clay (~100°C, palaeodepth of  $\leq 3$  km) implies that this clay-rich fault core must form late in the evolution of the HBF as such a shallow formation depth would mean it would likely have been exhumed if it formed earlier. Based on the kinematics in the footwall damage zone (**Fig. 3.3c**) and field-scale observations of the clay (e.g., fault-parallel foliations, incorporation of orientated wall rocks clasts, foliations wrapping around clasts, elongation of the clasts parallel to the HBF and the smectite-illite mineralogy) (**Fig. 3.10**, **Fig. 3.11**, **Table 3.2**) we propose the clay has a syn-faulting origin and formed as a result of shallow, low temperature, shear-enhanced chemical reactions between wall rocks of contrasting chemistry during latest sinistral strike-slip motion of the HBF. The fault zone must have been passively exhumed from  $\leq 3$  km depth as the nature and mineralogy of the fault rocks implies there has been little or no displacement, and no structural overprinting during exhumation (the strike-slip kinematics are clear in all four fault core units). Unfortunately, there are no clear field-scale kinematic indicators within the clay that would help to constrain the kinematics either to motion in the Carboniferous to Permian (Kemp *et al.* 2019) or related to crustal-scale exhumation in the Cretaceous to Palaeogene (c.f. Andersen *et al.* 1999).

Since the strike-slip faults (i.e. Reidel shears) offset previously deformed units of the Highland Border Ophiolite (**Fig. 3.3**), clay authigenesis must be younger than the emplacement and deformation in the Highland Border Ophiolite and associated reverse motion on the HBF. Based on palaeomagnetic results, Elmore *et al.* (2002) suggest the dolomitisation of serpentinite in footwall damage zone 1 occurred in the Permian at 260 Ma. Clay growth must also be younger than the fossils, which assuming the bryozoans belong to the order Fenestrata (as identified by P. D. Taylor,

pers. comm. 2018), are Ordovician to Permian in age. The presence of these ancient fossils within the clay therefore constrains the age of clay authigenesis to younger than Ordovician-Permian. To our knowledge this is the first time that the age of fossils preserved within a fault gouge have been used to constrain the relative age of that fault. Further microstructural and isotopic analyses (e.g.,  $^{40}\text{Ar}$ - $^{39}\text{Ar}$  radiometric dating) are needed to fully constrain the absolute timing and nature of fluids controlling clay authigenesis and slip behaviour on this plate boundary fault.

Both wall rocks are incorporated into the fault zone through chemical and mechanical alteration spanning the entire range of chemical and physical processes responsible for grain size reduction and wall rock comminution in a fault zone. In addition, the preservation of fragile fossils within the clay suggests strain within the units remain highly localised despite the fault having accumulated between 30-100 km of lateral offset (the exact magnitude of slip is debated in the literature). From the preservation of the textures in the clay, and the remarkable preservation of delicate fossil fragments it is clear that strain localisation by grain size reduction is principally concentrated on the margins of the fault core.

### 3.9.2. How Representative is the HBF of Active Plate Boundary Faults?

The rocks on either side of the HBF at Stonehaven are similar lithologies to those cut by the \$25M SAFOD (San Andreas Fault Observatory at Depth) drilling project through creeping sections of the strike-slip San Andreas fault (SAF) (Bradbury *et al.* 2011; Holdsworth *et al.* 2011) and sections of New Zealand's Alpine Fault (Barth *et al.* 2013; Toy *et al.* 2015). SAFOD drill core revealed the presence of a clay gouge 2.6 m thick (Bradbury *et al.* 2011). Comparable to the red foliated chaotic breccia of the HBF, the SAFOD clay is composed of a dark greyish-black to greenish-black, highly-sheared, foliated matrix that wraps around centimetre-scale clasts of serpentinite and sedimentary wall rocks that are elongate parallel to the foliation (Bradbury *et al.* 2011). Structurally foliated fault rocks with clasts derived from the wall rocks are common along many strike-slip plate boundary faults (e.g., Faulkner *et al.* 2003; Barth *et al.*

2013). The SAFOD clays have been interpreted as the product of fluid-assisted, shear-enhanced, metasomatic reactions between serpentinite, tectonically emplaced from a source in the Coastal Range Ophiolite (cf. the HBO), and quartzo-feldspathic crustal wall rocks (cf. the Dalradian) of contrasting chemistry (Bradbury *et al.* 2011; Moore & Rymer 2012).

Laboratory friction experiments involving SAFOD gouge at hydrothermal conditions (temperature  $\geq 200^{\circ}\text{C}$ ) have demonstrated that due to the chemical contrast between the rock types, aseismic slip (creep) is initiated as soon as serpentinite and quartzo-feldspathic crustal rocks are sheared against each other (Moore and Lockner, 2013). This is attributed to a solution transfer process, modifying the chemistry of the pore fluids within serpentinite, thereby promoting creep along serpentinite-bearing crustal faults at otherwise seismogenic depths (Moore and Lockner, 2013). Long-term shearing of these two chemically different rocks results in the authigenesis of mechanically weak minerals such as clay and talc, considered important in the mechanical behaviour of a fault. Laboratory experiments on the mechanical properties of clay mixtures suggest they would locally promote creep rather than stick-slip (i.e., the clay would retard fault rupture propagation and act as a barrier to earthquake propagation) (Scholz 1998; Ikari *et al.* 2009; Behnsen & Faulkner 2012). These comparable observations on the SAFOD gouge may have implications for understanding palaeo-slip behaviour and clay authigenesis at the Stonehaven section of the HBF.

### *3.9.3. Along-Strike Variability and Its Implication for Rupture Propagation*

By necessity, drilling projects at active plate boundary faults such as the SAFOD and the Japan Trench Drilling Project, effectively sample one only or two transects across a fault, limiting the ability to capture along-strike variability in fault zone properties. Whilst along-strike variability is commonly observed on small-scale faults (e.g., Sosio De Rosa *et al.* 2018), our field observations demonstrate that in present space (i.e.,

modern day) seismogenic plate boundary faults can also vary in thickness, structure and composition along-strike over different length scales (Fig. 3.13, Fig. 3.14). This variability effect will likely be larger down-dip for strike-slip boundaries as fault geometrical variability is smoothed in the direction parallel to slip (Sagy *et al.* 2007).

Plate boundaries are bi-material interfaces bringing together materials of different mechanical and chemical properties (e.g., the Highland Border Ophiolite and Dalradian). However, studies that investigate rupture propagation at plate boundaries typically assume constant fault properties along-strike and down-dip (e.g., Cochard & Rice 2000; Aochi & Madariaga 2003; Shi & Ben-Zion 2006; Ampuero & Ben-Zion 2008). Structural and compositional fault properties spatially impact how and where earthquakes rupture, nucleate and propagate (e.g., Aochi & Madariaga 2003; Heermance *et al.* 2003; Wibberley *et al.* 2008; Kirkpatrick & Shipton 2009). Dynamic weakening processes and energy loss during earthquake slip is dependent on the physical properties of the fault core (Shipton *et al.* 2006b; Kirkpatrick & Shipton 2009). Kirkpatrick *et al.* (2018), demonstrated that due to the along-strike variation in slip zone thickness, slip-weakening mechanisms such as thermal pressurisation must have been spatially variable during seismic slip. Most slip-weakening mechanisms are triggered by frictional heating. Therefore, if the units within the fault core have variable thickness, then the heating effect and consequently the lubrication effect that determines the size of the rupture, will also be variable (the thinner the unit the faster the heating) (Kirkpatrick *et al.* 2018). Along-strike thickness variations is expected to be a common feature of all faults (Kirkpatrick *et al.* 2018). Therefore, earthquake models for seismogenic plate boundaries must consider, or else assess tolerance and sensitivity to, along-strike variation in the thickness of units within the fault core, as well as the composition (e.g., the localised green gouge in Log 4).

### 3.10. Conclusion

This paper delivers a level of detail on the along-strike internal fault core structure of a major plate boundary fault that has rarely been seen before. The well-exposed Stonehaven section of the Highland Boundary fault core is composed of four

structurally and chemically distinct clay-rich units. Field and mineralogical observations suggest clay authigenesis occurred as a result of shallow, low temperature, shear-enhanced chemical reactions between wall rocks of contrasting chemistry during the latest sinistral strike-slip motion of the HBF.

The internal structure and mineralogy of the Highland Boundary fault at Stonehaven is comparable to other segments of plate boundary faults (e.g., the creeping section of the San Andreas fault in California and in places part of the Alpine Fault, New Zealand). Whilst along-strike variability is commonly observed on small-scale faults, our field observations demonstrate that in present space (modern-day surface exposures) the core of seismogenic plate boundary faults can also vary in thickness and composition along-strike over centimetre and metre length scales. In the case of the HBF at Stonehaven, the thickness and composition varies along-strike but the structure of the fault (e.g., a single fault core surrounded by a damage zone on either side) does not. Earthquake rupture mechanics critically depend on the physical properties of fault rock assemblages. Therefore, models that investigate rupture propagation at active plate boundaries should incorporate, or else assess tolerance and sensitivity to, variable fault core thickness, structure and composition.

The authors note that it is not clear if this 560 m section at Stonehaven is sufficient to characterise the entire structure of the HBF. However, the observations presented make a valuable contribution to the global dataset of plate boundary fault zone structures and may also serve as a model for the processes acting in other fault systems hosted in similar mineralogies, such as the San Andreas Fault and sections of New Zealand's Alpine Fault. If possible, detailed field mapping should be carried out at several other sections of the HBF (e.g., Balmaha, Innellan) to investigate what happens at the continental scale.



# Chapter 4 - Do Plate Boundary and Intraplate Fault Systems Evolve in a Similar Way with Repeated Slip Events?

*This chapter is published as: McKay, L., Lunn, R.J., Shipton, Z.K., Pytharouli, S., Roberts, J.J., 2021. Do intraplate and plate boundary fault systems evolve in a similar way with repeated slip events? Earth and Planetary Science Letters, 559, 1-18. doi: 10.1016/j.epsl.2021.116757*

*Note, following the Viva examination and recommendations from the examiners, minor additions and modifications have been made to this chapter that are not included in the published article (Appendix 3).*

## *Abstract*

As repeated slip events occur on a fault, energy is partly dissipated through rock fracturing and frictional processes in the fault zone and partly radiated to the surface as seismic energy. Numerous field studies have shown that the core of intraplate faults is thicker on average with increasing total displacement (and hence slip events). In this study we compile data on the fault core thickness, total displacement and internal structure (e.g., fault core composition, host rock juxtaposition, slip direction, fault type, and/or the number of fault core strands) of plate boundary faults to compare to intraplate faults (within the interior of tectonic plates). Fault core thickness data show that plate boundary faults are anomalously narrow by comparison to intraplate faults and that they remain narrow regardless of how much total displacement (hence how many slip events) they have experienced or the local structure of the fault. By examining the scaling relations between seismic moment, average displacement and surface rupture length for plate boundary and intraplate fault ruptures, we find that for a given value of average displacement in an individual earthquake, plate boundary fault earthquakes typically have a greater seismic moment (and hence earthquake magnitude) than intraplate events. We suggest that narrow plate boundary faults do not process intact rock as much during seismic events as intraplate faults. Thus, plate boundary faults dissipate less energy than intraplate faults during earthquakes meaning that for a given value of average displacement, more energy is radiated to the surface manifested as higher magnitude earthquakes. By contrast, intraplate faults dissipate more energy and get thicker as fault slip increases, generating complex zones of damage in the surrounding rock and propagating through linkage with neighboring structures. The more complex the fault geometry, the more energy has to be consumed at depth during an earthquake and the less energy reaches the surface.

## 4.1. Introduction

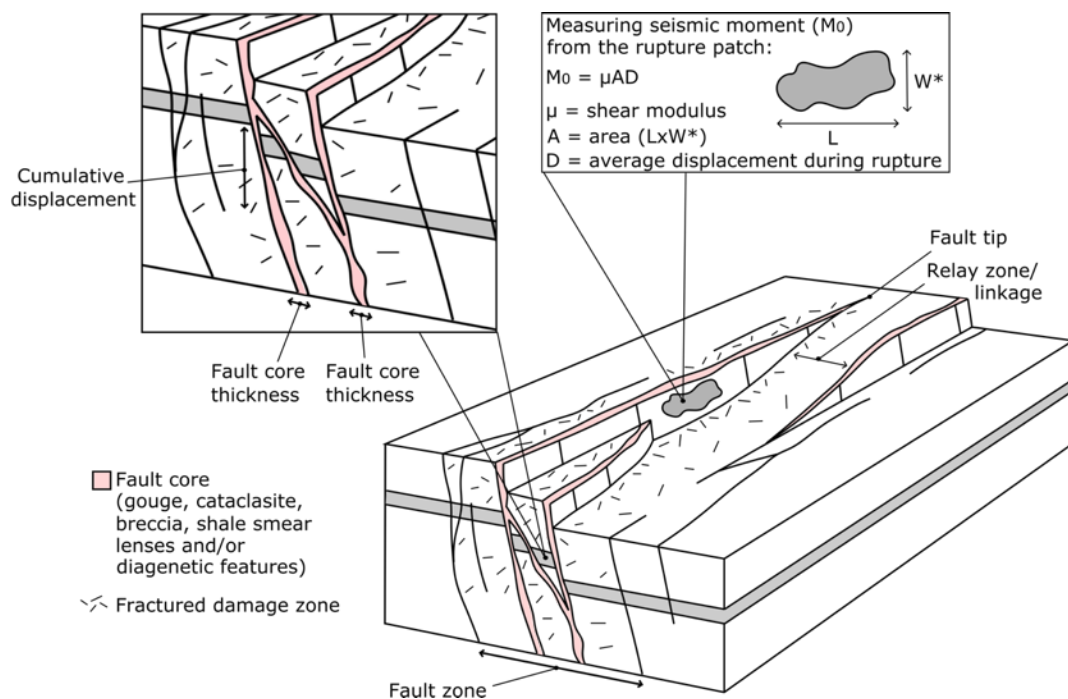
The earthquake energy balance as defined by Kanamori & Anderson (1975; see also Kanamori & Brodsky, 2001 and references therein) states that the total energy released during an earthquake is partly absorbed on the fault plane by fracturing and frictional dissipation and partly radiated out of the source as seismic waves. This can be expressed simply as equation(4.1):

$$E_T = (E_G + E_F) + E_R \quad (\text{eq. 4.1})$$

where  $E_T$  is the total energy released,  $E_G$  is the fracture energy needed to create a new surface area,  $E_F$  is the frictional energy required to slide along that surface and  $E_R$  is radiated energy. Seismic data can be used to estimate  $E_G$  and  $E_R$  (from a power-law dependence with slip and from the seismic moment, respectively) but not  $E_F$  (Shearer 2009). From a geological perspective, when considering the processes active along faults during coseismic slip,  $E_G$  and  $E_F$  cannot be separated (Shipton et al., 2006a). This is because there are several physical processes that occur near the rupture front and in the surrounding rock (termed damage zone; **Fig. 4.1**) that involve frictional and/or fracture energy (Shipton et al., 2006a). These include gouge production, cataclasis, fracturing in the damage zone, the dissolution and growth of minerals and slip weakening mechanisms such as thermal pressurisation or silica gel formation (e.g., Kirkpatrick and Shipton, 2009). All of these consume energy, preventing it radiating to the surface. Together, they are referred to as the dissipative energy ( $E_G + E_F$ ). During repeated slip events, energy will continue to be dissipated by these processes in the fault zone (both in the fault core and damage zone).

The physical processes that occur during rupture control the evolution of the fault over time, and hence with increasing total fault displacement. Compilations of data from multiple fault studies show that, in general, fault zones get thicker as total displacement increases (e.g., Childs et al., 2009; Shipton et al., 2006b; Torabi et al., 2019; Van Der Zee et al., 2008; Wibberley et al., 2008), albeit with a large range in magnitude of width for a given displacement (Shipton et al 2006b). Torabi et al. (2019) suggest that the exponent and intercept of the power law change depending on the lithology of the

faulted rock.. It is thought that this increase in thickness is due to the linkage of fault segments via relay formation and breaching (Childs et al., 2009, 2017; Fossen & Rotevatn, 2016 and references therein; Fig. 4.1). That is, low displacement faults represent a stage of early growth and are thin but evolve into wide fault zones as they extend in length, link with adjacent faults and become more complex in structure. However, the vast majority of the faults in these datasets are from intraplate settings (faults within the interior of tectonic plates and not the boundary of such plates).



**Fig. 4.1.** Schematic diagram defining the terms used in this chapter. Note, the width dimension,  $W$ , for the slip patch shown in the top right inset is different to fault core thickness (measured orthogonal to the fault plane) and width (apparent thickness, often measured horizontally). The average displacement during rupture,  $D$  (in the top left inset), is the displacement during a single rupture event, measured in the direction of slip along the rupture patch. This is distinct from cumulative fault displacement, which is an accumulation of the displacement for all rupture/slip events. Figure modified from Childs et al. (2009).

The relationship between the total displacement on a fault and the evolution of fault core thickness has not previously been explored for plate boundary faults, even though these are responsible for ~90% of global seismicity (USGS, 2016). Here, we compile and harmonise a global dataset of intraplate and plate boundary fault core thickness and total displacement data in order to examine whether these fault systems evolve in

a similar way with repeated slip events. Given the interdependence between fault structure and earthquake processes (e.g., Kirkpatrick & Shipton, 2009), we then examine the local structure (fault core composition, wall rock juxtapositions, fault type and number of fault core stands) between all plate boundary faults in our dataset and compare the fault complexity (defined here as steps per unit length) between intraplate and plate boundary faults. Further, we examine the scaling relations between seismic moment, average displacement and surface rupture length to compare estimates of radiated seismic energy for intraplate and plate boundary fault events of the same average displacement. Finally, we infer how fault zone processes could cause the systematic differences observed between plate boundary and intraplate fault systems.

## 4.2. Methods

We first compiled data on fault core thickness (as defined in **Fig. 4.1**) and total displacement from the peer-reviewed scientific literature (**Table 4.1**). A fault is typically composed of one or more high-strain fault core(s) surrounded by an associated fractured damage zone (c.f. Caine et al., 1996; **Fig. 4.1**). The critical distinction between fault core and fault damage zone is that the latter does not accommodate significant shear displacement (Sutherland *et al.* 2012). Here we focus on the fault core because the majority of earthquake slip is accommodated by the core and the core thickness is more easily constrained than the damage zone thickness (see Savage and Brodsky, 2011). As the classification method and terminology used to describe fault architecture can be ambiguous (Shipton *et al.* 2019), we developed an approach designed to harmonise the reported data to facilitate comprehensive comparison. To ensure consistency in our dataset, we only include studies where the thickness and composition (fault rock type) of the fault core are clearly defined and are reported as being distinct from the damage zone. Therefore, as in Torabi et al. (2019), we define the fault core thickness as the cumulative, across-fault thickness of gouge, breccia, cataclasite, shale smear, lenses and/or diagenetic features on both sides of the principal slip plane within a single fault core strand (**Fig. 4.1**). If more than one fault core is described for a single fault zone, we estimate the fault core thickness as the total thickness of each of the fault core strands and not the collective thickness

across multiple fault cores (i.e., the host rock entrained between the strands is not included in the thickness measurements). To ensure the definition of thickness is consistent, studies that report fault core thickness but provide no information on its composition/structure are not included. Total displacement is measured from slip vector orientations and the separation of markers across the fault (**Fig. 4.1**). When a range of total displacement values are reported in the literature, we calculated and plotted the arithmetic mean  $\pm$  the difference to the minimum and maximum value. For example, if the total displacement was reported to be 100 to 150 km, we considered the fault offset to be  $125 \pm 25$  km. The  $\pm$  values are plotted as error bars in **Fig. 4.2**, although are smaller than the data symbols. A detailed description of this compiled dataset is given in Appendix 4.

We use the same criteria to compile data for plate boundary faults, where the fault core refers to zones accommodating most of the strain across the fault. In total we found data for 75 sites on 13 plate boundary faults (**Table 4.2**). Our dataset combines our own field observations of the exhumed Highland Boundary fault (McKay *et al.* 2020) with field and borehole studies of both modern and ancient examples of plate boundary faults. These include the San Andreas fault (Holdsworth *et al.* 2011; Moore & Rymer 2012), North Anatolian fault (Dor *et al.* 2008), Alpine fault (Barth *et al.* 2013; Toy *et al.* 2015, 2017), Carboneras fault (Faulkner *et al.* 2003), Median Tectonic Line (Wibberley & Shimamoto 2003), Nankai Trough (Ujiié & Kimura 2014), Japan Trench (Kirkpatrick *et al.* 2015), Chelungpu thrust (Heermance *et al.* 2003; Yeh *et al.* 2007), Longmenshan thrust (Li *et al.* 2013) and ancient subduction boundaries from the compilation of Rowe *et al.* (2013). Where available, we include all reported data points along a single plate boundary fault to capture the spatial heterogeneity along-strike. Using this data, we then construct schematic structural logs to compare the local structure both along an individual plate boundary and between plate boundaries.

Several studies have demonstrated that fault complexity decreases as a function of increased displacement (Wesnousky 1988; Stirling *et al.* 1996; de Jossineau & Aydin 2009). That is large displacement faults appear to be geometrically simpler with a

smoothened and straightened fault trace compared to small displacement faults with a more stepped per unit length surface geometry (Wesnousky 1988). However, like data for fault core thickness and total displacement, the data in previous compilations on fault complexity have never been distinguished by plate boundary or intraplate fault type and subsequently never been compared to establish if there are any systematic differences between the two systems. In order to test whether large displacement plate boundary faults have simpler geometries in comparison to intraplate faults data were compiled from the literature for steps per unit length in surface geometry from plate boundary or intraplate faults (**Table 4.3**). The data were then filtered to only include data with a step size of greater than 50 m. This step size was chosen as it was a value that is able to be picked out and mapped from seismic data (tomography). Geometrical variability is smoothed in the direction parallel to slip (Sagy *et al.* 2007) so the along-strike geometry will be different for strike-slip and dip-slip faults. As such, data in this dataset were only included from strike-slip fault systems to allow for comparison.

To complement our findings on intraplate and plate boundary fault structure, composition and geometry, we gather data from the peer-reviewed scientific literature to examine earthquake scaling relations between intraplate and plate boundary fault events. We focus on the scaling relations between seismic moment, average displacement and surface rupture length. We extend the dataset of Scholz *et al.* (1986) by determining which earthquakes in the Wells & Coppersmith (1994) dataset are plate boundary or intraplate fault events and by adding in examples from Wesnousky (2006; 2008) (**Table 4.4**, **Table 4.5**). We separate the data based on fault type (plate boundary and intraplate fault events) and also by the method in which the seismic moment was determined (derived from seismological observations or from field observations). The calculation of seismic moment from field observations uses an estimate of the average fault displacement (**Fig. 4.1**). Since our aim is to investigate the relationship between seismic moment, average displacement and surface rupture length, our analyses focus on those events for which the seismic moment has been determined from the frequency spectrum of the recorded displacement (frequency spectrum analyses or moment

tensor solutions). Thus, we ensure all measurements are independently derived and prevent a circular argument; no assumptions are made about the fault dimensions in modelling the seismic energy release (seismic moment).

### 4.3. Comparing Fault Core Thickness and Total Displacement for Plate Boundary and Intraplate Faults

Like previous compilations (Shipton *et al.* 2006a; Van Der Zee *et al.* 2008; Wibberley *et al.* 2008; Childs *et al.* 2009; Torabi *et al.* 2019), we obtain a statistically significant (p value 0.0004), positive power-law trend between fault core thickness and total displacement for intraplate faults over several orders of magnitude (**Fig. 4.2a**). In our dataset there are a higher number of lower displacement intraplate faults (between 0.01 m and 24 m), perhaps reflecting the difficulty in identifying a reliable or preserved displacement marker for faults with larger total displacement. For intraplate faults with total displacement values between 0.01 m and 24 m the trendline sits in the middle of the data. Yet when the total displacement of intraplate faults is >24 m the trendline does not plot in the centre of the data and thus underpredicts the thickness of larger displacement intraplate faults (displacement >24 m).

Based on the observed relationship for intraplate faults, plate boundary faults with large total displacement values (>1000 m) would be expected to have wide fault cores. However, we find plate boundary faults are distinct from the trend (**Fig. 4.2b**). Instead, plate boundary faults are consistently narrow with fault core thicknesses between 0.07 m and ~35 m and there is no statistically significant (p value 0.155) relationship with total displacement. This finding is regardless of either the fault type (strike-slip or convergent, there are no data for divergent boundaries) or the distance along-strike. Interestingly, whilst plate boundary faults are consistently 1-2 orders of magnitude narrower than would be predicted by the trend for intraplate faults, their variability along-strike is similar; the thickness of both intraplate and plate boundary faults ranges by 2-3 orders of magnitude for a single value of displacement on an individual fault.

Therefore, despite plate boundary faults being consistently narrower, the along-strike variance in fault thickness is similar.

Reference	Total displacement (m)	Fault core thickness (m)	Fault core composition	Host lithology $\pm$ fault type
Bastesen and Braathen (2010)	0.04 - 400	0.004 - 11	g + b	Carbonates, normal
Bastesen et al. (2013)	0.3-951	0.009 – 2.186	g + b + s	Sedimentary and carbonates, normal
Childs et al. (1996)	0.02 - 15	0.001 – 0.09	g + b	Sedimentary, normal
Di Toro and Pennacchioni (2005)*	0.009 -10.65	0.0002 – 0.375	c + p	Tonalite, strike-slip
Evans (1990)†	0.0015 - 3000	0.0001 - 12	g	Bismark fault, normal?
Foxford et al. (1998)*†	4.06 – 936.17	0.079 – 20.67	g + c + b	Sedimentary, normal
Gudmundsson et al. (2013)	1- 48	0.1 – 4.5	g + b	Lava flows, normal
Knott et al. (1996)*	0.001 – 2107.9	0.0009 – 92.68	g + c	Sedimentary, normal
Little (1995)*	0.124 - 7.23	0.0005 – 0.04	g	Sedimentary, strike-slip
Marrett and Allmedinger (1990)*	0.004 – 550.81	0.0004 – 8.30	g	Sedimentary, thrust
Segall and Pollard (1983)*; Segall and Simpson (1986)*	0.044 – 1.448	0.02 – 1.165	g	Granite, strike-slip
Shipton et al. (2005)*	3 – 24.12	0.003 – 0.275	g + c	Sedimentary, normal
Shipton et al. (2006)*	0.009 - 146	0.001 – 10.8	g + b + c	Granite/ignimbrite, strike-slip/normal
Sperrevik et al. (2002)	0.001 - 10	0.00025 – 0.7	g	Sedimentary, normal
Torabi et al. (2019)	0.016-800	0.001-10	g + b + s	Sedimentary and carbonates, normal and strike-slip
Van Der Zee and Urai (2005)†	0.001 – 0.5	0.001 – 0.1	g	Sedimentary, normal
Van Der Zee et al. (2008)†	0.2 – 10.5	0.003 – 2.5	g	Sedimentary, normal
Wibberley et al. (2008)	0.006 – 20000	0.0001 – 100	g	Sedimentary, all

\* Data used in the compilation of Shipton et al. (2006)

† Data used in the compilation of Van Der Zee et al. (2008)

**Table 4.1.** Compiled dataset of fault core thickness and total displacement observations for intraplate faults used in **Fig. 4.2a**. The dataset only includes papers that have clearly defined the fault core thickness and composition (g, gouge; b, breccia; c, cataclasite; p, pseudotachylyte; s, shale smear) as being separate from the damage zone. The reader is referred to the original paper for details of the datasets.



Plate boundary (type) and location	Total displacement (km)	Fault core thickness (m)	Fault core composition	Drill core (depth in m) or field exposure	Source*
<b>Highland Boundary fault (sinistral strike-slip)</b>					
Stonehaven Log 1	115 ± 85	5.7	g + b	field exposure	1, 2, 3
Stonehaven Log 2	115 ± 85	~3	g + b	field exposure	1, 2, 3
Stonehaven Log 4	115 ± 85	2.95	g + b	field exposure	1, 2, 3
Stonehaven Log 5	115 ± 85	10.7	g + b	field exposure	1, 2, 3
Stonehaven Log 6	115 ± 85	7.7	g + b	field exposure	1, 2, 3
Stonehaven Garron Point 1	115 ± 85	7.5	g + b	field exposure	1, 2, 3
Stonehaven Garron Point 2	115 ± 85	7.45	g + b	field exposure	1, 2, 3
Stonehaven Garron Point 3	115 ± 85	7.8	g + b	field exposure	1, 2, 3
Stonehaven Garron Point 4	115 ± 85	8.15	g + b	field exposure	1, 2, 3
Stonehaven Garron Point 5	115 ± 85	8.4	g + b	field exposure	1, 2, 3
Stonehaven Garron Point 6	115 ± 85	8.5	g + b	field exposure	1, 2, 3
Stonehaven Garron Point 7	115 ± 85	8.2	g + b	field exposure	1, 2, 3
Stonehaven Garron Point 8	115 ± 85	8.4	g + b	field exposure	1, 2, 3
Stonehaven Garron Point 9	115 ± 85	6.15	g + b	field exposure	1, 2, 3
Stonehaven Garron Point 10	115 ± 85	5	g + b	field exposure	1, 2, 3
Stonehaven Garron Point 11	115 ± 85	5.45	g + b	field exposure	1, 2, 3
Stonehaven Garron Point 12	115 ± 85	5.6	g + b	field exposure	1, 2, 3
Stonehaven Garron Point 13	115 ± 85	5.3	g + b	field exposure	1, 2, 3
Stonehaven Garron Point 14	115 ± 85	6.2	g + b	field exposure	1, 2, 3
Stonehaven Garron Point 15	115 ± 85	9	g + b	field exposure	1, 2, 3
Stonehaven Garron Point 16	115 ± 85	10.55	g + b	field exposure	1, 2, 3
Stonehaven Garron Point 17	115 ± 85	10.2	g + b	field exposure	1, 2, 3
Stonehaven Garron Point 18	115 ± 85	10	g + b	field exposure	1, 2, 3
<b>San Andreas fault (dextral strike-slip)</b>					
SAFOD Hole G runs 1-3	282.5 ± 32.5	9.1	g	drill core (2640)	4, 4a, 4b, 5, 6
SAFOD Hole G runs 4-6	282.5 ± 32.5	2.48	g	drill core (2690)	4, 4a, 4b, 5, 6
Nelson Creek	282.5 ± 32.5	0.15	g	field exposure	4, 4a, 4b, 7
Punchbowl	44	0.3	g	field exposure	8, 9
San Gabriel	55 ± 5	~4.2	c	field exposure	10, 11, 12
<b>Alpine fault (dextral strike-slip)</b>					
DFDP-1A	≥ 470	11	g + c	drill core (91)	13, 14
DFDP-1B	≥ 470	28 (or 2)	g + c	drill core (128)	13, 14, 15, 16
Martyr River	≥ 470	1.5	g + c	field exposure	14
McKenzie Creek	≥ 470	1.1	g	field exposure	14
Hokuri Creek	≥ 470	12	g	field exposure	14

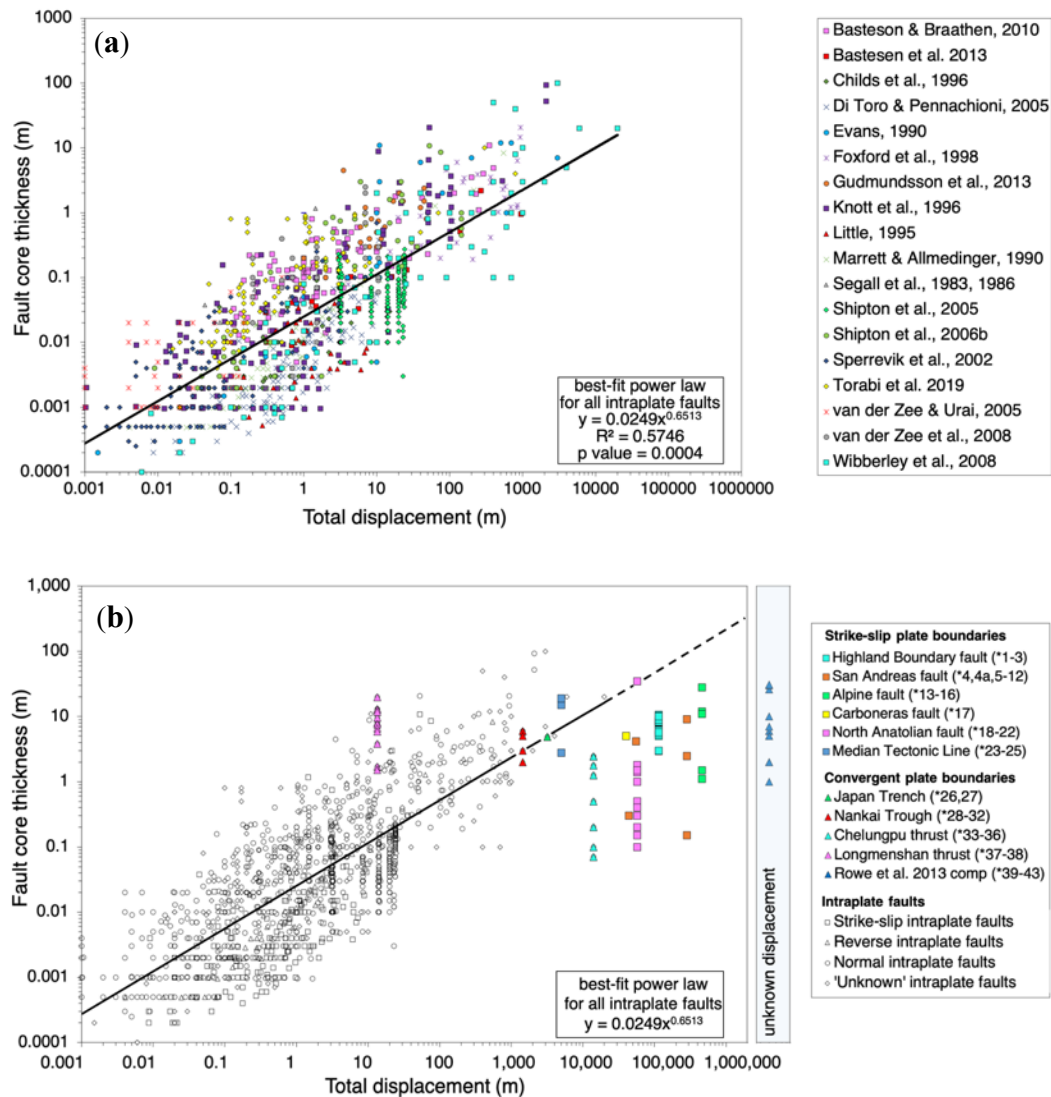
Plate boundary (type) and location	Total displacement (km)	Fault core thickness (m)	Fault core composition	Drill core (depth in m) or field exposure	Source*
<b>Carboneras fault (sinistral strike-slip)</b>					
El Saltador Alto	27.5 ± 12.5	~5	g	field exposure	17, 17a
<b>North Anatolian fault (dextral strike-slip)</b>					
Ladik	57.5 ± 32.5	1.8	g	field exposure	18-21
Bademci	57.5 ± 32.5	0.3-1.4	g	field exposure	18-21
Hamamli	57.5 ± 32.5	~35	g	field exposure	18-21
Gerede-Mudurnu	57.5 ± 32.5	0.2 - 0.3	g	field exposure	18-20, 22
Gerede-Mudurnu	57.5 ± 32.5	1 - 1.5	g	field exposure	18-20, 22
Niksar-Erzincan	57.5 ± 32.5	0.4 - 0.5	g	field exposure	18-20, 22
Niksar-Erzincan	57.5 ± 32.5	0.1 - 0.15	g	field exposure	18-20, 22
<b>Median Tectonic Line (dextral strike-slip)</b>					
Tsukide	>5	15	g	field exposure	23, 24
Matsusaka-Iitaka (ITA)	>5	2.8	g	drill core	23, 25
Hole 1					
Tsukide ('Moonrise')	>5	19	g	drill core	23, 25
<b>Japan Trench (convergent)</b>					
JFAST C0019†	3.2	≤4.86	g	drill core (821)	26, 27
<b>Nankai Trough (convergent)</b>					
NanTroSEIZE C0004	> 1.45	< 3	g + b	drill core (256)	28-31
NanTroSEIZE C0007	> 1.45	< 2	g + b	drill core (398.5)	28, 29
ODP Leg 196, Site 808†	> 1.45	6	g + b	drill core	28, 32
ODP Leg 196, Site 808†	> 1.45	6	g + b	drill core	28, 32
ODP Leg 196, Site 808†	> 1.45	5	g + b	drill core	28, 32
<b>Chelungpu fault (convergent)</b>					
TCDP Hole A FZA1111	> 14	2.45	g + b + c	drill core (1106)	33, 34
TCDP Hole A FZA1153	> 14	2.45	g + b	drill core (1150)	33, 34
TCDP Hole A FZA1221	> 14	1.26	g + c	drill core (1219)	33, 34
TCDP Hole B FZB1136	> 14	1.77	g + b	drill core (1135)	33, 35
Tali River, Takeng	> 14	0.07 – 0.2	g	field exposure	33, 36
Chingshui River, Tongtou Bridge	> 14	0.1 – 0.5	g	field exposure	33, 36
<b>Longmenshan thrust (convergent)</b>					
WFSD-1 FZ333	0.0155+0.0015	17	g + b + c	drill core (333)	37, 38
WFSD-1 FZ590	0.0155+0.0015	19.8	g + b + c	drill core (590)	37, 38
WFSD-1 FZ608	0.0155+0.0015	8.12	g + b + c	drill core (608)	37, 38
WFSD-1 FZ621	0.0155+0.0015	9.7	g + b + c	drill core (621)	37, 38
WFSD-1 FZ628	0.0155+0.0015	13.12	g + b + c	drill core (628)	37, 38
WFSD-1 FZ639	0.0155+0.0015	3.84	g + b + c	drill core (639)	37, 38
WFSD-1 FZ646	0.0155+0.0015	7.66	g + b + c	drill core (646)	37, 38
WFSD-1 FZ655	0.0155+0.0015	6.66	g + b + c	drill core (655)	37, 38
WFSD-1 FZ669	0.0155+0.0015	12.8	g + b + c	drill core (669)	37, 38
WFSD-1 FZ678	0.0155+0.0015	11.83	g + b + c	drill core (678)	37, 38
WFSD-1 FZ759	0.0155+0.0015	5.9	g + b + c	drill core (759)	37, 38
WFSD-1 FZ970	0.0155+0.0015	1.52	g + b + c	drill core (970)	37, 38
<b>Northern Barbados accretionary prism (convergent)</b>					
ODP Leg 171, Site 1047†	?	10, 26	g + b	drill core (633)	39
<b>Shimanto accretionary complex (convergent)</b>					
Okistu mélange†	?	2-5	c + p	field exposure	40
Mugi mélange†	?	1-2	c + p	field exposure	41
Mugi mélange†	?	19	c	field exposure	42

Plate boundary (type) and location	Total displacement (km)	Fault core thickness (m)	Fault core composition	Drill core (depth in m) or field exposure	Source*
<b><i>Pasagshak Point Thrust (convergent)</i></b>					
Kodiak Island, Alaska†	?	7-31	c + p	field exposure	43

\*References: 1-McKay et al. (2020); 2-Tanner (2008); 3-Cawood et al. (2012); 4-Matthews (1976); 4a-Wesnousky (1988); 4b-Dibblee (1989); 5-Wesnousky (2005); 6-Holdsworth et al. (2011); 7-Bradbury et al. (2011); 8-Moore & Rymer (2012); 9-Chester and Logan (1986); 10-Schulz and Evans (2000); 11-Chester et al. (1993); 12-Dor et al. (2006); 13-Toy et al. (2015); 14-Barth et al. (2013); 15-Schuck et al. (2020); 16-Boulton et al. (2014); 17-Faulkner et al. (2003); 17a-Rutter et al. (2012); 18-Armijo et al. (1999); 19-Hubert-Ferrari et al. (2002); 20-Sengör et al. (2005); 21-Dor et al. (2008); 22-Uysal et al. (2016); 23-Okada (1980); 24-Wibberley and Shimamoto (2003); 25-Shigematsu et al. (2012); 26-Chester et al. (2013); 27-Kirkpatrick et al. (2015); 28-Moore et al. (2009); 29-Ujiié and Kimura (2014); 30-Hirono et al. (2016); 31-Sakaguchi et al. (2011); 32-Shipboard Scientific Party (2002); 33-Heermance and Evans (2006); 34-Yeh et al. (2007); 35-Hirono et al. (2007); 36-Heermance et al. (2003); 37-Li et al. (2009); 38-Li et al. (2013); 39-Shipboard Scientific Party (1998); 40-Ikesawa et al. (2003); 41-Ujiié et al. (2007a); 42-Ujiié et al. (2007b); 43-Rowe et al. (2011).

† Data used in the compilation of Rowe et al. (2013)

**Table 4.2.** Compiled dataset of fault core thickness and total displacement observations for plate boundary faults used in **Fig. 4.2b**. The dataset only includes papers that have clearly defined the fault core thickness and composition (g, gouge; b, breccia; c, cataclasite; p, pseudotachylyte; s, shale smear) as being separate from the damage zone.



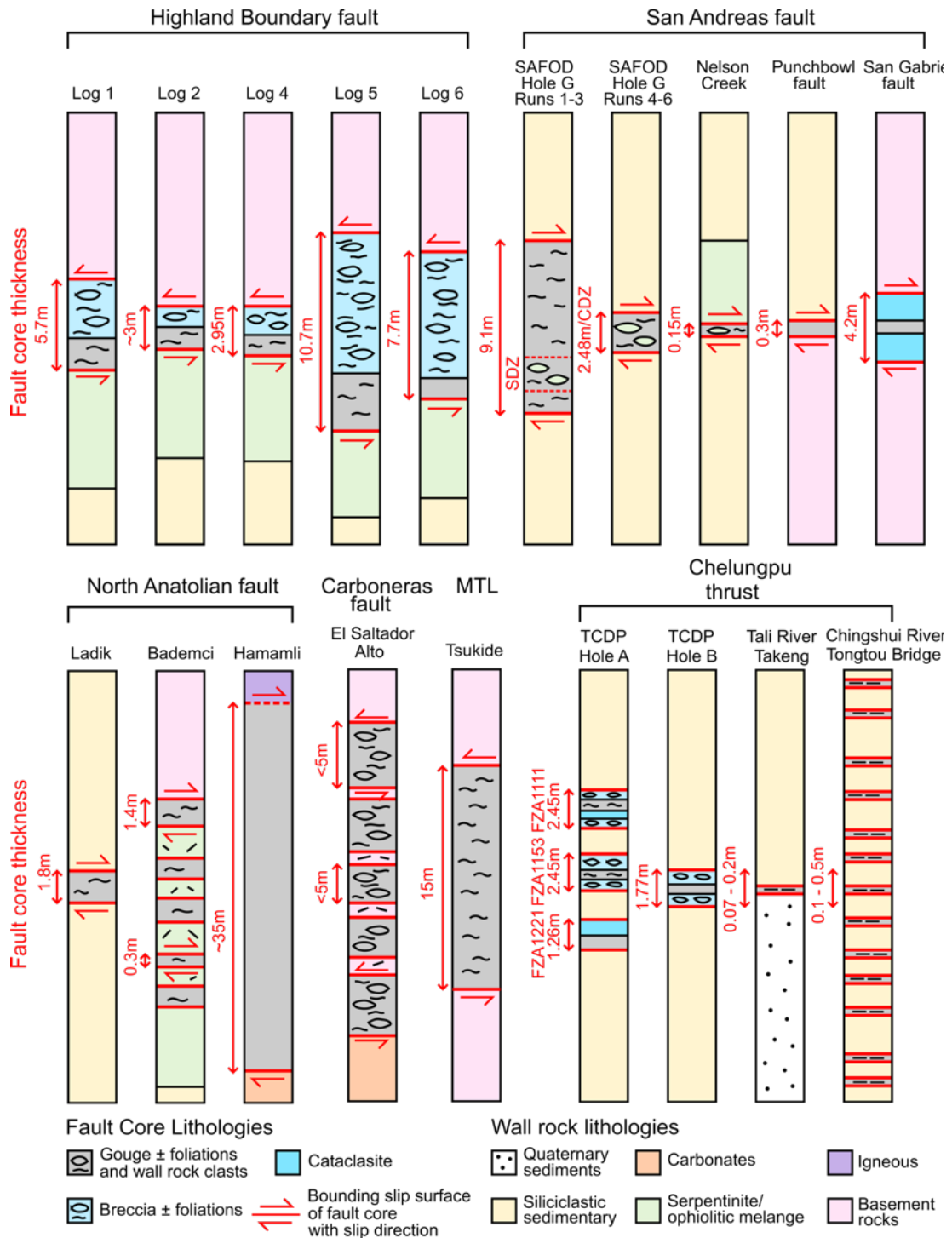
**Fig. 4.2.** Log-log plot of fault core thickness and total displacement for **(a)** intraplate faults and **(b)** plate boundary (colour) faults vs. intraplate (greyscale) faults. The trendline shows the linear, statistically significant ( $p$  value 0.0004) relationship between fault core thickness and total displacement for intraplate faults and is extrapolated to large displacement values. There is no trend for plate boundary faults ( $p$  value 0.155). Error bars for individual displacement and fault core thickness are smaller than the size of each data point (see **Table 4.2** and Appendix 4 for errors/uncertainty ranges associated with each data point). Displacement is unknown for the data in the Rowe et al. (2013) compilation due to a lack of preserved displacement markers. Strike-slip faults are represented by squares, reverse/thrust faults by triangles, normal faults by circles and an unknown sense of motion by diamonds. See the Appendix 4 a description of data. \*: 1-McKay et al. (2020); 2-Tanner (2008); 3-Cawood et al. (2012); 4-Matthews (1976); 4a-Wesnousky (1988); 5-Wesnousky (2005); 6-Holdsworth et al. (2011); 7-Bradbury et al. (2011); 8-Moore & Rymmer (2012); 9-Chester and Logan (1986); 10-Schulz and Evans (2000); 11-Chester et al. (1993); 12-Dor et al. (2006); 13-Toy et al. (2015); 14-Barth et al. (2013); 15-Schuck et al. (2020); 16-Boulton et al. (2014); 17-Faulkner et al. (2003); 18-Armijo et al. (1999); 19-Hubert-Ferrari et al. (2002); 20-Sengör et al. (2005); 21-Dor et al. (2008); 22-Uysal et al. (2016); 23-Okada (1980); 24-Wibberley and Shimamoto (2003); 25-Shigematsu et al. (2012); 26-Chester et al. (2013); 27-Kirkpatrick et al. (2015); 28-Moore et al. (2009); 29-Ujiie and Kimura (2014), 30-Shipboard Scientific Party (2002); 31-Hirono et al. (2016); 32-Sakaguchi et al. (2011); 33-Heermance and

*Evans (2006); 34-Yeh et al. (2007); 35-Hirono et al. (2007); 36-Heermance et al. (2003); 37-Li et al. (2009); 38-Li et al. (2013); 39-Shipboard Scientific Party (1998); 40-Ikesawa et al. (2003); 41-Ujiie et al. (2007a); 42-Ujiie et al. (2007b); 43-Rowe et al. (2011).*

#### 4.4. Plate Boundary Fault Structure and Composition

Data from intraplate faults show that, in general, low displacement faults represent a stage of early growth and are thin but evolve into wide fault zones as they extend in length, link with adjacent faults and develop more complex structures (Childs et al., 2009, 2017; Fossen & Rotevatn, 2016 and references therein; **Fig. 4.1**, **Fig. 3.1**). Based on this rationale we could hypothesise that plate boundary fault cores are consistently narrower than intraplate faults because they have simple, uniform structures. To test this, we constructed schematic structural logs for each plate boundary exposure and drill core intersection reported in the published scientific literature. **Fig. 4.3** shows a sub-set of these logs: the full set is available in the Appendix 4 (**Fig. S1** and **S2**). Whilst all these plate boundary faults are narrow, their structures are not the same or simple. For example, the Highland Boundary fault (HBF) is a sinistral strike-slip fault with  $115 \pm 85$  km total displacement (McKay et al., 2020 and references therein). In all mapped exposures the fault core is a single strand that varies in thickness between 2.95 to 10.7 m (**Fig. 4.3**) (McKay *et al.* 2020). The host rocks remain constant along-strike as the fault separates serpentinite from basement rocks at all exposures. In contrast, the fault core of the dextral strike-slip North Anatolian fault (NAF) remains narrow despite juxtaposing different host rock lithologies along-strike (**Fig. 4.3**) (Dor *et al.* 2008). Unlike the HBF and NAF, the Chelungpu thrust is a convergent boundary with a minimum of 14 km total displacement (Heermance & Evans 2006). The fault principally slips within siliciclastic sedimentary rocks. At some exposures the fault core is composed of a single strand that varies in thickness between 0.07 to 1.77 m (Heermance *et al.* 2003; Yeh *et al.* 2007). At other exposures the fault core consists of a number of strands 0.1 to 2.45 m wide (**Fig. 4.3**) (Heermance *et al.* 2003; Yeh *et al.* 2007). Thus, the fact that plate boundaries are narrow appears not to be related to the host rock, slip directions, plate boundary type (strike-slip or convergent), distance

along-strike or the number of fault strands. These all vary but the plate boundaries remain comparatively narrow.



**Fig. 4.3.** Schematic structural logs illustrating fault core thickness and composition for plate boundary faults. MTL, Median Tectonic Line.

Based on this small dataset it may be the case that the fault core is narrowest when the fault is hosted between wall rocks of contrasting competencies i.e., mechanically weak serpentinite against basement or sedimentary rock, compared to basement against basement or sedimentary against sedimentary with similar competencies. For example, the San Andreas fault is narrowest (0.15 m) when serpentinite juxtaposes sedimentary rocks (Moore & Rymer 2012) and widest (9.1 m) when sedimentary rock juxtaposes sedimentary rock (Holdsworth *et al.* 2011) (**Fig. 4.3**). This suggests the strength contrast between the faulted layers (mechanical stratigraphy) may, in part, control the variations in fault core thickness along-strike, but it clearly does not control the average thickness.

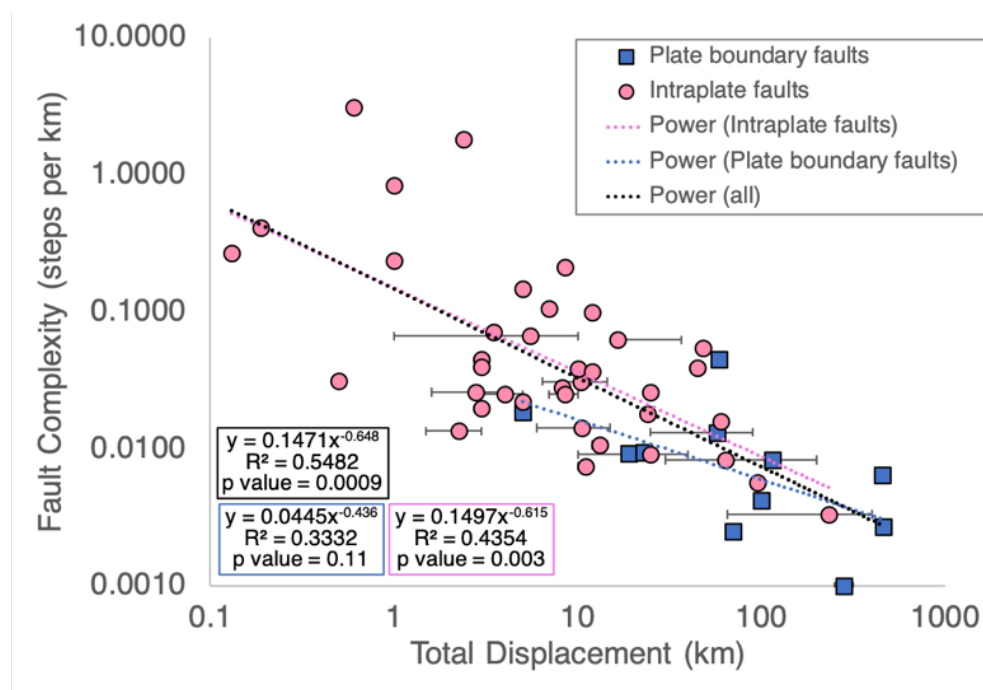
Several studies have demonstrated that fault complexity decreases as a function of increased displacement (Wesnousky 1988; Stirling *et al.* 1996; de Jossineau & Aydin 2009). Based on this rationale we could hypothesise that plate boundary faults with large displacements have less complex geometries than intraplate faults with smaller displacements. To test this, we compared the fault complexity between plate boundary and intraplate strike-slip fault systems. The data show a statistically significant ( $p$  value = 0.0009) relationship between fault displacement and fault complexity (steps per unit length) (**Fig. 4.4**). That is, large displacement plate boundary faults have fewer steps per unit km and thus smoother and simpler geometries compared to smaller displacement intraplate faults. Further work is needed to expand the dataset in order to determine if they are part of a single population or can be split into two different populations.

Fault	Fault type	Fault length (km)	Scale	Fault displacement (km)	No. of steps	Step size (km)	Steps per km	Source*
<i>Plate boundary faults</i>								
HBF	S-SS	120	-	115 ± 85	1	~5	0.0083	1
San Andreas	D-SS	1000	1/2940000	282.5 ± 32.5	1	~1	0.0010	2
North Anatolian	D-SS	989	1/4550000	57.5 ± 32.5	13	1-10	0.0133	2
Wairau	D-SS	100	1/550000	455 ± 25	-	>1	0.0065	3
Hope	D-SS	220	1/560000	19	-	>1	0.0093	3
Altun	S-SS	1600	1/5000000	70 ± 5	-	>1	0.0025	3
Kunlun	SS	1500	1/10000000	100	6	>1	0.0042	4 (5)
Marmara	SS	114	1/1300000	59	5	>1	0.0459	6 (5)
Chamam	S-SS	460	1/2500000	460	1	>1	0.0027	7 (5)
Median	D-SS	215	1/1330000	5	-	>1	0.0185	3
Tectonic Line								
Great Sumatran	D-SS	1900	1/4620000	23	18	>1	0.0095	8 (5)
<i>Intraplate faults</i>								
Newport-Inglewood	D-SS	60	1/1050000	5.5 ± 4.5	4	2-3	0.0667	2
Whittier-Elsinore	D-SS	330	1/4000000	25 ± 15	3	3	0.0091	2
San Jacinto	D-SS	239	1/323000	25	6	1-8	0.0261	2
Garlock	S-SS	240	1/3030000	64	2	0.5-3	0.0083	2
Calaveras	D-SS	220	1/345000	24	4	2-7	0.0182	2
Helendale	D-SS	80	1/530000	3	-	>1	0.0450	3
Calico-Mequite	D-SS	125	1/870000	8.2	-	>1	0.0280	3
Pisgah	D-SS	64	1/500000	10.4 ± 4	-	>1	0.0310	3
Camp Rock	D-SS	73	1/570000	2.8 ± 1.2	-	>1	0.0260	3
Lenwood	D-SS	75	1/480000	2.25 ± 0.75	-	>1	0.0135	3
San Miguel-Vallecitos	D-SS	160	1/1090000	0.5	-	>1	0.0315	3
Neodani	S-SS	100	1/670000	4 ± 1	-	>1	0.0250	3
Atera	S-SS	60	1/600000	8.5 ± 1.5	-	>1	0.0250	3
Atotsugawa	D-SS	60	1/590000	3	-	>1	0.0400	3
Tanna	S-SS	30	1/310000	1	-	>1	0.8350	3
Wellington	D-SS	200	1/1820000	11 ± 1	-	>1	0.0075	3
Haiyuan	S-SS	280	1/1670000	13.25 ± 1.25	-	>1	0.0107	3
Valley of Fire State Park	D-SS	-	1/37000	2.4	-	0.03-0.05	1.8100	5
Valley of Fire State Park	D-SS	-	1/37000	0.6	-	0.03-0.05	3.0900	5
Las Vegas Shear Zone	SS	150	1/1030000	48	8	>1	0.0549	9 (5)
Mattinata	S-SS	150	1/510000	5	3	~5	0.0223	10 (5)
Mae Kuang	SS	30	1/360000	3.5	2	~1	0.0714	11 (5)
Coloso	S-SS	80	1/180000	5	12	~0.5	0.1487	12 (5)
Buesaco	D-SS	29	1/77000	0.188	12	0.2-0.5	0.4116	13 (5)
Gemini	S-SS	9.3	1/62500	0.131	2	~0.1	0.2688	14 (5)
Amanos	S-SS	200	1/800000	45	8	2-10	0.0390	15 (5)
East Hatay	S-SS	100	1/800000	10	4	>1	0.0383	15 (5)
Ludlow	D-SS	75	1/1750000	12	8	?	0.1000	16 (5)
Blackwater	D-SS	60	1/1750000	7	6	?	0.1064	16 (5)
Gowk	D-SS	150	1/1950000	12	5	1-5	0.0366	17 (5)
Jid	D-SS	60	1/230000	1	14	~0.5	0.2368	18 (5)
Roum	SS	35	1/180000	8.5	7	?	0.2110	19 (5)
Arima-Taktsuki	D-SS	60	1/440000	16.5 ± 20	4	1-5	0.0625	5
Quijang	D-SS	70	1/50000	10.5 ± 4.5	1	~3	0.0143	20
Owens Valley	D-SS	100	-	3	2	2-5	0.0200	21(20)
Karakorum	D-SS	1500	-	232.5 ± 167.5	5	~5	0.0033	22, 23 (20)



Fault	Fault type	Fault length (km)	Scale	Fault displacement (km)	No. of steps	Step size (km)	Steps per km	Source*
Ganzi-Yushu	S-SS	500	-	60	8	5-10	0.0160	24(20)
East Lut	SS	700	-	95	4	~1	0.0057	25(20)

**Table 4.3.** Compiled dataset of fault geometries (steps per unit length) for plate boundary and intraplate strike-slip faults. SS: strike-slip; S-SS: sinistral strike-slip; D-SS: dextral strike-slip. \*Sources: 1-Tanner (2008); 2-Wesnousky, (1988); 3-Stirling et al. (1996); 4-Fu and Awata (2007); 5-de Jossineau and Aydin (2009); 6-Le Pichon Aycy et al. (2001); 7-Lawrence et al. (1992); 8-Sieh and Natawidjaja (2000); 9-Langenheim et al. (2001); 10-Brankman and Aydin (2004); 11-Rhodes et al. (2004); 12-Cembrano et al. (2005); 13-Rovida and Tibaldi (2005); 14-Pachell and Evans (2002); 15-Tatar et al. (2004); 16-Jachens et al. (2002); 17-Walker and Jackson (2002); 18-Walker et al. (2006); 19-Nemer and Meghraoui (2006); 20-Manighetti et al. (2015); 21-Bacon and Pezzopane (2007); 22-Robinson (2009); 23-Chevalier et al. (2012); 24-Li et al. (2012); 25-Walpersdorf et al. (2014). Value in brackets mean referenced in.



**Fig. 4.4.** Log-log plot of total displacement and fault complexity (defined as steps per km) for plate boundary (blue squares) and intraplate (pink circles) strike-slip fault systems.

## 4.5. Comparing Plate Boundary and Intraplate Fault Earthquake Events

To examine whether there is any evidence in the seismological literature for a difference in the energy emitted by intraplate and plate boundary faults we examined the scaling relations between seismic moment, average displacement and surface

rupture length. Seismic moment ( $M_0$ ) is a measure of the “size” or “work” of an earthquake (Bormann et al., 2013). It can be calculated from fault slip dimensions measured in the field or from aftershock distributions using the formula (equation(4.2)):

$$M_0 = \mu AD \quad (\text{eq. 4.2})$$

where,  $\mu$  is the shear modulus, A is the event rupture area and D is the average displacement on the fault during coseismic rupture i.e. the average displacement caused by the individual seismic event (**Fig. 4.1**; Kanamori & Anderson, 1975; Kanamori & Brodsky, 2001). The approach for the calculation of the area depends to a degree on the source (kinematic) model (circular, rectangular, elliptical), for example for small faults and earthquakes, Brune’s circular model is considered adequate. The rectangular plane is considered adequate for large earthquakes. Alternatively,  $M_0$  can be measured from the source spectra of body or surface waves (from the integral of the far-field displacement, or from the amplitude of the near-field displacement) or is derived from a moment tensor solution (Bormann et al., 2013). As such, calculating the seismic moment from spectral analyses is independent from average displacement. Whilst  $M_0$  is not a direct measure of energy, it is linearly related to the radiated seismic energy ( $E_R$ ) by the formula (equation(4.3)):

$$E_R \approx \eta_R \frac{\Delta\sigma_S}{2\mu} M_0 \quad (\text{eq. 4.3})$$

where,  $\eta_R = E_R / (E_R + E_G)$  is radiated efficiency and  $\Delta\sigma_S$  is the static stress drop, i.e., the difference between shear stresses on the fault before and after the earthquake (Bormann et al., 2013; Venkataraman & Kanamori, 2004 and references therein). As stated by Kanamori & Brodsky (2004),  $M_0$  is also linearly related to the magnitude ( $M_w$ ) by the formula (equation(4.4)):

$$M_w = (\log M_0 - 9.1) / 1.5 \quad (\text{eq. 4.4})$$

Thus, the higher the seismic moment, the higher the radiated seismic energy and the higher the magnitude of the resulting earthquake.

We find that for a given value of average displacement, plate boundary fault earthquakes typically have a greater seismic moment (**Fig. 4.5a**) and rupture a longer length at the surface (**Fig. 4.5b**) compared to intraplate faults. Values for seismic

moment in *Fig. 4.5a* are taken from Wells and Coppersmith (1994) and only where such values have been derived from spectral analysis of the seismic data (i.e., are independent of measured displacement). Our analyses show the best-fit line derived only from those events for which seismic moment has been derived from spectral analyses (as explained previously); however, for information, seismic events with field-derived seismic moments are also included on (*Fig. 4.5*) (unfilled symbols) and clearly show the same trends. These findings imply that plate boundary faults do not dissipate as much energy as intraplate faults during earthquakes meaning that for a given value of average displacement, more energy is radiated to the surface resulting in a greater seismic moment and hence a higher magnitude earthquake.

Location	Earthquake	Date	Fault type	Mw	Seismic moment (Nm)	Surface rupture length (km)	Avg. Displacement (m)	Source *
USA, CA	Fort Tejon	1857	RL	8.3	6.70E+21	297	6.4	1
USA, CA	San Francisco	1906	RL	7.8	7.90E+21	432	3.3	1
USA, CA	Parkfield	1966	RL	6.4	2.70E+19	38.5		1
USA, CA	Superstition Hills	1987	RL	6.6	9.20E+19	27	0.54	1
Turkey	Erzincan	1939	RL	7.8	5.75E+21	360		1
Turkey	Kastamonu/Tosya –Ladik	1943	RL	7.5	2.60E+21	280		1
Turkey	Bolu-Gerede	1944	RL	7.5	2.70E+21	180	1.8	1
Turkey	Varto	1966	RL	6.8	2.35E+20	30	0.15	1
Turkey	Mudurna Valley	1967	RL	7.4	1.13E+21	80	1.63	1
Turkey	Bingol	1971	LL	6.7	1.00E+20	38		1
Turkey	Caldiran	1976	RL	7.3	7.90E+20	55	2.05	1
Guatemala	Motagua	1976	LL	7.5	3.10E+21	235	2.6	1
USA, CA	Imperial Valley/El Centro	1940	RL	7.2	2.70E+20	60	1.5	1
USA, CA	Borrogo Mountain	1968	RL	6.8	1.00E+20	31	0.18	1
USA, CA	Coyote Lake	1979	RL	5.7	5.10E+18	14.4		1
USA, CA	Imperial Valley/El Centro	1979	RL	6.7	7.12E+19	30.5	0.18	1
USA, CA	Elmore Ranch	1987	LL	6.2	2.60E+19	10		1
Turkey	Canakkale/Yenice –Gönen	1953	RL	7.2	7.70E+20	58	2.1	1
China	Kansu/Haiyuan	1920	LL	8.5	1.20E+22	220	7.25	1
China	Tonghai	1970	RL	7.5	8.70E+20	48	2.1	1
China	Luhuo	1973	LL	7.3	1.80E+21	89	1.3	1
China	Daofu	1981	LL	6.8	1.01E+20	44		1
Turkey	Duzce	1999	RL	7	5.40E+19	40		2, 3
Turkey	Izmit	1999	RL	7.1	2.19E+20	145		2, 3
China	Kunlun	2001	LL	7.8	5.85E+20	431		2, 3
Alaska	Denali	2002	RL	7.6	5.65E+20	302		2, 3
Turkey	Niksar-Erbaa	1942	RL-N	7.2	2.50E+20	47	0.66	1
Turkey	Lice	1975	R	6.7	7.40E+19	26	0.5	1
Turkey	Pasinier/Erzincan	1983	LL-R	6.9	1.405E+20	12		1

\* 1 - Wells and Coppersmith (1994); 2 – Wesnousky (2006); 3 – Wesnousky (2008)

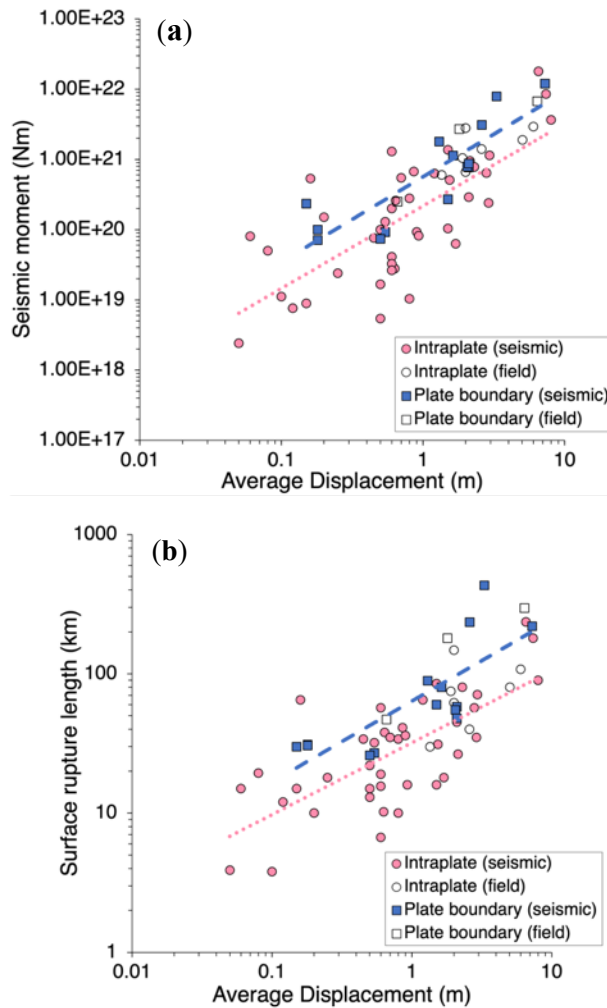
**Table 4.4.** Compiled dataset of plate boundary fault earthquake events used in **Fig. 4.5**. Mw, magnitude; RL, right lateral; LL, left lateral; N, normal; R, reverse

Location	Earthquake	Date	Fault type	Mw	Seismic moment (Nm)	Surface rupture length (km)	Average Displacement (m)	Source*
USA, CA	Hayward	1868	RL	6.8	1.56E+20	48		1
USA, CA	Owens Valley	1872	RL-N	8	2.92E+21	108	6	1
USA, CA	Kern County	1952	R-LL	7.7	1.30E+21	57	0.6	1
USA, CA	San Fernando/Sylmar	1971	R-LL	6.5	1.04E+20	16	1.5	1
USA, CA	Oroville	1975	N-RL	5.6	1.18E+19	3.8		1
USA, CA	Homestead Valley	1979	RL	5.6	2.41E+18	3.9	0.05	1
USA, CA	Greenville	1980	RL	5.9	6.00E+18	6.2		1
USA, CA	Coalinga, Nunez	1983	R	5.4	1.50E+18	3.3		1
USA, CA	Landers	1992	RL	7.6	1.14E+21	71	2.95	1
USA, CA	Eureka Valley	1993	N	5.8	1.50E+19	4.4		1
USA, Nevada	Pleasant Valley	1915	N	7.6	6.60E+20	62	2	1
USA, Nevada	Cedar Mountain	1932	RL	7.2	1.97E+20	61		1
USA, Nevada	Rainbow Mountain	1954	N	6.3	2.40E+19	18	0.25	1
USA, Nevada	Stillwater	1954	N	6.9	7.60E+19	34	0.45	1
USA, Nevada	Fairview Peak	1954	RL-N	7.2	6.40E+20	57	2.8	1
USA, Nevada	Dixie Valley	1954	RL-N	6.8	2.90E+20	45	2.1	1
USA, MT	Hebgen Lake	1959	N	7.6	9.50E+20	26.5	2.14	1
USA, Idaho	Borah Peak	1983	N-LL	7.3	2.80E+20	34	0.8	1
Mexico	Pitayacachi/Sonora	1887	N	7.4	1.05E+21	75	1.9	1
Mexico	San Miguel	1956	RL-R	6.9	1.00E+20	22	0.5	1
Canada	Ungava	1989	R	6.3	1.04E+19	10	0.8	1
Australia	Meckering	1968	R-RL	6.9	9.30E+19	36	0.9	1
Australia	Cadoux	1979	R	6.1	1.67E+19	15	0.5	1
Australia	Marryat Creek	1986	R-LL	5.8	5.40E+18	13	0.5	1
Australia	Tennant Creek	1988	R	6.3	2.80E+19	10.2	0.63	1
Australia	Tennant Creek	1988	R-LL	6.4	4.10E+19	6.7	0.6	1
Australia	Tennant Creek	1988	R	6.7	8.20E+19	16	0.93	1
Greece	Thessaloniki	1978	N	6.4	5.02E+19	19.4	0.08	1
Greece	Kalamata	1986	N	5.8	8.90E+18	15	0.15	1
Greece	Corinth	1981	N	6.4	2.65E+19		0.6	1
Greece	Corinth	1981	N	6.4	3.29E+19	19	0.6	1
Greece	Corinth	1981	N	6.7	1.00E+20		0.6	1
Bulgaria	Papzili	1928	N	6.9	5.50E+20	50		1
Albania	Dibra	1967	RL-N	6.6	1.50E+20	10	0.2	1
Turkey	Alaschir Valley	1969	N	6.5	1.30E+20	32	0.54	1
Turkey	Gediz	1970	N	7.1	6.70E+20	41	0.86	1
China	Wuqai	1985	R	7.3	2.46E+20	15		1
China	Lancang-Gengma	1988	RL	7.3	5.47E+20	35	0.7	1
China	Gengma, Yunnan	1988	RL	7.2	2.00E+20	15.6	0.6	1
China	Changma	1932	R-LL	7.7	2.80E+21	148	2	1
China	Kehetuohai-E/Fuyun	1931	RL	7.9	8.5E+28	180	7.38	1
China	Damxung	1951	RL	8	3.65E+21	90	8	1
Japan	Nobi	1891	LL	8	1.90E+21	80	5.04	1
Japan	Rikuu/Senya	1896	R	7.2	1.40E+21	40	2.59	1
Japan	North Izu	1930	LL-R	7.3	2.40E+20	35	2.9	1
Mongolia	Gobi-Altai	1957	LL	7.9	1.80E+22	236	6.54	1
Mongolia	Mogod	1967	RL	7.4	3.90E+20	40		1
Iran	Salmas	1930	N-RL	7.4	6.00E+20	30	1.35	1
Iran	Ipak/Buin Zahra	1962	R	7.2	1.17E+21	99		1
Iran	Dasht-e-Bayaz	1968	LL	7.2	7.80E+20	80	2.3	1
Iran	Bob-Tangol	1977	RL	5.8	7.60E+18	12	0.12	1
Iran	Tabas-e-Golshan	1978	R	7.5	1.37E+21	85	1.5	1
Iran	Kurizan	1979	RL-R	6.7	9.10E+19	17		1
Iran	Koli	1979	LL-R	7.1	6.30E+20	65	1.2	1
Iran	Golbaf	1981	R-RL	6.7	8.07E+19	15	0.06	1
Iran	Sirch	1981	R-RL	7.1	5.35E+20	65	0.16	1

Location	Earthquake	Date	Fault type	Mw	Seismic moment (Nm)	Surface rupture length (km)	Average Displacement (m)	Source*
Iran	Rudbar-Tarom	1990	R-LL	7.7	1.47E+21	80		1
North Yemen	Dhamer	1982	N	6	3.64E+19	15		1
West Africa	Guinea	1983	RL-N	6.2	3.40E+19	9.4		1
Algeria	El Asnam	1980	R	7.3	5.08E+20	31.2	1.54	1
Algeria	Constantine	1985	LL	5.9	1.11E+19	3.8	0.1	1
Algeria	Chenoua	1989	R	5.7	1.04E+19	4		1
Peru	Ancash	1946	N	7.2	9.40E+20	21		1
Peru	Cuzco	1986	N	4.6	7.70E+17	2.5		1
USSR	Armenia/Spitak	1988	R-RL	6.8	1.53E+20	25		1
Italy	Avezzano	1915	N	7	9.70E+19	20		1
Columbia	Popayan	1983	SS/N	4.9	3.50E+18	1.3		1
New Zealand	Edgecumbe	1987	N	6.6	6.30E+19	18	1.7	1
Italy	South Apennines/Irpinia	1980	N	6.9	2.60E+20	38	0.64	1
Japan	North Izu	1930	LL-R	7.3	2.40E+20	35		1
Columbia	Popayan	1983	SS/N	4.9	3.50E+18	1.3		1
Iran	Fandoqa	1998	SS-N	6.6	1.05E+19	25		2, 3
USA, CA	Hector Mine	1999	SS-R	6.9	6.45E+19	44		2, 3

\* 1 - Wells and Coppersmith (1994); 2 – Wesnousky (2006); 3 – Wesnousky (2008)

**Table 4.5.** Compiled dataset of intraplate fault earthquake events used in **Fig. 4.5**. Mw, magnitude; RL, right lateral; LL, left lateral; N, normal; R, reverse



**Fig. 4.5.** Comparing intraplate and plate boundary fault earthquake events. **(a)** Log-log plot of average displacement against seismic moment. We separate the data based on fault type (plate boundary fault – squares; intraplate faults – circles) and also the method in which the seismic moment was determined (derived from seismological data – colour; derived from field data – unfilled). We only show the best-fit line where the seismic moment has been derived from seismological data as the axes are truly independent. The fit line colour matches data points (blue - plate boundary; pink - intraplate events). **(b)** Log-log plot of average displacement and surface rupture length of the fault associated with the earthquake event. The average displacement is not available for all events; therefore, the plots do not show exactly the same events.

## 4.6. Discussion

For the first time fault core thickness and total displacement data have been compared for plate boundary and intraplate faults. We observe that the evolution of plate boundary faults is different to the more widely studied and better understood evolution of intraplate faults. Plate boundary faults are anomalous when compared to the global

population of intraplate faults; they have narrower fault cores and the fault core thickness does not increase with increasing displacement. Keren & Kirkpatrick (2016) previously observed that the damage zone thickness of the Japan Trench was anomalously narrow and did not follow the damage zone thickness to total displacement trend described for intraplate faults (Mayolle et al., 2019 and references therein). It may therefore be possible that a similar compilation of fault damage zone thicknesses may also show that plate boundary faults have anomalously narrow damage zones compared to intraplate faults. This would make sense given plate boundary fault zones dissipate less energy (**Fig. 4.5**) therefore less energy is available to deform the surrounding rock as much. Data on fault core thickness were only included in **Fig. 4.2** where the difference between the fault core and the fault damage zone was clearly described. Future research could explore whether fault damage zones are also anomalously narrow on plate boundary faults.

Scholz et al. (1986), state that intraplate fault cores are thin (gouge thicknesses 1-10 m), whereas plate boundary faults are wide (gouge thicknesses 100-1000 m) as a result of increased continuous dynamic wear of the wall rock with increased total displacement. However, no data are provided to back up this statement and our compilation of published data (**Fig. 4.2**) contradicts their proposition. Delogkos et al. (2020), suggest that all increases in fault zone thickness are the result of structural linkage and that once they reach a sufficient thickness they can accommodate slip events without continuous processing of the wall rock. From our compilation of plate boundary structures (**Fig. 4.3**), we suggest plate boundary fault cores are consistently narrow regardless of their structure. The fault core composition, host rock, slip direction, fault type, and/or the number of fault core strands all vary, both along an individual plate boundary and on comparison between different plate boundaries, but in all examples the fault core remains consistently narrow.

We suggest plate boundary faults remain narrow as they are not required to grow in the same way as intraplate faults. Intraplate faults get thicker with increasing displacement through lateral tip processing and/or linkage with other fault segments



via relay formation and breaching (Childs et al., 2009, 2017; Fossen & Rotevatn, 2016 and references therein; **Fig. 4.1**). That is, low displacement faults represent a stage of early growth and are thin but evolve into wide fault zones as they extend in length, link with adjacent faults and become more complex in structure. Plate boundary faults start as pre-existing, inherited structures on regional-scale zones of weakness. As such, their tips do not terminate within intact rock - they terminate at triple junctions with other plate boundaries (McKenzie & Morgan 1969). Tectonic plates are continually moving, albeit very slowly, and are constantly rearranging themselves in response to each other. For instance, the boundary between the North American and Pacific Plate has evolved and grown through time from a subduction boundary to the present-day San Andreas transform fault. As a result, while plate boundary faults still grow and evolve through time as triple junctions and plates move apart relative to each other, they are not required to grow in length either by damaging intact rock at their tips or by linking with other pre-existing structures (as shown for intraplate faults in **Fig. 4.1**). The lack of linkage zones will tend to produce smoother structures (as shown in **Fig. 4.4**). The lack of a relationship between fault zone thickness and total displacement on plate boundaries tends to support the hypothesis of Delogkos et al. (2020) for growth of intraplate faults. They suggest that fault cores increase in thickness only due to progressive fault linkage, and that once they reach a sufficient thickness they can accommodate slip events without continuous processing of the wall rock – as appears to be the case for plate boundary faults.

Several authors have demonstrated that the more total displacement a fault accumulates, the smoother and straighter its surface geometry (e.g., Brodsky et al., 2011; de Joussineau & Aydin, 2009; Sagy et al., 2007; Stirling et al., 1996; Wesnousky, 1988). Therefore, plate boundary faults with large total displacement values should be expected to have smooth and straight surface geometries as proposed by Wesnousky (1988) and demonstrated in **Fig. 4.4**. Using a combination of rock friction experiments and numerical modelling, Zielke et al. (2017) discuss the role of fault roughness on the stress drop and earthquake magnitude and postulate that smoother faults generate larger earthquakes compared to rougher faults under the same

tectonic loading conditions. That is, faults with smoother surfaces do not need to consume as much energy to slip (i.e. dissipate less energy) compared to faults with rougher surfaces. The observations we present supports the hypothesis of Zielke et al. (2017). **Fig. 4.5b** demonstrates that for a given value of average displacement plate boundary faults rupture a longer length at the surface compared to intraplate faults. This implies that it may not be as easy to terminate a rupture on a plate boundary than on a rougher intraplate fault, which makes sense if they are narrow (**Fig. 4.2**), smooth (**Fig. 4.4**) and terminate at triple junctions and not within intact rock. Further, as demonstrated by the 1992 Landers earthquake, extra energy is required to hop over segments within faults (Hauksson *et al.* 1993). Earthquakes that propagate along a smoother fault will therefore find less energy being absorbed through segment hopping and/or the processing of intact rock allowing more energy to be radiated to the surface as observed from the compiled datasets. Therefore, plate boundary faults, which are long structures where the ongoing evolution of the structure does not necessitate deformation of the host rock blocks around stepover regions that produce complex geometries, will absorb less energy through segment hopping. By contrast, intraplate faults dissipate energy and get thicker as fault slip increases, generating complex zones of damage in the surrounding rock and propagating through linkage with neighbouring structures (**Fig. 4.1**). The more complex the final fault geometry, the more energy has to be consumed at depth and the less energy reaches the surface (Ross *et al.* 2018).

## 4.7. Conclusion

Fault cores are well documented as getting thicker and developing more complex geometries with increasing total displacement, albeit with a wide range in thicknesses at a single value of displacement. This increase in thickness occurs through the linkage of fault segments with increasing total displacement and/or repeated rupture events which comminute fault slip surfaces and progressively fracture the surrounding intact rock at the fault tips and in a zone of damage that surrounds the fault. We have compiled data from the peer-reviewed literature to show that this relationship between fault core thickness and increasing displacement does not hold for plate boundary faults, which are anomalously narrow by comparison to intraplate faults and do not

show the same trend of increasing average thickness with increasing displacement. From a compilation of plate boundary structures, we find plate boundary faults remain narrow regardless of how many earthquake events they have experienced or their local fault structure (fault core composition, host rock juxtaposition, slip direction, fault type, and/or the number of fault core strands). By examining the scaling relations between seismic moment, average displacement and surface rupture length for plate boundary and intraplate fault ruptures, we confirm that plate boundary faults display a greater seismic moment than intraplate faults for a given displacement and show that they also rupture a longer length. We propose that this occurs because plate boundary faults are anomalously narrow, they are comparatively smooth and terminate at triple junctions and not intact rock, and since our data show they do not increase in thickness with increasing displacement, they are not processing intact rock as much during seismic events. Thus, plate boundary faults do not dissipate as much energy as intraplate faults during earthquakes meaning that for a given value of average displacement, more energy is radiated to the surface resulting in higher magnitude earthquakes.

# Chapter 5 – The Temporal Evolution of a Plate Boundary Fault Core: A Case Study of the Highland Boundary Fault at Stonehaven

*This chapter is in preparation to be submitted to the Journal of the Structural Geology. Co-authors include Shipton, Z.K., Lunn, R.J., and Andrews B.*

## *Abstract*

The presence of clay-rich fault rocks within the fault core influences the slip behaviour of faults during earthquake rupture. Clay-rich fault cores are often found within plate boundary faults. Fault rocks exhumed at Earth's surface develop through progressive deformation at a range of crustal conditions. The exhumed fault core is thus complicated by overprinting and the result of multiple integrated events on a fault over time. Therefore, only considering the present-day structure of the fault, and not how it evolved, is a finite view of that fault. In this study we present detailed observations of the core of an ancient plate boundary fault in Scotland (the Highland Boundary Fault) in outcrop and to microstructural scale. The relative timing of fault rock lithologies is investigated and we suggest mechanisms by which the fault core evolved through time. Our fault core observations suggest both wall rocks have been incorporated into the fault core and that both chemical and physical processes have been responsible for grain size reduction and wall rock comminution. The fault core units remain distinct due to a contrast in the way the wall rocks have been processed over time (chemical vs. mechanical). A process of multi-event evolution has likely caused the mechanical properties of the fault core to vary, becoming either stronger or weaker with each progressive phase of deformation. In turn, this will have affected the ability of the Highland Boundary Fault to host earthquakes through time.

## 5.1. Introduction

Earthquakes occurring along plate boundary faults represent a significant hazard and account for ~90% of global seismicity (USGS, 2016). The earthquake potential of a given fault, or fault segment, depends on the mechanical strength of faults in the system (Imber *et al.* 2008; Collettini *et al.* 2019). This in turn is influenced by the spatial and temporal thickness, composition and structure of the fault core (Wibberley *et al.* 2008; Faulkner *et al.* 2010; Rowe *et al.* 2013). The fault core can be structurally and lithologically variable (Heermance *et al.* 2003; Kirkpatrick *et al.* 2008, 2018; Barth *et al.* 2013; Sosio De Rosa *et al.* 2018a; McKay *et al.* 2020) and is typically composed of variably cohesive fault rock such as clay-rich gouge, cataclasite and/or breccia (Sibson 1977; Caine *et al.* 1996). The structural style can vary from a single fault core surrounded by an associated fractured damage zone (Holdsworth *et al.* 2011; McKay *et al.* 2020) to complex systems composed of multiple fault core strands that entrain lenses of variably fractured wall rock between the branches (Schuck *et al.* 2020).

Outcrop and drilling studies reveal that unlike intraplate faults, plate boundary fault cores are anomalously thin (0.07 to ~35 m) and display variable degrees of strain localisation (McKay *et al.* 2021 and references therein). The presence of clay-rich fault rocks, even when it constitutes only a small percentage of the fault rock assemblage, can alter the bulk mechanical strength of the fault and lead to strain localisation and/or deformation (Wibberley *et al.* 2008; Collettini *et al.* 2009a; Faulkner *et al.* 2010). For instance, the currently active creeping section of the San Andreas Fault is attributed to the presence of mechanically weak smectite within the fault core (Bradbury *et al.* 2011; Holdsworth *et al.* 2011; Moore & Rymer 2012; Moore & Lockner 2013). Clay-rich fault rocks are particularly important in plate boundary fault systems as they are commonly observed within the fault cores of these type of faults, regardless of their structural style (McKay *et al.* 2021 and references therein).

Increased fault complexity results from the interaction of mechanical and chemical processes (Sibson 1977; Childs & Watterson 1996; Childs *et al.* 2009, 2017; Caine *et*

*al.* 2010; Fossen & Rotevatn 2016 and references therein). Mechanical processes tend to weaken the fault core through grain size reduction and include abrasion, wall rock wear and the incorporation of wall rock as clasts and lenses into the fault zone. Fault rocks develop through progressive shearing initially forming fault-bounded lenses that ultimately become comminuted to cataclasite, breccia or gouge (e.g., Childs *et al.* 2009). Shearing can also cause elongated wall rock clasts and fault rock fabric to develop in systematic Reidel shear geometries (Haines *et al.* 2013; Warr *et al.* 2014). Chemical processes may increase or decrease the mechanical strength of the fault core and include cementation, silification, dissolution-precipitation reactions (e.g., pressure-solution seams and the presence of soluble minerals such as feldspar, quartz and calcite) and the fluid-assisted chemical alteration of the wall rocks into fault rock. The interplay of both processes is well-documented along the San Andreas fault where fault gouge has formed as a result of fluid-assisted, shear enhanced, chemical reactions between wall rocks of contrasting chemistry (Bradbury *et al.* 2011; Moore & Rymer 2012). The generation of shears within the gouge enable fluids to infiltrate the low permeability fault-gouge and drive subsequent dissolution and precipitation reactions in a metasomatic exchange process resulting in permeability enhancement (Lockner *et al.* 2011; Moore & Rymer 2012; Moore & Lockner 2013; Warr *et al.* 2014).

Outcrop and drilling studies have substantially contributed to our understanding of large faults both at the surface and at depth, respectively. Fault rocks exhumed at Earth's surface develop through progressive deformation at a range of crustal conditions. The exhumed fault core is thus complicated by overprinting and the result of multiple integrated events on a fault over time. Therefore, only considering the present-day structure of a fault, and not how it evolved through time over the full range of depths that the fault was active in the past, is a finite view of that fault.

The fault core is the result of multiple, perhaps even tens of thousands, of events on a single fault integrated over time (e.g., reactivations, repeated ruptures, varying wall rock juxtapositions, etc.). Mechanical and chemical processes can vary through time, occurring at the same time in different parts of the fault system, or at different times

in the same part of the fault (e.g., Solum *et al.* 2010). Consequently, the fault core may contain multiple fault rocks each with different chemical and mechanical properties (e.g., the Highland Boundary fault in Scotland; McKay *et al.* 2020), thus impacting the bulk mechanical strength of the fault through time. Chemical fluid-rock interactions and resulting mineralogical and textural alterations (e.g., the formation of clay gouge) are associated with fault-rock weakening (Collettini *et al.* 2009b; Solum *et al.* 2010; Bradbury *et al.* 2011; Ikari *et al.* 2011; Lockner *et al.* 2011; Barth *et al.* 2013). However, precipitation, mineralisation and repeated cementation or brecciation contribute to fault strengthening (Caine *et al.* 2010; Lawther *et al.* 2016; Callahan *et al.* 2019). These processes all lead to what we see, and are able to study, in the fault core today and it is therefore important to consider the processes that caused the observed field observations (i.e., origin of clays in the fault rocks and their distributions).

This paper documents the structure of the Highland Boundary Fault in outcrop and to microstructural scale and presents an evidenced based six-stage model for the evolution of fault rock through time.

## 5.2. Geological Setting: The Highland Boundary Fault

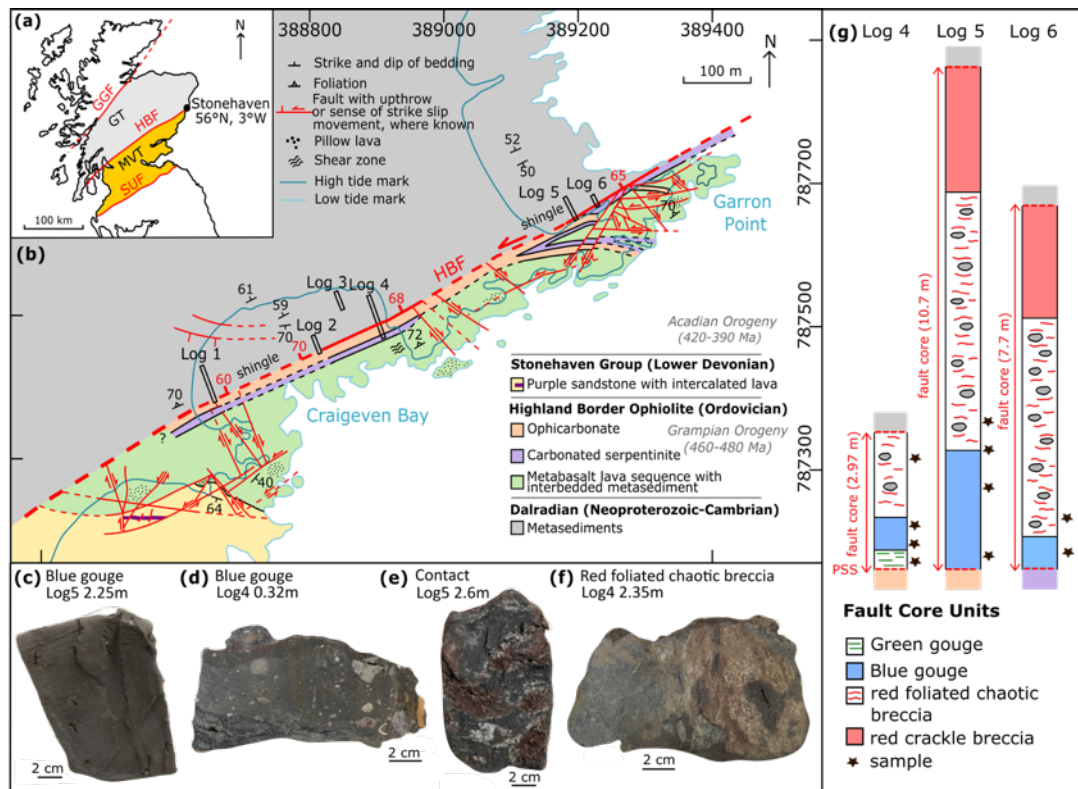
The Highland Boundary fault (HBF) is a mature, ancient plate boundary fault with a long and complex history (e.g., Bluck, 1985; Dewey and Strachan, 2003; Tanner, 2008; Cawood *et al.*, 2012). The fault is considered to have been active during two events of the Caledonian Orogeny: the early Ordovician Grampian Orogeny (480-460 Ma) and the mid-Devonian Acadian Orogeny (420-390 Ma) (Chew & Strachan 2014). Early fault motion was believed to be reverse, inheriting the subduction interface and emplacing the Highland Border Ophiolite immediately prior to the Grampian Orogeny (Chew *et al.* 2010). During the later Acadian Orogeny (ca. 420 Ma), the HBF was reactivated in sinistral strike-slip motion (Chew *et al.* 2010; Chew & Strachan 2014). The magnitude of strike-slip displacement is debated (Dewey & Strachan 2003; Cawood *et al.* 2012). Like other terrane-bounding, crustal-scale Caledonian faults in Scotland it would not be surprising if the HBF accommodated minor motion at

younger ages associated with late Acadian orogenic collapse (Chew & Stillman 2009), North Sea extension (Fossen *et al.* 2016) or North Atlantic opening (e.g., Le Breton *et al.* 2013).

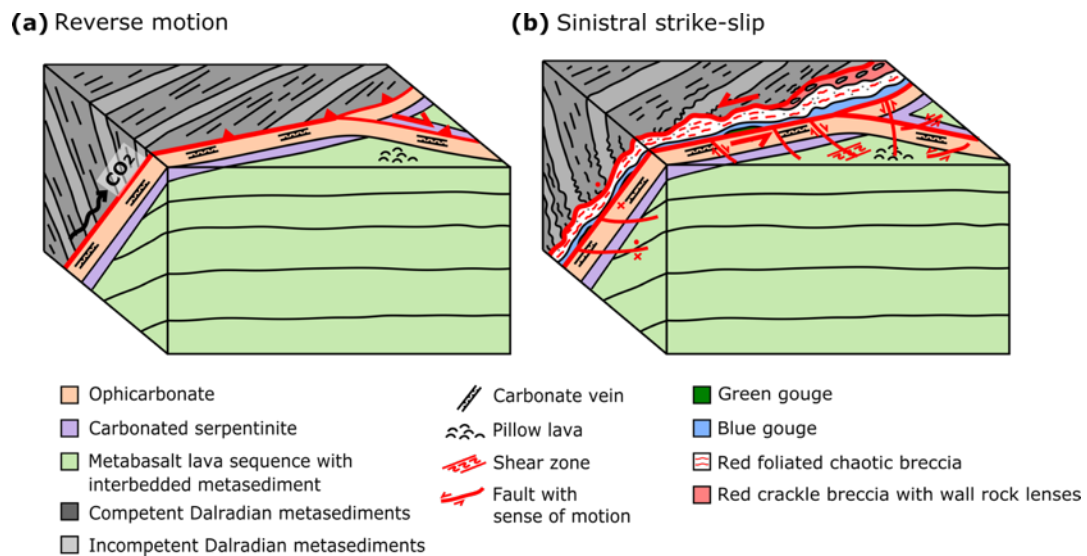
Today, the remarkably straight fault trace extends for over 240 km NE to SW across Scotland and separates the Scottish Highlands from the Midland Valley of Scotland (**Fig. 5.1a**). The fault is best exposed along a coastal section ~1 km north of Stonehaven. Here, the principal slip surface (PSS) is marked by a relatively straight (strike:  $059 \pm 8^\circ$ ;  $n = 70$ ), steep (dip:  $66 \pm 7^\circ$ ;  $n = 70$ ), NW-dipping contact that separates carbonate-rich serpentinites from quartzo-feldspathatic crustal rocks of distinct terranes; the Highland Border Ophiolite and Dalradian respectively (**Fig. 5.1**) (McKay *et al.* 2020).

This study is based on data collected from the exposure near Stonehaven. The Highland Border Ophiolite south of the PSS consists of three distinct units exposed near Stonehaven (**Fig. 5.1b**): (1) an intensely faulted, fractured and veined, buff-coloured dolomitised serpentinite properly termed ophicarbonite (formed from the alteration of serpentinite via a CO<sub>2</sub> rich fluid in a process known as natural carbonation; Tominga *et al.* 2017); (2) a carbonated serpentinite displaying a chaotic network of cross-cutting calcite veins; and, (3) a fractured metabasalt lava sequence with sporadic pillow lavas and interbedded ferruginous chert and siliceous siltstone/shale (McKay *et al.* 2020, **Fig. 5.1b**). Veins in the ophicarbonite are parallel to the PSS, filled by multiphase carbonate (massive dolomite in the centre with isopachous sparry calcite lining the vein wall) and are indicative of crack-seal growth and reverse motion of the HBF (McKay *et al.* 2020). Numerous small offset (c. 5-10 m) sinistral and dextral strike-slip faults, arranged in Riedel shear geometries relative to the PSS, are found within the Highland Border Ophiolite indicative of sinistral strike-slip motion on the HBF (**Fig. 5.1b**; McKay *et al.* 2020). These small faults offset the veins in the ophicarbonite suggesting reverse faulting pre-dates strike-slip faulting (**Fig. 5.2**), conforming to the paleogeographic observations of Chew & Strachan (2014).





**Fig. 5.1.** The Highland Boundary Fault. (a) Simplified geological map of Scotland showing the location of the study site from McKay et al. (2020). (b) Geological map of the Highland Boundary fault from McKay et al. (2020). PSS defined by thick, red NE-SE trending line. The location of the structural logs are indicated by the black rectangles. (c) Hand specimen of the blue gouge from Log 5, 2.25 m from the PSS. (d) Hand specimen of the blue gouge from Log 4, 0.32 m from the PSS. (e) Hand specimen of the contact between the blue gouge and red foliated chaotic breccia from Log 5, 2.6 m from the PSS. (f) Hand specimen of the red foliated chaotic breccia from Log 4, 2.35 m from the PSS. The hand specimen samples are all aligned in the same relative orientation. (g) Structural logs showing the internal structure and fault core units of the Highland Boundary fault. Sample locations are indicated by the black stars. Samples are named by the log they were collected from and the distance along the log from the PSS to the Dalradian. For example, the green gouge sample is named Log4-0.1m. The key for the wall rock lithologies are given in panel (b).



**Fig. 5.2.** Simplified, schematic 3D block diagram of the HBF at Stonehaven. **(a)** Early reverse motion involving the formation of ophicarbonates and fault-parallel carbonate veins. **(b)** Sinistral strike-slip motion associated with the formation of the clay-rich fault core. Fault structure observations are presented in McKay *et al.* (2020).

Chlorite- to biotite-grade metasedimentary rocks of the Dalradian Supergroup are found north of the fault core (**Fig. 5.1b**). At Stonehaven, the Dalradian consists of a succession of interbedded competent (e.g., metagreywacke which locally contain quartz granules) and less competent (e.g., micaceous pelite) beds of differing mechanical strengths (McKay *et al.* 2020). The beds are folded into a series of open, plunging folds with the axial plane sub-parallel to the HBF, and display evidence of fault-related deformation such as alteration, subsidiary fractures and brecciation (McKay *et al.* 2020).

Detailed field mapping by McKay *et al.* (2020) reveals the Stonehaven section of the HBF is composed of a structurally and compositionally variable fault core that formed during sinistral strike-slip (**Fig. 5.2**). The fault core consists of four distinct units that remain unmixed: (1) a localised green gouge; (2) a blue gouge of high plasticity (**Fig. 5.1c-d**); (3) a red foliated chaotic breccia where the foliations wrap around cm-scale clasts of wall rock (**Fig. 5.1f**); and, (4) a red crackle breccia with large, elongated wall-

rock lenses (McKay *et al.* 2020). Localised pods of the red foliated chaotic breccia are found within the blue clay at the contact (**Fig. 5.1e**), but overall the units remain unmixed.

Across-fault transects perpendicular to the fault plane (known as structural logs; locations given in (**Fig. 5.1b**) reveal that the total thickness of the fault core varies between 2.95 and 10.7 m over this 560 m along-strike section (McKay *et al.* 2020). Not every unit is continuous along-strike and each unit varies in thickness. For example, the green gouge is only observed at one location (Log 4) so could either represent a zone of localised alteration, or a remnant fragment of a reworked, previously extensive, fault core lithology. While the fault core varies in thickness, the overall structure of the fault does not change, i.e. localisation occurs within a single fault core strand at all locations along the fault (**Fig. 5.1g**).

## 5.3. Methods

### 5.3.1. Microstructural Analysis

Samples were recovered from three structural logs – Log 4, Log 5 and Log 6. These logs were chosen for sampling because: (i) Log 4 has the thinnest fault core (2.95 m) with two distinct fault core units (the blue gouge and red foliated chaotic breccia), (ii) Log 5 has the widest fault core (10.7 m) consisting of three distinct units (the blue gouge, red foliated chaotic breccia and red crackle breccia), and (iii) Log 6 has different wall rock juxtapositions compared to Log 4 and 5 (carbonated serpentinite juxtaposes the fault and not ophicarbonates) (**Fig. 5.1g**). In total, ten thin sections were prepared from samples of three different fault core units – green gouge (1 sample), blue gouge (6 samples) and the red foliated chaotic breccia (3 samples). Samples are named by the log they were collected from and the distance along the log from the PSS to the Dalradian. The location of the samples are indicated by star symbols in **Fig. 5.1g**. The red crackle breccia could not be sampled due to its crumbly texture. With permission to sample at this Site of Special Scientific Interest, we limited samples to those exposed by digging through beach shingle. The nature of the clay and difficulties

of sampling at this site meant it was not always possible to get a fully orientated sample; in places we had to dig through a deep shingle layer to expose the clay, sections of the clay were lifted out with a shovel-tip, avoiding very large boulders. Thus, some samples are fully orientated with respect to the PSS of the HBF, while some are orientated relative to other features. All thin sections were taken from fully orientated samples.

Thin sections were analysed using a Nikon Eclipse LV 100ND petrographic microscope at the University of Strathclyde, with images captured using a Nikon DS-Ri2 5 Megapixel digital camera. Scanned thin section images were imported into ArcGIS and scaled for further analysis. Features such as clasts, strain shadows, fabrics and veins were identified and digitised into different layers within ArcGIS. For polygon features (clasts, veins and strain shadows), the ArcGIS minimum bounding geometry tool was used to add a layer containing the best fit ‘rectangle by width’. This returned the area, perimeter, length and width of the rectangle (used as a proxy for the long axis and short axis of the feature, the a and b axis respectively) and the orientation of the long axis. This information was then extracted into Excel to calculate the aspect ratio (ratio of long axis to short axis), orientation of the long axis relative to the mean PSS of the HBF as determined from field mapping in McKay et al. (2020) and relative circularity of the clasts. As outlined in Mort & Woodcock (2008), circularity was calculated using the formula (equation 5.1):

$$circularity = 4\pi \left( \frac{area}{perimeter^2} \right) \quad \text{eq. (5.1)}$$

Where a value of 1 represents a perfectly circular shape. The clast size, orientation, aspect ratio and circularity were then compared between the thin sections of different fault core units (green gouge, blue gouge and red foliated chaotic breccia) and from different locations along the fault (Log 4, 5 and 6). The median is reported for each property along with the Coefficient of Quartile Variation (CQV), which is a measure of relative dispersion that is based on interquartile range. Since CQV is unitless, it is useful for comparison of variables with different units (i.e., area in cm<sup>2</sup>, length of the long axis in cm, aspect ratio and circularity which are both unitless). For linear features (e.g., clay fabrics), the orientation was assessed using the ‘sets’ function of the ArcGIS

toolbox Network GT (Nyberg *et al.* 2018) and calculated relative to the mean orientation of the PSS of the HBF as determined in McKay *et al.* (2020). The orientation of clasts and linear features was only assessed for fully orientated samples.

### 5.3.2. XRD Analysis

Following on from the mineralogy presented in McKay *et al.* (2020) we selected two samples from both the blue gouge and red foliated chaotic breccia for detailed XRD analysis. Based on similar studies aiming to constrain the timing and origin of clay gouge at other plate boundary faults (e.g., Boles *et al.*, 2015; Ring *et al.*, 2017), the samples were first separated by centrifuge into different size fractions: 1-0.5  $\mu\text{m}$  (coarse) and  $<0.2 \mu\text{m}$  (fine). The purpose of this was to attempt to remove any coarse-grained impurities (e.g., quartz, calcite etc.) from the fine-grained clay minerals. Recovered fractions were then oven dried at 105°C prior to analysis.

XRD of both oriented samples (used for mineral identification) and randomly oriented samples (used for polytype quantification) was conducted at the James Hutton Institute. For mineral identification, small portions of the size fractions were dispersed in small volumes of water, then prepared as oriented mounts using the filter peel transfer technique and scanned using Cobalt  $K\alpha$  radiation from 3-45° 2 $\theta$  in the air-dried state, after glycolation, and after heating to 300 °C for one hour. Clay minerals identified were quantified using a mineral intensity factor approach based on calculated XRD patterns (Hillier 2003). Uncertainty is estimated as better than  $\pm 5$  wt.% at the 95% confidence level.

For polytype analysis, the separated size fractions were gently disaggregated and loaded into sample holders taking care to avoid preferred orientation and to obtain as random a preparation as possible. XRD patterns were recorded from 3-80° 2 $\theta$  using Cobalt  $K\alpha$  radiation. Due to the complexity of the mineralogical compositions polytype analysis was made by a normalised full pattern reference intensity ratio (RIR) method using natural standards for all minerals identified in each size fraction,

including 1Md and 2M1 illite polytype patterns. Due to some difficulties with the fitting of standards for some minerals (e.g., the large percentage of chlorite), the results are considered semi-quantitative.

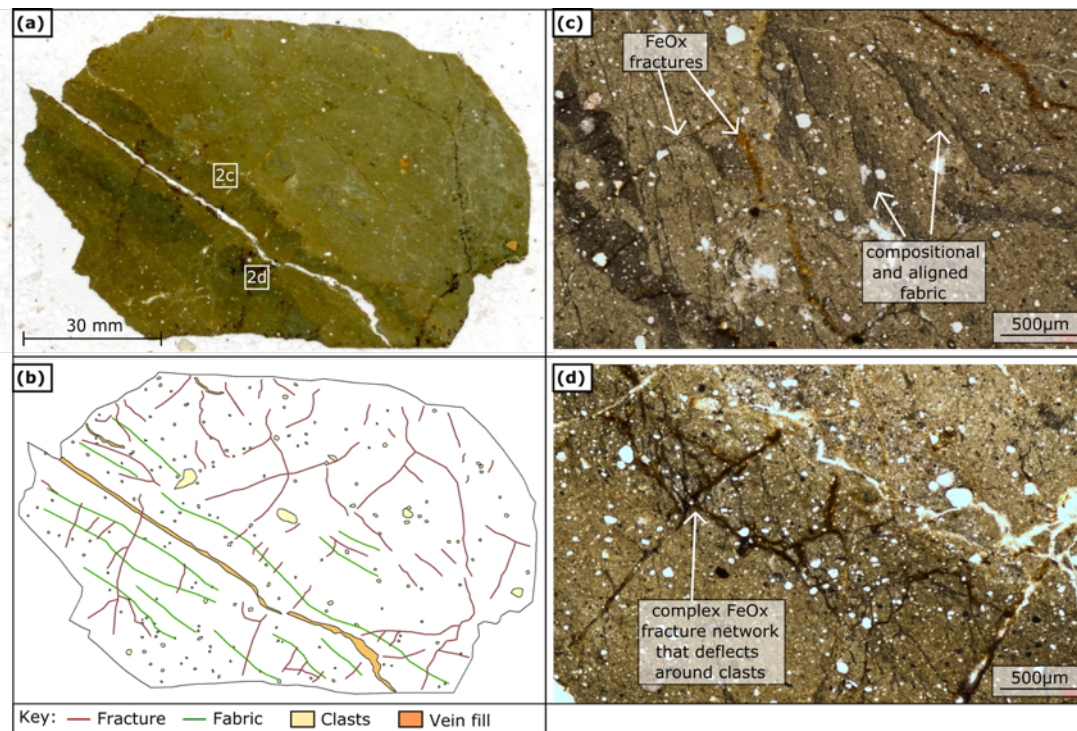
## 5.4. Microstructural Observations of the Highland Boundary

### Fault Core

In this section key microstructural observations are presented for each fault core unit. The representative thin sections and images from each unit.

#### *5.4.1. Green Gouge*

The green gouge consists of small, rounded clasts embedded in a green-brown, fine-grained clayey gouge matrix (**Fig. 5.3a-b**). The clasts (n=178) range in 2D area from 0.10 to 19.71 cm<sup>2</sup> (median = 0.31 cm<sup>2</sup>, CQV = 0.34), long axis length from 0.39 to 7.97 cm (median = 0.75 cm, CQV = 0.21), aspect ratio from 1.00 to 2.68 (median = 1.35, CQV = 0.11) and circularity of 0.61 to 0.92 (median = 0.82, CQV = 0.04) (**Table 5.1, Table 5.2**). The matrix has colour (compositional) variations, and some matrix patches and fractures have a preferred orientation (**Fig. 5.3c**). A complex, multi-generational, cross-cutting FeOx fracture network is evident (**Fig. 5.3d**), which appears to deflect around clasts. The cross-cutting relationships and relative timing of the fracture network has not been analysed in detail as part of this study.



**Fig. 5.3.** Thin section of green gouge (Log4-0.1m). Sample is not orientated so cannot determine orientation of fabric or veins with respect to the HBF. (a) Scanned thin section photo. (b) Digitised thin section. (c) Photomicrograph showing compositional, aligned fabric (clay minerals) and fracture networks. The white splodges are pore space/voids. (d) Photomicrograph showing complex multi-generational FeOx fracture network. Both photomicrographs are in plane polarised light. The white splodges are pore space/voids

#### 5.4.2. Blue Gouge

The blue gouge consists of sub-rounded to rounded, spherical to elongate polymineralic clasts embedded in a dark-brown, fine-grained clayey gouge matrix. The majority of clasts (~80%) are composed of quartz and sericitised feldspar and quartz. The other 20% consists of mafics, opaques, FeOx and quartz with bulging metamorphic textures. Combining the data from all six samples of the blue gouge, the clasts ( $n=4895$ ) range in 2D area from 0.06 to 12820.65 cm<sup>2</sup> (median = 1.28 cm<sup>2</sup>, CQV = 0.56), long axis length from 0.31 to 125.95 cm (median = 1.61 cm, CQV = 0.32), aspect ratio from 1.00 to 8.03 (median = 1.43, CQV = 0.15) and circularity of 0.20 to 0.94 (median = 0.80, CQV = 0.05) (*Table 5.1, Table 5.2*).

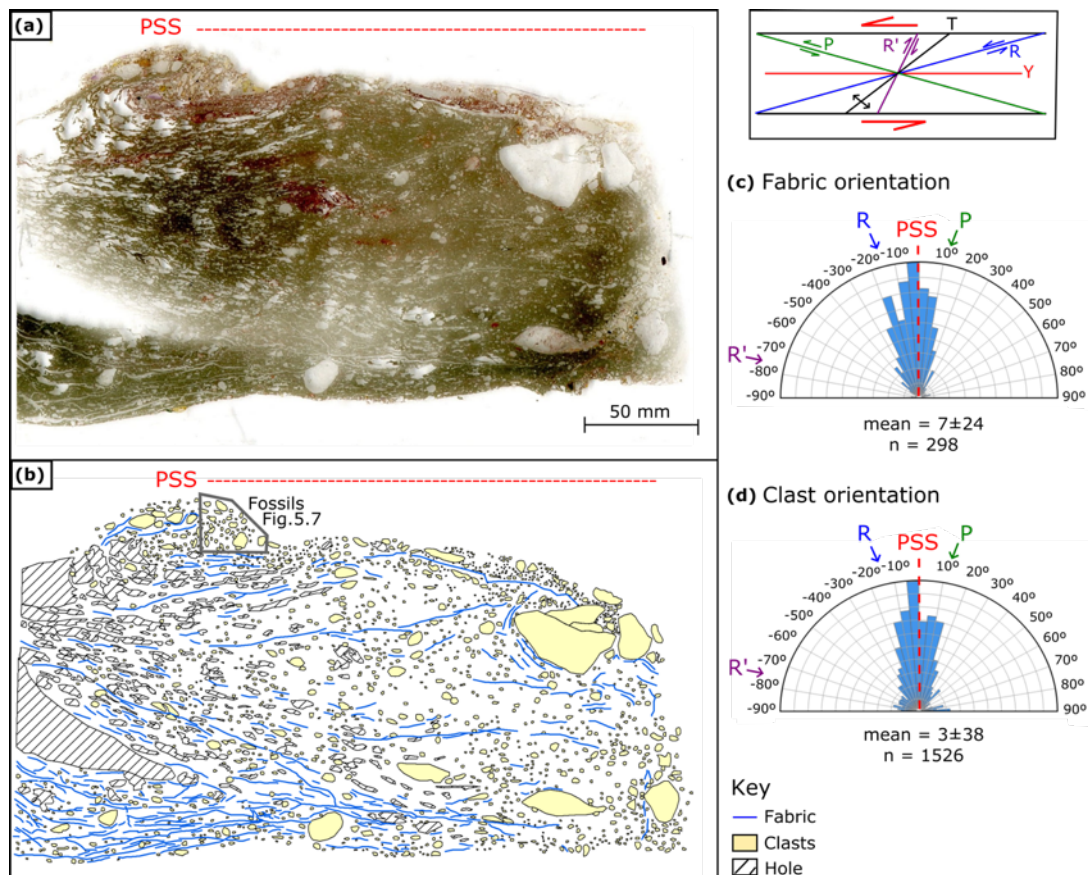
Some clasts and matrix patches have a preferred orientation exhibiting a fabric (, **Fig. 5.5**, **Fig. 5.6a**), although the foliation can deflect and wrap around the clasts (**Fig. 5.6b**). For instance, in sample Log4-0.32m (**Fig. 5.1d**), the clasts and fabric are aligned parallel,  $\sim 15^\circ$  anticlockwise or  $\sim 10^\circ$  clockwise from the PSS of the HBF (**a-b**) in Y-, R- or P-shear geometries respectively (**c-d**). In sample Log5-2.25m (**Fig. 5.1c**), the fabric is aligned at high angles ( $60\text{--}75^\circ$  anticlockwise) from the PSS in R'-shear geometries (**Fig. 5.5c**). Strain shadows are visible at different scales (**Fig. 5.5a-b**). Strain shadow geometries are  $\sigma$ -type shadows (**Fig. 5.6g**), providing evidence of strain and are aligned in the same direction as the fabric. Parallel, opening-mode veins are also present, aligned at  $\sim 55^\circ$  anticlockwise from the PSS (**Fig. 5.5a-b** which may represent extensional T-shears. The veins are mineralised with altered, sericitised clay present at the margins.

Typically, the clasts within the blue clay are sub-rounded to rounded (median circularity = 0.80,  $n = 4895$ ; **Table 5.2**) so a preferred orientation of the long axis is not always visible (**Fig. 5.5d**). A few clasts resemble clay-clast aggregates (CCA's; sensu Boutareaud *et al.*, 2008) (**Fig. 5.6c-d**). 'Snowballed' clay rims are observed around rotated, rounded clasts and the fabric swirls around the clast (**Fig. 5.6c**). While some clasts have rounded edges suggestive of mechanical wear, others have tapered, elongate geometries with pressure solution seams along the edges (**Fig. 5.6e**), suggesting a combination of shearing and chemical alteration (Sills *et al.* 2009). Some clasts display an internal fabric (**Fig. 5.6e**) and/or wings (**Fig. 5.6g**) suggestive of local shearing. Some clasts also have undulated margins (**Fig. 5.6f**) suggestive of melt corrosion/frictional melt. Late-stage veining along a pre-existing fabric is evident in **Fig. 5.6h**. There appears to be a late-stage brittle overprint on top of the ductile shearing features (**Fig. 5.6**).

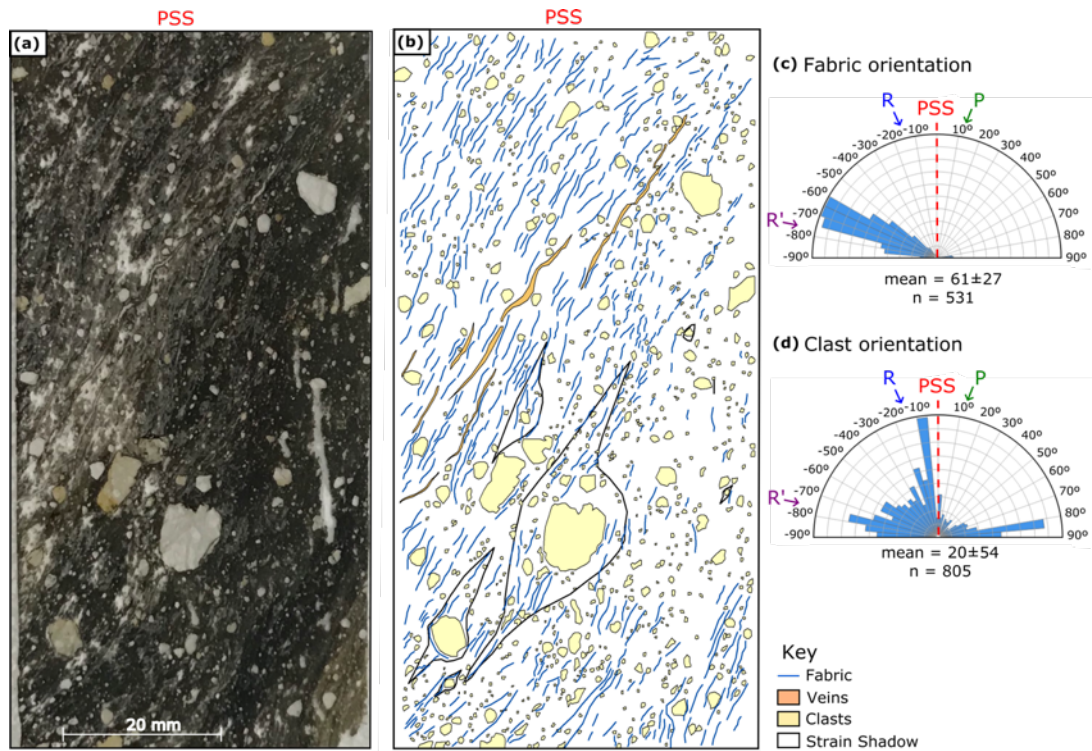
Surprisingly, marine microfossils are found in sections of this unit (**Fig. 5.7**). These include relatively intact fragments of ancient bryozoans, possibly belonging to the extinct order Fenestrata, brachiopods and an echinoid spine (McKay *et al.* 2020). These fossils are not ubiquitous throughout the blue gouge. Instead, they are only



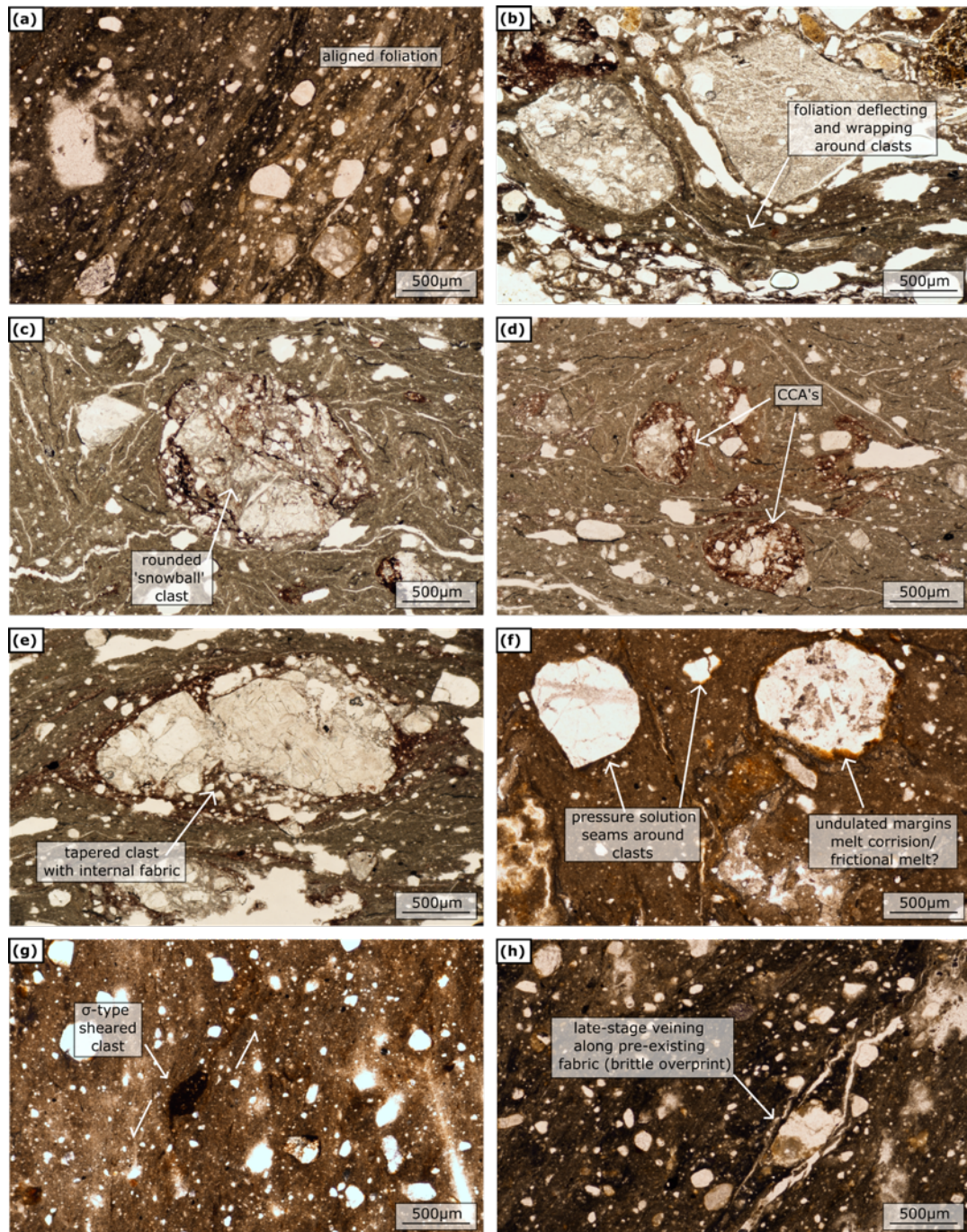
observed in one sample (sample Log4-0.32m) and are localised within the sample (see ). Both primary fabrics and secondary recrystallisation/growth textures are observed. However, despite the fossils being preserved within a high-strain fault gouge, there is no evidence of internal strain (e.g., microfracturing or shear indicators) within the fossil fragments. This suggests strain is not uniform throughout the blue gouge.



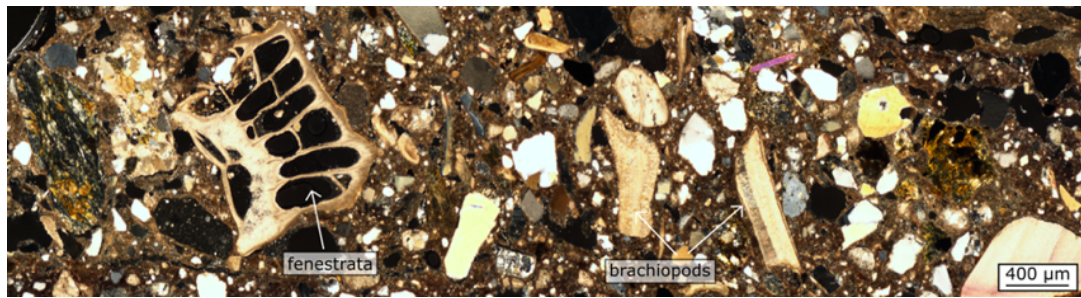
**Fig. 5.4.** Thin section of blue gouge (Log4-0.32m). **(a)** Scanned thin section photo. **(b)** Digitised thin section. **(c)** Rose diagram of the orientation of the fabric with respect to the PSS of the HBF at  $0^\circ$ . The  $\pm$  refers to standard deviation. **(d)** Rose diagram of the orientation of the long axis of the clasts with respect to the PSS of the HBF at  $0^\circ$ . (inset) Geometric features of an idealised Reidel shear zone in a sinistral strike-slip regime. All rose diagrams were created using GeoRose software.



**Fig. 5.5.** Thin section of blue gouge (Log5-2.25m). **(a)** Scanned thin section photo. **(b)** Digitised thin section. **(c)** Rose diagram of the orientation of the fabric with respect to the PSS of the HBF at  $0^\circ$ . The  $\pm$  refers to standard deviation. **(d)** Rose diagram of the orientation of the long axis of the clasts with respect to the PSS of the HBF at  $0^\circ$ . All rose diagrams were created using GeoRose software.



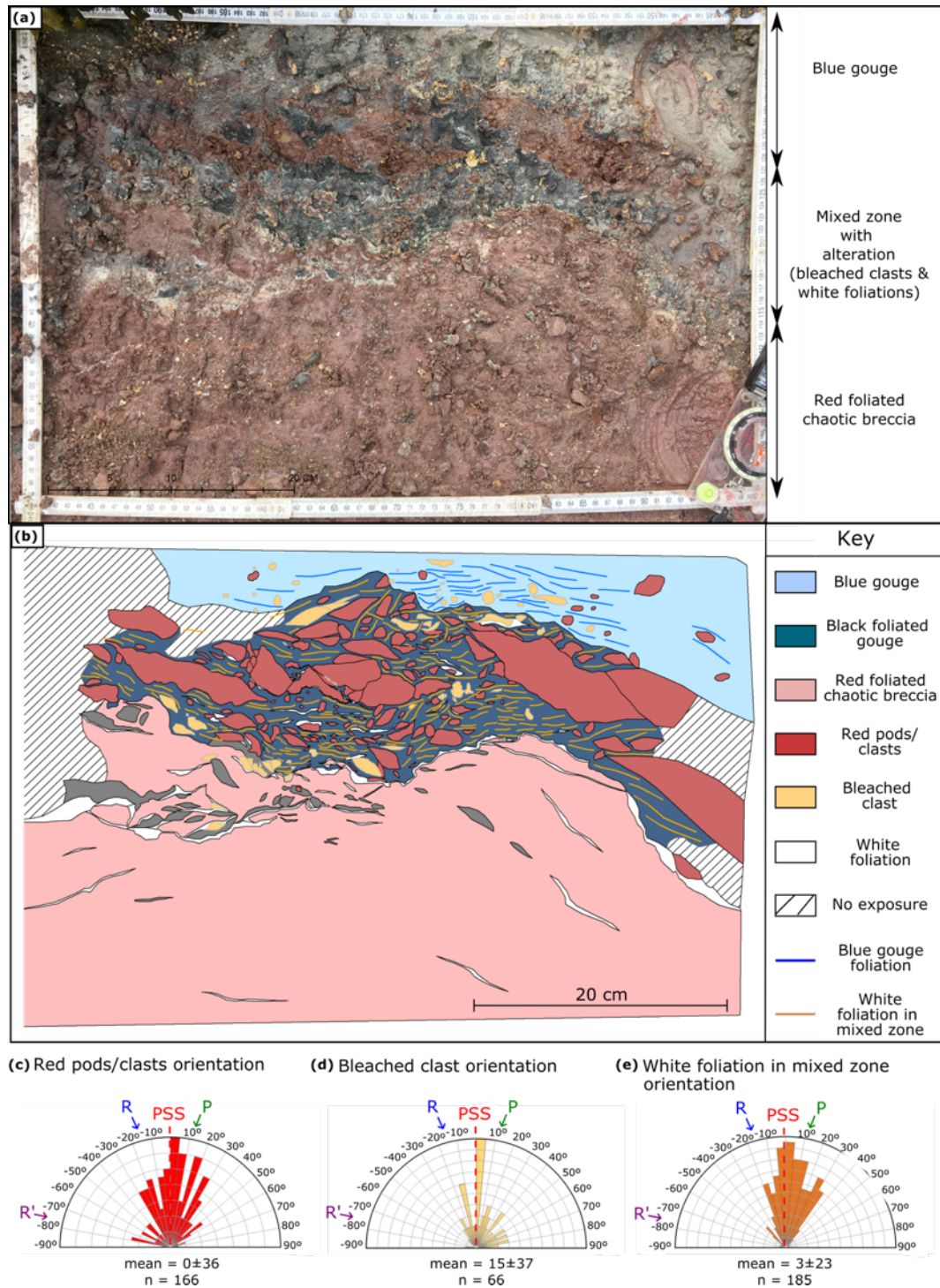
**Fig. 5.6.** Photomicrographs of the blue gouge all aligned in the same relative orientation to the HBF. (a) Aligned steeply dipping ( $60\text{--}75^\circ$  from the PSS of the HBF) fabric in sample Log5-2.25m. (b) Fabric deflecting and wrapping around clasts in sample Log4-0.32m. (c) Rounded 'snowball' clast in sample Log4-0.32m. (d) Clay clast aggregates (CCA's) in sample Log4-0.32m. (e) Tapered clast with dissolution-precipitation seams around the edges in sample Log4-0.32m. (f) Clasts with pressure solutions seams and undulated margins indicative of melt corrosion/frictional melt in sample Log5-0.3m. (g)  $\sigma$ -type strain shadow showing evidence of shear strain in sample Log5-0.3m. (h) Late-stage veining along a pre-existing fabric in sample Log5-2.25m. All images in plane polarised light.



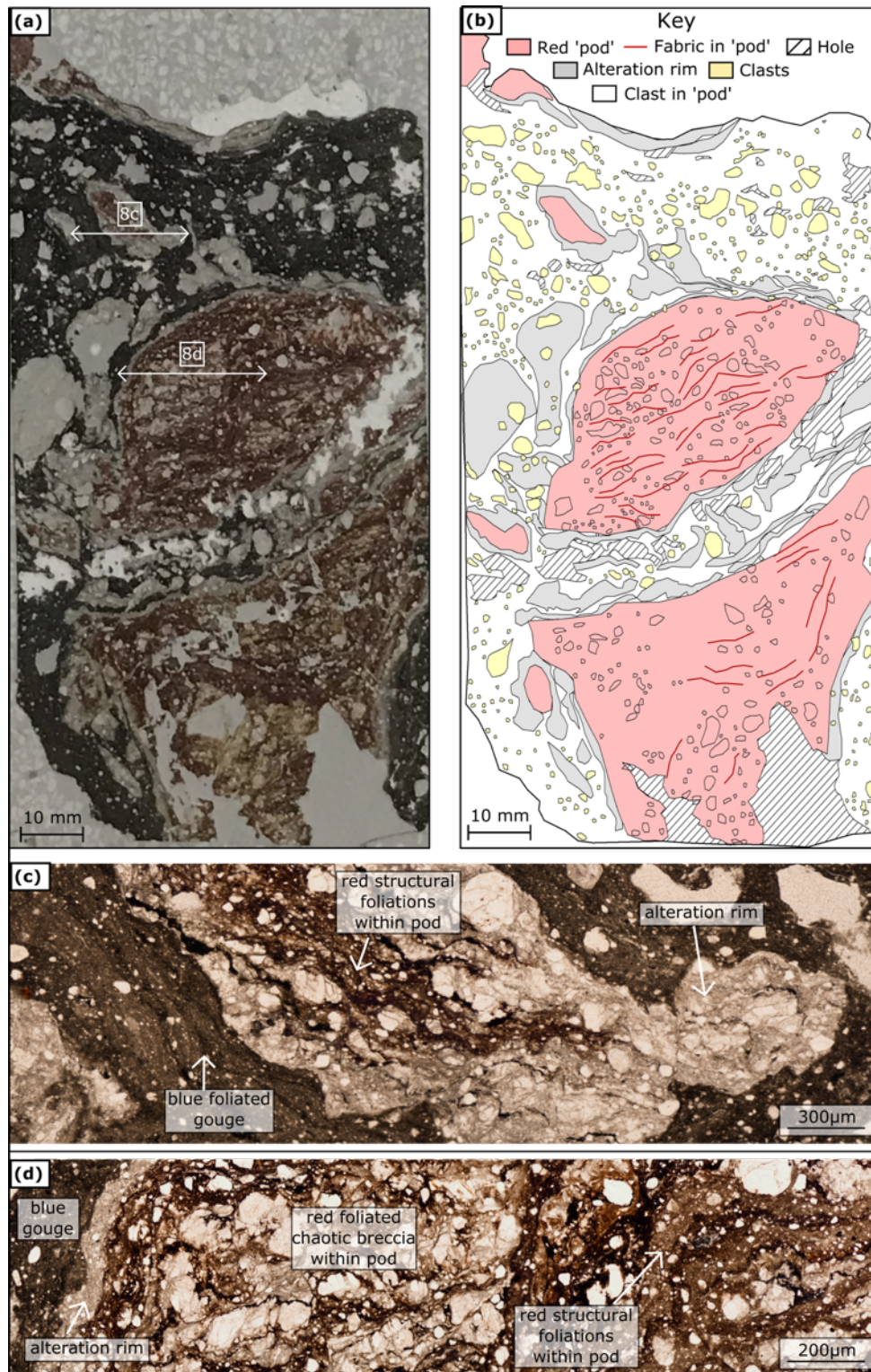
**Fig. 5.7.** Localised section of microfossils within the blue gouge (see for location). This thin section is not orientated with respect to the PSS of the HBF. Image in plane polarised light.

### 5.4.3. Contact between the Blue Gouge and Red Foliated Chaotic Breccia

A ~20 cm wide zone of enhanced alteration defines the contact between the blue gouge and red foliated chaotic breccia (**Fig. 5.8a-b**). Within this zone, ‘pods’ of the red foliated chaotic breccia, herein referred to as red pods, are found within the blue gouge (**Fig. 5.8, Fig. 5.9**). The internal structure of the pods displays a fabric similar to that in the red foliated chaotic breccia (see Section 5.4.4. below): a red compositional foliation that deflects and wraps around sub-rounded to sub-angular clasts (**Fig. 5.9d**). The red pods have an elongate, lens shaped geometry and the long axis ranges from 2-3 cm in the field (**Fig. 5.8**) and 0.69-14.52 mm in thin section (**Fig. 5.9**). White foliations (presumably altered) and alteration rims that contain an internal structure and clasts, wrap around the pods (**Fig. 5.9a-c**). White foliations (presumably altered/bleached) and bleached clasts are found within the alteration zone and up to 2 cm from its margins (**Fig. 5.8**). The red pods, bleached clasts and white foliations are all aligned in Y-, P- or R-shear Reidel geometries (**Fig. 5.8c, d, e**).



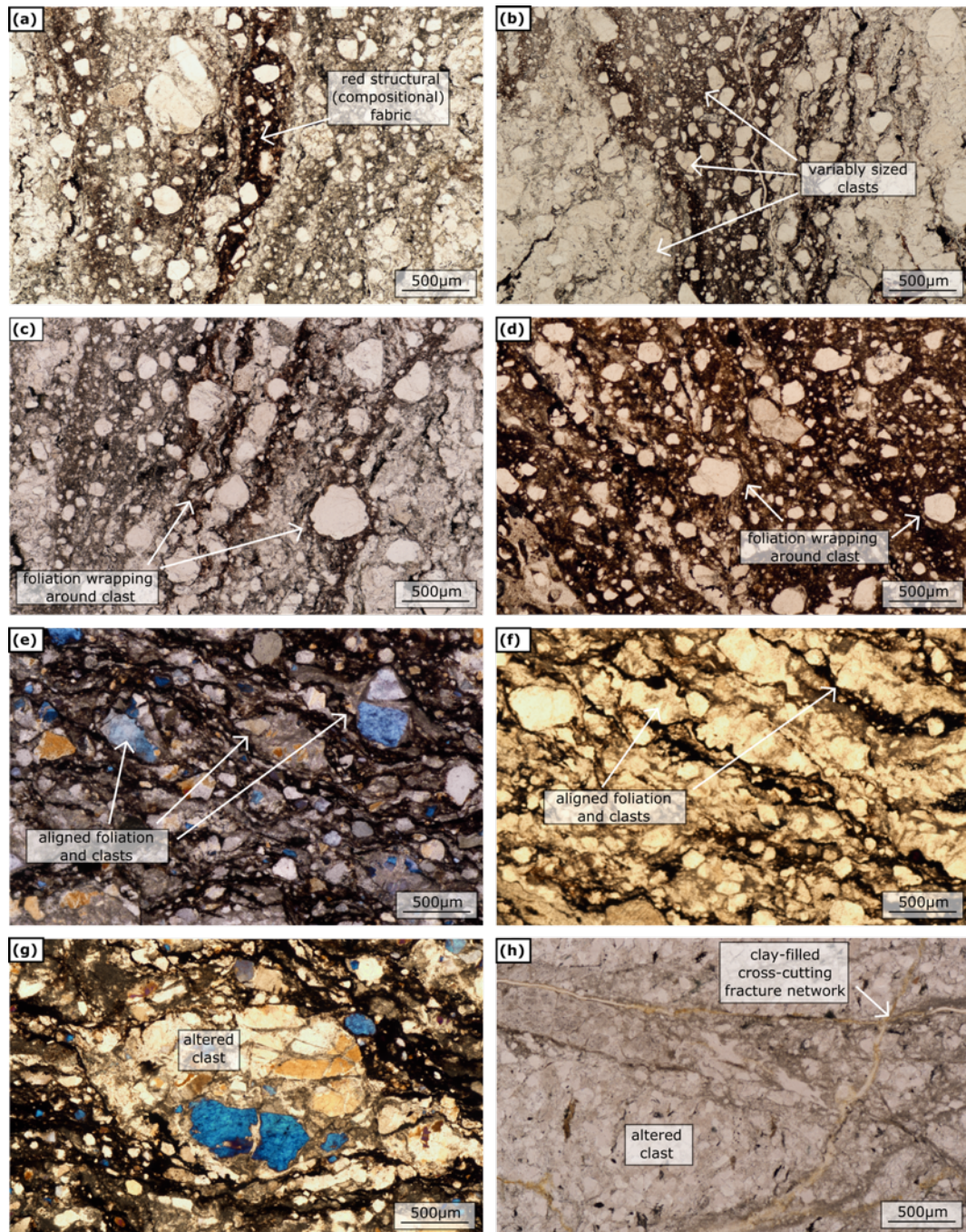
**Fig. 5.8.** Contact between the blue gouge and red foliated chaotic breccia at Log5, 2.6m from the PSS of the HBF. (a) Field photograph orientated sub-parallel to the HBF (orientation of ruler at strike  $062^\circ$ ). (b) Digitised field photograph. (c) Rose diagram of the orientation of the long axis of the red pods/clasts with respect to the PSS of the HBF at  $0^\circ$ . (d) Rose diagram of the orientation of the long axis of the bleached clasts with respect to the PSS of the HBF at  $0^\circ$ . (e) Rose diagram of the orientation of the white foliation in the mixed zone with respect to the PSS of the HBF at  $0^\circ$ . All rose diagrams were created using GeoRose software.



**Fig. 5.9.** Thin section of the contact between the blue gouge and red foliated chaotic breccia (Log5-2.6m). Sample not orientated. (a) Scanned thin section photo. (b) Digitised thin section. (c) Photomicrograph showing red pods within the blue foliated gouge. The pods have white alteration rims and display an internal fabric. (d) Photomicrograph showing the internal structure of the red pods (clasts and foliation). Both photomicrograph images are in PPL.

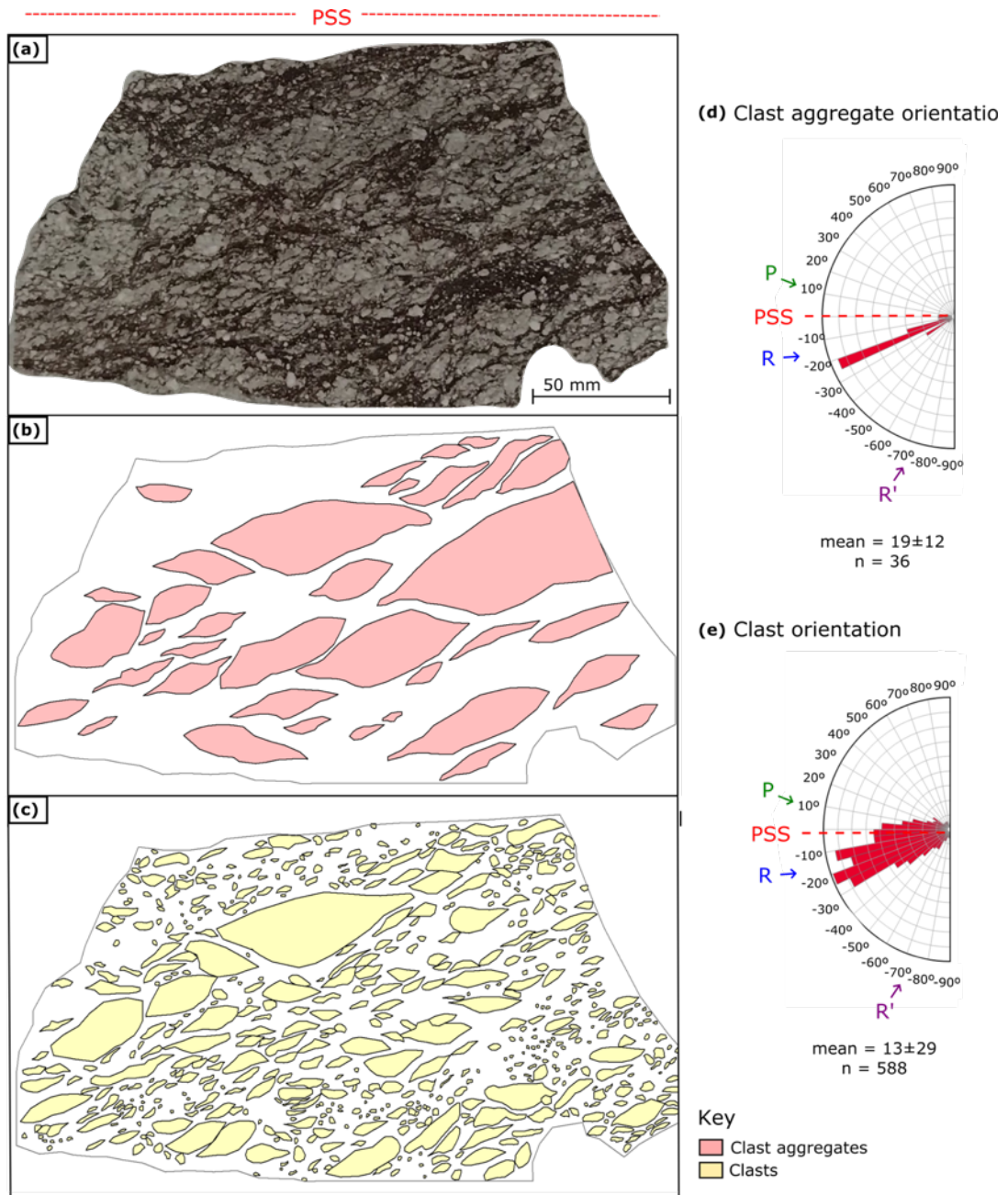
#### 5.4.5. Red Foliated Chaotic Breccia

The red foliated chaotic breccia consists of sub-rounded to sub-angular, circular to elongate polymineralic clasts embedded in a dark brown to red, fine-grained clayey gouge matrix (**Fig. 5.10**). Red, hematitic foliations define a clear structural fabric (**Fig. 5.10a**). The compositional (colour) foliations are generally aligned parallel or sub-parallel to the PSS of the HBF but anastomose and wrap around variably altered, poorly sorted (in size not composition), centimetre-scale, metasedimentary clasts of the Dalradian (**Fig. 5.10b-d**). Combining data from all three samples of the red foliated chaotic breccia, the clasts (n=1594) range in 2D area from 0.16 to 5855.12 cm<sup>2</sup> (median = 3.17 cm<sup>2</sup>, CQV = 0.7), long axis length from 0.57 to 99.76 cm (median = 2.85 cm, CQV = 0.5), aspect ratio from 1.02 to 10.28 (median = 1.72, CQV = 0.3) and circularity of 0.16 to 0.94 (median = 0.75, CQV = 0.16) (**Table 5.1, Table 5.2**). The clasts have a preferred alignment displaying a weak fabric (**Fig. 5.10e-f**). For instance, in sample Log6-1m, the long axis of the clasts and aggregates of clasts are aligned parallel or sub-parallel (10-20°) to the PSS of the HBF (**Fig. 5.11a-e**). The clasts do not display tails or strain shadows. Pressure solution seams around the clasts and evidence of dissolution-precipitation is common (e.g., **Fig. 5.10e**). The clasts display an internal fabric, are highly altered and show evidence of a cross-cutting network of fractures that may be filled with clay (**Fig. 5.10g-h**).



**Fig. 5.10.** Photomicrographs of the red foliated chaotic breccia all aligned in the same relative orientation to the HBF. **(a)** Evidence of red structural (compositional) fabric in sample Log4-2.35m. **(b)** Evidence of variable sized clasts in sample Log4-2.35m. **(c)** Fabric deflecting and wrapping around clasts in sample Log4-2.35m. **(d)** Fabric deflecting and wrapping around clasts in sample Log5-2.9m. **(e)** Aligned foliation and clasts in sample Log6-1m. **(f)** Aligned foliation and clasts in sample Log6-1m. **(g)** Altered clast in sample Log6-1m. **(h)** Altered clast displaying an internal fabric and evidence of late-stage clay-filled fracture network in sample Log4-2.35m. Images a-d, e and f are in PPL. Images e and g are in cross-polarised light.

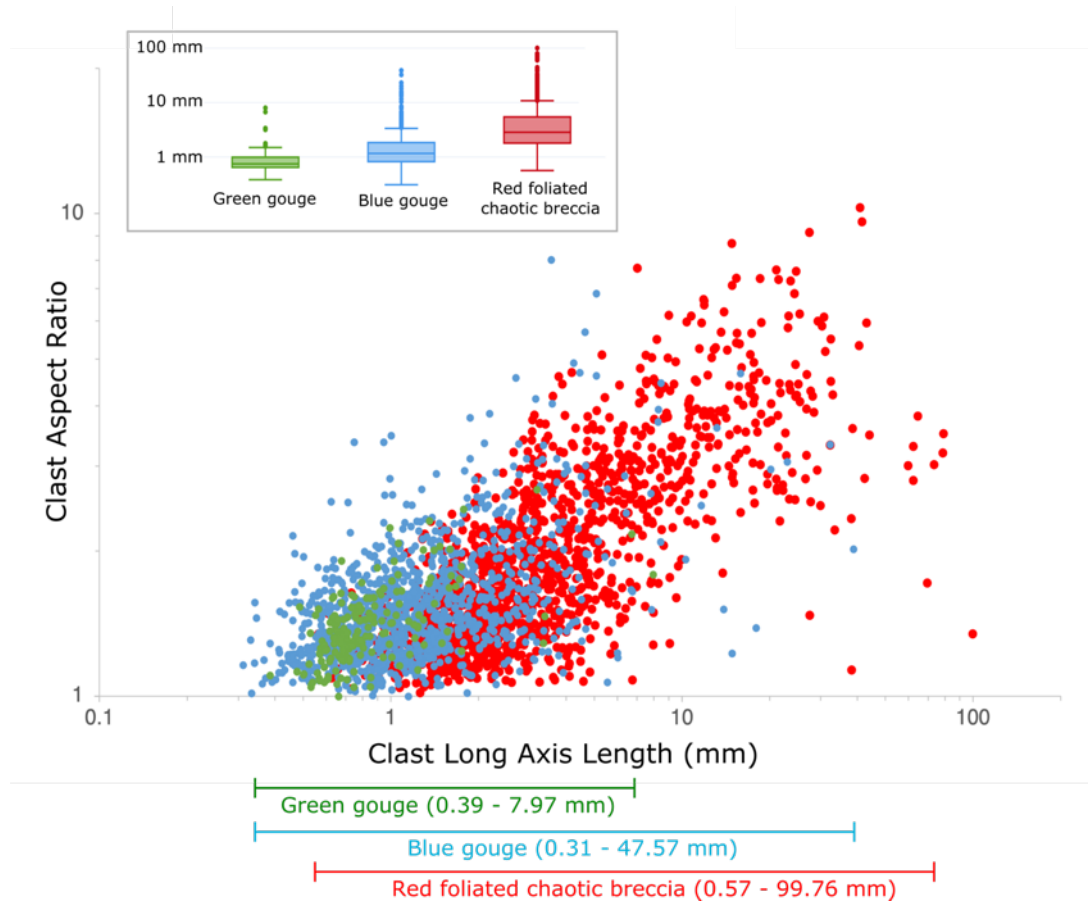




**Fig. 5.11.** Thin section of red foliated chaotic breccia (Log6-1m). **(a)** Scanned thin section photo. **(b)** Digitised thin section showing aggregates of clasts. **(c)** Digitised thin section showing individual clasts. **(d)** Rose diagram showing the orientation of the long axis of the clast aggregates with respect to the PSS of the HBF at  $0^\circ$ . The  $\pm$  refers to standard deviation. **(e)** Rose diagram showing the orientation of the long axis of the clasts with respect to the PSS of the HBF at  $0^\circ$ . All rose diagrams were created using GeoRose software.

#### 5.4.5. Clasts within the Fault Core

Our data suggest the clasts become smaller and more equidimensional towards the PSS. Clasts are present in every unit with sizes from sub-millimetre to tens of centimetres and have a wide range of aspect ratios (**Fig. 5.12**). Clasts range from equidimensional (aspect ratio = 1) to lenticular in shape and are typically composed of variably altered, metasedimentary clasts of the Dalradian wall rock. Smaller clasts are more equidimensional, whereas larger clasts have a wider range of aspect ratios (**Fig. 5.12**). For instance, in the green gouge, which is closest to the PSS in Log 4, the clasts are small (ranging from 0.39 to 7.97 mm) and have aspect ratios that range from 1.00 to 2.68. In the blue gouge, which is closest to the PSS in all other logs (**Fig. 5.1g**), the clasts are larger (ranging from 0.31 to 47.53 mm) and have aspect ratios that range from 1.00 to 8.03. In the red foliated chaotic breccia, which is furthest away from the PSS, the clasts are larger still (ranging from 0.57 to 99.76 mm) and have a larger range of aspect ratios from 1.02 to 10.28 (**Table 5.2**). This suggests clasts are plucked from the Dalradian wall rock and the corners are preferentially attacked for comminution until a lozenge eventually diminishes to a more equant grain in a self-similar pattern through rolling, fracturing and/or abrasion.



**Fig. 5.12.** Clast aspect ratio plotted against clast long axis length across all fault core units. (inset) Boxplots show the distribution of clast long axis length for each fault core unit. Despite the outliers there is still an increase in clast long axis length from green gouge to blue gouge to red foliated chaotic breccia.

FC Unit	Sample	# clasts	Clast Area (mm <sup>2</sup> )			Length of Long Axis (mm)			Aspect Ratio			Circularity		
			Median	Range	CQV	Median	Range	CQV	Median	Range	CQV	Median	Range	CQV
GG	Log4-0.1m	178	0.31	0.10-19.71	0.34	0.75	0.39-7.97	0.21	1.35	1.00-2.68	0.11	0.82	0.61-0.92	0.04
BG	Log4-0.32m	1085	0.67	0.06-510.84	0.61	1.16	0.31-38.78	0.38	1.47	1.00-8.03	0.16	0.79	0.26-0.93	0.06
BG	Log4-0.8m	716	1.31	0.21-752.46	0.45	1.61	0.66-47.53	0.27	1.40	1.01-3.52	0.12	0.80	0.45-0.94	0.05
BG	Log5-0.3m	447	1.40	0.36-527.24	0.37	1.68	0.75-31.50	0.23	1.40	1.03-2.94	0.13	0.78	0.45-0.93	0.06
BG	Log5-2.25m	805	1.13	0.15-402.23	0.56	1.61	0.59-25.54	0.32	1.48	1.02-4.18	0.16	0.74	0.28-0.93	0.08
BG	Log5-2.6m	677	1.66	0.30-64.89	0.54	1.76	0.69-14.52	0.32	1.41	1.00-4.41	0.16	0.80	0.20-0.94	0.05
BG	Log6-0.5m	723	2.16	0.36-50.643	0.59	2.05	0.71-43.96	0.36	1.41	1.02-4.65	0.14	0.82	0.25-0.94	0.05
RFCB	Log4-2.35m	116	1.88	0.16-5855.12	0.69	1.96	0.57-99.76	0.43	1.41	1.04-6.93	0.14	0.81	0.01-0.95	0.05
RFCB	Log5-2.9m	714	2.54	0.39-1605.97	0.61	2.38	0.74-79.21	0.38	1.55	1.02-10.28	0.29	0.78	0.16-0.93	0.09
RFCB	Log6-1m	588	4.98	0.46-1091.49	0.71	4.14	0.89-73.49	0.54	2.30	1.06-7.71	0.30	0.65	0.18-0.94	0.20

**Table 5.1.** Summary of clast area, length of long axis, aspect ratio and circularity for each sample in this study. Data determined from thin section analysis. GG, Green gouge; BG, Blue gouge; RFCB, Red foliated chaotic breccia; CQV, Coefficient of Quartile Variation determined by the formula  $(Q3-Q1)/(Q3+Q1)$ , where  $Q3$  and  $Q1$  are the third and first quartile respectively. The CQV value is unitless.

FC Unit	# clasts	Clast Area (mm <sup>2</sup> )			Length of Long Axis (mm)			Aspect Ratio			Circularity		
		Median	Range	CQV	Median	Range	CQV	Median	Range	CQV	Median	Range	CQV
GG	178	0.31	0.10-19.71	0.34	0.75	0.39-7.97	0.21	1.35	1.00-2.68	0.11	0.82	0.61-0.92	0.04
BG	4894	1.28	0.06-752.46	0.56	1.61	0.31-47.53	0.32	1.43	1.00-8.03	0.15	0.80	0.20-0.94	0.05
RFCB	1594	3.17	0.16-5855.12	0.70	2.85	0.57-99.76	0.50	1.72	1.02-10.28	0.30	0.75	0.16-0.94	0.16

**Table 5.2.** Summary of clast area, length of long axis, aspect ratio and circularity by fault core unit. Data determined from thin section analysis. GG, Green gouge; BG, Blue gouge; RFCB, Red foliated chaotic breccia; CQV, Coefficient of Quartile Variation determined by the formula  $(Q3-Q1)/(Q3+Q1)$ , where  $Q3$  and  $Q1$  are the third and first quartile respectively. The CQV value is unitless.

## 5.5. Mineralogy

XRD reveals that the mineralogy of the blue gouge and red foliated chaotic breccia are complex. Minerals include illite plus mixed-layer illite/smectite, chlorite, kaolinite, quartz, halite, hematite, rutile, calcite and anatase (**Table 5.2**). Clays identified in the blue gouge include chlorite, kaolinite, illite, mixed-layer illite smectite and quartz (**Table 5.3**). In sample Log5-0.3m chlorite is the most abundant clay. The red foliated chaotic breccia consists of illite plus mixed-layer illite smectite, kaolinite and quartz  $\pm$  hematite and calcite (**Table 5.3**). The majority of clay is illite plus mixed-layer illite-smectite. Unlike the blue gouge no chlorite is present.

Fault gouge generated in brittle fault zones contains crushed rock fragments including metamorphic or magmatic muscovite derived from the wall rock with variable quantities of newly grown authigenic illite, which can be distinguished from each other by the type of crystallographic stacking, called polytypism (Verma & Krishna 1966). In all HBF samples, greater than 50% of the illite is of the 1M<sub>d</sub> polytype regardless of the lithology (**Table 5.4**). The most widely accepted interpretation is that the 1M<sub>d</sub> polytype is diagnostic of authigenic fault-derived illite formed in the fault during movement (Hower *et al.* 1963; Reynolds 1963; Srodon & Eberl 1984; Grathoff *et al.* 2001; Haines & Van Der Pluijm 2010). However, the 2M<sub>1</sub> polytype, widely accepted as being diagnostic of detrital wall rock material, i.e., derived from metamorphic or magmatic muscovite in the wall rocks (Hower *et al.* 1963; Reynolds 1963; Srodon & Eberl 1984; Grathoff *et al.* 2001; Haines & Van Der Pluijm 2010), is also identified except in the finest size fractions of the blue gouge (**Table 5.4**). However, it should be noted that none of the many published fault-dating studies has provided direct evidence that 1M authigenesis is syn-kinematic.

Sample	Fault core unit	% clay*	Relative % of minerals								
			Illite	Chl	Kaol	Qtz	Hal	Hem	Rutile	Calc	Anat
Log4 0.8m 1-0.5µm	BG	78	24	12	42	17		2	1		2
Log4 0.8m <0.2 µm	BG	89	64	17	8	3	7				
Log5 0.3m 1-0.5µm	BG	81	13	48	20	14		1	1		3
Log5 0.3m <0.2 µm	BG	94	26	55	13	2	2				2
Log4 2.65m 1-0.5µm	RFCB	89	64		25	7		4			
Log4 2.65m <0.2 µm	RFCB	92	89		3	2	6				
Log5 2.6m 1-0.5µm	RFCB	75	56		19	11		13			1
Log5 2.6m <0.2 µm	RFCB	71	66		5	2	17			10	

\* Clay proportions are further explained in **Table 5.4**.

**Table 5.3.** XRD results of the semi-quantitative mineralogical composition (wt.%) of the recovered size fractions. Chl, Chlorite; Kaol, Kaolinite; Qtz, Quartz; Hal, Halite; Hem, Hematite; Calc, Calcite; Anat, Anatase. BG, Blue gouge; RFCB, Red foliated chaotic breccia. Four samples are shown with two size fractions for each sample.

Sample	Fault core unit	Relative % of clay minerals			Illite polytypes	
		Chlorite (Tri)	Kaolinite	I+I/S-ML	Relative % of 1M <sub>d</sub>	Relative % of 2M <sub>1</sub>
Log4 0.8m 1-0.5µm	BG	16	32	52	100	0
Log4 0.8m <0.2 µm	BG	13	4	83	66	34
Log5 0.3m 1-0.5µm	BG	54	12	34	100	0
Log5 0.3m <0.2 µm	BG	42	2	56	79	21
Log4 2.65m 1-0.5µm	RFCB	0	12	88	53	47
Log4 2.65m <0.2 µm	RFCB	0	2	98	71	29
Log5 2.6m 1-0.5µm	RFCB	0	10	90	66	34
Log5 2.6m <0.2 µm	RFCB	0	4	96	83	17

**Table 5.4.** XRD results showing the relative percentages of clay minerals in the various clay fractions as determined from oriented specimens. Four samples are shown with two size fractions for each sample. Chlorite(Tri), Trioctahedral Chlorite; I+I/S-ML = Illite plus mixed-layer illite/smectite. Illite polytypes obtained by full pattern fitting of 1M<sub>d</sub> and 2M<sub>1</sub> illite standards. BG, Blue gouge; RFCB, Red foliated chaotic breccia.

## 5.6. Synthesis of Key Results

The key results for each fault core unit are summarised in **Table 5.5**. These observations are used to infer fault core processes and form the framework of our fault core evolution model in Section 5.7.

	<b>Green Gouge</b>	<b>Blue Gouge</b>	<b>Red Foliated Chaotic Breccia</b>
Field Observations	Green gouge, foliated, relatively homogenous with very small reworked clast. Clasts are rounded.	Blue gouge, high plasticity like modelling clay, foliated, small altered and reworked clasts. Clasts are rounded.	Grey and silty with red, hematitic foliations that define a clear structural fabric. Foliations typically sub-parallel to the PSS but wrap around variably altered wall rocks clasts. Clasts are sub-rounded to angular and lens-shaped in places.
Thin Section Description	Small, rounded clasts embedded in a green-brown, fine-grained clayey gouge matrix	Small, sub-rounded to rounded, circular to elongate polymineralic clasts embedded in a dark-brown, fine-grained clayey gouge matrix	Sub-rounded to sub-angular, spherical to elongate polymineralic clasts embedded in a dark brown to red, fine-grained clayey gouge matrix.
Microstructures	Aligned fabric, complex cross-cutting FeOx fracture network	Clasts and fabric aligned in Reidel shear geometries, fabric wraps around clasts, $\sigma$ -type strain shadows, clay clast aggregates, mix of rounded rotated clasts or elongate tapered clasts, pressure solution seams, microfossils, late-stage veining/brittle overprint	Clasts and fabric aligned parallel or sub-parallel to PSS, foliation wraps around clasts, pressure solution seams around rims of clasts, no shear indicators
Clast long axis length (mm)	0.39 - 7.97	0.31 - 47.57	0.57 – 99.76
Aspect ratio of clasts	1.00 – 2.68	1.00 – 8.03	1.02 – 10.28
Mineralogy	(similar to the blue gouge - refer to McKay et al. 2020)	chlorite, kaolinite, illite, mixed-layer illite smectite and quartz	illite plus mixed-layer illite smectite, kaolinite and quartz $\pm$ hematite and calcite)

**Table 5.5.** Synthesis of key results for each fault core unit

## 5.7. Discussion

### 5.7.1. *A Model of Fault Core Evolution*

The detailed field, microstructural, and XRD observations presented above help constrain the history of the HBF, in particular how such a large offset fault can develop multiple fault core units that have distinct boundaries and remain unmixed. To explain our observations, we propose a six-stage fault core evolution consisting of an early stage of reverse motion followed by a five-stage sinistral strike-slip faulting regime (**Fig. 5.13**). This model helps explain the progression deformation of the HBF at a range of crustal conditions that lead to the development the current fault rock. The observed fault core units are the result of the evolving interplay between the chemical and mechanical processing of the wall rocks during these six stages.

#### **Stage 1: Chemical alteration of carbonated serpentinite to ophicarbonite.**

Early in the fault's history, the HBF juxtaposed carbonated serpentinite and quartzofeldspathic wall rocks of distinct terranes: the Highland Border Ophiolite and Dalradian respectively (Tanner & Sutherland 2007; Leslie 2009). Serpentinite is mechanically weak (Escartín *et al.* 2001) and found along many sections of plate boundary faults (e.g., sections of the San Andreas and Alpine fault; Moore and Rymer, 2012; Barth *et al.*, 2013). Reverse faulting along the HBF resulted in deformation focussed in the mechanically weaker carbonated serpentinite wall rocks (**Fig. 5.13a**). Through natural carbonation (Tominga *et al.* 2017), serpentinite was chemically altered to ophicarbonite (stage 1; **Fig. 5.13**). This initial phase of early dextral reverse motion of the HBF enabled CO<sub>2</sub>-rich fluids to transport up or along (direction not known) the fault, dolomitising serpentinite (Elmore *et al.* 2002) and forming fault-parallel, steeply-dipping multiphase carbonate veins as described in McKay *et al.* (2020) (**Fig. 5.2**). Palaeomagnetic and stable isotope studies of Cambrian–Ordovician serpentinite in the Highland Border Ophiolite indicate the HBF was a conduit for CO<sub>2</sub>-rich fluids in the Carboniferous-Permian (Masters *et al.* 2000; Elmore *et al.* 2002). The origin of the fluids could be related to the intrusion of late Carboniferous dykes in



central Scotland and/or to reactivation of the HBF in the Carboniferous–Permian (Elmore *et al.* 2002).

**Stage 2: Breakdown of ophicarbonated wall rock.** During the initial stages of a sinistral strike-slip faulting regime the ophicarbonated wall rock deformed with Reidel shear geometries at different scales (stage 2; **Fig. 5.13**). This is evident from field mapping e.g., the orientation of mapped faults (**Fig. 5.1b**, **Fig. 5.2**), and microstructural observations (**Fig. 5.3**, ).

**Stage 3: Mechanical processing of the Dalradian wall rock resulting in the formation of the red foliated chaotic breccia and wall rock clasts.** After the alteration of carbonated serpentinite to ophicarbonated wall rock the mechanical strength contrast between the wall rocks changed – the Dalradian metasediments to the north of the fault were now mechanically weaker than the ophicarbonated wall rock (**Fig. 5.13a**). At this point the fault brittlely deformed with the breakdown of the Dalradian wall rocks via grain size reduction and plucking (stage 3; **Fig. 5.13**). The HBF fault core in our study exhibits the process of grain size reduction *in situ* spanning nearly the full range of stages. Within the Dalradian, the metagreywacke beds, which locally contain quartz granules, are mechanically stronger and more coherent than interbedded micaceous pelites (**Fig. 5.13a**). After plucking, these metagreywackes account for the majority of clasts in the fault core clays (**Fig. 5.6**, **Fig. 5.10**). Individual and aggregated quartz and calcite granules are common in the red foliated chaotic breccia (**Fig. 5.10**), presumably sourced from the competent protoliths (e.g., sedimentary granule conglomerates/metagreywackes) in the Dalradian. The mechanically weaker pelite beds presumably disaggregate at the grain-scale forming the clayey matrix of the red foliated chaotic breccia. The illite within the red foliated chaotic breccia consists of both the 1M<sub>d</sub> and 2M<sub>1</sub> polytypes (**Table 5.2**). The 2M<sub>1</sub> polytype is diagnostic of detrital wall rock material, while the 1M<sub>d</sub> polytype is primarily a very fine-grained material diagnostic of authigenic fault-derived illite (Hower *et al.* 1963; Reynolds 1963; Srodon & Eberl 1984; Grathoff *et al.* 2001; Haines & Van Der Pluijm 2010). Therefore, the red foliated

chaotic breccia has been derived from the wall rock (e.g., plucking and breakdown of the Dalradian) and altered through faulting.

**Stage 4: Smoothness evolution of clasts, dissolution-precipitation and fault core widening.** We show that plucked Dalradian clast shape and roundness spans the entire range from lozenge-shaped in the red crackle breccia, sub-angular to sub-rounded in the red foliated chaotic breccia (**Fig. 5.10, Fig. 5.11**) to sub-equant clasts in the blue gouge (**Fig. 5.6**) and finally small, rounded, circular clasts in the green gouge (**Fig. 5.3**). A compilation of clast data from all fault core units shows that larger clasts are more lenticular, whereas smaller clasts have a narrower range of aspect ratios and are more equidimensional (**Fig. 5.12**). The clasts therefore become smaller and more equidimensional towards the PSS (**Table 5.1**), suggesting the Dalradian continually becomes incorporated into the fault zone resulting in fault core widening. This smoothness evolution, sympathetic with ever-greater alignment with the fault-tectonic fabric, suggests, unsurprisingly, that corners are preferentially attacked for comminution until a lozenge eventually diminishes to a more equant grain in a self-similar pattern through rolling, fracturing and/or abrasion. This process is not unique to the HBF and can occur across many plate boundary and intraplate faults (e.g., Gabrielsen *et al.* 2016; Shervais & Kirkpatrick 2016).

**Stage 5: Chemical processing of the ophiolitic wall rocks resulting in the formation of the blue and green gouges.** On-going fault-enhanced, fluid-rock interactions produced a fault core rich in weak clay minerals, facilitating strain localisation and potentially reducing overall fault strength. We propose this occurs over three stages, similar to that described for the San Andreas fault (e.g., Warr *et al.*, 2014).

**Stage 5a: Injection of fluids along Reidel shears.** As a prerequisite to the formation of clay gouge it is likely that fluids infiltrating along the brittle shear fractures drove subsequent dissolution-precipitation reactions (evidence for dissolution-precipitation evident in **Fig. 5.6**). As demonstrated for the San Andreas

fault core, the alteration of serpentinite to clay is a process favoured by alkaline, hydrous fluids with pH >10 (Moore and Lockner, 2013). This is characteristic of groundwaters associated with ultramafic bodies, and is required for the dissolution and transport of Al and Si required for clay growth.

**Stage 5b: Clay neoformation on shear fractures.** The blue gouge started forming from chemical alteration and grain size reduction of the ophiocarbonate along the Reidel shear fractures. Clay growth was aligned in the direction of slip in Reidel shear geometries (, **Fig. 5.5**). Fabric development and grain size reduction were controlled by deformation (i.e., in the direction on the Reidel shears). Most of the illite found within the blue gouge (100% in coarsest size fractions) is of 1M<sub>a</sub> polytype (**Table 5.2**), diagnostic of authigenic fault-derived clay.

**Stage 5c: Clay fabric development.** Once most of the serpentinite had broken down into the blue (or green) gouge slip was accommodated by ductile flow along the clay fabric resulting in foliations wrapping around pre-existing clasts of the Dalradian wall rock that had previously been incorporated into the fault core (**Fig. 5.6b, Fig. 5.5c**). Based on mineralogical observations presented in McKay *et al.*, (2020) we suggest the green gouge, only observed at one location, represents a zone of localised alteration and similarly formed from the ophiolite units. The clasts were reworked and sheared into strike-slip geometries: for example, some clasts with  $\sigma$ -type wings and strain shadows are aligned in the same direction as the fabric (**Fig. 5.6g, Fig. 5.5f**), suggesting strain. Although the presence of relatively intact microfossils within the gouge (**Fig. 5.7**) suggests strain must be localised and not homogenous throughout the unit.

The rheology and deformation mechanisms active during strain may be controlled by differences in strain rate (Rutter & Elliot 1976; Rutter 1983). The action of different deformation mechanisms, or the same set of deformation mechanisms acting at different relative slip rates to accommodate the strain, may result in different rock fabrics (Rowe *et al.* 2011). The slip rate on plate boundary faults ranges from fast slip during earthquakes (of the order of 1 m s<sup>-1</sup>) to plate-boundary slip rates (of the order

of millimetres or centimetres per year or less) (Rowe *et al.* 2011 and references therein). The resulting fault rock fabrics, which is the result of the interaction of multiple processes, can therefore indicate aseismic and/or coseismic slip (Rowe *et al.* 2011).

CCA's, similar to those in **Fig. 5.6** have been observed within the core of many seismogenic plate boundary faults. Warr and Cox (2001) identified a CCA fabric within the core of the Alpine fault in New Zealand where rounded quartz clasts are surrounded by a 'snowballed' rim of smectite. More recently, CCA's have been identified in the core of the San Andreas fault and the Chelungpu fault in Taiwan (Janssen *et al.* 2014). Experimental evidence from high velocity shear experiments suggest CCA's are an indicator of coseismic slip with thermal pressurisation and/or fluidisation responsible for their formation (Boutareaud *et al.* 2008, 2010; Boullier *et al.* 2009; Ferri *et al.* 2010). However, based on rotary shear experiments on simulated gouges over a larger range of experimental conditions (e.g. slip rate and displacement), Han and Hirose (2012) suggest they are only diagnostic of particle rolling and not frictional sliding at coseismic slip rates. Despite CCA's not providing cogent evidence of coseismic slip, the undulated margins of some clasts in the blue gouge (**Fig. 5.6f**) are suggestive of melt corrosion/frictional melt and thus seismic slip.

Other fabrics in the gouge and red foliated chaotic breccia are indicative of aseismic slip/plate rate creep and interpreted to have formed by a combination of processes at a strain rate that can be accommodated by combination of grain breakage and sliding, and pressure solution along grain contacts (Rowe *et al.* 2011). Solution creep contributes to grain-scale alignment in the matrix, as well as the strong preferred orientation of clasts (**Fig. 5.4**, **Fig. 5.5**, **Fig. 5.11**). The variability in the long-axis orientations (**Fig. 5.12**) allows the possibility of clast rotation.

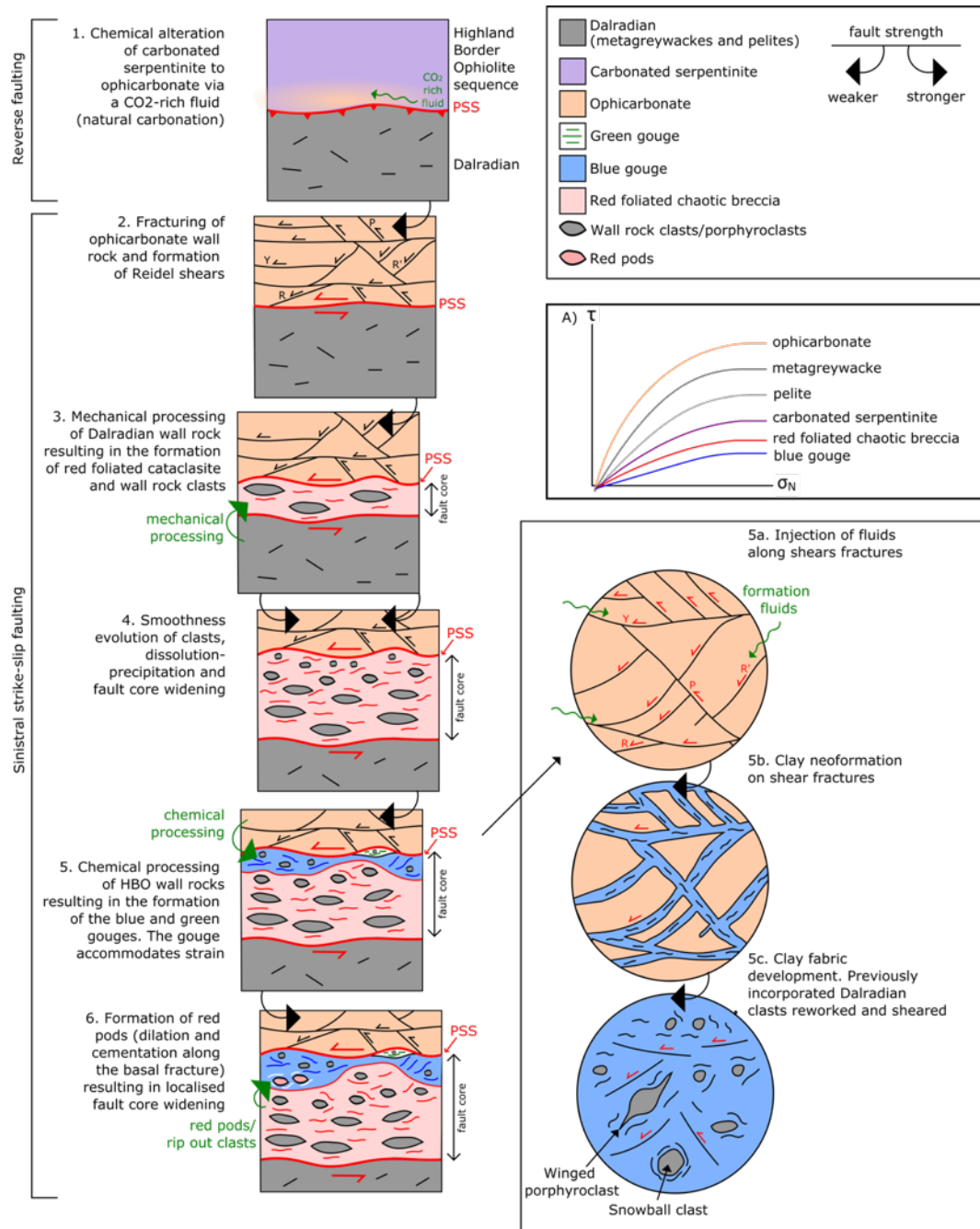
These observations suggest long-term evolution of the gouge/breccias is punctuated by seismic events (e.g., frictional melt). However, further detailed microstructural

observations (e.g., scanning electron microscopy) and experimental deformation studies (e.g., high velocity rock friction) are needed to validate this hypothesis.

**Stage 6: Formation of red pods (i.e., rip out clasts) resulting in localised fault core widening.** After the formation of the blue gouge from the chemical alteration of the ophiolitic wall rocks, the fault underwent episodic widening resulting in the formation of the red pods. The localised red pods at the contact between the blue gouge and red foliated chaotic breccia (**Fig. 5.8**) represent ripout clasts similar to those described for other strike-slip faults (Swanson 1989, 2005; DiToro & Pennacchioni 2005). For instance, when the fault became locked, or there was a reason for widening, the fault plucked out bits of the sidewall forming ripout clasts adjacent to the leading slip plane. The ripout clasts were initially displaced into the fault core through dilation and cementation, resulting in the incorporation of altered sidewall material (i.e. altered red foliated chaotic breccia) into the blue gouge with geometries consistent with the sinistral sense of shear of the bounding faults (**Fig. 5.8**). The red pods, bleached clasts and white altered foliation are all aligned in Y-, P- or R-shear Reidel geometries (**Fig. 5.8c, d, e**) suggesting that small-scale, antithetic and synthetic shears, and associated fluid flow along these shears, appears to ‘mix’ the zone i.e., the units are not chemically mixed. As observed for other faults, the formation of these ripout clasts are a function of fault roughness – they represent asperities that were sheared off from a rough surface (e.g., Shervais & Kirkpatrick 2016). The formation of these red pods (i.e. ripout clasts) may explain the heterogeneity in fault core thickness observed over a short distance along the fault length (McKay *et al.* 2020). The fact that the red pods are found in the blue gouge, and not the other way around, suggests the red cataclasite is older than the blue gouge, conforming to this model.

This six-stage evolution presents a scenario explaining why the core of this large offset plate boundary fault uniquely consists of distinct fault core units that remain unmixed. We suggest the units remain unmixed as there is a difference in the way in which the wall rocks have been processed through time. The red foliated chaotic breccia formed mechanically through grinding and plucking of the Dalradian during slip. Whereas,

the blue gouge, and presumably the green gouge, formed from the fluid-derived, chemical alteration of serpentinite along shear fractures. Once gouge forms, only chemical processes occur and not mechanical ones. Theoretically, given the blue gouge has a higher bulk percentage of clay (*Table 5.2*), the blue clay is mechanically weaker than the red foliated chaotic breccia and therefore accommodated and localised strain. McKay *et al.* (2021) demonstrate that plate boundary faults cores are thin, suggesting the formation of gouge acts as a buffer for accumulating thickness. In other words, once a gouge forms, the fault can happily slide without breaking down the wall rocks further (this only requires a thin zone; think of oil on a table, you only need a little bit to slide; cf. Ma *et al.* 2003). Hence, there is no reason for the fault to get any thicker, nor for the fault core units to mix. Dalradian clasts are only found within the green and blue gouges as they are previously incorporated in the fault core during an earlier stage of faulting. This model outlines the relative timing of fault core evolution based on field and microstructural observations alone. Dating (e.g., radiometric dating on illite) is required to provide absolute ages.



**Fig. 5.13.** Conceptual model of the Highland Boundary fault core evolution based on field, microstructural and XRD observations. (1) Initial processing of carbonated serpentinite associated with early reverse motion. (2-6) Evolution of the fault core associated with sinistral strike-slip. Fig. 5a-c are zoomed in sections depicting the evolution of the blue gouge from ophicarbonate. Tendency towards fault core weakening or strengthening and differences in fault core processes reflect the mechanical properties of the fault units (inset): (A) Hypothetical coefficient of friction estimates for each fault rock unit illustrating the relative strength of each fault rock (not to scale).

### 5.7.2. *Impact on Fault Strength and Ability to Host Earthquakes Through Time*

Our model demonstrates that alteration weakening and/or precipitation-strengthening can occur at the same time in different parts of the fault system, or at different times in the same part of the fault (**Fig. 5.13**). For instance, through the alteration of serpentinite to ophicarbonates the wall rock was strengthened (stage 1; **Fig. 5.13A**). However, later mechanical fracturing in the same part of the fault (stage 2; **Fig. 5.13**) or subsequent chemical alteration to mechanically weak gouge reduced the fault strength (stage 5; **Fig. 5.13**). Within the red foliated chaotic breccia, grain size reduction and clay authigenesis weakened the fault core (stage 3 and stage 4; **Fig. 5.13**). However, precipitation reactions and mineralisation/cementation of the clay with quartz or calcite (**Table 5.2**) would have simultaneously strengthened and widened the fault core (stage 4; **Fig. 5.13**) (Woodcock *et al.* 2007; Faulkner *et al.* 2008; Caine *et al.* 2010; Callahan *et al.* 2019). The incorporation of sidewall material (e.g., ripout clasts stage 6; **Fig. 5.13**) can also help roughen, widen and/or strengthen the fault core (e.g., Caine *et al.*, 2010; Callahan *et al.*, 2019). Precipitation-strengthening and/or alteration-weakening reactions add spatial and temporal heterogeneity to fault rock properties and fault zone evolution, and may help explain the along-strike variation in fault core thickness as observed in McKay *et al.* (2020).

This multi-event evolution caused the mechanical properties of the HBF fault core to vary through time, becoming either stronger or weaker with each deformation phase. In turn, this will have affected the fault's ability to host earthquakes through time. Given the potential for clays to retard fault rupture propagation (e.g., Ikari *et al.* 2009; Tembe *et al.* 2010; Behnsen & Faulkner 2012; Sone *et al.* 2012) it is crucial to understand the controls on the presence, distribution and thickness of such units when assessing earthquake risk. The bulk mechanical properties of a fault with a single gouge composition along-strike will be very different to the bulk mechanical behavior of a fault zone that contains multiple units of varying mechanical behaviors (e.g., the HBF) (Xu *et al.* 2012). The varying type of fault rock found within the HBF allows



for the possibility of ‘mixed-mode’ seismicity, with fault creep occurring within velocity strengthening clay-rich gouge (cf. the blue gouge) (Behnsen & Faulkner 2012) and seismic events occurring within velocity weakening serpentinites (cf. carbonated serpentinite or ophiocarbonate) (Reinen 2000). Alternatively, the long-term evolution of the gouge during aseismic creep may have been punctuated by seismic events as demonstrated by the undulated margins of some clasts (**Fig. 5.6f**). If these varying fault core units change as the fault grows (as demonstrated in **Fig. 5.13**), then the bulk mechanical properties will also evolve over geological time, and the resulting earthquakes may be more or less damaging.

## 5.8. Conclusion

In this paper we present detailed field, microstructural and XRD observations of the Highland Boundary fault in order to comment on how strain is localised and the processes leading to the genesis of multiple, distinct fault rock units within the core of this ancient plate boundary fault. Both wall rocks are incorporated into the fault core through a range of chemical and physical processes responsible for grain size reduction and wall rock comminution in a fault zone. We suggest the fault core units remain distinct as they formed at different stages of faulting and by different mechanisms. The red foliated chaotic breccia formed first from mechanical processing, i.e., plucking, abrasion and wear of the Dalradian wall rock during slip. The blue gouge formed later due to fluid-derived, chemical alteration of serpentinitic wall rocks along shear fractures. The blue gouge is more clay-rich, and hence weaker than the red, leading to strain localisation. Radiometric dating is needed to provide an absolute age and validate these observations. Regardless of the timing, this multi-event evolution caused the mechanical properties of the HBF fault core to vary through time, becoming either stronger or weaker with each deformation phase. In turn, this will have affected the fault's ability to host earthquakes of different sizes through time.

## Chapter 6 – Discussion and Conclusion

In this thesis the first detailed field, mineralogical and microstructural observations of the HBF are presented in order to better understand the internal structure of the fault core and its spatial and temporal evolution. These detailed observations were then compiled with data from the peer-reviewed scientific literature for both plate boundary and intraplate faults in order to systematically compare the two types of fault system. A detailed discussion of results has been presented at the end of each research chapter, each of which has either been published as a paper or is going to be submitted. This chapter serves to discuss speculative issues that arose from this work which have not previously been discussed in the foregoing chapters. Suggestions for further work that can help resolve these speculative issues are given in Chapter 7.

### 6.1. Understanding the Evolution of the Highland Boundary Fault

#### *6.1.1. Evidence of Slip Weakening Mechanisms*

Results in Chapters 3 and 5 demonstrate that the physical properties of the HBF vary in space (metre-scale variability) in the present day and over geological time, and that this is likely to have caused variations and complexities in their slip style and mechanical behaviour (**Fig. 5.13**). Assessing the metre-scale variability of a fault is crucial for understanding the processes that occur during an earthquake, in particular dynamic weakening mechanisms (Chester *et al.* 2005; Wibberley & Shimamoto 2005; Kirkpatrick & Shipton 2009; Fagereng & Toy 2011; Kirkpatrick *et al.* 2018). This thesis has not explored dynamic weakening mechanisms for the HBF. However, it is clear that the variable fault core composition and thicknesses observed will have had implications for the dynamic reduction of friction during past earthquakes along this plate boundary. For instance, for thermally driven processes such as thermal pressurisation, flash heating and melt lubrication, the rate of heating will depend on

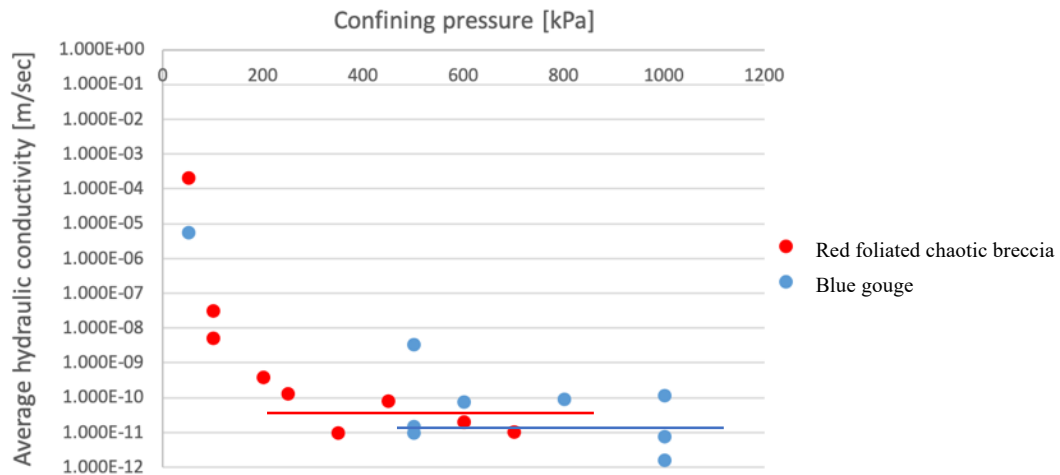
the properties and mineralogy of the rock being heated (heat capacity) and on the thickness of the unit being heated – thinner layers heat faster than thicker layers. Thus, if the fault core has variable thickness, then the heating and consequently the lubrication effect will also be variable (Kirkpatrick *et al.* 2018).

Geochemistry would help to understand dynamic weakening mechanisms but in order to fully understand which dynamic weakening mechanism were active at the HBF, a suite of other data is needed including radiometric dating to get the P-T-t path, thermochronology to work out delta T and mechanical properties (both static and dynamic). Preliminary hydraulic conductivity measurements on the blue gouge and red foliated chaotic breccia suggest that both these fault core units have very low hydraulic conductivities, which in turn will affect which slip weakening mechanism(s) might have been active.

Preliminary hydraulic conductivity tests were conducted on two samples from Log 4 only (one from the blue gouge and one from the red foliated chaotic breccia) using the ErgoTech® permeability cell at the University of Strathclyde. Cores 1.5 inches in diameter and <7 cm in length, were cut perpendicular to the foliations. The samples were sealed in the core holder and subjected to an injection of fresh water at increased pressures. The flow rate of water through the sample was measured and hydraulic conductivity (K in m/s) was calculated using Darcy's Law (equation (6.1)):

$$K = \frac{QL}{Aht} \quad (\text{eq. 6.1})$$

where, Q is the flow rate of water (m<sup>3</sup>/s), L is the length of core, A is the cross-sectional area (m<sup>2</sup>), h is the pressure difference (m H<sub>2</sub>O) and t is the time (s) required for the pressure difference. A dynamic viscosity of 0.002 Pa/s and a density of 998.2 kg/m<sup>3</sup> was assumed for water.



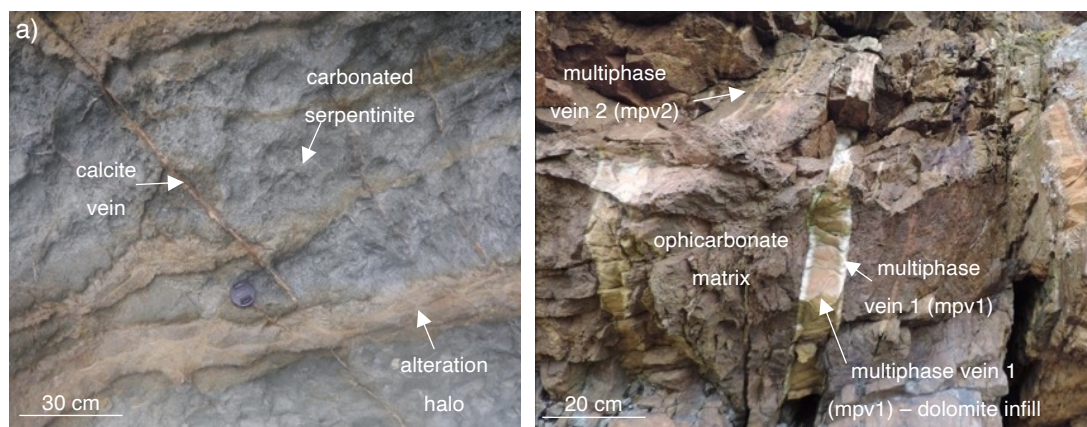
**Fig. 6.1** Preliminary hydraulic conductivity measurements of the blue gouge and red foliated chaotic breccia of the HBF fault core.

By taking the mean measurement of the plateau at increased confining pressures (shown as solid lines with the respective colours), the blue gouge has a hydraulic conductivity of  $10^{-11}$  m/s, while the red foliated chaotic breccia stabilises at a hydraulic conductivity between  $10^{-10}$  m/s and  $10^{-11}$  m/s (**Fig. 6.1**). These values are consistent with measures of permeability from fault gouges of the Median Tectonic Line (Matsumoto & Shigematsu 2018). The lower hydraulic conductivity of the blue gouge is consistent with the increased percentage of clay within this unit (**Table 3.1**). Since both of these units are continuous along-strike (at the Stonehaven section at least), the fault core would therefore have been a barrier to cross-fault fluid flow. Thermal pressurisation requires low permeability to enable frictional heating to heat up the fluids. The HBF fault core permeabilities are low (**Fig. 6.1**), but from the microscopic observations there is evidence of early fluid alteration (**Fig. 5.13**), so this mechanism of dynamic weakening may not have been active until permeability dropped.

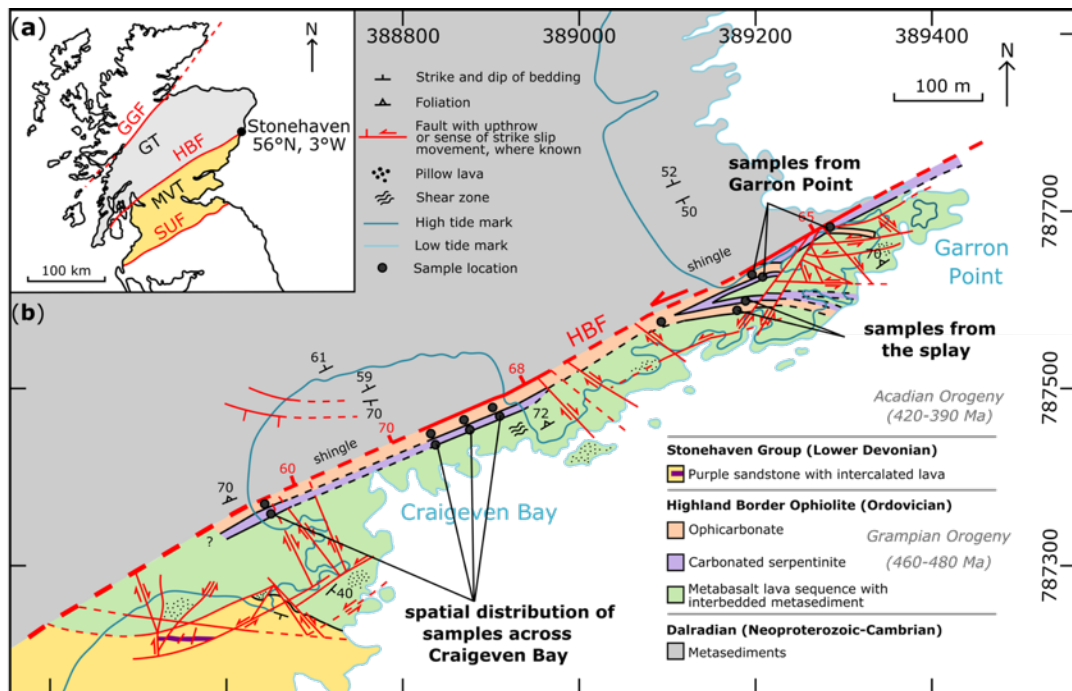
### 6.1.2. Evolution of the Damage Zone

In this study the focus has exclusively been on the evolution of the HBF fault core as that is where the majority of earthquake slip is accommodated. In order to fully constrain and understand how and why the HBF fault core evolved an understanding of the evolution of the damage zones are necessary.

In order to constrain the isotopic composition and fluid sources from which the carbonate in the Highland Border Ophiolite (footwall damage zone) grew, preliminary measurements of carbonate  $\delta^{13}\text{C}$  and  $\delta^{18}\text{O}$  were carried out. With permission from Scottish Natural Heritage, samples were collected from various units of the Highland Border Ophiolite and analysed via mass spectrometry at the Scottish Universities Environmental Research Centre (SUERC). Samples were collected from: 1) the carbonated serpentinite including the calcareous matrix, calcite veins and the dolomitic alteration halos around some fractures (Fig. 6.2a); and, 2) the ophicarbonates including the dolomitised matrix, and dolomite and calcite from the multiphase veins (Fig. 6.2b). See Chapter 3 for a more detailed description of these units. In total 30 samples were collected from the field. See Fig. 6.3 for a map of the sample locations. Each sample was then milled using a computer-controlled micromill with a 3 mm drill bit to generate 103 powdered samples, each weighing ~0.5 mg, for stable isotope analysis ( $\delta^{13}\text{C}$  and  $\delta^{18}\text{O}$ ).

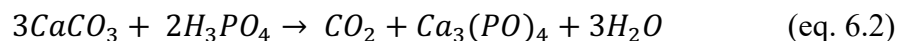


**Fig. 6.2.** Photographs of carbonate units within the Highland Border Ophiolite (footwall damage zone). **a)** Carbonated serpentinite with calcite veins and fractures displaying an alteration halo. **b)** Ophicarbonates with multiphase carbonate veins (massive dolomite in the centre with sparry calcite lining the vein walls).



**Fig. 6.3.** Map of the HBF showing sample locations. 30 samples were collected in total from these approximate locations (cannot show on the scale of the map). Samples were collected with increasing distance along the principal slip surface and with increasing distance away/across strike from the principal slip surface.

In order to produce the  $\text{CO}_2$  for  $\delta^{13}\text{C}$  and  $\delta^{18}\text{O}$  analyses, the carbonate powders were reacted overnight, in sealed tubes, with 103% phosphoric acid at  $70^\circ\text{C}$ . Calcium phosphate and water were formed as by-products (equation (6.2)):



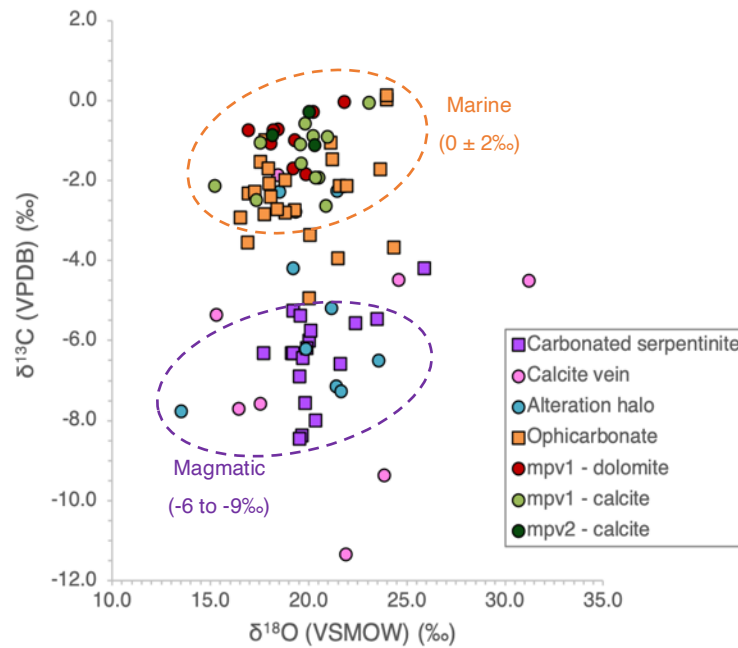
The following day the product  $\text{CO}_2$  was cryogenically purified before transfer to a collection vessel that was attached to a mass spectrometer for measurement. The  $\text{CO}_2$  gas was analysed on a gas course isotope ratio Analytical Precision mass spectrometer at SUERC. In addition to the samples, a series of international (NBS-18) and ‘in-house’ carbonate standards (e.g., Marble-MAB), of known isotopic signature, were also analysed at the beginning and at the end of the analytical sequence, with quality control samples (i.e., blanks) run approximately every 10 samples. The SUERC gas inlet mass spectrometer measured the carbon and oxygen isotopes relative to the in-house reference gas, which was then corrected relative to the international standard.

Stable isotope data are reported using delta notation in per mil (‰) relative to Vienna Standard Mean Ocean Water (VSMOW) for  $\delta^{18}\text{O}$  and Vienna Pee Dee Belemnite (VPDB) for  $\delta^{13}\text{C}$  according to equation 6.3:

$$R_{\text{sample}} [\text{‰}] = \left[ \frac{R_{\text{sample}} - R_{\text{standard}}}{R_{\text{standard}}} \right] \times 1000 \quad (\text{eq. 6.3})$$

where, R represents the ratio of the heavy isotope to light isotope ( $^{18}\text{O}/^{16}\text{O}$  and  $^{14}\text{C}/^{13}\text{C}$ ) of samples and reference materials, respectively. Each sample was measured 4 times on the mass spectrometer. The first number was ignored, and the reported value is the average of the last 3 measurements.

The preliminary  $\delta^{13}\text{C}$  and  $\delta^{18}\text{O}$  measurements from the Highland Border Ophiolite (footwall damage zone) are shown in (**Fig. 6.4**).  $\delta^{13}\text{C}$  ranges from 0.1‰ to -11.3‰ (VPDB) across all units. Ophicarbonates and their associated multiphase carbonate veins typically have  $\delta^{13}\text{C}$  values between 0.1‰ and -3‰ (VPDB), indicative of a marine signature (Shanks *et al.* 1995; Veizer *et al.* 1999; Masters *et al.* 2000). Whereas the carbonated serpentines and their associated calcite veins typically have  $\delta^{13}\text{C}$  values between -5.5‰ and -8.5‰ (VPDB). The isotopic composition of carbon in seawater can be modified by hydrothermal circulation through mafic/ultramafic rocks and seafloor sediments (Veizer *et al.*, 1999, Masters *et al.* 2000 and references therein). Values in the order of -5.5‰ and -8.5‰ are therefore indicative of a magmatic/average crustal carbon signature (Ohmoto & Rye 1979). The dolomitic alteration halos around some of the fractures in the carbonated serpentinite have a spread of values between these two systems with a mixed marine-magmatic  $\delta^{13}\text{C}$  signature (**Fig. 6.4**).



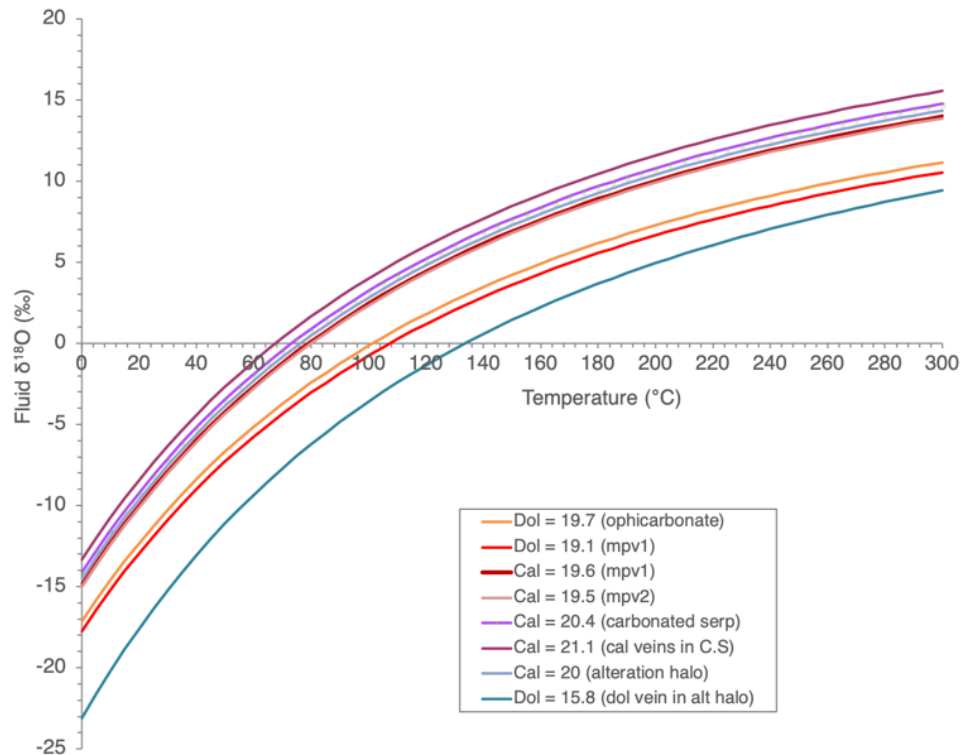
**Fig. 6.4.** Conventional  $\delta^{13}\text{C}$  and  $\delta^{18}\text{O}$  isotope data determined via mass spectrometry. Values are reported using delta notation in per mil (‰) relative to Vienna Standard Mean Ocean Water (VSMOW) for  $\delta^{18}\text{O}$  and Vienna Pee Dee Belemnite (VPDB) for  $\delta^{13}\text{C}$ . Each sample was measured four times on the mass spectrometer. The first number was ignored, and the reported value is the average of the last three measurements.

While the  $\delta^{13}\text{C}$  values appear to indicate two different systems (marine and magmatic), the  $\delta^{18}\text{O}$  values are more consistent (except a few outliers) with a mean value of  $19.3 \pm 3.6\text{‰}$  (VSMOW) across all lithologies (**Fig. 6.4**). These  $\delta^{13}\text{C}$  and  $\delta^{18}\text{O}$  values are similar to those reported for typical hydrothermal Lost City-type environments (Kelley *et al.* 2005). The Lost City hydrothermal field is an area of marine alkaline hydrothermal vents located on the Atlantic Massif ~15 km west of the Mid-Atlantic ridge: a divergent plate boundary located in the Atlantic Ocean (Kelley *et al.* 2005). It is a long-lived site of active and inactive ultramafic-hosted serpentinisation. The reaction between serpentinite and sea water produces methane and hydrogen which are fundamental to microbial life (Kelley *et al.* 2005). Therefore, one hypothesis is the carbonated serpentinite in the Highland Border Ophiolite (footwall damage zone) are the result of hydrothermal alteration by seawater with the addition of magmatic  $\text{CO}_2$  i.e., a serpentinite mound above a  $\text{CO}_2$ -rich hydrothermal field on the Iapetus ocean-floor. Based on field evidence it is assumed that sections of the carbonated serpentinite were later chemically altered to ophicarbonates during early reverse motion of the HBF



(Fig. 5.13). This initial phase of early dextral reverse motion of the HBF enabled CO<sub>2</sub>-rich fluids to transport up or along (direction not known) the fault, dolomitising serpentinite (Elmore *et al.* 2002) and forming fault-parallel, steeply-dipping multiphase carbonate veins as described in McKay *et al.* (2020) (Fig. 5.2). Based on the isotopic signatures these fluids must have been marine in origin (Fig. 6.4).

$\delta^{18}\text{O}$  values can be used to predict the temperature of the fluid from which the carbonate precipitated. Using the stable isotope fractionation calculator for either dolomite  $\leftrightarrow$  water or calcite  $\leftrightarrow$  water, and a range of equations calculated from first principles (e.g., Horita 2014), the mean  $\delta^{18}\text{O}$  values for each lithology was used to predict the temperature of the fluid from which  $\delta^{18}\text{O}$  precipitated (Fig. 6.5). Assuming the fluid precipitated from marine seawater ( $\delta^{18}\text{O}$  value of 0‰), the temperature predictions range from 65°C to 135°C. For instance, taking the mean  $\delta^{18}\text{O}$  value of 19.7‰ (VSMOW) for ophicarbonates, the temperature of the fluid from which  $\delta^{18}\text{O}$  precipitated from, assuming a pure marine seawater at 0‰ (Shanks *et al.* 1995; Veizer *et al.* 1999; Masters *et al.* 2000), is ~100°C (Fig. 6.5). Taking the mean  $\delta^{18}\text{O}$  value of 20.4‰ (VSMOW) for carbonated serpentinite, the temperature of the fluid from which  $\delta^{18}\text{O}$  precipitated from, assuming a magmatic fluid with a signature of 6‰ to 9‰ (Ohmoto & Rye 1979), is 110-160°C. Therefore, one could hypothesise that the ophicarbonates formed from marine waters at 100°C (at a Mid Ocean Ridge given the elevated temperature), while the carbonated serpentinite formed from magmatic water at 110-160°C. Constraining the source and temperature of paleofluids responsible for carbonate formation in the Highland Border Ophiolite (footwall damage zone) would make a great addition to the fault core data presented in this study and is highly recommended as future work (see Section 7).



**Fig. 6.5.** Measured  $\delta^{18}\text{O}$  versus temperature for measured  $\delta^{18}\text{O}$  isotope values in calcite and dolomite. Temperatures were calculated using the stable isotope fractionation calculator and equations outlined in Horita (2014).

### 6.1.3. The Evolution of the Highland Boundary Fault System (Fault Core + Damage Zone)

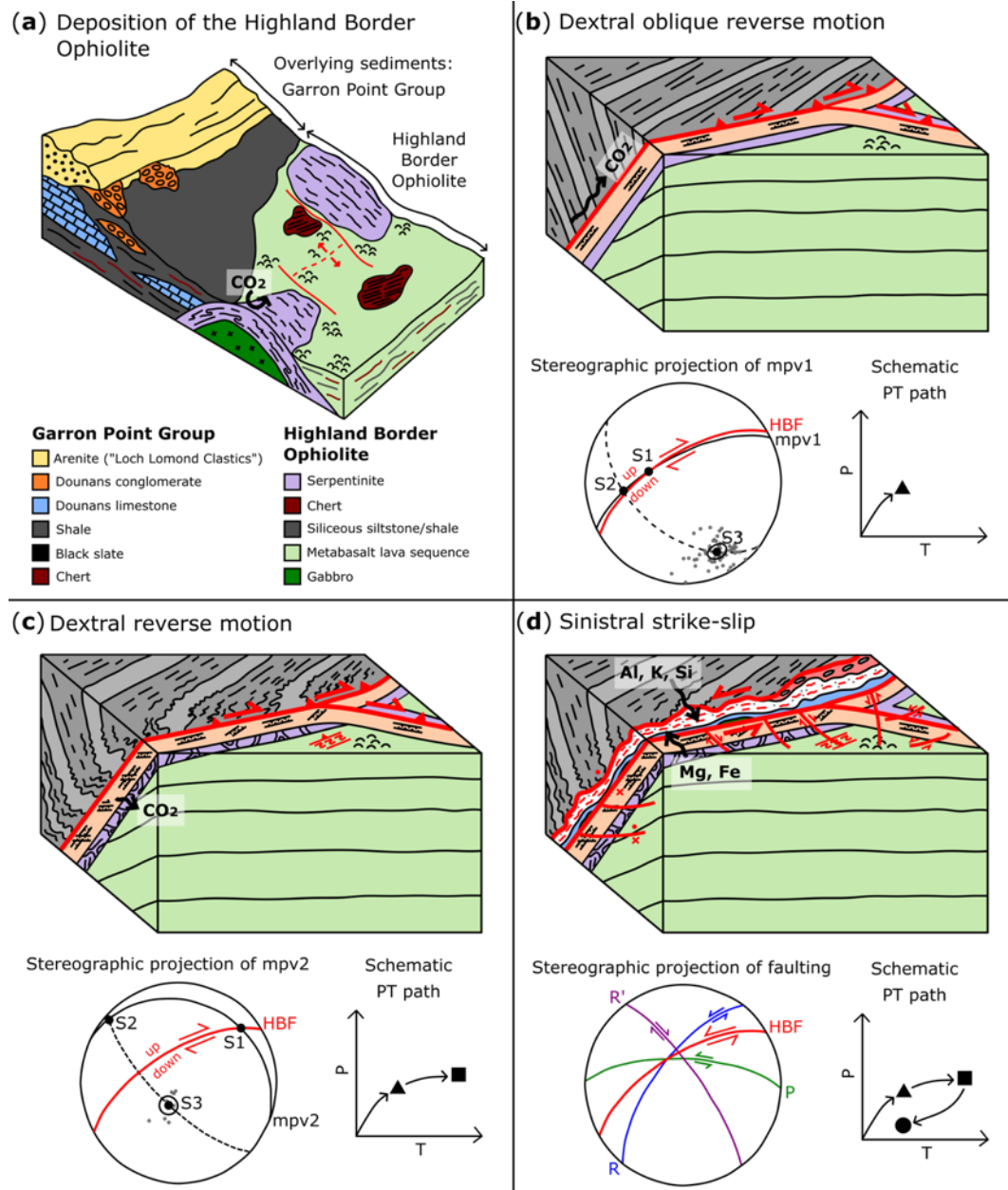
By combining all field and mineralogical observations in this thesis with previous studies a simple 4-stage tectonic evolution model for the whole Highland Boundary fault system (fault core + damage zone) is proposed (Fig. 6.6). The first stage involves the deposition of the Highland Border Ophiolite and overlying sediments in a shallow, hyper-extended hydrothermal basin (Tanner & Sutherland 2007; Henderson *et al.* 2009; Leslie 2009) (Fig. 6.6a), similar to that reported for Alpine Ligurian ophiolites (Manatschal & Muntener 2009). Here, based on the isotopic evidence presented in Fig. 6.4, it can be assumed that the carbonated serpentinite formed through hydrothermal alteration and  $\text{CO}_2$ –water–rock reactions on the seafloor. This is consistent with findings by Masters *et al.* (2000).

Field evidence presented in Chapter 3 (and plotted on stereonet in **Fig. 6.6b,c**) suggest that the multiphase veins in the ophicarbonates are fault-related extensional opening mode fractures that provide evidence for two early phases of oblique (dextral) reverse motion of the HBF. The second stage in the model therefore involves early dextral reverse motion of the HBF enabling CO<sub>2</sub>-rich fluids to come up the fault leading to the dolomitisation of serpentinite (the product being ophicarbonate) and the formation of fault-parallel, steeply-dipping multiphase carbonate veins termed mpv1. The ophicarbonate therefore formed from the alteration of serpentinite via a CO<sub>2</sub>-rich fluid in a process known as natural carbonation; Tominga *et al.* 2017). Shallow, low temperature faulting (~100°C) is inferred due to the co-existence of quartz and serpentinite in XRD samples (**Fig. 3.15**) (Streit *et al.* 2012) and the measured average  $\delta^{18}\text{O}$  value of 19.7‰ (VSMOW) where modelling estimates predict a temperature of ~100°C for waters of marine origin (**Fig. 6.4, Fig. 6.5**).

The third stage involves dextral reverse motion of the HBF forming the second set of shallow-angle, multiphase carbonate veins in the ophicarbonate termed mpv2 that cross-cut the first set. This is likely due to a clockwise rotation of the stress field between the two sets of multiphase veins (**Fig. 6.6c**). Remobilisation of CO<sub>2</sub>-rich fluids may have created the fractures with dolomitic alteration halos in the carbonated serpentinite at this stage, although this has not been studied in enough detail to be certain. The alteration halos have a spread of isotope values with a mixed marine-magmatic  $\delta^{13}\text{C}$  signature (**Fig. 6.4**). A possible scenario includes a later high-pressure injection (similar to hydraulic fracturing) of a marine fluid into the previously carbonated serpentinite. Similar structures are evident in the analogous Ligurian Ophiolite in Italy (Boschi *et al.* 2009). The marine fluid would then have mixed with the magmatic waters within the host rock forming an alteration halo around the fractures, localised to the carbonated serpentinite only. This suggests that permeability was compartmentalised within the carbonated serpentinite. The fractures can be traced from the carbonated serpentinite into the ophicarbonate (**Fig. 6.7**), however, the alteration halos are only observed in carbonated serpentinite. The permeability will

have been lowered in the ophicarbonates due to the deposition of carbonate in the pore space, therefore, alteration halos were less likely to develop.

The final stage of the model involves sinistral strike-slip motion of the HBF resulting in the formation of the narrow fault core with several distinct fault core units (**Fig. 6.6d**). This stage is sub-divided into distinct events (**Fig. 5.13**) which are discussed in Chapter 5. What can be observed within the HBF today is the frozen-in finite record of multiple earthquakes on a fault and the models presented here are an attempt at peeling away the record of processes that occurred on the fault and are by no means complete.



**Fig. 6.6.** Schematic tectonic evolution model for the Highland Boundary fault system (fault core + damage zone). **(a)** Deposition of the Highland Border Ophiolite and its overlying sediments in a hyper-extended hydrothermal basin (as evident in Leslie, 2009). Mid Ocean Ridge processes will have 'switched' off before sedimentation started). Lithologies from Tanner & Sutherland (2007), modified after Bluck (2002); **(b)** Dextral oblique reverse motion indicated by steeply dipping, fault-parallel, multiphase carbonate veins (mpv1) in ophiolite; **(c)** Dextral reverse motion indicated by shallow angled, multiphase carbonate veins (mpv2) in ophiolite that cross-cut the first set, and; **(d)** The most recent sinistral strike-slip that involves the formation of the fault core as we see today. This can be sub-divided further into different stages (see Fig. 5.13).



**Fig. 6.7.** Field photograph of the ophicarbonates and carbonated serpentinite units of the Highland Border Ophiolite (footwall damage zone).

## 6.2. Why are Plate Boundary Fault Cores Narrow?

Field evidence in Chapter 3 demonstrate that the fault core of the HBF is narrow (**Fig. 3.13, Fig. 3.14**). In Chapter 4, it was suggested that all plate boundary faults have anomalously narrow fault cores compared to intraplate faults of the same offset, as they are not required to grow in the same way as intraplate faults. Compilations of data from multiple fault studies show that, in general, intraplate faults get thicker with increasing displacement through lateral tip processing and/or linkage with other fault segments via relay formation and breaching (Shipton *et al.* 2006a; Van Der Zee *et al.* 2008; Wibberley *et al.* 2008; Childs *et al.* 2009, 2017; Fossen & Rotevatn 2016; Torabi *et al.* 2019). That is, low displacement faults represent a stage of early growth and are thin but evolve into wide fault zones as they extend in length, link with adjacent faults and become more complex in structure. Plate boundary faults start as pre-existing, inherited structures on regional-scale zones of weakness. As such, their tips do not terminate within intact rock - they terminate at triple junctions with other plate boundaries (McKenzie & Morgan 1969). Tectonic plates are continually moving, albeit very slowly, and are constantly rearranging themselves in response to each other. For instance, the boundary between the North American and Pacific Plate has evolved and grown through time from a subduction boundary to the present-day San Andreas transform fault. As a result, while plate boundary faults still grow and evolve through time as triple junctions and plates move apart relative to each other, they are not

required to grow in length either by damaging intact rock at their tips or by linking with other pre-existing structures.

Another hypothesis to explain why plate boundary fault cores are consistently narrower than intraplate faults is that they have simple, uniform structures. To test this, schematic structural logs were constructed for each plate boundary exposure and drill core intersection in the compilation presented in Chapter 4 (**Fig. 4.3**). This demonstrated that the internal structure of plate boundary faults is not simple or uniform. The fault core composition, host rock, slip direction, fault type, and/or the number of fault core strands all vary, both along an individual plate boundary and between plate boundaries, but in all examples the fault core remains consistently narrow. However, while plate boundary faults are far from simple and uniform, they are consistently narrow regardless of their local fault structure.

If plate boundary faults represent pre-existing structures which are not required to grow through linkage, then their geometry should be smoother and less complex than intraplate faults as demonstrated in the compilation presented in Chapter 4 (**Fig. 4.4**). This can be observed for the HBF, which like the SAF, has a long and straight surface fault trace with few overlap zones or steps mapped along strike (Tanner 2008). The principal slip surface was also remarkably straight at the field-scale (m-scale) (**Fig. 3.2**).

The dataset comparing the fault complexity between intraplate and plate boundary strike-slip faults (**Fig. 4.4, Table 4.3**) was included in Chapter 4 but not the associated published paper (Appendix 3) due to the relative paucity of data compared to the compilations examining fault core thickness and seismic moment. There are also several problems with this fault complexity dataset. First is the issue of the size of the steps, which is biased towards features that are both exposed and visible at a scale that humans can realistically observe and measure (Shipton *et al.* 2019). For instance, if you were mapping a small displacement fault, it is easier and less time consuming to map smaller steps. In comparison, if you were mapping the surface geometry of a large

plate boundary fault the map will cover a larger scale and not pick out small breaks in geometry as would be mapped for small displacement intraplate faults. In other words, the scale of mapping will be different between faults of different displacements. Different techniques will therefore be used for mapping at different scales (e.g., field data which in turn depends on the displacement of the fault and scale of human mapping/bias, or seismic data which only picks out larger steps). Subjective bias also exists in defining and characterising the breaks in fault geometries. For example, there is no standard definition of what constitutes ‘fault steps’, and different geologists classify and measure the ‘fault steps’ differently. Some authors report them as ‘steps’ whereas, others report them as ‘jogs’. A fault step can evolve into a lens (Childs & Watterson 1996; Gabrielsen *et al.* 2016; Fossen 2020). 2D exposures cannot unpick the geometry of steps versus lenses, while 3D exposures such as Volcanic Tableland in northern Owens Valley, California (Dawers *et al.* 1993) has a dataset-specific image resolution problem as well as operator bias (Bond *et al.* 2007). So there will inevitably be a level of subjective bias within this dataset that is based on the geologist’s experience, the terminology they use and the focus of their study (Shipton *et al.* 2019).

The last issue, which also relates to all the compilations presented in Chapter 4, is how do we define a plate boundary fault? Different geologists may classify what counts as a plate boundary fault differently. For example, in this study the Hope fault and Wairau fault are included as plate boundary faults as they branch off the Alpine fault. But are they the main plate boundary and should they really be included? Subjective bias inevitably exists in compilations such as those presented in Chapter 4 as again, there is no standard definition for what to include as a plate boundary fault. Every fault in some way or another is related to plate tectonics.

Nevertheless, regardless of the inherent biases, that data presented in Chapter 4 suggests that larger displacement plate boundary faults have smoother and simpler geometries in comparison to smaller displacement intraplate faults. The results, in part, may be due to the way the faults grew and evolved (i.e., plate boundary faults start as a pre-existing structure whereas intraplate faults grow through linkage). As

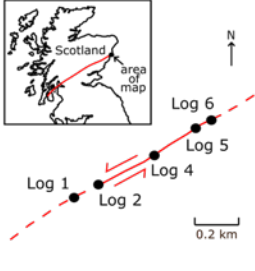

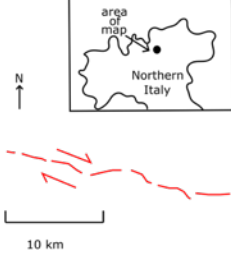


demonstrated by the 1992 Landers earthquake, extra energy is required to hop over segments within faults (Hauksson *et al.* 1993). Earthquakes that propagate along a smoother fault will therefore find less energy being absorbed through segment hopping and/or the processing of intact rock allowing more energy to be radiated to the surface as observed from the compiled dataset in Chapter 4 (**Fig. 4.5a**). Therefore, plate boundary faults, which are long structures where the ongoing evolution of the structure does not necessitate deformation of the host rock blocks around stepover regions that produce complex geometries, will absorb less energy through segment hopping. The lack of a relationship between fault core thickness and total displacement on plate boundaries tends to support the hypothesis of Delogkos *et al.* (2020) for intraplate faults, i.e. that fault cores increase in thickness only due to progressive fault linkage, and that once they reach a sufficient thickness they can accommodate slip events without continuous processing of the wall rock – as appears to be the case for plate boundary faults. As hypothesised for the Highland Boundary fault core evolution in Chapter 5 (**Fig. 5.13**), once gouge forms the fault can accommodate further slip events without breaking down the wall rocks further. This implies that once a low strength/friction surface has been established, the plate boundary fault core does not increase in thickness as: a) it does not need to; and b) the ongoing evolution of the structure does not necessitate deformation of the host rock blocks around stepover regions that produce complex geometries.

Further, plate boundary fault zones contain large volumes of fluids at high fluid pressures. For example, large quantities of circulated fluids are present at convergent plate boundaries due to the subduction of hydrated oceanic crust and prograde metamorphic dehydration reactions (Peacock *et al.* 2011; Moreno *et al.* 2014). These regions of high fluid pressures would lubricate the plate boundary fault and facilitate earthquake nucleation by reducing the effective normal stress. This in turn facilitates fault slip without the continuous processing of wall rocks.

In contrast, intraplate faults get longer through time through linkage with neighboring structures. This generates faults with complex geometries that get thicker as fault slip

increases. An example of the intraplate seismogenic Gole Larghe fault is given in *Table 6.1* to highlight the complex geometries of intraplate faults compared to the smoother, straighter and less complex geometries of plate boundary faults such as the HBF and SAF. Results in Chapter 4 suggest earthquakes that propagate along intraplate faults dissipate more energy compared to plate boundary faults (**Fig. 4.5**). Thus, the more complex the fault geometry, the more energy has to be consumed at depth during an earthquake and the less energy reaches the surface. This is summarised in *Table 6.1*. The purpose of this Table is two-fold: 1) to show the similarities between the HBF and SAF; and 2) show the differences between plate boundary and intraplate faults. This in turn summarises the main findings of this thesis: 1) there are similarities in the internal structure of plate boundary faults specifically they all have narrow fault cores regardless of their displacement or local fault structure; and 2) plate boundary faults and intraplate faults evolve differently with repeated slip events. One significant conclusion of this work is that plate boundary faults have evolved structural characteristics (compared to interplate faults) that allow them to efficiently dissipate seismic energy. This helps to explain why lithospheric deformation is localised within them (i.e., they remain in the same place for extended periods of time) and has significance for development and maintenance of the entire plate tectonic system of the Earth.

	PLATE BOUNDARY FAULTS		INTRAPLATE FAULT
	Highland Boundary Fault Stonehaven segment	San Andreas Fault Parkfield segment	Gole Larghe Fault
			
Fault surface geometry	Smooth and straight	Smooth and straight	Complex with numerous splay faults
Displacement	115 ± 85 km	282 ± 32.5 km	0.008 to 10.65 m
Internal structure	Single fault core at all locations sampled	Single fault core at all locations sampled	Complex system with single or multiple fault core strands at different locations
Fault core thickness	2.97 to 10.7 m	0.15 to 9.1 m	0.0002 to 0.375 m
Fault gouge thickness	0.65 to 2.65 m	0.15 to 9.1 m	?
Mean fault core thickness ± stdev	7.3 ± 2.18 m	3.91 ± 4.64 m	0.01 ± 0.04m
Variance in fault core thickness	1 order of magnitude	1 order of magnitude	3 orders of magnitude
Number of fault core measurements	18	3	109
Fault core thickness vs displacement	Does not increase with increased displacement	Does not increase with increased displacement	Increases with increased displacement
Seismic moment for a given displacement	Low	Low	High
Energy dissipation for a given displacement	Dissipates less energy more radiated to surface as higher magnitude EQ's	Dissipates less energy more radiated to surface as higher magnitude EQ's	Dissipates more energy less radiated to surface
Summary	<p>Narrow fault cores regardless of total displacement (and hence number of EQ's) or local fault structure. Long structures not formed via linkage (a pre-existing structure at the edge of two plates that terminates at a triple junction not intact rock). These structural characteristics allow plate boundary faults to efficiently dissipate seismic energy: less energy is absorbed through segment hopping, allowing more energy to be radiated to surface manifested as higher magnitude EQ's. In other words, plate boundary faults do not process intact rock as much as intraplate faults during seismic events. This helps to explain why lithospheric deformation is localised within plate boundaries.</p>		<p>Gets wider as fault slip increases, generating complex zones of damage in surrounding rock and propagating through linkage. The more complex the final fault geometry the more energy is consumed at depth during an EQ and less reaches the surface i.e., smaller magnitude EQ's compared to narrow, less complex plate boundary faults.</p>

**Table 6.1.** Synthesis of the major findings of this thesis. Fault complexity defined as steps per unit length, Highland Boundary fault references: Tanner (2008); Cawood et al. (2012); McKay et al. (2020). San Andreas fault references: Matthews (1976); Wesnousky (2005); Bradbury et al. (2011); Holdsworth et al. (2011); Moore & Rymer (2012). Gole Larghe fault references: DiToro and Pennacchioni (2005); Mittempergher et al. (2009).

### 6.3. Conclusions

A combination of detailed geological fieldwork, compilation of published datasets and laboratory analyses were used to answer the six research questions presented in Chapter 1. The key findings for each research question are detailed below:

**RQ1: What is the internal structure of the HBF in terms of fault core and damage zone and what fault rock lithologies are present?**

Detailed field mapping reveals that the Stonehaven section of the HBF is composed of a structurally and compositionally variable fault core that formed during sinistral strike-slip. The fault core consists of four distinct units that remain unmixed: (1) a localised green gouge; (2) a blue gouge of high plasticity; (3) a red foliated chaotic breccia where the foliations wrap around cm-scale clasts of wall rock and, (4) a red crackle breccia with large, elongate wall-rock lenses. Localised pods of the red foliated chaotic breccia are found within the blue clay at the contact but overall, the units remain unmixed. Not every unit is continuous along-strike and each unit varies in thickness. While the fault core varies in thickness, the overall structure of the fault does not change, i.e. localisation occurs within a single fault core strand, separated by a damage zone on either side (the Dalradian and Highland Border Ophiolite respectively), at all studied locations along the fault.

**RQ2: How does the internal structure of the HBF vary spatially (in present space) and temporally (through time)? What implications does this have for the mechanical properties of the fault and its ability to host earthquakes through time?**

Detailed structural logs demonstrate that the internal structure of the Highland Boundary fault core varies in thickness and composition along strike over centimetre to metre length scales in present space. Earthquake rupture mechanics critically depend on the physical properties of fault rock assemblages. Therefore, models that investigate rupture propagation at active plate boundaries should incorporate, or else assess tolerance and sensitivity to, spatially variable fault core thickness and composition.

Based on detailed microstructural and XRD observations, a multi-event evolution of the Highland Boundary fault core is proposed. The observations suggest that both wall rocks are incorporated into the fault core through a range of chemical and physical processes responsible for grain size reduction and wall rock comminution in a fault zone. Field observations suggest as the fault core units formed at different stages of faulting and by different mechanisms, they remained distinct. The red foliated chaotic breccia formed first from mechanical processing, i.e., plucking, abrasion and wear of the Dalradian wall rock during slip. The blue gouge formed later due to fluid-derived, chemical alteration of serpentinitic wall rocks along shear fractures. The blue gouge is more clay-rich, and hence weaker than the red, leading to strain localisation. This multi-event evolution caused the mechanical properties of the Highland Boundary fault core to vary through time, becoming either stronger or weaker with each deformation phase. In turn, this will have affected the fault's ability to host earthquakes of different sizes through time.

**RQ3: How comparable is the internal structure of the HBF to other plate boundary faults?**

All the observations of plate boundary faults compiled in Chapter 4 have a comparable fault core thickness ranging between 0.07 and ~35 m. They are anomalously narrow compared to intraplate faults of the same offset. Plate boundary faults remain narrow regardless of how many slip events they have experienced or their local fault structure (fault core composition, host rock juxtaposition, slip direction, fault type, and/or the number of fault core strands). For all the plate boundary faults where observations were made at more than one point, local fault structure varies but remains comparatively narrow.

**RQ4: Do plate boundary and intraplate faults evolve similarly with repeated slip events (and hence earthquakes)?**

Plate boundary and intraplate faults evolve differently with displacement. Intraplate faults get thicker and develop more complex geometries with increasing total

displacement. Plate boundary faults are anomalously narrow by comparison to intraplate faults and remain narrow regardless of how much total displacement (and hence slip events and/or earthquakes) they have experienced or the local structure of the fault.

**RQ5: Do plate boundary faults and intraplate faults radiate energy and process intact rocks the in same way during seismic events?**

For a given value of displacement in an individual earthquake, plate boundary fault earthquakes typically have a greater seismic moment (and hence earthquake magnitude) than intraplate events. It is proposed that this occurs because plate boundary faults are anomalously narrow, they are comparatively smooth, and terminate at triple junctions rather than intact rock. Since the data show they do not increase in thickness with increasing displacement, they are not processing intact rock as much during seismic events. Thus, plate boundary faults do not dissipate as much energy as intraplate faults during earthquakes meaning that for a given value of average displacement, more energy is radiated to the surface resulting in higher magnitude earthquakes. By contrast, intraplate faults dissipate more energy and get thicker as fault slip increases, generating complex zones of damage in the surrounding rock and propagating through linkage with neighboring structures. The more complex the fault geometry, the more energy has to be consumed at depth during an earthquake and the less energy reaches the surface.

**RQ6: How do plate boundary fault cores evolve and why?**

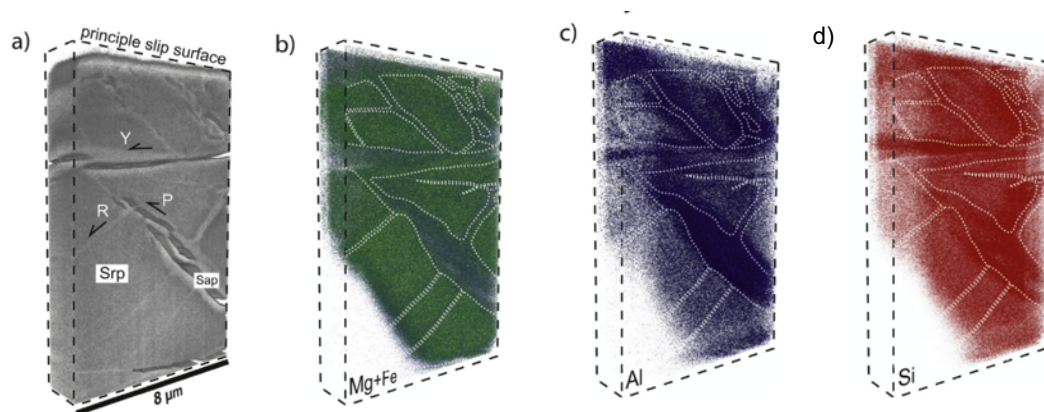
While we are a long way off from fully answering this question, the findings presented in this thesis advance our understanding of the internal structure and evolution of plate boundary fault cores. Importantly, they are dissimilar to intraplate faults and do not evolve in the same way with repeated slip events. These findings have implications for understanding how earthquakes behave. This work raised some interesting questions and discussion, however, in the absence of detailed geochemistry and mechanical testing further work is required. See Chapter 7 for suggestions.

## Chapter 7 – Future Work

This chapter outlines some suggestions for future work.

### 1. 3D Microstructural Studies

The observations presented in Chapter 5 describe the 2D nature of the HBF fault core microstructures and microchemistry from the hand-specimen scale down to the microscopic scale. However, in order to reconstruct the 3D microstructural and microchemical features over the range of nanometres to tens of micrometres, a focused ion beam-scanning electron microscopy (FIB-SEM) study, similar to ones on the San Andreas fault gouge (Warr *et al.* 2014), is suggested. This technique combines the imaging capabilities of modern field-emission SEM (resolution < 2 nm) with the polishing and milling powder of FIB. The SEM is also equipped with Energy Dispersive X-ray spectrometry (EDX) analyses for elemental mapping (**Fig. 7.1a-d**). This type of study would provide new insights about clay creep mechanisms and fabric evolution from the crystal lattice-scale to the scale of clay shear fabrics.



**Fig. 7.1** Example of 3D reconstructions of FIB slices from the San Andreas fault gouge. Clay shear fabrics are observed. **a)** Back scattered electron image. **b)** EDX mapping of Mg (green) + Fe (blue). **c)** EDX mapping of Al. **d)** EDX mapping of Si. In all EDX plots, the darker more intense colouration is of areas of greater elemental concentrations. Figure from Warr *et al.* (2014). Refer to the original paper for more information.

## 2. Argon Radiometric Dating

The XRD data presented in Chapter 5 (**Table 5.4**) confirm that datable fault-derived illite (1M<sub>d</sub> polytype) is found within both the blue gouge and red foliated chaotic breccia, albeit of a higher abundance in the latter. The models in **Fig. 5.13** and **Fig. 6.6** provide relative timings of events from field and microstructural evidence. The exact timing of clay growth and the nature of the fluid responsible for neomineralisation during faulting is unclear from field and microstructural evidence alone. One approach to constrain the timing of clay growth, and hence strike-slip faulting, would be to date the illitic clay via  $^{40}\text{Ar}/^{39}\text{Ar}$ , or  $^{40}\text{K}/^{40}\text{Ar}$  radiometric dating. The half-lives are  $1269 \pm 13$  Ma and 1250 Ma, respectively (Kelley 2002).

Previous studies have reliably constrained the timing and origin of illitic fault gouge at other plate boundary faults through  $^{40}\text{Ar}/^{39}\text{Ar}$  geochronology (e.g. the North Anatolian fault [Boles *et al.* 2015] and Alpine fault [Ring *et al.* 2017]). Kemp *et al.* (2019), successfully dated fault gouge from the Sronlairig Fault, a subvertical fault that splays of the Great Glen Fault GGF, using  $^{40}\text{K}/^{40}\text{Ar}$  geochronology. Like the HBF, the Great Glen Fault is another major terrane bounding fault in Scotland that formed during the Caledonian Orogeny. The gouge recovered from the Sronlairig Fault has remarkable similarities to the blue gouge of the HBF with an overall sinistral strike-slip sense of motion (G. Leslie, pers. comm. 2021).  $^{40}\text{K}/^{40}\text{Ar}$  geochronology revealed a Carboniferous age for the Sronlairig gouge (Kemp *et al.* 2019). Given the similarities in both gouges, it would not be surprising if the blue gouge of the HBF has a similar Carboniferous age.

The working hypothesis is presented in Section 5.7.1, where the blue gouge has a younger age than the red foliated chaotic breccia as a result of distinct events, meaning that the mechanical properties of the fault have changed through time (**Fig. 5.13**). If this model is proved true by radiometric dating, then the bulk properties changed as the fault grew, and the earthquakes produced from slip along the fault may also have evolved in size and radiated energy (damage) through time. Alternatively, but unlikely given they are unmixed and have distinct chemical and mechanical properties, both



units have the same age. Regardless of the result, dating the HBF fault core will be significant for understanding the tectonic evolution, and if very young neotectonics, of the British Isles.

### 3. Oxygen and Hydrogen Isotopes

In addition to constraining the timing of clay authigenesis through argon radiometric dating, oxygen and hydrogen isotopic analyses on each of the size fractions could be conducted. This would yield information on the source and temperature of the fluid(s) forming the clay and help constrain how and why the HBF fault core evolved. The hypothesis is presented in **Fig. 5.13**, where the blue gouge forms from the fluid-assisted, chemical breakdown of serpentinitic wall rocks. The alteration of serpentinite to clay is a process favoured by alkaline, hydrous fluids (Moore and Lockner, 2013), whereby pH conditions ( $>10$ ), characteristic of groundwaters associated with ultramafic bodies, are required for the dissolution and transport of aluminium and silica required for clay growth. The illite-smectite mineralogy presented in **Table 3.2** suggests the clays formed from a low temperature fluid at  $100^{\circ}\text{C}$ - $110^{\circ}\text{C}$ . No fluid is required for the mechanical breakdown of the Dalradian via grinding and plucking into the red foliated chaotic breccia. Combining oxygen and hydrogen isotopes with the argon radiometric dating will offer vital insights to particular stages of fault evolution and help unravel the sequence of tectono-thermal events on the HBF.

### 4. Experimental Deformation Experiments

In order to determine the mechanical properties of the HBF fault core units several experimental deformation studies could be carried out. These include rotary shear experiments to measure the frictional properties of the HBF fault rocks. To the best of my knowledge no experimental deformation studies exist on ophicarbonates. This would allow the true friction of coefficient values to be added to **Fig. 5.13**, which is currently hypothesised based on values from the literature and field observations.

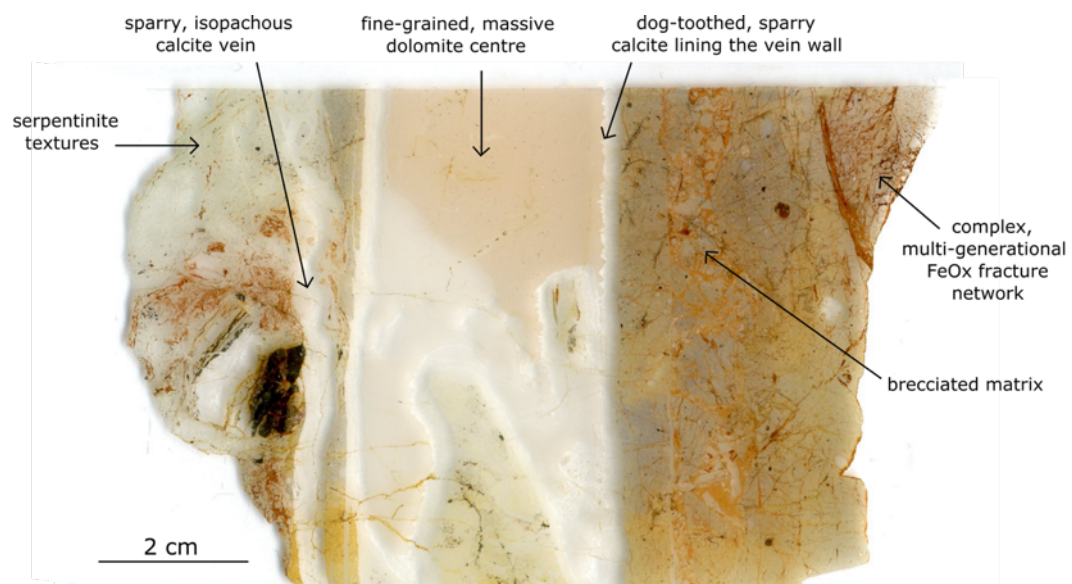
As a follow up to the microstructural observations presented in Chapter 5, low to high velocity rotary shear experiments, similar to those in Bullock *et al.* (2015), could be

carried out on the HBF fault core units to assess how grain- and aggregate-scale deformation mechanisms influence frictional behaviour. For example, experiments could be terminated at three different stages to enable systematic sampling and observation of microstructural evolution during slip. The three stages could be: stage (1) after the application of a normal load prior to shearing, stage (2) on attainment of peak friction, before slip weakening has occurred; and (3) on attainment of steady state friction, subsequent to weakening. Given that clay minerals display different frictional behaviours when they wet compared to a dry state (e.g., Behnsen and Faulkner, 2012), experiments should also be performed under room humidity (dry) and water-saturated conditions. For instance, Bullock *et al.* (2015) demonstrated that given their interconnected network of fabrics, slip does not become localised in wet clay-bearing gouges. Wet clay-bearing gouges have low friction values, which in turn, will reduce the amount of frictional heat generated. In contrast, in the dry gouges cataclasis must occur before slip can localise and trigger dynamic weakening, and thus, dry gouges have a greater resistance to frictional sliding than wet gouges (Bullock *et al.* 2015). This type of study would allow an assessment of how microstructures observed in the HBF fault core units affect slip behaviour and potentially provide information on slip weakening mechanisms during past earthquakes. In addition, measurement of the shear strength and plasticity (as described in Reeves *et al.* (2006)) of the HBF fault core clays would allow the concepts of soil mechanics to be applied to the study of the fault slip mechanisms.

### 5. 2D and 3D Microstructural Studies of the Damage Zone/Host Rock

Following on from the microstructural study of the clay-rich fault core in Chapter 5, 2D and 3D microstructural studies (thin section and SEM analysis, respectively) could be carried out on the damage zone/host rocks in order to better constrain the deformation history of the HBF. In particular these studies of slip mechanisms ideally should be constrained by understanding the stress that a fault was under at the time of slip, ambient temperature and fluid pressures/compositions. One particular example could be a detailed microstructural study of the multiphase carbonate veins described in Section 3.5. The formation and composition of veins and deformation mechanisms

operative in the vein material can inform about stress conditions, fluid sources and circulation, and chemical alteration processes (e.g., Gratier *et al.* 2003; Ferrill *et al.* 2004). For instance, the dog-toothed, sparry calcite lining the vein wall (**Fig. 7.2**) has mechanical twins. The thickness and morphology of the calcite twins can be used as a geothermometer for low-grade metamorphic conditions (c.f. Ferrill *et al.*, 2004). Vein systems in tectonically active regions record multiple episodes of fault reactivation manifested by crack-seal extension veins (c.f. Ramsay 1980). Therefore, a detailed microstructural study of these multiphase carbonate veins may inform us of any reactivation of the HBF and thus, better constrain the timing of subsequent clay authigenesis.



**Fig. 7.2.** Thin section showing the multiphase carbonate vein in ophi-carbonate.

## 6. Carbonate Clumped Isotope Thermometry on the Highland Border Ophiolite (Footwall Damage Zone)

Carbonate clumped isotope thermometry is a powerful technique for reconstructing the thermal history of carbonate minerals and fluids in geodynamic, structural, topographic and basin evolution models (Eiler 2011; Huntington & Lechler 2015 and references therein). The thermometer is based on how the various isotopes of carbon ( $^{12}\text{C}$ ,  $^{13}\text{C}$ ) and oxygen ( $^{16}\text{O}$ ,  $^{17}\text{O}$ ,  $^{18}\text{O}$ ) are distributed in the lattice of the carbonate

crystal (with a mass of 47,  $\Delta 47$ ). It measures the degree to which the heavy, rare isotopes ( $^{13}\text{C}$  and  $^{18}\text{O}$ ) bond with, or near, each other relative to the more abundant light isotopes ( $^{12}\text{C}$  and  $^{16}\text{O}$ ) (Ghosh *et al.* 2006; Schauble *et al.* 2006; Eiler 2011). This “clumping” of heavy isotopes is temperature dependent and thus records the temperature of mineral formation (Schauble *et al.* 2006). Clumped isotopes are measured simultaneously with conventional measurements of carbonate  $\delta^{13}\text{C}$  and  $\delta^{18}\text{O}$  values, which together constrain the isotopic composition of the parent water from which the carbonate grew. These techniques can help constrain paleoenvironmental conditions or basin temperatures and fluid sources. Clumped isotope thermometry and  $\delta^{13}\text{C}$ -  $\delta^{18}\text{O}$  compositions have successfully been applied to constrain the origin of paleofluids responsible for carbonate vein formation in samples recovered from the San Andreas fault (Luetkemeyer *et al.* 2016). The preliminary carbonate  $\delta^{13}\text{C}$  and  $\delta^{18}\text{O}$  values discussed in Chapter 6 give a testable hypothesis for clumped isotopes: the ophicarbonates formed from marine waters at  $100^\circ\text{C}$ , while the carbonated serpentinite formed from magmatic water at  $220^\circ\text{C}$  (**Fig. 6.5**).

### 7. Calcite Dating of the Highland Border Ophiolite

In addition to constraining the source and temperature of paleofluids from clumped isotope thermometry, the calcite could also be dated using the new image-based, uranium-lead (U-Pb) method developed by Dave Chew’s research group at Trinity College Dublin. The approach involves identifying and mapping zones with a high U/Pb ratio by laser ablation inductively coupled plasma mass spectrometry (LA-ICPMS). This avoids the problems of low uranium contents and/or high initial lead in calcite/dolomite that have hindered previous approaches of U-Pb calcite dating. This new U-Pb image mapping approach is advantageous as it spatially links age information with compositional, textural or structural features determined from scanning-electron microscopy (SEM) images or elemental maps. Detailed SEM and thin section analysis would be a prerequisite for this work.

### 8. Detailed Field Mapping of the Dalradian Damage Zone

Similar to the fault core mapping in Chapter 3, detailed field mapping via the use of structural logs could be carried out on the Dalradian wall rocks. This would better constrain the along-strike variation in damage zone thickness as currently there is only one measurement from Log 3 (*Fig. 3.2*). This could then be added to a compilation of damage zone thickness data from the literature to assess if, in comparison to intraplate faults, plate boundary faults also have a narrow damage zone. The Dalradian north of the HBF is intensely fractured. Natural fracture networks exert a strong control on the hydro-geological and mechanical properties of a rock mass and are useful indicators of paleo-stress directions (Andrews *et al.* 2019). Therefore, fracture mapping, similar to that described in Andrews *et al.* (2019), would be useful for constraining the overall structural evolution of the HBF.

### 9. Field Mapping of Other Locations Along the HBF

For reasons explained in Chapter 2, this study only samples a tiny 560 m section, and thus a tiny part of any palaeo-rupture events, along this >240 km long past seismogenic plate boundary fault. 560 m is only equal to a quarter of a seismic wave (Wells & Coppersmith 1994). Detailed field mapping could be carried out at several other sections of the HBF (e.g., Balmaha, Innellan) to investigate what happens at the continental scale. At Balmaha the host rock juxtapositions are different from those at Stonehaven. If the fault core could be exposed it can therefore be examined to what extent the host rock juxtapositions have on the fault core thickness, composition and strength. For example, if the fault juxtaposes quartz-rich Old Red Sandstone (as at Balmaha) then the resulting fault rock composition will be different, the fault core will have been stronger, and the resulting earthquakes will have been different.

### 10. A Comparison of Plate Boundary Fault and Intraplate Fault Geometry

Finally, while the compiled dataset in *Table 4.3* demonstrates that there is a statistically significant relationship between total fault displacement and fault complexity (steps per unit length) additional literature reviews and comparative studies are required to validate this working hypothesis. This is highly recommended as there are currently

no studies in the literature that examine the difference(s) between plate boundary and intraplate fault core complexity.

# References

## Journals and Books

- Ampuero, J.-P. & Ben-Zion, Y. 2008. Cracks, pulses and macroscopic asymmetry of dynamic rupture on a bimaterial interface with velocity-weakening friction. *Geophysical Journal International*, **173**, 674–692, <https://doi.org/10.1111/j.1365-246X.2008.03736.x>.
- Andersen, T.B., Torsvik, T.H., Eide, E.A., Osmundsen, P.T. & Faleide, J.I. 1999. Permian and Mesozoic extensional faulting within the Caledonides of central south Norway. *Journal of the Geological Society*, **156**, 1073–1080, <https://doi.org/10.1144/gsjgs.156.6.1073>.
- Andrews, B., Roberts, J., Shipton, Z., Bigi, S., Chiara Tartarello, M. & Johnson, G. 2019. How do we see fractures? Quantifying subjective bias in fracture data collection. *Solid Earth*, **10**, 487–516, <https://doi.org/10.5194/se-10-487-2019>.
- Andrews, D.J. 2005. Rupture dynamics with energy loss outside the slip zone. *Journal of Geophysical Research: Solid Earth*, **110**, 1–14.
- Aochi, H. & Madariaga, R. 2003. The 1999 Izmit, Turkey, earthquake: Nonplanar fault structure, dynamic rupture process, and strong ground motion. *Bulletin of the Seismological Society of America*, **93**, 1249–1266, <https://doi.org/10.1785/0120020167>.
- Armijo, R., Meyer, B., Hubert, A. & Barka, A. 1999. Westward propagation of the North Anatolian fault into the northern Aegean: Timing and kinematics. *Geology*, **27**, 267–270.
- Aydin, A. & Du, Y.. 1995. Surface Rupture at a Fault Bend - the 28-June-1992 Landers, California, Earthquake. *Bulletin of the Seismological Society of America*, **85**, 111–128.

- Bacon, S.N. & Pezzopane, S.K. 2007. A 25,000-year record of earthquakes on the Owens Valley fault near Lone Pine, California: Implications for recurrence intervals, slip rates, and segmentation models. *GSA Bulletin*, **119**, 823–847, <https://doi.org/10.1130/B25879.1>.
- Barka, A.A. 1996. Slip distribution along the north anatolian fault associated with the large earthquakes of the period 1939 to 1967. *Bulletin of the Seismological Society of America*, **86**, 1238–1254.
- Barka, A.A. & Kadinsky-Cade, K. 1988. Strike-slip fault geometry in Turkey and its influence on earthquake activity. *Tectonics*, **7**, 664–684.
- Barth, N.C., Boulton, C., Carpenter, B.M., Batt, G.E. & Toy, V.G. 2013. Slip localization on the southern Alpine Fault New Zealand. *Tectonics*, **32**, 620–640, <https://doi.org/10.1002/tect.20041>.
- Bastesen, E. & Braathen, A. 2010. Extensional faults in fine grained carbonates - analysis of fault core lithology and thickness-displacement relationships. *Journal of Structural Geology*, **32**, 1609–1628, <https://doi.org/10.1016/j.jsg.2010.09.008>.
- Bastesen, E., Braathen, A. & Skar, T. 2013. Comparison of scaling relationships of extensional fault cores in tight carbonate and porous sandstone reservoirs. *Petroleum Geoscience*, **19**, 385–398, <https://doi.org/10.1144/petgeo2011-020>.
- Behnsen, J. & Faulkner, D.R. 2012. The effect of mineralogy and effective normal stress on frictional strength of sheet silicates. *Journal of Structural Geology*, **42**, 49–61, <https://doi.org/10.1016/j.jsg.2012.06.015>.
- Bluck, B.J. 1985. The Scottish paratectonic Caledonides. *Scottish Journal of Geology*, **21**, 437–464.
- Bluck, B.J. 2002. The Midland Valley terrane. In: Trewin, N. H. (ed.) *The Geology of Scotland*. Geological Society London, 149–166.



- Boles, A., van der Pluijm, B.A., Mulch, A., Mutlu, H., Uysal, I.T. & Warr, L.N. 2015. Hydrogen and  $^{40}\text{Ar}/^{39}\text{Ar}$  isotope evidence for multiple and protracted paleofluid flow events within the long-lived North Anatolian Keirogen (Turkey). *Geochemistry, Geophysics, Geosystems*, **16**, 1975–1987, <https://doi.org/10.1002/2015GC005810>.
- Bond, C.E., Shipton, Z.K., Jones, R.R., Butler, R.W.H. & Gibbs, A.D. 2007. Knowledge transfer in a digital world: Field data acquisition, uncertainty, visualization, and data management. *Geosphere*, **3**, 568–576, <https://doi.org/10.1130/GES00094.1>.
- Bormann, P., Wendt, S. & Di Giacomo, D. 2013. Seismic Sources and Source Parameters. In: Bormann, P. (ed.) *New Manual of Seismological Observatory Practice 2 (NMSOP2)*. Pastdam, Deutsches GeoForschungsZentrum GFZ, 1–259., [https://doi.org/10.2312/GFZ.NMSOP-2\\_ch3](https://doi.org/10.2312/GFZ.NMSOP-2_ch3).
- Boschi, C., Dini, A., Dallai, L., Ruggieri, G. & Gianelli, G. 2009. Enhanced  $\text{CO}_2$ -mineral sequestration by cyclic hydraulic fracturing and Si-rich fluid infiltration into serpentinites at Malentrata (Tuscany, Italy). *Chemical Geology*, **265**, 209–226, <https://doi.org/10.1016/j.chemgeo.2009.03.016>.
- Boullier, A.M., Yeh, E.C., Boutareaud, S., Song, S.R. & Tsai, C.H. 2009. Microscale anatomy of the 1999 Chi-Chi earthquake fault zone. *Geochemistry, Geophysics, Geosystems*, **10**, 1–25, <https://doi.org/10.1029/2008GC002252>.
- Boulton, C., Moore, D.E., Lockner, D.A., Toy, V.G., Townend, J. & Sutherland, R. 2014. Frictional properties of exhumed fault gouges in DFDP-1 cores, Alpine Fault, New Zealand. *Geophysical Research Letters*, **41**, 356–362, <https://doi.org/10.1002/2013GL058236>.
- Boutareaud, S., Calugaru, D.G., Han, R., Fabbri, O., Mizoguchi, K., Tsutsumi, A. & Shimamoto, T. 2008. Clay-clast aggregates: A new textural evidence for seismic fault sliding? *Geophysical Research Letters*, **35**, 1–5, <https://doi.org/10.1029/2007GL032554>.

- Boutareaud, S., Boullier, A.-M., Andréani, M., Calugaru, D.-G., Beck, P., Song, S.-R. & Shimamoto, T. 2010. Clay clast aggregates in gouges: New textural evidence for seismic faulting. *Journal of Geophysical Research*, **115**, 1–15, <https://doi.org/10.1029/2008JB006254>.
- Bradbury, K.K., Evans, J.P., Chester, J.S., Chester, F.M. & Kirschner, D.L. 2011. Lithology and internal structure of the San Andreas fault at depth based on characterization of Phase 3 whole-rock core in the San Andreas Fault Observatory at Depth (SAFOD) borehole. *Earth and Planetary Science Letters*, **310**, 131–144, <https://doi.org/10.1016/j.epsl.2011.07.020>.
- Bradbury, K.K., Davis, C.R., Shervais, J.W., Janecke, S.U. & Evans, J.P. 2014. Composition, Alteration, and Texture of Fault-Related Rocks from Safod Core and Surface Outcrop Analogs: Evidence for Deformation Processes and Fluid-Rock Interactions. *Pure and Applied Geophysics*, **172**, 1053–1078, <https://doi.org/10.1007/s00024-014-0896-6>.
- Brankman, C.M. & Aydin, A. 2004. Uplift and contractional deformation along a segmented strike-slip fault system: the Gargano Promontory, southern Italy. *Journal of Structural Geology*, **26**, 807–824, <https://doi.org/10.1016/j.jsg.2003.08.018>.
- Brantut, N. & Platt, J.D. 2017. Dynamic Weakening and the Depth Dependence of Earthquake Faulting. In: Thomas, M. Y., Mitchell, T. M. & Bhat, H. S. (eds) *Fault Zone Dynamic Processes: Evolution of Fault Properties During Seismic Rupture*.
- Brodsky, E.E. & Kanamori, H. 2001. Elastohydrodynamic lubrication of faults. *Journal of Geophysical Research*, **106**, 16,357-16,374.
- Brodsky, E.E., Gilchrist, J.J., Sagy, A. & Collettini, C. 2011. Faults smooth gradually as a function of slip. *Earth and Planetary Science Letters*, **302**, 185–193, <https://doi.org/10.1016/j.epsl.2010.12.010>.

- Bullock, R.J., De Paola, N. & Holdsworth, R.E. 2015. An experimental investigation into the role of phyllosilicate content on earthquake propagation during seismic slip in carbonate faults. *Journal of Geophysical Research: Solid Earth*, **120**, 3187–3207, <https://doi.org/10.1002/2015JB011914>. Received.
- Byerlee. 1978. Friction of Rocks. *Pure Applied Geophysics*, **116**, 615–626.
- Byrne, D.E., Davis, D.M. & Sykes, L.. 1988. Loci and maximum size of thrust earthquakes and the mechanics of the shallow region of subduction zones. *Tectonics*, **7**, 833–857.
- Caine, J.S., Evans, J.P. & Forster, C.B. 1996. Fault zone architecture and permeability structure. *Geology*, **24**, 1025–1028, [https://doi.org/10.1130/0091-7613\(1996\)024<1025](https://doi.org/10.1130/0091-7613(1996)024<1025).
- Caine, J.S., Bruhn, R.L. & Forster, C.B. 2010. Internal structure, fault rocks, and inferences regarding deformation, fluid flow, and mineralization in the seismogenic Stillwater normal fault, Dixie Valley, Nevada. *Journal of Structural Geology*, **32**, 1576–1589, <https://doi.org/10.1016/j.jsg.2010.03.004>.
- Callahan, O.A., Eichhubl, P., Olson, J.E. & Davatzes, N.C. 2019. Fracture Mechanical Properties of Damaged and Hydrothermally Altered Rocks, Dixie Valley-Stillwater Fault Zone, Nevada, USA. *Journal of Geophysical Research: Solid Earth*, **124**, 4069–4090, <https://doi.org/10.1029/2018JB016708>.
- Carpenter, B.M., Kitajima, H., Sutherland, R., Townend, J., Toy, V.G. & Saffer, D.M. 2014. Hydraulic and acoustic properties of the active Alpine Fault, New Zealand: Laboratory measurements on DFDP-1 drill core. *Earth and Planetary Science Letters*, **390**, 45–51, <https://doi.org/10.1016/j.epsl.2013.12.023>.
- Cawood, P.A., Merle, R.E., Strachan, R.A. & Tanner, P.W.G. 2012. Provenance of the Highland Border Complex: constraints on Laurentian margin accretion in the Scottish Caledonides. *Journal of the Geological Society London*, **169**, 575–586, <https://doi.org/10.1144/0016-76492011-076>.

- Cembrano, J., González, G., Arancibia, G., Ahumada, I., Olivares, V. & Herrera, V. 2005. Fault zone development and strain partitioning in an extensional strike-slip duplex: A case study from the Mesozoic Atacama fault system, Northern Chile. *Tectonophysics*, **400**, 105–125, <https://doi.org/10.1016/j.tecto.2005.02.012>.
- Chester, F.M. & Logan, J.M. 1986. Implications for mechanical properties of brittle faults from observations of the Punchbowl fault zone, California. *Pure and Applied Geophysics*, **124**, 79–106, <https://doi.org/10.1007/BF00875720>.
- Chester, F.M., Evans, J.P. & Biegel, R.L. 1993. Internal Structure and Weakening Mechanisms of the San Andreas Fault. *Journal of Geophysical Research*, **98**, 771–786.
- Chester, F.M., Rowe, C.D., et al. 2013. Structure and Composition of the Plate-Boundary Slip Zone for the 2011 Tohoku-Oki Earthquake. *Science*, **342**, 1208–1211, <https://doi.org/10.1126/science.1242366>.
- Chester, J.S., Chester, F.M. & Kronenberg, A.K. 2005. Fracture surface energy of the Punchbowl fault, San Andreas system. *Nature*, **437**, 133–136, <https://doi.org/10.1038/nature03942>.
- Chevalier, M.-L., Tapponnier, P., Van Der Woerd, J., Ryerson, F.J., Finkel, R.C. & Li, H. 2012. Spatially constant slip rate along the southern segment of the Karakorum fault since 200 ka. *Tectonophysics*, **530–531**, 152–179, <https://doi.org/10.1016/j.tecto.2011.12.014>.
- Chew, D.M. 2003. Structural and stratigraphic relationships across the continuation of the Highland Boundary Fault in western Ireland. *Geological Magazine*, **140**, 73–85, <https://doi.org/10.1017/s0016756802007008>.
- Chew, D.M. & Stillman, C.J. 2009. Late Caledonian orogeny and magmatism. In: Holland, C. H. & Sanders, I. . (eds) *The Geology of Ireland*. Edinburgh, Dunedin Academic Press, 143–173.

- Chew, D.M. & Strachan, R.A. 2014. The Laurentian Caledonides of Scotland and Ireland. *In: Corfu, F., Gasser, D. & Chew, D. M. (eds) New Perspectives on the Caledonides of Scandinavia and Related Areas*. Geological Society London, Special Publications, 390, 45–91., <https://doi.org/10.1144/SP390.16>.
- Chew, David M., Daly, J.S., Magna, T., Page, L.M., Kirkland, C.L., Whitehouse, M.J. & Lam, R. 2010. Timing of ophiolite obduction in the Grampian orogen. *Bulletin of the Geological Society of America*, **122**, 1787–1799, <https://doi.org/10.1130/B30139.1>.
- Chew, D. M., Daly, J.S., Magna, T., Page, L.M., Kirkland, C.L., Whitehouse, M.J. & Lam, R. 2010. Timing of ophiolite obduction in the Grampian orogen. *Geological Society of America Bulletin*, **122**, 1787–1799, <https://doi.org/10.1130/B30139.1>.
- Childs, C. & Watterson, J. 1996. *A Model for the Structure and Development of Fault Zones*.
- Childs, C., Nicol, A., Walsh, J.J. & Watterson, J. 1996. Growth of vertically segmented normal faults. *Journal of Structural Geology*, **18**, 1389–1397.
- Childs, C., Manzocchi, T., Walsh, J.J., Bonson, C.G., Nicol, A. & Schöpfer, M.P.J. 2009. A geometric model of fault zone and fault rock thickness variations. *Journal of Structural Geology*, **31**, 117–127, <https://doi.org/10.1016/j.jsg.2008.08.009>.
- Childs, C., Holdsworth, R.E., Jackson, C.A.-L., Manzocchi, T., Walsh, J.J. & Yielding, G. 2017. Introduction to the geometry and growth of normal faults. *In: Childs, C., Holdsworth, R. E., Jackson, C. A.-L., Manzocchi, T., Walsh, J. J. & Yielding, G. (eds) The Geometry and Growth of Normal Faults*. Geological Society London, Special Publications, 439, 1–9., <https://doi.org/10.1144/SP439.24>.
- Cochard, A. & Rice, J.R. 2000. Fault rupture between dissimilar materials: Ill-

- posedness, regularization, and slip-pulse response. *Journal of Geophysical Research*, **105**, 25891–25907, <https://doi.org/10.1029/2000JB900230>.
- Cohee, B.P. & Beroza, G.C. 1994. Slip Distribution of the 1992 Landers Earthquake and Its Implications for Earthquake Source Mechanics. *Bulletin of the Seismological Society of America*, **84**, 692–712.
- Collettini, C., Viti, C., Smith, S.A.F. & Holdsworth, R.E. 2009a. Development of interconnected talc networks and weakening of continental low-angle normal faults. *Geology*, **37**, 567–570, <https://doi.org/10.1130/G25645A.1>.
- Collettini, C., Niemeijer, A., Viti, C. & Marone, C. 2009b. Fault zone fabric and fault weakness. *Nature*, **462**, 907–911, <https://doi.org/10.1038/nature08585>.
- Collettini, C., Tesei, T., Scuderi, M.M., Carpenter, B.M. & Viti, C. 2019. Beyond Byerlee friction, weak faults and implications for slip behavior. *Earth and Planetary Science Letters*, **519**, 245–263, <https://doi.org/10.1016/j.epsl.2019.05.011>.
- Cowie, P.A. & Scholz, C.H. 1992. *Physical Explanation for the Displacement-Length Relationship of Faults Using a Post-Yield Fracture Mechanics Model*.
- Curry, G.B. 1986. Fossils and tectonics along the Highland Boundary Fault in Scotland. *Journal of the Geological Society London*, **143**, 193–198.
- d'Alessio, M.A., Blythe, A.E. & Bürgmann, R. 2003. No frictional heat along the San Gabriel fault, California: Evidence from fission-track thermochronology. *Geology*, **31**, 541–544, [https://doi.org/10.1130/0091-7613\(2003\)031<0541:NFHATS>2.0.CO;2](https://doi.org/10.1130/0091-7613(2003)031<0541:NFHATS>2.0.CO;2).
- Dawers, N., Anders, M. & Scholz, C.H. 1993. Growth of normal faults: Displacement-length scaling. *Geology*, **21**, 1107–1110.
- de Jossineau, G. & Aydin, A. 2009. Segmentation along Strike-Slip Faults Revisited. *Pure and Applied Geophysics*, **166**, 1575–1594,

<https://doi.org/10.1007/s00024-009-0511-4>.

- Delogkos, E., Manzocchi, T., Childs, C., Camanni, G. & Roche, V. 2020. The 3D structure of a normal fault from multiple outcrop observations. *Journal of Structural Geology*, **136**, 1–18, <https://doi.org/10.1016/j.jsg.2020.104009>.
- Dewey, J.F. & Strachan, R.A. 2003. Changing Silurian – Devonian relative plate motion in the Caledonides : sinistral transpression to sinistral transtension. *Journal of the Geological Society London*, **160**, 219–229, <https://doi.org/10.1144/0016-764902-085>.
- Dibblee, T.W. 1989. The San Andreas Fault and major rock terranes of California displaced by it and its tectonics. In: *In: Baldwin, E., Jones & et al (eds) Annual Field Trip Guidebook*. South Coast Geological Society, 223–275.
- Dilek, Y. & Furnes, H. 2014. Ophiolites and their origins. *Elements*, **10**, 93–100, <https://doi.org/10.2113/gselements.10.2.93>.
- DiToro, G. & Pennacchioni, G. 2005. Fault plane processes and mesoscopic structure of a strong-type seismogenic fault in tonalites (Adamello batholith, Southern Alps). *Tectonophysics*, **402**, 55–80, <https://doi.org/10.1016/j.tecto.2004.12.036>.
- DiToro, G., Goldsby, D.L. & Tullis, T.E. 2004. Friction falls towards zero in quartz rock as slip velocity approaches seismic rates. *Nature*, **427**, 436–439, <https://doi.org/10.1038/nature02249>.
- DiToro, G., Hirose, T., Nielsen, S., Pennacchioni, G. & Shimamoto, T. 2006. Natural and Experimental Evidence of Melt Lubrication of Faults During Earthquakes. *Science*, **311**, 647–649, <https://doi.org/10.1038/nature02249>.
- DiToro, G., Han, R., et al. 2011. Fault lubrication during earthquakes. *Nature*, **471**, 494–498, <https://doi.org/10.1038/nature09838>.
- Dolan, J.F. & Haravitch, B.D. 2014. How well do surface slip measurements track slip at depth in large strike-slip earthquakes? The importance of fault structural

- maturity in controlling on-fault slip versus off-fault surface deformation. *Earth and Planetary Science Letters*, **388**, 38–47, <https://doi.org/10.1016/j.epsl.2013.11.043>.
- Dor, O., Rockwell, T.K. & Ben-Zion, Y. 2006. Geological Observations of Damage Asymmetry in the Structure of the San Jacinto, San Andreas and Punchbowl Faults in Southern California: A Possible Indicator for Preferred Rupture Propagation Direction. *Pure and Applied Geophysics*, **163**, 301–349, <https://doi.org/10.1007/s00024-005-0023-9>.
- Dor, O., Yildirim, C., Rockwell, T.K., Ben-Zion, Y., Emre, O., Sisk, M. & Duman, T.Y. 2008. Geological and geomorphologic asymmetry across the rupture zones of the 1943 and 1944 earthquakes on the North Anatolian Fault: possible signals for preferred earthquake propagation direction. *Geophysical Journal International*, **173**, 483–504, <https://doi.org/10.1111/j.1365-246X.2008.03709.x>.
- Eiler, J.M. 2011. Paleoclimate reconstruction using carbonate clumped isotope thermometry. *Quaternary Science Reviews*, **30**, 3575–3588, <https://doi.org/10.1016/j.quascirev.2011.09.001>.
- Elmore, R.D., Parnell, J., Engel, M.H., Baron, M., Woods, S., Abraham, M. & Davidson, M. 2002. Palaeomagnetic dating of fluid-flow events in dolomitized rocks along the Highland Boundary Fault, central Scotland. *Geofluids*, **2**, 299–314, <https://doi.org/10.1046/j.1468-8123.2002.00045.x>.
- Escartín, J., Hirth, G. & Evans, B. 2001. Strength of slightly serpentinized peridotites: Implications for the tectonics of oceanic lithosphere. *Geology*, **29**, 1023–1026.
- Evans, J.P. 1990. Thickness-displacement relationships for fault zones. *Journal of Structural Geology*, **12**, 1061–1065.
- Fagereng, Å. & Toy, V.G. 2011. Geology of the earthquake source: An introduction.



- Geological Society Special Publication*, **359**, 1–16,  
<https://doi.org/10.1144/SP359.1>.
- Faulkner, D.R., Lewis, A.C. & Rutter, E.H. 2003. On the internal structure and mechanics of large strike-slip fault zones: Field observations of the Carboneras fault in southeastern Spain. *Tectonophysics*, **367**, 235–251,  
[https://doi.org/10.1016/S0040-1951\(03\)00134-3](https://doi.org/10.1016/S0040-1951(03)00134-3).
- Faulkner, D.R., Mitchell, T.M., Rutter, E.H. & Cembrano, J. 2008. On the structure and mechanical properties of large strike-slip faults. *In*: Wibberley, C. A. J., Kurz, W., Imber, J., Holdsworth, R. E. & Collettini, C. (eds) *The Internal Structure of Fault Zone: Implications for Mechanical and Fluid-Flow Properties*. Geological Society London Special Publications 299, 139–150.,  
<https://doi.org/10.1144/SP299.9>.
- Faulkner, D.R., Jackson, C.A.L., Lunn, R.J., Schlische, R.W., Shipton, Z.K., Wibberley, C.A.J. & Withjack, M.O. 2010. A review of recent developments concerning the structure, mechanics and fluid flow properties of fault zones. *Journal of Structural Geology*, **32**, 1557–1575,  
<https://doi.org/10.1016/j.jsg.2010.06.009>.
- Ferri, F., Di Toro, G., Hirose, T. & Shimamoto, T. 2010. Evidence of thermal pressurization in high-velocity friction experiments on smectite-rich gouges. *Terra Nova*, **22**, 347–353, <https://doi.org/10.1111/j.1365-3121.2010.00955.x>.
- Ferrill, D.A., Morris, A.P., Evans, M.A., Burkhard, M., Groshong, R.H. & Onasch, C.M. 2004. Calcite twin morphology: a low-temperature deformation geothermometer. *Journal of Structural Geology*, **26**, 1521–1529,  
<https://doi.org/10.1016/j.jsg.2003.11.028>.
- Fossen, H. 2010. *Structural Geology*. Cambridge University Press.
- Fossen, H. 2020. Fault classification, fault growth and displacement. *In*: Scarselli, N., Adam, J., Chiarella, D., Roberts, D. G. & Bally, A. W. (eds) *Regional*

- Geology and Tectonics: Principles of Geologic Analysis*. Elsevier, 119–147.,  
<https://doi.org/10.1016/b978-0-444-64134-2.00007-9>.
- Fossen, H. & Rotevatn, A. 2016. Fault linkage and relay structures in extensional settings—A review. *Earth Science Reviews*, **154**, 14–28,  
<https://doi.org/10.1016/j.earscirev.2015.11.014>.
- Fossen, H., Khani, F., Faleide, J.I., Ksienzyk, A.K. & Dunlap, & W.J. 2016. Post-Caledonian extension in the West Norway-northern North Sea region: the role of structural inheritance. *In*: Childs, C., Holdsworth, R. E., Jackson, C. A.-L., Manzocchi, T., Walsh, J. J. & Yielding, G. (eds) *The Geometry and Growth of Normal Faults*. Geological Society London, Special Publications, 439, 1–22.,  
<https://doi.org/10.1144/SP439.6>.
- Foxford, K.A., Walsh, J.J., Watterson, J., Garden, I.R., Guscott, S.C. & Burley, S.D. 1998. Structure and content of the Moab Fault Zone, Utah, USA, and its implications for fault seal prediction. *In*: Jones, G., Fisher, Q. J. & Knipe, R. J. (eds) *Faulting, Fault Sealing and Fluid Flow in Hydrocarbon Reservoirs*. Geological Society London, Special Publications, 147, 87–103.,  
<https://doi.org/10.1144/GSL.SP.1998.147.01.06>.
- Frost, B.R. & Beard, J.S. 2007. On Silica Activity and Serpentinization. *Journal of Petrology*, **48**, 1351–1368, <https://doi.org/10.1093/petrology/egm021>.
- Fu, B. & Awata, Y. 2007. Displacement and timing of left-lateral faulting in the Kunlun Fault Zone, northern Tibet, inferred from geologic and geomorphic features. *Journal of Asian Earth Sciences*, **29**, 253–265,  
<https://doi.org/10.1016/j.jseas.2006.03.004>.
- Gabrielsen, R.H., Bratthen, A., Kjemperud, M. & Valdresbraten, M.L.R. 2016. The geometry and dimensions of fault-core lenses. *In*: Childs, C., Holdsworth, R. E., Jackson, C. A. L., Manzocchi, T., Walsh, J. J. & Yielding, G. (eds) *The Geometry and Growth of Normal Faults*. Geological Society London, Special Publications, 439.

- Ghosh, P., Adkins, J., et al. 2006. 13C-18O bonds in carbonate minerals: a new kind of paleothermometer. *Geochimica et Cosmochimica Acta*, **70**, 1439–1456.
- Giacco, F., Saggese, L., De Arcangelis, L., Lippiello, E. & Pica Ciamarra, M. 2015. Dynamic Weakening by Acoustic Fluidization during Stick-Slip Motion. *Physical Review Letters*, **115**, 1–5, <https://doi.org/10.1103/PhysRevLett.115.128001>.
- Gilbert, G.K. 1883. A theory of the earthquakes of the Great Basin, with a practical application. *Salt Lake City Tribune*, reprinted in the *American Journal of Science*, **27**, 49–53.
- Goldsby, D.L. & Tullis, T.E. 2002. Low frictional strength of quartz rocks at subseismic slip rates. *Geophysical Research Letters*, **29**, 1–4, <https://doi.org/10.1029/2002GL015240>.
- Goldsby, D.L. & Tullis, T.E. 2011. Flash Heating Leads to Low Frictional Earthquake Slip Rates. *Science*, **334**, 216–218.
- Grathoff, G.H., Moore, D.M., Hay, R.L. & Wimmer, K. 2001. Origin of illite in the Lower Paleozoic of the Illinois Basin: evidence for brine migration. *Geological Society of America Bulletin*, **113**, 1092–1104.
- Gratier, J.-P., Favreau, P. & Renard, F. 2003. Modeling fluid transfer along California faults when integrating pressure solution crack sealing and compaction processes. *Journal of Geophysical Research*, **108**, 1–25, <https://doi.org/10.1029/2001JB000380>.
- Gudmundsson, A., De Guidi, G. & Scudero, S. 2013. Length-displacement scaling and fault growth. *Tectonophysics*, **608**, 1298–1309, <https://doi.org/10.1016/j.tecto.2013.06.012>.
- Haines, S.H. & Van Der Pluijm, B.A. 2010. Dating the detachment fault system of the Ruby Mountains, Nevada: Significance for the kinematics of low-angle normal faults. *Tectonics*, **29**, 1–12, <https://doi.org/10.1029/2009TC002552>.

- Haines, S.H., Kaproth, B., Marone, C., Saffer, D.M. & Van Der Pluijm, B.A. 2013. Shear zones in clay-rich fault gouge : A laboratory study of fabric development and evolution. *Journal of Structural Geology*, **51**, 206–225, <https://doi.org/10.1016/j.jsg.2013.01.002>.
- Han, R. & Hirose, T. 2012. Clay-clast aggregates in fault gouge: An unequivocal indicator of seismic faulting at shallow depths? *Journal of Structural Geology*, **43**, 92–99, <https://doi.org/10.1016/j.jsg.2012.07.008>.
- Harte, B., Booth, J.E., Dempster, T.J., Fettes, D.J., Mendum, J.R. & Watts, D. 1984. Aspects of the post-depositional evolution of the Dalradian and Highland Boundary rocks in the southern Highlands of Scotland. *Transactions of the Royal Society of Edinburgh: Earth Sciences*, **75**, 151–163.
- Hauksson, E., Jones, L.M., Huiton, K. & Eberhart-Phillips, D. 1993. *The 1992 Landers Earthquake Sequence: Seismological Observations*, <https://doi.org/10.1029/93JB02384>.
- Heermance, R., Shipton, Z.K. & Evans, J.P. 2003. Fault structure control on fault slip and ground motion during the 1999 rupture of the Chelungpu fault, Taiwan. *Bulletin of the Seismological Society of America*, **93**, 1034–1050, <https://doi.org/10.1785/0120010230>.
- Heermance, R. V & Evans, J.P. 2006. Geometric evolution of the Chelungpu fault, Taiwan: the mechanics of shallow frontal ramps and fault imbrication. *Journal of Structural Geology*, **28**, 929–938, <https://doi.org/10.1016/j.jsg.2006.01.015>.
- Henderson, W.G., Tanner, P.W.G. & Strachan, R.A. 2009. The Highland Border Ophiolite of Scotland; observations from the Highland workshop field excursion of April 2008. *Scottish Journal of Geology*, **45**, 13–18, <https://doi.org/10.1144/0036-9276/01-381>.
- Hillier, S. 2003. Quantitative analysis of clay and other minerals in sandstones by X-ray powder diffraction (XRPD). In: RH, W. & S, M. (eds) *Clay Minerals in*

- Sandstones*. Association of Sedimentologists Special Publication 34, 213–251.
- Hirono, T., Yeh, E.-C., et al. 2007. Nondestructive continuous physical property measurements of core samples recovered from hole B, Taiwan Chelungpu-Fault Drilling Project. *Journal of Geophysical Research*, **112**, 7404, <https://doi.org/10.1029/2006JB004738>.
- Hirono, T., Tsuda, K., Tanikawa, W., Ampuero, J.-P., Shibasaki, B., Kinoshita, M. & Mori, J.J. 2016. Near-trench slip potential of megaquakes evaluated from fault properties and conditions. *Scientific Reports*, **6**, 1–13, <https://doi.org/10.1038/srep28184>.
- Hirose, T. & Shimamoto, T. 2005. Growth of molten zone as a mechanism of slip weakening of simulated faults in gabbro during frictional melting. *Journal of Geophysical Research*, **110**, 1–18, <https://doi.org/10.1029/2004JB003207>.
- Holdsworth, R.E., Van Diggelen, E.W.E., Spiers, C.J., De Bresser, J.H.P., Walker, R.J. & Bowen, L. 2011. Fault rocks from the SAFOD core samples: Implications for weakening at shallow depths along the San Andreas Fault, California. *Journal of Structural Geology*, **33**, 132–144, <https://doi.org/10.1016/j.jsg.2010.11.010>.
- Holdsworth, R E, Van Diggelen, E.W.E., Spiers, C.J., De Bresser, J.H.P., Walker, R.J. & Bowen, L. 2011. Fault rocks from the SAFOD core samples: Implications for weakening at shallow depths along the San Andreas Fault, California. *Journal of Structural Geology*, **33**, 132–144, <https://doi.org/10.1016/j.jsg.2010.11.010>.
- Horita, J. 2014. Oxygen and carbon isotope fractionation in the system dolomite-water-CO<sub>2</sub> to elevated temperatures. *Geochimica et Cosmochimica Acta*, **129**, 111–124.
- Hower, J., Hurley, P.M., Pinson, W.H. & Fairburn, H.. 1963. The dependence of K–Ar age on the mineralogy of various particle size ranges in a shale. *Geochimica*

- et Cosmochimica Acta*, **27**, 405–410.
- Hower, J., V. Eslinger, E., Hower, M.E. & Perry, E.A. 1976. Mechanism of burial metamorphism of argillaceous sediment: Mineralogical and chemical evidence. *GSA Bulletin*, **87**, 725–737.
- Hubert-Ferrari, A., Armijo, R., King, G., Meyer, B. & Barka, A. 2002. Morphology, displacement, and slip rates along the North Anatolian Fault, Turkey. *Journal of Geophysical Research: Solid Earth*, **107**, 1–33, <https://doi.org/10.1029/2001JB000393>.
- Huntington, K.W. & Lechler, A.R. 2015. Carbonate clumped isotope thermometry in continental tectonics. *Tectonophysics*, **647–648**, 1–20, <https://doi.org/10.1016/j.tecto.2015.02.019>.
- Hyndman, R., Yamano, M. & Oleskevich, D. 1997. The seismogenic zone of subduction thrust faults. *The Island Arc*, **6**, 244–260.
- Ikari, M.J., Saffer, D.M. & Marone, C. 2009. Frictional and hydrologic properties of clay-rich fault gouge. *Journal of Geophysical Research: Solid Earth*, **114**, 1–18, <https://doi.org/10.1029/2008JB006089>.
- Ikari, M.J., Niemeijer, A.R. & Marone, C. 2011. The role of fault zone fabric and lithification state on frictional strength, constitutive behavior, and deformation microstructure. *Journal of Geophysical Research*, **116**, 1–25, <https://doi.org/10.1029/2011JB008264>.
- Ikesawa, E., Sakaguchi, A. & Kimura, G. 2003. Pseudotachylyte from an ancient accretionary complex: Evidence for melt generation during seismic slip along a master décollement? *Geology*, **31**, 637–640, [https://doi.org/10.1130/0091-7613\(2003\)031<0637:PFAAAC>2.0.CO;2](https://doi.org/10.1130/0091-7613(2003)031<0637:PFAAAC>2.0.CO;2).
- Ikin, N.P. 1983. Petrochemistry and tectonic significance of the Highland Border Suite mafic rocks. *Journal of the Geological Society London*, **140**, 267–278, <https://doi.org/10.1144/gsjgs.140.2.0267>.

- Imber, J., Holdsworth, R.E., Smith, S. a. F., Jefferies, S.P. & Collettini, C. 2008. Frictional-viscous flow, seismicity and the geology of weak faults: a review and future directions. *Geological Society, London, Special Publications*, **299**, 151–173, <https://doi.org/10.1144/SP299.10>.
- Jachens, R.C., Langenheim, V.E. & Matti, J.C. 2002. Landers Fault Ruptures to Offsets on Neogene Faults and Distribution of Late Cenozoic Basins in the Eastern California Shear Zone. *Bulletin of the Seismological Society of America*, **92**, 1592–1605.
- Janssen, C., Wirth, R., et al. 2014. Faulting processes in active faults - Evidences from TCDP and SAFOD drill core samples. *Journal of Structural Geology*, **65**, 100–116, <https://doi.org/10.1016/j.jsg.2014.04.004>.
- Kanamori, H. & Anderson, D.L. 1975. Theoretical Basis of Some Empirical Relations in Seismology. *Bulletin of the Seismological Society of America*, **65**, 1073–1095.
- Kanamori, H. & Brodsky, E.E. 2001. The physics of earthquakes. *Physics Today*, **54**, 34–40, <https://doi.org/10.1063/1.1387590>.
- Kanamori, H. & Brodsky, E.E. 2004. The physics of earthquakes. *Reports on Progress in Physics*, **67**, 1429–1496, <https://doi.org/10.1088/0034-4885/67/8/R03>.
- Kanamori, R. & Rivera, L. 2006. Energy Partitioning During an Earthquake. In: Abercrombie, R., McGarr, A., Di Toro, G. & Kanamori, H. (eds) *Earthquakes: Radiated Energy and the Physics of Faulting*. American Geophysical Union. Washington D.C., 3–13.
- Kelley, D.S., Karson, J. a, et al. 2005. A Serpentinite-Hosted Ecosystem: The Lost City Hydrothermal Field. *Science*, **307**, 1428–1434, <https://doi.org/10.1126/science.1102556>.
- Kelley, S. 2002. K-Ar and Ar-Ar dating. In: *Noble Gases in Geochemistry and*

- Cosmochemistry*. Reviews in Mineralogy and Geochemistry, 785–818.,  
<https://doi.org/10.2138/rmg.2002.47.17>.
- Kemp, S.J., Gillespie, M.R., Leslie, G.A., Zwingmann, H., Diarmad, S. & Campbell, G. 2019. Clay mineral dating of displacement on the Sronlairig Fault: implications for Mesozoic and Cenozoic tectonic evolution in northern Scotland. *Clay Minerals*, **54**, 181–196, <https://doi.org/10.1180/clm.2019.25>.
- Keren, T.T. & Kirkpatrick, J.D. 2016. The damage is done: Low fault friction recorded in the damage zone of the shallow Japan Trench decollement. *Journal of Geophysical Research: Solid Earth*, **131**, 3804–3824, <https://doi.org/10.1002/2015JB012311>.
- Kirkpatrick, J.D. & Shipton, Z.K. 2009. Geologic evidence for multiple slip weakening mechanisms during seismic slip in crystalline rock. *Journal of Geophysical Research*, **114**, 1–14, <https://doi.org/10.1029/2008JB006037>.
- Kirkpatrick, J.D., Shipton, Z.K., Evans, J.P., Micklethwaite, S., Lim, S.J. & McKillop, P. 2008. Strike-Slip Fault Terminations at Seismogenic Depths: The Structure and Kinematics of the Glacier Lakes Fault, Sierra Nevada United States. *Journal of Geophysical Research*, **113**, 1–15, <https://doi.org/10.1029/2007JB005311>.
- Kirkpatrick, J.D., Shipton, Z.K. & Persano, C. 2009. Pseudotachylytes: Rarely Generated, Rarely Preserved, or Rarely Reported? *Bulletin of the Seismological Society of America*, **99**, 382–388, <https://doi.org/10.1785/0120080114>.
- Kirkpatrick, J.D., Rowe, C.D., White, J.C. & Brodsky, E.E. 2013. Silica gel formation during fault slip: Evidence from the rock record. *Geology*, **41**, 1015–1018, <https://doi.org/10.1130/G34483.1>.
- Kirkpatrick, J.D., Rowe, C.D., et al. 2015. Structure and lithology of the Japan Trench subduction plate boundary fault. *Tectonics*, **34**, 53–69, <https://doi.org/10.1002/2014TC003695>.



- Kirkpatrick, J.D., Shervais, K.A.H. & Ronayne, M.J. 2018. Spatial Variation in the Slip Zone Thickness of a Seismogenic Fault. *Geophysical Research Letters*, **45**, 7542–7550, <https://doi.org/10.1029/2018GL078767>.
- Knott, S.D., Beach, A., Brockbank, P.J., Lawson Brown, J., McCallum, J.E. & Welbon, A.I. 1996. Spatial and mechanical controls on normal fault populations. *Journal of Structural Geology*, **18**, 359–372.
- Lachenbruch, A.H. 1980. Frictional Heating, Fluid Pressure, and the Resistance to Fault Motion. *Journal of Geophysical Research*, **85**, 6097–6112.
- Langenheim, V.E., Grow, J.A., Jachens, R.C., Dixon, G.L. & Miller, J.J. 2001. Geophysical constraints on the location and geometry of the Las Vegas Valley Shear Zone, Nevada. *Tectonics*, **20**, 189–209, <https://doi.org/10.1029/1999TC001159>.
- Lawrence, R.D., Hasan Khan, S. & Nakata, T. 1992. Chaman fault, Pakistan-Afghanistan. *Annales Tectonicae*, **6**, 196–223.
- Lawther, S.E.M., Dempster, T.J., Shipton, Z.K. & Boyce, A.J. 2016. Effective crustal permeability controls fault evolution: An integrated structural, mineralogical and isotopic study in granitic gneiss, Monte Rosa, northern Italy. *Tectonophysics*, **690**, 160–173, <https://doi.org/10.1016/j.tecto.2016.07.010>.
- Le Breton, E., Cobbold, P.R. & Zanella, A. 2013. Cenozoic reactivation of the Great Glen Fault, Scotland: additional evidence and possible causes. *Journal of the Geological Society London*, **170**, 403–415, <https://doi.org/10.1144/jgs2012-067>.
- Le Pichon Aycy, X., Sengör, A.M.C., et al. 2001. The active Main Marmara Fault. *Earth and Planetary Science Letters*, **192**, 595–616.
- Leslie, A.G. 2009. Border skirmish. *Geoscientist*, **19**, 17–19.
- Li, C.-Y., Pang, J.-Z. & Zhang, Z.-Q. 2012. Characteristics, Geometry, and Segmentation of the Surface Rupture Associated with the 14 April 2010 Yushu

- Earthquake, Eastern Tibet, China. *Bulletin of the Geological Society of America*, **102**, 1618–1638, <https://doi.org/10.1785/0120110261>.
- Li, H., Si, J., et al. 2009. Co-seismic Rupture and Maximum Displacement of the 2008 Wenchuan Earthquake and its Tectonic Implications. *Quaternary Science*, **29**, 387–402.
- Li, H., Wang, H., et al. 2013. Characteristics of the fault-related rocks, fault zones and the principal slip zone in the Wenchuan Earthquake Fault Scientific Drilling Project Hole-1 (WFSD-1). *Tectonophysics*, **584**, 23–42, <https://doi.org/10.1016/j.tecto.2012.08.021>.
- Lin, A., Ouchi, T., Chen, A. & Maruyama, T. 2001. Co-seismic displacements, folding and shortening structures along the Chelungpu surface rupture zone occurred during the 1999 Chi-Chi (Taiwan) earthquake. *Tectonophysics*, **330**, 225–244.
- Little, T.A. 1995. Brittle deformation adjacent to the Awatere strike-slip fault in New Zealand: Faulting patterns, scaling relationships, and displacement partitioning. *GSA Bulletin*, **107**, 1255–1271.
- Lockner, D.A., Morrow, C., Moore, D. & Hickman, S. 2011. Low strength of deep San Andreas fault gouge from SAFOD core. *Nature*, **472**, 82–85, <https://doi.org/10.1038/nature09927>.
- Luetkemeyer, P.B., Kirschner, D.L., Huntington, K.W., Chester, J.S., Chester, F.M. & Evans, J.P. 2016. Constraints on paleofluid sources using the clumped-isotope thermometry of carbonate veins from the SAFOD (San Andreas Fault Observatory at Depth) borehole. *Tectonophysics*, **690**, 174–189, <https://doi.org/10.1016/j.tecto.2016.05.024>.
- Ma, K.-F., Mori, J., Lee, S.-J. & Yu, S.B. 2001. Spatial and Temporal Distribution of Slip for the 1999 Chi-Chi, Taiwan, Earthquake. *Bulletin of the Seismological Society of America*, **91**, 1069–1087.

- Ma, K.-F., Brodsky, E.E., Mori, J., Ji, C., Song, T.-R.A. & Kanamori, H. 2003. Evidence for fault lubrication during the 1999 Chi-Chi, Taiwan, earthquake (Mw7.6). *Geophysical Research Letters*, **30**, 1–4, <https://doi.org/10.1029/2002GL015380>.
- Madariaga, R., Ampuero, J.P. & Adda-Bedia, M. 2006. Seismic Radiation From Simple Models of Earthquakes. In: Abercrombie, R., McGarr, A., Di Toro, G. & Kanamori, H. (eds) *Earthquakes: Radiated Energy and the Physics of Faulting, Geophysical Monograph Series 170*. American Geophysical Monograph Series, 223–236., <https://doi.org/10.1029/170GM23>.
- Mai, P.M. & Beroza, G.C. 2002. A spatial random field model to characterize complexity in earthquake slip. *Journal of Geophysical Research: Solid Earth*, **107**, 1–21, <https://doi.org/10.1029/2001JB000588>.
- Manatschal, G. & Muntener, O. 2009. A type sequence across an ancient magma-poor ocean-continent transition: the example of the western Alpine Tethys ophiolites. *Tectonophysics*, **473**, 4–19, <https://doi.org/10.1016/j.tecto.2008.07.021>.
- Manighetti, I., Caulet, C., De Barros, L., Perrin, C., Cappa, F. & Gaudemer, Y. 2015. Generic along-strike segmentation of Afar normal faults, East Africa: Implications on fault growth and stress heterogeneity on seismogenic fault plates. *Geochemistry Geophysics Geosystems*, **15**, 443–467, <https://doi.org/10.1002/2014GC005684>.Key.
- Marrett, R. & Allmedinger, R.W. 1990. Kinematic analysis of fault-slip data. *Journal of Structural Geology*, **12**, 973–986.
- Marshak, S. 2001. *Earth: Portrait of a Planet*. W. W. Norton & Company.
- Masters, R.L., Ague, J.J. & Rye, D.M. 2000. An oxygen and carbon isotopic study of multiple episodes of fluid flow in the Dalradian and Highland Border Complex, Stonehaven, Scotland. *Journal of the Geological Society London*, **157**, 367–379,

<https://doi.org/10.1144/jgs.157.2.367>.

- Matsumoto, N. & Shigematsu, N. 2018. In-situ permeability of fault zones estimated by hydraulic tests and continuous groundwater-pressure observations. *Earth, Planets and Space*, **70**, 1–12, <https://doi.org/10.1186/s40623-017-0765-5>.
- Matthews, V. 1976. Correlation of Pinnacles and Neenach Volcanic Formations and Their Bearing on San Andreas Fault Problem. *AAPG Bulletin*, **60**, 2128–2141.
- Mayolle, S., Soliva, R., Caniven, Y., Wibberley, C., Ballas, G., Milesi, G. & Dominguez, S. 2019. Scaling of fault damage zones in carbonate rocks. *Journal of Structural Geology*, **124**, 35–50, <https://doi.org/10.1016/j.jsg.2019.03.007>.
- McCarthy, W., Reavy, R., Stevenson, C. & Petronis, M. 2015. Late Caledonian transpression and the structural controls on pluton construction; new insights from the Omey Pluton, western Ireland. *Earth and Environmental Science Transactions Of The Royal Society Of Edinburgh*, **106**, 11–28, <https://doi.org/10.1017/S1755691015000201>.
- McKay, L., Shipton, Z.K., Lunn, R.J., Andrews, B., Raub, T.D. & Boyce, A.J. 2020. Detailed Internal Structure and Along-Strike Variability of the Core of a Plate Boundary Fault: The Highland Boundary Fault, Scotland. *Journal of the Geological Society London*, **177**, 283–296, <https://doi.org/https://doi.org/10.1144/jgs2018-226>.
- McKay, L., Lunn, R.J., Shipton, Z.K., Pytharouli, S. & Roberts, J.J. 2021. Do intraplate and plate boundary fault systems evolve in a similar way with repeated slip events? *Earth and Planetary Science Letters*, **559**, 1–18, <https://doi.org/10.1016/j.epsl.2021.116757>.
- McKenzie, D.P. & Morgan, W.J. 1969. Evolution of Triple Junctions. *Nature*, **224**, 125–133.
- Melosh, H.J. 1996. Dynamical weakening of faults by acoustic fluidization. *Nature*, **379**, 601–606.

- Mendum, J.R. & Noble, S.R. 2010. Mid-Devonian sinistral transpressional movements on the Great Glen Fault: the rise of the Rosemarkie Inlier and the Acadian Event in Scotland. *In*: Law, R. D., Butler, R. W. ., Holdsworth, R. E., Krabbendam, M. & Strachan, R. A. (eds) *Continental Tectonics and Mountain Building: The Legacy of Peach and Horne*. Geological Society London, Special Publications, 335, 161–187., <https://doi.org/10.1144/SP335.8>.
- Mitterpergher, S., Pennacchioni, G. & Di Toro, G. 2009. The effects of fault orientation and fluid infiltration on fault rock assemblages at seismogenic depths. *Journal of Structural Geology*, **31**, 1511–1524, <https://doi.org/10.1016/j.jsg.2009.09.003>.
- Mizoguchi, K., Hirose, T., Shimamoto, T. & Fukuyama, E. 2008. Internal structure and permeability of the Nojima fault, southwest Japan. *Journal of Structural Geology*, **30**, 513–524, <https://doi.org/10.1016/j.jsg.2007.12.002>.
- Monaghan, A.A. 2014. The Carboniferous shales of the Midland Valley of Scotland: geology and resource estimation. *British Geological Survey for Department of Energy and Climate Change, London, UK*.
- Moore, Diane E & Lockner, D.A. 2013. Chemical controls on fault behavior: Weakening of serpentinite sheared against quartz-bearing rocks and its significance for fault creep in the San Andreas system. *Journal of Geophysical Research: Solid Earth*, **118**, 1–13, <https://doi.org/10.1002/jgrb.50140>.
- Moore, Diane E. & Lockner, D.A. 2013. Chemical controls on fault behavior: Weakening of serpentinite sheared against quartz-bearing rocks and its significance for fault creep in the San Andreas system. *Journal of Geophysical Research: Solid Earth*, **118**, 2558–2570, <https://doi.org/10.1002/jgrb.50140>.
- Moore, D.E. & Rymer, M.J. 2007. Talc-bearing serpentinite and the creeping section of the San Andreas fault. *Nature*, **448**, 795–797, <https://doi.org/10.1038/nature06064>.

- Moore, D.E. & Rymer, M.J. 2012. Correlation of clayey gouge in a surface exposure of serpentinite in the San Andreas Fault with gouge from the San Andreas Fault Observatory at Depth (SAFOD). *Journal of Structural Geology*, **38**, 51–60, <https://doi.org/10.1016/j.jsg.2011.11.014>.
- Moore, D.M. & Reynolds, R.C. 1997. *X-Ray Diffraction and the Identification and Analysis of Clay Minerals*. Oxford, Oxford University Press.
- Moore, G.F., Park, J.O., et al. 2009. Structural and seismic stratigraphic framework of the NanTroSEIZE Stage 1 transect. In: Kinoshita, M., Tobin, H., et al. (eds) *Proceedings of the Integrated Drilling Program*. Washington D.C., Integrated Ocean Drilling Program Management International, 1–46., <https://doi.org/10.2204/iodp.proc.314315316.102.2009>.
- Moreno, M., Haberland, C., Oncken, O., Rietbrock, A., Angiboust, S. & Heidbach, O. 2014. Locking of the Chile subduction zone controlled by fluid pressure before the 2010 earthquake. *Nature Geoscience*, **7**, 292–296, <https://doi.org/10.1038/ngeo2102>.
- Mort, K. & Woodcock, N.H. 2008. Quantifying fault breccia geometry: Dent Fault, NW England. *Journal of Structural Geology*, **30**, 701–709.
- Nemer, T. & Meghraoui, M. 2006. Evidence of coseismic ruptures along the Roum fault (Lebanon): a possible source for the AD 1837 earthquake. *Journal of Structural Geology*, **28**, 1483–1495, <https://doi.org/10.1016/j.jsg.2006.03.038>.
- Noda, H. & Lapusta, N. 2013. Stable creeping fault segments can become destructive as a result of dynamic weakening. *Nature*, **493**, 518–521.
- Nyberg, B., Nixon, C.W. & Sanderson, D.J. 2018. NetworkGT: A GIS tool for geometric and topological analysis of two-dimensional fracture networks. *Geosphere*, **14**, 1618–1634, <https://doi.org/10.1130/GES01595.1>.
- Ohmoto, H. & Rye, R.O. 1979. Isotopes of sulphur and carbon. In: Barnes, H. L. (ed.) *Geochemistry of Hydrothermal Ore Deposits*. New York, John Wiley &

- Sons, Ltd, 509–567.
- Okada, A. 1980. Quaternary faulting along the Median Tectonic Line of Southwest Japan, in *The Median Tectonic Line of Southwest Japan*,. *Memoirs of the Geological Society Japan*, **18**, 78–108.
- Pachell, M.A. & Evans, J.P. 2002. Growth, linkage, and termination processes of a 10-km-long strike-slip fault in jointed granite: the Gemini fault zone, Sierra Nevada, California. *Journal of Structural Geology*, **24**, 1903–1924.
- Parnell, J., Baron, M. & Boyce, A. 2000. Controls on kaolinite and dickite distribution, Highland Boundary Fault Zone, Scotland and Northern Ireland. *Journal of the Geological Society London*, **157**, 635–640, <https://doi.org/10.1144/jgs.157.3.635>.
- Peacock, D.C.. 1991. Displacements and segment linkage in strike-slip fault zones. *Journal of Structural Geology*, **13**, 1025–1035.
- Peacock, S.M., Christensen, N.I., Bostock, M.G. & Audet, P. 2011. High pore pressures and porosity at 35 km depth in the Cascadia subduction zone. *Geology*, **39**, 471–474, <https://doi.org/10.1130/G31649.1>.
- Perrin, C., Manighetti, I., Ampuero, J., Cappa, F. & Gaudemer, Y. 2016. Location of largest earthquake slip and fast rupture controlled by along-strike change in fault structural maturity due to fault growth. *Journal of Geophysical Research : Solid Earth*, **121**, 3666–3685, <https://doi.org/10.1002/2015JB012671>.Received.
- Ramsay, D.M. 1962. The Highland Boundary Fault, reverse or wrench fault? *Nature*, **195**, 1190–1191.
- Ramsay, J.G. 1980. Crack-seal mechanism of rock deformation. *Nature*, **284**, 135–139.
- Reeves, G., Sims, I. & Cripps, J.. 2006. *Clay Materials Used in Construction*. Geological Society London Engineering Geology Special Publication No 21.

- Reinen, L.A. 2000. Slip styles in a spring-slider model with a laboratory-derived constitutive law for serpentinite. *Geophysical Research Letters*, **27**, 2037–2040.
- Rempel, A.W. & Rice, J.R. 2006. Thermal pressurization and onset of melting in fault zones. *Journal of Geophysical Research: Solid Earth*, **111**, <https://doi.org/10.1029/2006JB004314>.
- Reynolds, R. 1963. Potassium–rubidium ratios and polymorphism in illites and microclines from the clay size fractions of Proterozoic carbonate rocks. *Geochimica et Cosmochimica Acta*, **27**, 1097–1112.
- Rhodes, B.P., Perez, R., Lamjuan, A. & Kosuwan, S. 2004. Kinematics and tectonic implications of the Mae Kuang Fault, northern Thailand. *Journal of Asian Earth Sciences*, **24**, 78–89, <https://doi.org/10.1016/j.jseaes.2003.09.008>.
- Rice, J.R. 2006. Heating and weakening of faults during earthquake slip. *Journal of Geophysical Research: Solid Earth*, **111**, 1–29, <https://doi.org/10.1029/2005JB004006>.
- Rice, J.R. & Cocco, M. 2007. Seismic fault rheology and earthquake dynamics. In: MIT Press (ed.) *Tectonic Faults: Agents of Change on a Dynamic Earth*. Cambridge, Massachusetts, 99–137.
- Ring, U., Tonguc Uysal, I., et al. 2017a. Fault-gouge dating in the Southern Alps, New Zealand. *Tectonophysics*, **717**, 321–338, <https://doi.org/10.1016/j.tecto.2017.08.007>.
- Ring, U., Tonguc Uysal, I., et al. 2017b. Fault-gouge dating in the Southern Alps, New Zealand. *Tectonophysics*, **717**, 321–338, <https://doi.org/10.1016/j.tecto.2017.08.007>.
- Robinson, A.C. 2009. Geologic offsets across the northern Karakorum fault: Implications for its role and terrane correlations in the western Himalayan-Tibetan orogen, <https://doi.org/10.1016/j.epsl.2008.12.039>.



- Ross, Z.E., Kanamori, H., Hauksson, E. & Aso, N. 2018. Dissipative Intraplate Faulting During the 2016 M w 6.2 Tottori, Japan Earthquake. *Journal of Geophysical Research: Solid Earth*, **123**, 1631–1642, <https://doi.org/10.1002/2017JB015077>.
- Rovida, A. & Tibaldi, A. 2005. Propagation of strike-slip faults across Holocene volcano-sedimentary deposits, Pasto, Colombia. *Journal of Structural Geology*, **27**, 1838–1855, <https://doi.org/10.1016/j.jsg.2005.06.009>.
- Rowe, C.D., Meneghini, F. & Moore, J.C. 2011. Textural record of the seismic cycle: strain-rate variation in an ancient subduction thrust. *In*: Fagereng, Å., Toy, V. G. & Rowland, J. V. (eds) *Geology of the Earthquake Source: A Volume in Honour of Rick Sibson*. Geological Society London, Special Publications, 359, 77–95., <https://doi.org/10.1144/SP359.5>.
- Rowe, C.D., Moore, J.C. & Remitti, F. 2013. The thickness of subduction plate boundary faults from the seafloor into the seismogenic zone. *Geology*, **41**, 991–994, <https://doi.org/10.1130/G34556.1>.
- Rutter, E.H. 1983. Pressure solution in nature, theory and experiment. *Journal of the Geological Society*, **140**, 725–740, <https://doi.org/10.1017/S0016756800160285>.
- Rutter, E.H. & Elliot, D. 1976. The kinetics of rock deformation by pressure solution. *Philosophical Transactions of the Royal Society A*, **283**, 203–219.
- Rutter, E.H., Faulkner, D.R. & Burgess, R. 2012. Structure and geological history of the Carboneras Fault Zone, SE Spain: Part of a stretching transform fault system. *Journal of Structural Geology*, **45**, 68–71, <https://doi.org/10.1016/j.jsg.2012.08.009>.
- Sagy, A., Brodsky, E.E. & Axen, G.J. 2007. Evolution of fault-surface roughness with slip. *Geology*, **35**, 283–286, <https://doi.org/10.1130/G23235A.1>.
- Sakaguchi, A., Chester, F., et al. 2011. Seismic slip propagation to the updip end of

- plate boundary subduction interface faults: Vitrinite reflectance geothermometry on integrated ocean drilling program nanTro SEIZE cores. *Geology*, **39**, 395–398, <https://doi.org/10.1130/G31642.1>.
- Savage, H.M. & Brodsky, E.E. 2011. Collateral damage: Evolution with displacement of fracture distribution and secondary fault strands in fault damage zones. *Journal of Geophysical Research*, **116**, 1–14, <https://doi.org/10.1029/2010JB007665>.
- Schauble, E., Ghosh, P. & Eiler, J.M. 2006. Preferential formation of  $^{13}\text{C}$ - $^{18}\text{O}$  bonds in carbonate minerals, estimated using first-principle lattice dynamics. *Geochimica et Cosmochimica Acta*, **70**, 2510–2529.
- Schleicher, A., Sutherland, R., Townend, J., Toy, V. & Van Der Pluijm, B. 2015. Clay mineral formation and fabric development in the DFDP-1B borehole, central Alpine Fault, New Zealand. *New Zealand Journal of Geology and Geophysics*, **58**, 13–21, <https://doi.org/10.1080/00288306.2014.979841>.
- Schleicher, A.M., Warr, L.N. & Van Der Pluijm, B.A. 2009. On the origin of mixed-layered clay minerals from the San Andreas Fault at 2.5–3 km vertical depth (SAFOD drillhole at Parkfield, California). *Contributions to Mineralogy and Petrology*, **157**, 173–187, <https://doi.org/10.1007/s00410-008-0328-7>.
- Scholz, C.H. 1988. The brittle-plastic transition and the depth of seismic faulting. *Geologische Rundschau*, **77**, 319–328.
- Scholz, C.H. 1998. Earthquakes and friction laws. *Nature*, **391**, 37–42.
- Scholz, C.H. 2002. *The Mechanics of Earthquakes and Faulting*. Cambridge, U.K., Cambridge University Press.
- Scholz, C.H., Aviles, C.A. & Wesnousky, S.G. 1986. Scaling differences between large interplate and intraplate earthquakes. *Bulletin of the Seismological Society of America*, **76**, 65–70.

- Schuck, B., Schleicher, A., Janssen, C., Toy, V. & Dresen, G. 2020. Fault zone architecture of a large plate-bounding strike-slip fault: a case study from the Alpine Fault, New Zealand. *Solid Earth*, **11**, 95–124, <https://doi.org/10.5194/se-2019-109>.
- Schulz, S.E. & Evans, J.P. 2000. Mesoscopic structure of the Punchbowl Fault, Southern California and the geologic and geophysical structure of active strike-slip faults. *Journal of Structural Geology*, **22**, 913–930.
- Segall, P. & Pollard, D.D. 1980. Mechanics of Discontinuous Faults. *Journal of Geophysical Research*, **85**, 4337–4350.
- Segall, P. & Pollard, D.D. 1983. Nucleation and growth of strike slip faults in granite. *Journal of Geophysical Research*, **88**, 555–568.
- Segall, P. & Simpson, C. 1986. Nucleation of ductile shear zones on dilatant fractures. *Geology*, **14**, 56–59.
- Sengör, A.M.C., Tüysüz, O., et al. 2005. The North Anatolian Fault: A New Look. *Annual Review of Earth and Planetary Sciences*, **33**, 37–112, <https://doi.org/10.1146/annurev.earth.32.101802.120415>.
- Shanks, W.C., Böhlke, J.K. & Seal, R.R. 1995. Stable isotopes in mid-ocean ridge hydrothermal systems: Interactions between fluids, minerals, and organisms. In: Barnes, H. L. (ed.) *Seafloor Hydrothermal Systems: Physical, Chemical, Biological and Geological Interactions*. Geophysical Monograph Series, 194–221., <https://doi.org/10.1029/GM091p0194>.
- Shearer, P.M. 2009. *Introduction to Seismology*, 2nd ed. Cambridge, Cambridge University Press.
- Shervais, K.A.H. & Kirkpatrick, J.D. 2016. Smoothing and re-roughening processes: The geometric evolution of a single fault zone. *Journal of Structural Geology*, **91**, 130–143, <https://doi.org/10.1016/j.jsg.2016.09.004>.

- Shi, Z. & Ben-Zion, Y. 2006. Dynamic rupture on a bimaterial interface governed by slip-weakening friction. *Geophysical Journal International*, **165**, 469–484, <https://doi.org/10.1111/j.1365-246X.2006.02853.x>.
- Shigematsu, N., Fujimoto, K., Tanaka, N., Furuya, N., Mori, H. & Wallis, S. 2012. Internal structure of the Median Tectonic Line fault zone, SW Japan, revealed by borehole analysis. *Tectonophysics*, **532–535**, 103–118, <https://doi.org/10.1016/j.tecto.2012.01.024>.
- Shipboard Scientific Party. 1998. Site 1044, Site 1045, Site 1046 and Site 1047. *In*: Moore, J. C., Klaus, A. & et al. (eds) *Proceedings of the Ocean Drilling Program, Initial Reports, Leg 171A*. College Station, Texas, 19–91.
- Shipboard Scientific Party. 2002. Leg 196 summary: Deformation and fluid flow processes in the Nankai Trough accretionary prism: Logging while drilling and advanced CORKS. *In*: Mikada, H., Becker, K., Moore, J. C. & Klaus, A. (eds) *Proceedings of the Ocean Drilling Program, Initial Reports*. College Station, Texas, Ocean Drilling Program, 1–29.
- Shipton, Z.K., Evans, J.P. & Thompson, L.B. 2005. The Geometry and Thickness of Deformation-band Fault Core and its Influence on Sealing Characteristics of Deformation-band Fault Zones. *In*: Sorkhabi, R. & Tsuji, Y. (eds) *Faults, Fluid Flow and Petroleum Traps*. AAPG Memoir 85, 181–195., <https://doi.org/10.1306/1033723M853135>.
- Shipton, Z.K., Soden, A., Kirkpatrick, J.D., Bright, A.M. & Lunn, R.J. 2006a. How thick is a fault? Fault displacement thickness scaling revisited. *In*: Abercrombie, R., McGarr, A., Di Toro, G. & Kanamori, H. (eds) *Earthquakes: Radiated Energy and the Physics of Faulting, Geophysical Monograph Series 170*. Washington D.C., American Geophysical Union, 193–198., <https://doi.org/10.1029/170GM19>.
- Shipton, Z.K., Evans, J.P., Abercrombie, R.E. & Brodsky, E.E. 2006b. The Missing Sinks: Slip Localization in Faults, Damage Zones, and the Seismic Energy

- Budget. In: Abercrombie, R., McGarr, A., Di Toro, G. & Kanamori, H. (eds) *Earthquakes: Radiated Energy and the Physics of Faulting, Geophysical Monograph Series 170*. Washington D.C., American Geophysical Union, 217–222., <https://doi.org/10.1029/170GM22>.
- Shipton, Z.K., Roberts, J.J., Comrie, E.L., Kremer, Y., Lunn, R.J. & Caine, J.S. 2019. Fault fictions: cognitive biases in the conceptualization of faults zones. In: Ogilvie, S., Urai, J. L., Dee, S., Wilson, R. W. & Bailey, W. (eds) *Integrated Fault Seal Analysis*. Geological Society London, Special Publications 496., <https://doi.org/10.1144/SP496-2018-161>.
- Sibson, R.H. 1973. Interactions between Temperature and Pore-Fluid Pressure during Earthquake Faulting and a Mechanism for Partial or Total Stress Relief. *Nature*, **243**, 66–68.
- Sibson, R.H. 1975. Generation of Pseudotachylyte by Ancient Seismic Faulting. *Geophysical Journal of the Royal Astronomical Society*, **43**, 775–794, <https://doi.org/10.1111/j.1365-246X.1975.tb06195.x>.
- Sibson, R.H. 1977. Fault rocks and fault mechanics. *Journal of the Geological Society London*, **133**, 191–213.
- Sibson, R.H. 1989. Earthquake faulting as a structural process. *Journal of Structural Geology*, **11**, 1–14.
- Sibson, R.H. & Toy, V.G. 2006. The Habitat of Fault-Generated Pseudotachylyte: Presence vs. Absence of Friction-Melt. In: Abercrombie, R., McGarr, A., Di Toro, G. & Kanamori, H. (eds) *Earthquakes: Radiated Energy and the Physics of Faulting, Geophysical Monograph Series 170*. Washington D.C., American Geophysical Union, 153–166., <https://doi.org/10.1029/170GM16>.
- Sieh, K. & Natawidjaja, D. 2000. Neotectonics of the Sumatran fault, Indonesia. *Journal of Geophysical Research*, **105**, 28295–28326, <https://doi.org/10.1029/2000JB900120>.

- Sills, D., Chester, J.S. & Chester, F.M. 2009. Shape Preferred Orientation of Porphyroclasts in the Active Gouge Zones of the San Andreas Fault at SAFOD. *In: EOS Transactions American Geophysical Union, 90, 52, Fall Meeting Supplement, Abstract #T43A-2057.*
- Smith, S.A.F. & Faulkner, D.R. 2010. Laboratory measurements of the frictional properties of the Zuccale low-angle normal fault, Elba Island, Italy. *Journal of Geophysical Research, 115*, 1–17, <https://doi.org/10.1029/2008JB006274>.
- Solum, J.G., Davatzes, N.C. & Lockner, D.A. 2010. Fault-related clay authigenesis along the Moab Fault: Implications for calculations of fault rock composition and mechanical and hydrologic fault zone properties. *Journal of Structural Geology, 32*, 1899–1911, <https://doi.org/10.1016/j.jsg.2010.07.009>.
- Sone, H., Shimamoto, T. & Moore, D.E. 2012. Frictional properties of saponite-rich gouge from a serpentinite-bearing fault zone along the Gokasho-Arashima Tectonic Line, central Japan. *Journal of Structural Geology, 38*, 172–182, <https://doi.org/10.1016/j.jsg.2011.09.007>.
- Sosio De Rosa, S., Shipton, Z.K., Lunn, R.J., Kremer, Y. & Murray, T. 2018a. Along-strike fault core thickness variations of a fault in poorly lithified sediments, Miri (Malaysia). *Journal of Structural Geology, 116*, 189–206, <https://doi.org/10.1016/j.jsg.2018.08.012>.
- Sosio De Rosa, S., Shipton, Z.K., Lunn, R.J., Kremer, Y. & Murray, T. 2018b. Along-strike fault core thickness variations of a fault in poorly lithified sediments, Miri (Malaysia). *Journal of Structural Geology, 116*, 189–206, <https://doi.org/10.1016/j.jsg.2018.08.012>.
- Sperrevik, S., Gillespie, P.A., Fisher, Q.J., Halvorsen, T. & Knipe, R.J. 2002. Empirical estimation of fault rock properties. *Norwegian Petroleum Special Publications, 11*, 109–125.
- Srodon, J. & Eberl, D.D. 1984. Illite. *In: Bailey, W. (ed.) Reviews in Mineralogy.*

- Mineralogical Society of America, 495–555.
- Stephenson, D., Mendum, J.R., Fettes, D.J. & Leslie, A.G. 2013. The Dalradian rocks of Scotland: an introduction. *Proceedings of the Geologists' Association*, **124**, 3–82, <https://doi.org/10.1016/j.pgeola.2012.06.002>.
- Stirling, M.W., Wesnousky, S.G. & Shimazaki, K. 1996. Fault trace complexity, cumulative slip, and the shape of the magnitude-frequency distribution for strike-slip faults: A global survey. *Geophysical Journal International*, **124**, 833–868, <https://doi.org/10.1111/j.1365-246X.1996.tb05641.x>.
- Streit, E., Kelemen, P. & Eiler, J. 2012. Coexisting serpentine and quartz from carbonate-bearing serpentinized peridotite in the Samail Ophiolite, Oman. *Contributions to Mineralogy and Petrology*, **164**, 821–837, <https://doi.org/10.1007/s00410-012-0775-z>.
- Sutherland, R., Eberhart-Phillips, D., et al. 2007. Do great earthquakes occur on the alpine fault in central South Island, New Zealand? *In: Okaya, D., Stern, T. & Davey, F. (eds) A Continental Plate Boundary: Tectonics at South Island, New Zealand*. Geophysical Monograph Series, 235–251., <https://doi.org/10.1029/175GM12>.
- Sutherland, R., Toy, V.G., et al. 2012. Drilling reveals fluid control on architecture and rupture of the Alpine fault, New Zealand. *Geology*, **40**, 1143–1146, <https://doi.org/10.1130/G33614.1>.
- Swanson, M.T. 1989. Sidewall ripouts in strike-slip faults. *Journal of Structural Geology*, **11**, 933–948.
- Swanson, M.T. 2005. Geometry and kinematics of adhesive wear in brittle strike-slip fault zones. *Journal of Structural Geology*, **27**, 871–887, <https://doi.org/10.1016/j.jsg.2004.11.009>.
- Tanner, P.W.G. 2008. Tectonic significance of the Highland Boundary Fault, Scotland. *Journal of the Geological Society London*, **165**, 915–921,

<https://doi.org/10.1144/0016-76492008-012>.

- Tanner, P.W.G. & Sutherland, S. 2007. The Highland Border Complex, Scotland: a paradox resolved. *Journal of the Geological Society London*, **164**, 111–116, <https://doi.org/10.1144/0016-76492005-188>.
- Tatar, O., Piper, J.D.A., Gürsoy, H., Heimann, A. & Koc  bulut, F. 2004. Neotectonic deformation in the transition zone between the Dead Sea Transform and the East Anatolian Fault Zone, Southern Turkey: a palaeomagnetic study of the Karasu Rift Volcanism. *Tectonophysics*, **385**, 17–43, <https://doi.org/10.1016/j.tecto.2004.04.005>.
- Tembe, S., Lockner, D.A. & Wong, T. 2010. Effect of clay content and mineralogy on frictional sliding behavior of simulated gouges: Binary and ternary mixtures of quartz, illite, and montmorillonite. *Journal of Geophysical Research*, **115**, 1–22, <https://doi.org/10.1029/2009JB006383>.
- Tominga, M., Beinlich, A., Lima, E.A., Tivey, M.A., Hampton, B.A., Weiss, B. & Harigane, Y. 2017. Multi-scale magnetic mapping of serpentinite carbonation. *Nature Communications*, **8**, 1–10.
- Torabi, A., Johannessen, M.U. & Ellingsen, T.S.S. 2019. Fault Core Thickness: Insights from Siliciclastic and Carbonate Rocks. *Geofluids*, 1–24, <https://doi.org/10.1155/2019/2918673>.
- Toy, V.G., Boulton, C.J., et al. 2015. Fault rock lithologies and architecture of the central Alpine fault, New Zealand, revealed by DFDP-1 drilling. *Lithosphere*, **7**, 155–173, <https://doi.org/10.1130/L395.1>.
- Toy, V.G., Sutherland, R., et al. 2017. Bedrock geology of DFDP-2B, central Alpine Fault, New Zealand. *New Zealand Journal of Geology and Geophysics*, **60**, 497–518, <https://doi.org/10.1080/00288306.2017.1375533>.
- Trudgill, B. & Cartwright, J. 1994. Relay-ramp forms and normal-fault linkages, Canyonlands National Park, Utah. *Geological Society of America Bulletin*, **106**,



1143–1157.

- Ujiie, K. & Kimura, G. 2014. Earthquake faulting in subduction zones: insights from fault rocks in accretionary prisms. *Progress in Earth and Planetary Science*, **1**, 1–30, <https://doi.org/10.1186/2197-4284-1-7>.
- Ujiie, K., Yamaguchi, A., Kimura, G. & Toh, S. 2007a. Fluidization of granular material in a subduction thrust at seismogenic depths. *Earth and Planetary Science Letters*, **259**, 307–318, <https://doi.org/10.1016/j.epsl.2007.04.049>.
- Ujiie, K., Yamaguchi, H., Sakaguchi, A. & Toh, S. 2007b. Pseudotachylytes in an ancient accretionary complex and implications for melt lubrication during subduction zone earthquakes. *Journal of Structural Geology*, **29**, 599–613, <https://doi.org/10.1016/j.jsg.2006.10.012>.
- Uysal, I.T., Altunel, E, et al. 2016. Clay mineralogical and isotopic (K-Ar,  $\delta^{18}\text{O}$ ,  $\delta\text{D}$ ) constraints on the evolution of the North Anatolian Fault Zone, Turkey. *Earth and Planetary Science Letters*, **243**, 181–194, <https://doi.org/10.1016/j.epsl.2005.12.025>.
- Van Der Zee, W. & Urai, J.L. 2005. Processes of normal fault evolution in a siliciclastic sequence: a case study from Miri, Sarawak, Malaysia. *Journal of Structural Geology*, **27**, 2281–2300, <https://doi.org/10.1016/j.jsg.2005.07.006>.
- Van Der Zee, W., Wibberley, C.A.J. & Urai, J.L. 2008. The influence of layering and pre-existing joints on the development of internal structure in normal fault zones: the Lodève basin, France. In: Wibberley, C. A. J., Kurz, W., Imber, J., Holdsworth, R. E. & Collettini, C. (eds) *The Internal Structure of Fault Zones: Implications for Mechanical and Fluid-Flow Properties*. Geological Society London, Special Publications 299, 57–74., <https://doi.org/10.1144/SP299.4>.
- Veizer, J., Ala, D., et al. 1999.  $^{87}\text{Sr}/^{86}\text{Sr}$ ,  $\text{D}^{13}\text{C}$  and  $\text{D}^{18}\text{O}$  evolution of Phanerozoic seawater. *Chemical Geology*, **161**, 59–88, [https://doi.org/10.1016/S0009-2541\(99\)00081-9](https://doi.org/10.1016/S0009-2541(99)00081-9).

- Venkataraman, A. & Kanamori, H. 2004. Observational constraints on the fracture energy of subduction zone earthquakes. *Journal of Geophysical Research: Solid Earth*, **109**, 1–20, <https://doi.org/10.1029/2003JB002549>.
- Verma, A.R. & Krishna, P. 1966. *Polymorphism and Polytypism in Crystals*. John Wiley and Sons.
- Vermilye, J.. & Scholz, C.H. 1998. The process zone: A microstructural view of fault growth. *Journal of Geophysical Research: Solid Earth*, **103**, 12223–12237.
- Viete, D.R., Oliver, G.J.H., Fraser, G.L., Forster, M.A. & Lister, G.S. 2013. Timing and heat sources for the Barrovian metamorphism, Scotland. *Lithos*, **177**, 148–163, <https://doi.org/10.1016/j.lithos.2013.06.009>.
- Vorhies, S.H. & Ague, J.J. 2011. Pressure–temperature evolution and thermal regimes in the Barrovian zones, Scotland. *Journal of the Geological Society London*, **168**, 1147–1166, <https://doi.org/10.1144/0016-76492010-073>.
- Vrolijk, P. 1990. On the mechanical role of smectite in subduction zones. *Geology*, **18**, 703–707.
- Wald, D.J. & Heaton, T.H. 1994. Spatial and Temporal Distribution of Slip for the 1992 Landers, California, Earthquake. *Bulletin of the Seismological Society of America*, **84**, 668–691.
- Walker, R. & Jackson, J. 2002. Offset and evolution of the Gowk fault, S.E. Iran: a major intra-continental strike-slip system. *Journal of Structural Geology*, **24**, 1677–1698.
- Walker, R.T., Bayasgalan, A., et al. 2006. Geomorphology and structure of the Jid right-lateral strike-slip fault in the Mongolian Altay mountains. *Journal of Structural Geology*, **28**, 1607–1622, <https://doi.org/10.1016/j.jsg.2006.04.007>.
- Walpersdorf, A., Manighetti, I., et al. 2014. Present-day kinematics and fault slip rates in eastern Iran, derived from 11 years of GPS data. *Journal of Geophysical*

- Research: Solid Earth*, **119**, 1359–1383, <https://doi.org/10.1002/2013JB010620>.
- Walsh, J.J., Bailey, W.R., Childs, C., Nicol, A. & Bonson, C.G. 2003. Formation of segmented normal faults: a 3-D perspective. *Journal of Structural Geology*, **25**, 1251–1262.
- Warr, L.N. & Cox, S. 2001. Clay mineral transformations and weakening mechanisms along the Alpine Fault, New Zealand. In: Holdsworth, R. E., Magloughlin, J. F. & Knipe, R. J. (eds) *The Nature and Tectonic Significance of Fault Zone Weakening*. Geological Society London, Special Publications, 186, 85–101.
- Warr, L.N., Wojatschke, J., Carpenter, B.M., Marone, C., Schleicher, A.M. & van der Pluijm, B.A. 2014. A ‘slice-and-view’ (FIB-SEM) study of clay gouge from the SAFOD creeping section of the San Andreas Fault at ~2.7km depth. *Journal of Structural Geology*, **69**, 234–244, <https://doi.org/10.1016/j.jsg.2014.10.006>.
- Wells, D.L. & Coppersmith, K.J. 1994. New empirical relationships among magnitude, rupture length, rupture width, rupture area, and surface displacement. *Bulletin of the Seismological Society of America*, **84**, 974–1002.
- Wesnousky, S.G. 1988. Seismological and structural evolution of strike-slip faults. *Nature*, **335**, 340–343, <https://doi.org/10.1038/335340a0>.
- Wesnousky, S.G. 2005. The San Andreas and Walker Lane fault systems, western North America: transpression, transtension, cumulative slip and the structural evolution of a major transform plate boundary. *Journal of Structural Geology*, **27**, 1505–1512, <https://doi.org/10.1016/j.jsg.2005.01.015>.
- Wesnousky, S.G. 2006. Predicting the endpoints of earthquake ruptures. *Nature*, **444**, 358–360, <https://doi.org/10.1038/nature05275>.
- Wesnousky, S.G. 2008. Displacement and Geometrical Characteristics of Earthquake Surface Ruptures: Issues and Implications for Seismic-Hazard Analysis and the Process of Earthquake Rupture. *Bulletin of the Geological Society of America*,

- 98, 1609–1632, <https://doi.org/10.1785/0120070111>.
- Wibberley, C.A.J. & Shimamoto, T. 2003. Internal structure and permeability of major strike-slip fault zones: The Median Tectonic Line in Mie Prefecture, Southwest Japan. *Journal of Structural Geology*, **25**, 59–78, [https://doi.org/10.1016/S0191-8141\(02\)00014-7](https://doi.org/10.1016/S0191-8141(02)00014-7).
- Wibberley, C.A.J. & Shimamoto, T. 2005. Earthquake slip weakening and asperities explained by thermal pressurization. *Nature*, **436**, 689–692, <https://doi.org/10.1038/nature03901>.
- Wibberley, C.A.J., Yielding, G. & Di Toro, G. 2008. Recent advances in the understanding of fault zone internal structure: a review. *In*: Wibberley, C. A. J., Kurz, W., Imber, J., Holdsworth, R. E. & Collettini (eds) *Geological Society, London, Special Publications*. 5–33., <https://doi.org/10.1144/SP299.2>.
- Williams, J.N., Toy, V.G., Smith, S.A.F. & Boulton, C. 2017. Fracturing, fluid-rock interaction and mineralisation during the seismic cycle along the Alpine Fault. *Journal of Structural Geology*, **103**, 151–166, <https://doi.org/10.1016/j.jsg.2017.09.011>.
- Winchester, S. 2006. *A Crack in the Edge of the World: The Great American Earthquake of 1906*. London, UK, Penguin Books.
- Woodcock, N.H. & Mort, K. 2008. Classification of fault breccias and related fault rocks. *Geological Magazine*, **145**, 435–440, <https://doi.org/10.1017/S0016756808004883>.
- Woodcock, N.H., Dickson, J.A.D. & Tarasewics, J.P.T. 2007. Transient permeability and reseal hardening in fault zones: Evidence from dilation breccia textures. *In*: Lonergan, L., Jolly, R. J. ., Rawnsley, K. & Sanderson, D. J. (eds) *Fractured Reservoirs*. Geological Society London Special Publications 270, 43–53., <https://doi.org/10.1144/GSL.SP.2007.270.01.03>.
- Xu, S., Ben-Zion, Y. & Ampuero, J.-P. 2012. Properties of inelastic yielding zones

- generated by in-plane dynamic ruptures-II. Detailed parameter-space study. *Geophysical Journal International*, **191**, 1343–1360, <https://doi.org/10.1111/j.1365-246X.2012.05685.x>.
- Yeh, E.C., Sone, H., et al. 2007. Core description and characteristics of fault zones from Hole-A of the Taiwan Chelungpu-Fault Drilling Project. *Terrestrial, Atmospheric and Oceanic Sciences*, **18**, 327–357, [https://doi.org/10.3319/TAO.2007.18.2.327\(TCDP\)](https://doi.org/10.3319/TAO.2007.18.2.327(TCDP)).
- Zhang, P., Mao, F. & Slemmons, D.B. 1999. Rupture terminations and size of segment boundaries from historical earthquake ruptures in the Basin and Range Province. *Tectonophysics*, **308**, 37–52, [https://doi.org/10.1016/S0040-1951\(99\)00089-X](https://doi.org/10.1016/S0040-1951(99)00089-X).
- Zielke, O., Galis, M. & Mai, P.M. 2017. Fault roughness and strength heterogeneity control earthquake size and stress drop. *Geophysical Research Letters*, **44**, 777–783, <https://doi.org/10.1002/2016GL071700>.

## Websites

- USGS, 2014. Understanding plate motions [online] [Accessed 18 May 2020]. Available at: <https://pubs.usgs.gov/gip/dynamic/understanding.html>
- USGS, 2016. Earthquakes [online] [Accessed 18 May 2020]. Available at: <https://pubs.usgs.gov/gip/earthq1/>

## Appendix 1 – Published Paper Chapter 3

*Due to issues of copyright, this publication is not included in the digital version of this thesis.*

*Refer to: McKay, L., Shipton, Z.K., Lunn, R.J., Andrews, B., Raub, T.D., Boyce, A.J., 2020. Detailed Internal Structure and Along-Strike Variability of the Core of a Plate Boundary Fault: The Highland Boundary Fault, Scotland. Journal of the Geological Society, 177, 283-296. doi: 10.1144/jgs2018-226*

*Due to issues of copyright, this publication is not included in the digital version of this thesis.*

*Refer to: McKay, L., Shipton, Z.K., Lunn, R.J., Andrews, B., Raub, T.D., Boyce, A.J., 2020. Detailed Internal Structure and Along-Strike Variability of the Core of a Plate Boundary Fault: The Highland Boundary Fault, Scotland. Journal of the Geological Society, 177, 283-296. doi: 10.1144/jgs2018-226*

*Due to issues of copyright, this publication is not included in the digital version of this thesis.*

*Refer to: McKay, L., Shipton, Z.K., Lunn, R.J., Andrews, B., Raub, T.D., Boyce, A.J., 2020. Detailed Internal Structure and Along-Strike Variability of the Core of a Plate Boundary Fault: The Highland Boundary Fault, Scotland. Journal of the Geological Society, 177, 283-296. doi: 10.1144/jgs2018-226*



*Due to issues of copyright, this publication is not included in the digital version of this thesis.*

*Refer to: McKay, L., Shipton, Z.K., Lunn, R.J., Andrews, B., Raub, T.D., Boyce, A.J., 2020. Detailed Internal Structure and Along-Strike Variability of the Core of a Plate Boundary Fault: The Highland Boundary Fault, Scotland. Journal of the Geological Society, 177, 283-296. doi: 10.1144/jgs2018-226*

*Due to issues of copyright, this publication is not included in the digital version of this thesis.*

*Refer to: McKay, L., Shipton, Z.K., Lunn, R.J., Andrews, B., Raub, T.D., Boyce, A.J., 2020. Detailed Internal Structure and Along-Strike Variability of the Core of a Plate Boundary Fault: The Highland Boundary Fault, Scotland. Journal of the Geological Society, 177, 283-296. doi: 10.1144/jgs2018-226*

*Due to issues of copyright, this publication is not included in the digital version of this thesis.*

*Refer to: McKay, L., Shipton, Z.K., Lunn, R.J., Andrews, B., Raub, T.D., Boyce, A.J., 2020. Detailed Internal Structure and Along-Strike Variability of the Core of a Plate Boundary Fault: The Highland Boundary Fault, Scotland. Journal of the Geological Society, 177, 283-296. doi: 10.1144/jgs2018-226*

*Due to issues of copyright, this publication is not included in the digital version of this thesis.*

*Refer to: McKay, L., Shipton, Z.K., Lunn, R.J., Andrews, B., Raub, T.D., Boyce, A.J., 2020. Detailed Internal Structure and Along-Strike Variability of the Core of a Plate Boundary Fault: The Highland Boundary Fault, Scotland. Journal of the Geological Society, 177, 283-296. doi: 10.1144/jgs2018-226*

*Due to issues of copyright, this publication is not included in the digital version of this thesis.*

*Refer to: McKay, L., Shipton, Z.K., Lunn, R.J., Andrews, B., Raub, T.D., Boyce, A.J., 2020. Detailed Internal Structure and Along-Strike Variability of the Core of a Plate Boundary Fault: The Highland Boundary Fault, Scotland. Journal of the Geological Society, 177, 283-296. doi: 10.1144/jgs2018-226*

*Due to issues of copyright, this publication is not included in the digital version of this thesis.*

*Refer to: McKay, L., Shipton, Z.K., Lunn, R.J., Andrews, B., Raub, T.D., Boyce, A.J., 2020. Detailed Internal Structure and Along-Strike Variability of the Core of a Plate Boundary Fault: The Highland Boundary Fault, Scotland. Journal of the Geological Society, 177, 283-296. doi: 10.1144/jgs2018-226*

*Due to issues of copyright, this publication is not included in the digital version of this thesis.*

*Refer to: McKay, L., Shipton, Z.K., Lunn, R.J., Andrews, B., Raub, T.D., Boyce, A.J., 2020. Detailed Internal Structure and Along-Strike Variability of the Core of a Plate Boundary Fault: The Highland Boundary Fault, Scotland. Journal of the Geological Society, 177, 283-296. doi: 10.1144/jgs2018-226*

*Due to issues of copyright, this publication is not included in the digital version of this thesis.*

*Refer to: McKay, L., Shipton, Z.K., Lunn, R.J., Andrews, B., Raub, T.D., Boyce, A.J., 2020. Detailed Internal Structure and Along-Strike Variability of the Core of a Plate Boundary Fault: The Highland Boundary Fault, Scotland. Journal of the Geological Society, 177, 283-296. doi: 10.1144/jgs2018-226*



*Due to issues of copyright, this publication is not included in the digital version of this thesis.*

*Refer to: McKay, L., Shipton, Z.K., Lunn, R.J., Andrews, B., Raub, T.D., Boyce, A.J., 2020. Detailed Internal Structure and Along-Strike Variability of the Core of a Plate Boundary Fault: The Highland Boundary Fault, Scotland. Journal of the Geological Society, 177, 283-296. doi: 10.1144/jgs2018-226*

*Due to issues of copyright, this publication is not included in the digital version of this thesis.*

*Refer to: McKay, L., Shipton, Z.K., Lunn, R.J., Andrews, B., Raub, T.D., Boyce, A.J., 2020. Detailed Internal Structure and Along-Strike Variability of the Core of a Plate Boundary Fault: The Highland Boundary Fault, Scotland. Journal of the Geological Society, 177, 283-296. doi: 10.1144/jgs2018-226*

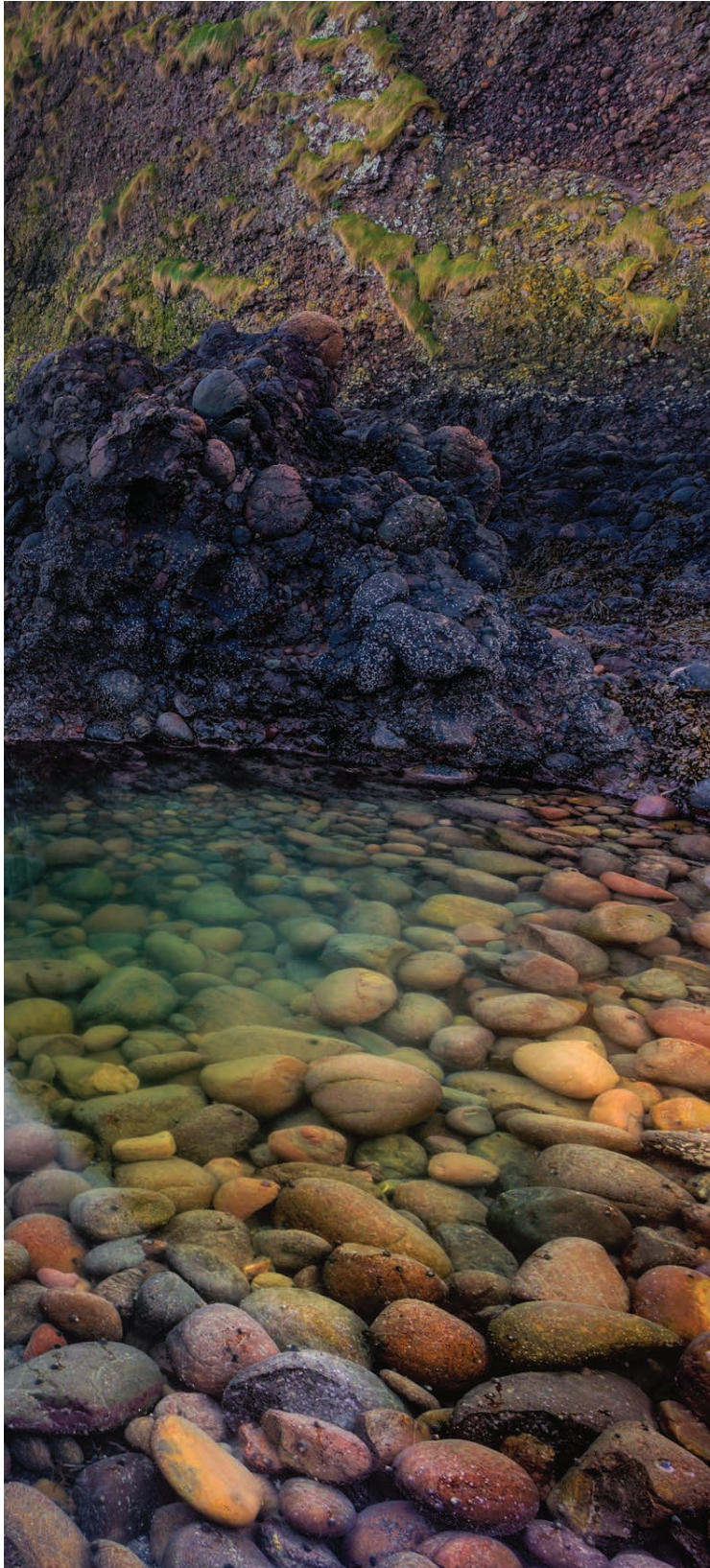
## Appendix 2 – Geoscientist Magazine

### Chapter 3



#### **CORE SURPRISE: WHAT'S INSIDE A PLATE BOUNDARY?**

Digging to expose clay 'inside' the Highland Boundary Fault, Lucy McKay, Zoe Shipton and Rebecca Lunn discover a remarkable sequence of clay and microfossils within the core of an ancient plate boundary



Despite the fact that 90% of global seismicity occurs at plate boundary faults, our understanding of their internal structure is lacking.

It's not easy to see inside a plate boundary fault – typically composed of a high-strain fault core surrounded by a fractured damage zone – and when we can, it often requires expensive drilling projects that yield limited information on the internal structure of the whole fault.

Understanding the internal structure of large faults is crucial, because their chemical and mechanical properties control how and where earthquakes rupture, nucleate and propagate. This in turn limits the size of the earthquake or the amount of radiated seismic energy, and consequently the severity of surface damage. The 1999 magnitude 7.7 earthquake along the Chelungpu plate boundary fault, for example – the second deadliest earthquake in Taiwan's recorded history – saw significant variations in slip and ground motion at different locations along the fault which resulted in large local variations in casualties and damage. Subsequent field investigations related these variations to changes in the fault's structure (i.e., clay width, geometry), which in turn controlled how the fault moved.

### Seeing inside

Opportunities to directly study the internal structure of plate boundary faults are few, since they are normally poorly exposed at the surface. One alternative is to drill into the plate boundary to collect geological data. Several drilling projects have recently been undertaken at active plate boundaries in order to explore their internal structure at depth, including at the San Andreas fault in California, the Alpine fault in New Zealand, the Japan Trench, the Nankai Trough offshore Japan and the Chelungpu Thrust in Taiwan.

Such projects, though, are expensive – the bill for the San Andreas Fault Observatory at Depth (SAFOD) project alone was \$25M. They are also limited in what they can tell us, effectively ►

WWW.GEOL.SOC.ORG.UK/GEOSCIENTIST | JULY 2020 | 11



Fig 1: The HBF looking northeast across Stonehaven and our team of geologists trying to 'dig' for the fault core amongst the very large boulders

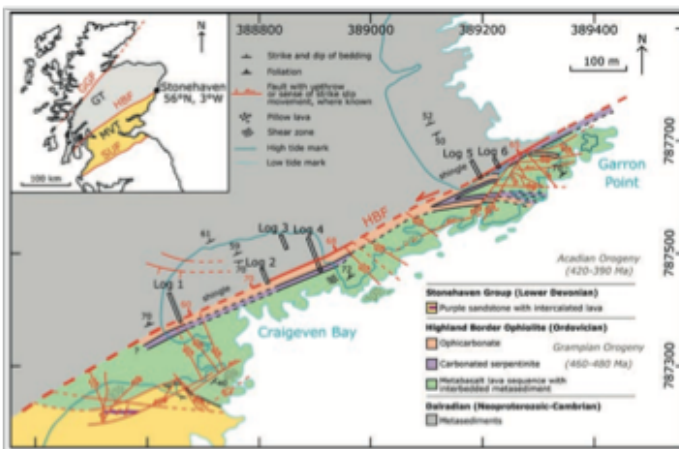
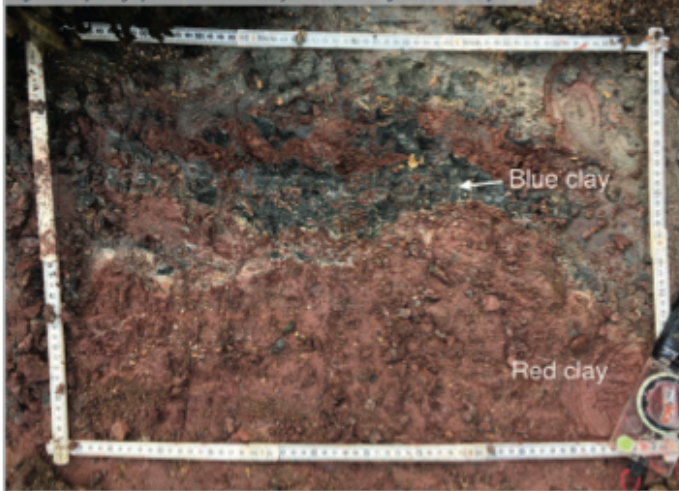


Fig 2: Our geological map of the HBF near Stonehaven. The fault cuts across Craigeven Bay and is only observed and mappable at low tide. The location of the structural logs are indicated with black rectangles

Fig 3: Field photograph of two different clays 'inside' the Highland Boundary fault



► sampling only spatially limited '1D' transects across a fault, which limits the ability to capture the variability in the internal structure at different locations along the fault.

Luckily, a rare opportunity to study the variability of the internal structure of an ancient plate boundary fault exists closer to home – and without the need for expensive drilling projects – in the form of the Highland Boundary Fault (HBF).

### The Highland Boundary Fault

The HBF is an important terrane boundary in UK geology which has been the subject of many regional tectonic studies. It separates the Scottish Highlands from the Midland Valley, extending for over 240 km NE-SW from Stonehaven on the northeast coast to the Isle of Arran in the west. It is also exposed at Comrie, Loch Ard Forest, Loch Lomond and the Cowal and Rosneath peninsulas. We explored several of these locations but found the best exposure along a coastal section ~1km north of Stonehaven.

On a rare, dry, late summer's day in August 2017, our team of geologists from the University of Strathclyde's Faults and Fluid Flow research group travelled from Glasgow to Stonehaven, having applied for and been granted permission from the Scottish Natural Heritage to 'dig' out the fault at several locations at the Stonehaven site.

### Tectonic history

The HBF has a long and complex tectonic history. It hasn't always been considered a plate boundary, nor were the rocks on the southern side of the fault, formerly referred to as the Highland Border Complex, considered to be part of an ophiolite sequence (a sequence commonly

associated with plate boundaries.)

These rocks include a diverse assemblage of altered serpentinites, metabasalt, amphibolite, basaltic pillow lava, conglomerate, arenite, black graphitic mudstone, limestone and chert. Recent reappraisal by Tanner & Sutherland (2007) suggests this assemblage belongs to an ophiolite sequence that lies in stratigraphic and structural continuity with the Dalradian, and not an exotic terrane as previously suggested (Bluck 1985). Field observations of the 'Highland Border Ophiolite (HBO)' from the British Geological Survey's Highland Workshop in 2008 (see Leslie et al. 2009 for detail), support Tanner & Sutherland's hypothesis.

Importantly, the orange-brown-weathered carbonated serpentinite (termed ophicarbonates) shows remarkable similarities to rocks from modern Iberia-type ocean-continent transitions and Ligurian-type ophiolites in northern Italy (not the classic Penrose-type ophiolite sequence).

All this suggests that the HBO represents a slice of exhumed serpenitised sub-continental mantle and associated sedimentary rocks, that formed part of the seafloor of an extended Dalradian basin, and was thrust onto the Dalradian block immediately before the start of the Grampian Orogeny and associated metamorphism 490 million years ago (Leslie et al. 2009).

At Stonehaven, as at many plate boundaries, oceanic serpentinite juxtaposes quartz and feldspar-rich crustal rocks of distinct terranes: the now termed Highland Border Ophiolite and Dalradian group, respectively (Fig. 1). We remapped this section of the HBF, focusing on its fault structure (Fig. 2). While the HBF is well-characterised in terms of regional tectonic importance, the only studies discussing mineralisation of the fault focus on the rock walls (on both sides), and do not address the internal fault zone structure.

### Exposing the fault core

Using spades and trowels, we scraped back the shingle from below the high tide mark, along as linear a transect as possible. This was easier said than done; in places the shingle layer was very deep, and we had to avoid some very large boulders.

We were surprised to unearth not one



Fig 4: Modelling a fish out of the blue clay

but several distinct clay-rich units. After our initial amazement, we mapped and collected samples, then replaced the shingle to maximize conservation before the tide covered our study area. The site is an important Site of Special Scientific Interest, and it was important to make sure our work left no permanent mark. We returned after six weeks to confirm that the area we had excavated was indistinguishable.

In order to characterize the variability of the internal structure at different locations, with further permission from the Scottish Natural Heritage, we returned to the site and collected a total of five across-fault transects (structural logs) through the fault core (locations given on the geological map; Fig. 2).

### What is 'inside' the HBF?

By digging to expose the fault core at five different localities, we are able to deliver a level of detail on the variability of an internal fault core structure of a major plate boundary fault that has rarely been seen before. Each log delivers structural detail equivalent to that revealed via drill core, but with the advantage of being able to trace the variation in fault zone structure through multiple logs hundreds of meters apart.

This work reveals the Stonehaven section of the HBF is composed of a remarkable sequence of fault rocks (Fig. 3). The fault core, which is between 2.95m

(Log 4) and 10.7m (Log 5) wide, is composed of four structurally and chemically distinct units – a localized green clay, a blue clay, a red foliated clay with structural fabrics and a unit consisting of large, lens-shaped clasts broken off the Dalradian wall rock (see McKay et al. 2020).

These fault core units are very different to each other and remain surprisingly unmixed, despite having accommodated offsets between 30 to 150 km. For instance, the blue clay is of high plasticity that feels exactly like modelling clay. In fact, one member of our team even managed to model a fish in the field (Fig. 4). The red foliated clay has a grey, silty texture with compositional (colour) foliations that wrap around wall rock clasts elongated parallel to the HBF. Surprisingly, despite the evidence of internal strain, relatively intact clasts of wall rock and ancient microfossils are preserved within the clay.

Similarly to other plate boundary settings where oceanic and crustal wall rocks juxtapose, our field and mineralogical observations (see McKay et al. 2020) suggest the HBF fault core likely formed through shallow, low-temperature, shear-enhanced, chemical reactions between the wall rocks of contrasting chemistry. In other words, the green and blue clay are derived from the HBO wall rocks, whereas the red foliated clay and lens unit are derived from the ►

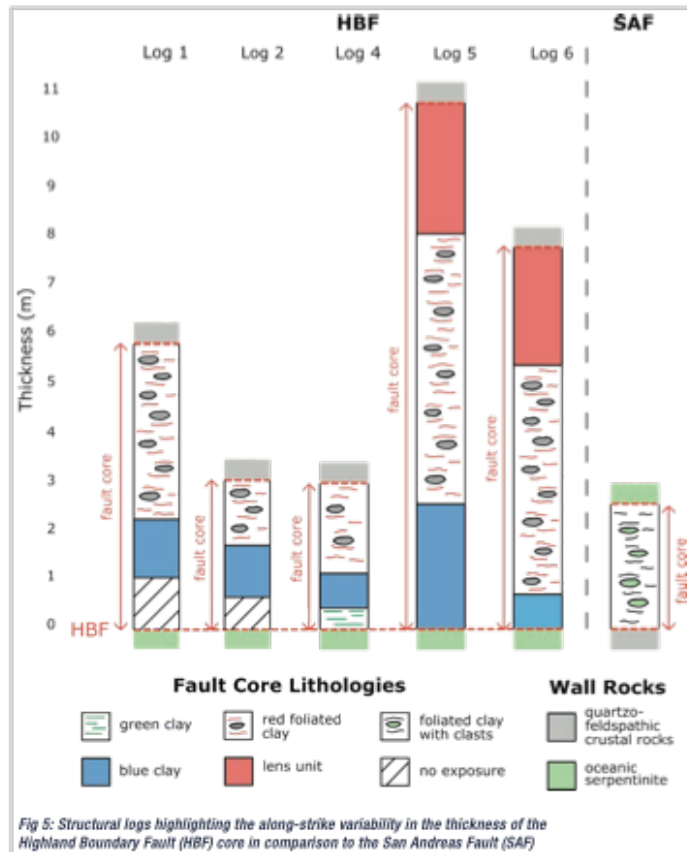


Fig 5: Structural logs highlighting the along-strike variability in the thickness of the Highland Boundary Fault (HBF) core in comparison to the San Andreas Fault (SAF)



14 | JULY 2020 | WWW.GEOLSOC.ORG.UK/GEOSCIENTIST

► Dalradian wall rocks. Our field observations confirm the HBF has dominant sinistral strike-slip, but also reveal that the thickness and composition of the HBF core is variable at different locations i.e. not every unit is continuous, and each unit has variable thickness (Fig. 5).

### Fault zone palaeontology!

One of the most surprising (and puzzling) discoveries was the preservation of relatively intact, ancient microfossils within the blue clay (Fig. 6). Initially, and rather disappointedly, we thought these were just modern-day fossils, and hence modern-day clay found on a beach. However, after discussion with Paul Taylor at the Natural History Museum it was confirmed that these fossils were indeed ancient bryozoans, possibly belonging to the order Fenestrata. They were found alongside brachiopods and echinoid spines.

Since we think that the blue clay is derived from the HBO, one hypothesis is that these shallow, marine fossils are derived from the sedimentary cover of the ophiolite sequence. Regardless of their origin, it is impressive that these delicate fossils remain relatively intact within a high-strain fault clay and show no evidence of internal strain (e.g. microfracturing or shear indicators). Strain within the clay must have been highly localized and principally concentrated on the margins of the fault core.

Clay growth must be younger than the fossils which, assuming the bryozoans belong to the order Fenestrata, are Ordovician to Permian in age but reached their largest diversity during the Carboniferous. The presence of these ancient fossils within the clay therefore constrains the age of the clay to younger than Ordovician-Permian. Obviously this does not provide a very tight age constraint, but to the best of our knowledge this is the first time that the age of fossils preserved within a fault clay have been used to constrain the relative age of that fault.

### How representative is the HBF of active plate boundary faults?

Our maps are the first time anyone has seen 'inside' this iconic plate boundary fault that is such an important part of UK geology. As well as contributing to the understanding of the sequence of events at the HBF system, our maps show the

HBF has remarkable similarities in thickness and composition with other plate boundary faults.

All plate boundary faults appear to have similar fault core thicknesses. For example, the San Andreas fault (SAF) clay as revealed by the \$25m SAFOD project has a fault thickness of 2.5m (similar in thickness to Log 2 and 4). It is composed of a dark greyish-black to greenish-black, highly-sheared, foliated clay that wraps around wall rock clasts that are elongated parallel to the foliation (similar to the red clay). Structurally foliated fault rocks with clasts derived from the wall rocks are common along many strike-slip plate boundary faults. In both the HBF and SAF, the clay formed as a result of fluid-assisted, shear-enhanced chemical reactions between wall rocks of contrasting chemistry.

### What can we learn from the Highland Boundary Fault?

The remarkable similarity between the HBF and other plate boundary faults confirms that our results are applicable to the growing number of studies into how fault structure controls earthquake ruptures. The magnitude and speed of rupture propagation and the frequency content of radiated seismic energy all affect how damaging an earthquake is, so understanding the internal structure of plate boundary faults is crucial if we are to better understand and mitigate damage.

If the thickness and composition of

the fault changes at different locations along the fault, which we have demonstrated they do for the HBF, then models of structural control on earthquakes must take this thickness variation into account. For instance, if the units within the fault core have variable thickness, then the effect of shear heating or lubrication by thermal pressurisation is likely to vary (the thinner the unit the faster the heating). Therefore, it is crucial to understand the controls on the presence and thickness of such units along the length of the fault. Drilling a few boreholes at a particular section of the fault is not enough to fully characterize the internal structure, and hence earthquake properties, of the entire plate boundary – variable fault core thickness and composition have to be accounted for.

### What next?

The next stage of this work, which forms part of my PhD, involves detailed microstructural (thin section) analysis and laboratory work on the blue and red clay. Not only will this help to unravel the history of this iconic UK tectonic structure, but it will provide new data on the interplay between fault processes and earthquake mechanics. Look out for a forthcoming publication with these observations!

We have also received funding from the Geological Society to attempt to constrain the timing and nature of fluids responsible for the growth of the blue and red clays. Any suggestions for further

work that will help understand the puzzling fault zone palaeontology will be most welcome...

Lucy McKay is a PhD student at the University of Strathclyde; e-mail: lucy.mckay@strath.ac.uk

### ACKNOWLEDGEMENTS

Thanks go to my supervisors at the University of Strathclyde – Zoe Shipton and Rebecca Lunn – and also to Adrian Boyce at SUERC and Tim Raub at the University of St Andrews. Thanks also must go to the Scottish Natural Heritage and local landowners for permission to sample at this Site of Special Scientific Interest. Also, to the team of 'diggers': Billy Andrews, Izabella Otalega, Lisa Millar, Carla Romano, Bruno Thomas and John Helstrip. This work was funded by an Environmental and Physical Science Research Council (EPSRC) Doctoral Training Partnership (DTP) award, and further ongoing laboratory work is funded by the Geological Society through the William Feamsides Fund.

### FURTHER READING

Black, B.L. (1985). The Scottish paralectonic Caledonides. *Scottish Journal of Geology*, 21, 437-464.

Leslie, A. (2009). Border Skirmish. *Geoscientist*, 19, 17-19.

McKay, L. et al. (2020). Detailed Internal Structure and Along-Strike Variability of the Core of a Plate Boundary Fault: The Highland Boundary Fault, Scotland. *Journal of the Geological Society*, 177, 283-296.

Tanner, P.W.G. & Sutherland, S. (2007). The Highland Border Complex, Scotland: a paradox resolved. *Journal of the Geological Society*, 164, 111-116.

Fig 8: Fossils in the blue clay





## Appendix 3 – Published Paper Chapter 4

Earth and Planetary Science Letters 559 (2021) 116757



Contents lists available at ScienceDirect

Earth and Planetary Science Letters

www.elsevier.com/locate/epsl



## Do intraplate and plate boundary fault systems evolve in a similar way with repeated slip events?



L. McKay\*, R.J. Lunn, Z.K. Shipton, S. Pytharouli, J.J. Roberts

Department of Civil and Environmental Engineering, University of Strathclyde, 75 Montrose Street, Glasgow G1 1XJ, UK

## ARTICLE INFO

## Article history:

Received 10 June 2020

Received in revised form 21 December 2020

Accepted 10 January 2021

Available online xxxxx

Editor: R. Bendick

## Dataset link:

<https://doi.org/10.15129/21271686-f115-4f9d-bf9a-ac681fd6f15b>

## Keywords:

plate boundary faults

intraplate faults

fault core

fault thickness

plate boundary fault internal structure

earthquake energy balance

## ABSTRACT

As repeated slip events occur on a fault, energy is partly dissipated through rock fracturing and frictional processes in the fault zone and partly radiated to the surface as seismic energy. Numerous field studies have shown that the core of intraplate faults is wider on average with increasing total displacement (and hence slip events). In this study we compile data on the fault core thickness, total displacement and internal structure (e.g., fault core composition, host rock juxtaposition, slip direction, fault type, and/or the number of fault core strands) of plate boundary faults to compare to intraplate faults (within the interior of tectonic plates). Fault core thickness data show that plate boundary faults are anomalously narrow by comparison to intraplate faults and that they remain narrow regardless of how much total displacement they have experienced or the local structure of the fault. By examining the scaling relations between seismic moment, average displacement and surface rupture length for plate boundary and intraplate fault ruptures, we find that for a given value of displacement in an individual earthquake, plate boundary fault earthquakes typically have a greater seismic moment (and hence earthquake magnitude) than intraplate events. We infer that narrow plate boundary faults do not process intact rock as much during seismic events as intraplate faults. Thus, plate boundary faults dissipate less energy than intraplate faults during earthquakes meaning that for a given value of average displacement, more energy is radiated to the surface manifested as higher magnitude earthquakes. By contrast, intraplate faults dissipate more energy and get wider as fault slip increases, generating complex zones of damage in the surrounding rock and propagating through linkage with neighbouring structures. The more complex the fault geometry, the more energy has to be consumed at depth during an earthquake and the less energy reaches the surface.

Crown Copyright © 2021 Published by Elsevier B.V. This is an open access article under the CC BY license (<http://creativecommons.org/licenses/by/4.0/>).

## 1. Introduction

The earthquake energy balance as defined by Kanamori and Anderson (1975) (see also Kanamori and Brodsky, 2001 and references therein) states that the total energy released during an earthquake is partly absorbed on the fault plane by fracturing and frictional dissipation and partly radiated out of the source as seismic waves. This can be expressed simply as equation (1):

$$E_T = (E_G + E_F) + E_R \quad (1)$$

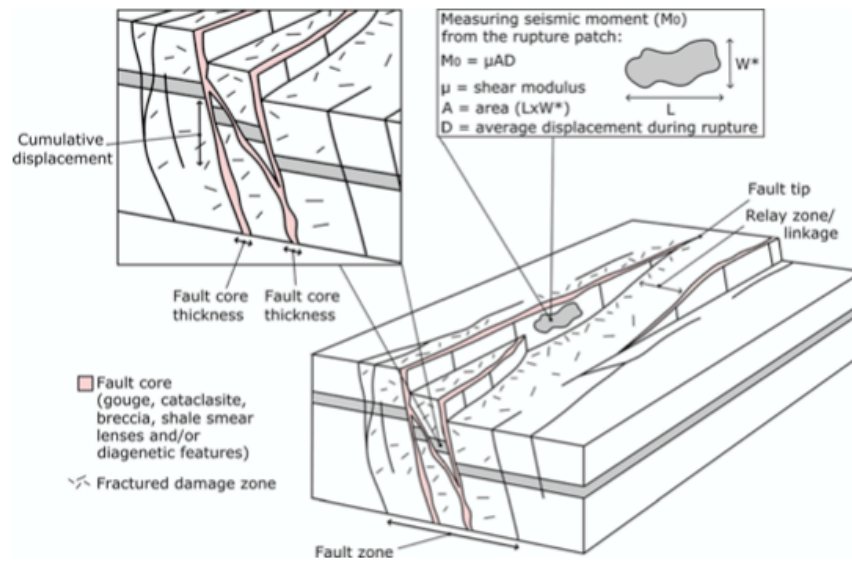
where  $E_T$  is the total energy released,  $E_G$  is the fracture energy needed to create a new surface area,  $E_F$  is the frictional energy required to slide along that surface and  $E_R$  is radiated energy. Seismic data can be used to estimate  $E_G$  and  $E_R$  (from a power-law

dependence with slip and from the seismic moment, respectively) but not  $E_F$  (Shearer, 2009). From a geological perspective, when considering the processes active along faults during coseismic slip,  $E_G$  and  $E_F$  cannot be separated because there are several physical processes that occur near the rupture front and in the surrounding rock (termed damage zone; Fig. 1) that involve frictional and/or fracture energy (Shipton et al., 2006a). These include gouge production, cataclasis, fracturing in the damage zone, the dissolution and growth of minerals and slip weakening mechanisms such as thermal pressurization or silica gel formation (e.g., Kirkpatrick and Shipton, 2009). All of these consume energy, preventing it radiating to the surface. Together, they are referred to as the dissipative energy ( $E_G + E_F$ ). During repeated slip events, energy will continue to be dissipated by these processes in the fault zone (both in the fault core and damage zone).

The physical processes that occur during rupture control the evolution of the fault over time, and hence with increasing total fault displacement. Compilations of data from multiple fault studies have shown that, in general, fault zones get thicker as to-

\* Corresponding author.

E-mail address: [lucy.mckay@strath.ac.uk](mailto:lucy.mckay@strath.ac.uk) (L. McKay).<https://doi.org/10.1016/j.epsl.2021.116757>0012-821X/Crown Copyright © 2021 Published by Elsevier B.V. This is an open access article under the CC BY license (<http://creativecommons.org/licenses/by/4.0/>).



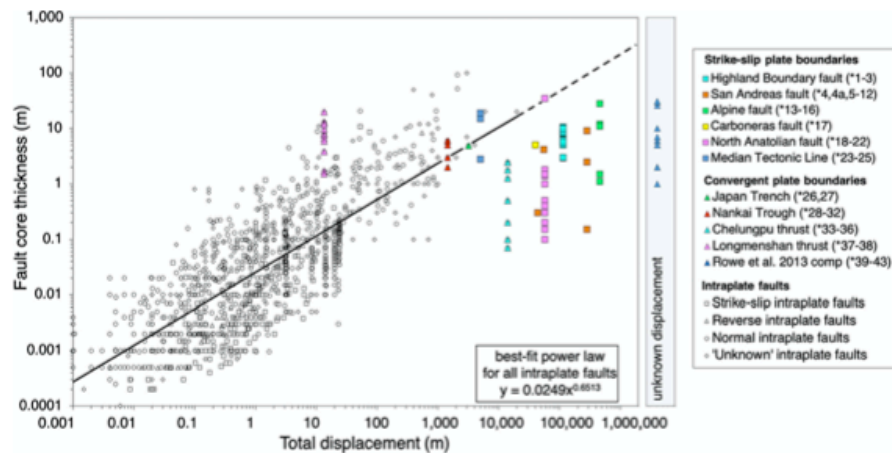
**Fig. 1.** Schematic diagram defining the terms used in this paper. Note, the width dimension,  $W$ , for the slip patch shown in the top right inset is different to *fault core thickness* (measured orthogonal to the fault plane) and *width* (apparent thickness, often measured horizontally). The average displacement during rupture,  $D$  (in the top left inset), is the displacement during a single rupture event, measured in the direction of slip along the rupture patch. This is distinct from cumulative fault displacement, which is an accumulation of the displacement for all rupture/slip events. Figure modified from Childs et al. (2009).

tal displacement increases (e.g., Childs et al., 2009; Shipton et al., 2006b; Torabi et al., 2019; Van Der Zee et al., 2008; Wibberley et al., 2008), albeit with a large range in magnitude of thickness for a given displacement (Shipton et al., 2006b). Torabi et al., 2019 suggest that the exponent and intercept of the power law change depending on the lithology of the faulted rock. It is thought that this increase in thickness is due to the linkage of fault segments via relay formation and breaching (Childs et al., 2009, 2017; Fosson and Rotevatn, 2016 and references therein; Fig. 1). That is, low displacement faults represent a stage of early growth and are thin but evolve into wide fault zones as they extend in length, link with adjacent faults and become more complex in structure. However, the vast majority of the faults in these datasets are from intraplate settings (faults within the interior of tectonic plates and not the boundary of such plates).

The relationship between the total displacement on a fault and the evolution of fault core thickness has not previously been explored for plate boundary faults, even though these are responsible for  $\sim 90\%$  of global seismicity. Here, we compile and harmonise a global dataset of intraplate and plate boundary fault core thickness and total displacement data in order to examine whether these fault systems evolve in a similar way with repeated slip events. Given the interdependence between fault structure and earthquake processes (e.g., Kirkpatrick and Shipton, 2009), we then examine the local structure (fault core composition, wall rock juxtapositions, fault type and number of fault core stands) between all plate boundary faults in our dataset. Further, we examine the scaling relations between seismic moment, average displacement and surface rupture length to compare estimates of radiated seismic energy for intraplate and plate boundary fault events of the same average displacement. Finally, we infer how fault zone processes could cause the systematic differences observed between plate boundary and intraplate fault systems.

## 2. Methods

We first compiled data on fault core thickness (as defined in Fig. 1) and total displacement from the peer-reviewed scientific literature. A fault is typically composed of one or more high-strain fault core(s) surrounded by an associated fractured damage zone (cf. Caine et al., 1996; Fig. 1). We focus on the fault core because the majority of earthquake slip is accommodated by the core and the core thickness is more easily constrained than the damage zone thickness (see Savage and Brodsky, 2011). As the classification method and terminology used to describe fault architecture can be ambiguous (Shipton et al., 2019), we developed an approach designed to harmonise the reported data to facilitate comprehensive comparison. To ensure consistency in our dataset, we only include studies where the thickness and composition (fault rock type) of the fault core are clearly defined and are reported as being distinct from the damage zone. Therefore, as in Torabi et al. (2019), we define the fault core thickness as the cumulative, across-fault thickness of gouge, breccia, cataclasite, shale smear, lenses and/or diagenetic features on both sides of the principal slip plane within a single fault core strand (Fig. 1). If more than one fault core is described for a single fault zone, we estimate the fault core thickness as the total thickness of each individual fault core strand and not the collective thickness across multiple fault cores (i.e., the host rock entrained between the strands is not included in the thickness dataset). To ensure the definition of thickness is consistent, studies which report fault core thickness but provide no information on its composition are not included. Total displacement is measured from slip vector orientations and the separation of markers across the fault (Fig. 1). When a range of total displacement values are reported in the literature, we calculated and plotted the arithmetic mean  $\pm$  the difference to the minimum and maximum value. For example, if the total displacement was reported to be 100 to 150 km, we considered the fault offset to be  $125 \pm 25$  km. The  $\pm$  values are plotted as error bars in (Fig. 2), though are smaller than



**Fig. 2.** Log-log plot of fault core thickness and total displacement for intraplate (greyscale) and plate boundary (colour) faults. The trendline shows the linear, statistically significant ( $p$  value 0.0004) relationship between fault core thickness and total displacement for intraplate faults and is extrapolated to large displacement values. There is no trend for plate boundary faults ( $p$  value 0.155). Error bars for individual displacement and fault core thickness are smaller than the size of each data point (see the Supplementary Information Table S1 for errors/uncertainty ranges associated with each data point). Displacement is unknown for the data in the Rowe et al. (2013) compilation due to a lack of preserved displacement markers. Strike-slip faults are represented by squares, reverse/thrust faults by triangles, normal faults by circles and an unknown sense of motion by diamonds. See the Supplementary Information for a description and sources of all data.

the data symbols and are given in the supplementary information (Table S1).

We use the same criteria to compile data for plate boundary faults, where the fault core refers to zones accommodating most of the strain across the fault. In total we find data for 75 sites on 13 plate boundary faults. Our dataset combines our own field observations of the exhumed Highland Boundary fault (McKay et al., 2020) with field and borehole studies of both modern and ancient examples of plate boundary faults. These include the San Andreas fault (Holdsworth et al., 2011; Moore and Rymer, 2012), North Anatolian fault (Dor et al., 2008), Alpine fault (Barth et al., 2013; Toy et al., 2015), Carboneras fault (Faulkner et al., 2003), Median Tectonic Line (Wibberley and Shimamoto, 2003), Nankai Trough (Ujii and Kimura, 2014), Japan Trench (Kirkpatrick et al., 2015), Chelungpu thrust (Heermance et al., 2003; Yeh et al., 2007), Longmenshan thrust (Li et al., 2013) and ancient subduction boundaries from the compilation of Rowe et al. (2013). Where available, we include all reported data points along a single plate boundary fault to capture the spatial heterogeneity along-strike. Using this data, we then construct schematic structural logs to compare the local structure both along an individual plate boundary and between plate boundaries.

To complement our findings on intraplate and plate boundary fault thicknesses, we gather data from the peer-reviewed scientific literature to examine earthquake scaling relations between intraplate and plate boundary fault events. We focus on the scaling relations between seismic moment, average displacement and surface rupture length. We extend the dataset of Scholz et al. (1986) by determining which earthquakes in the Wells and Coppersmith (1994) dataset are plate boundary or intraplate fault events and by adding in examples from Wesnousky (2006, 2008). We separate the data based on fault type (plate boundary and intraplate fault events) and also by the method in which the seismic moment was determined (derived from seismological observations or from field observations). The calculation of seismic moment from field observations uses an estimate of the average fault displacement (Fig. 1). Since our aim is to investigate the relationship between seismic moment, average displacement and surface rupture length, our analyses focus on those events for which the seismic mo-

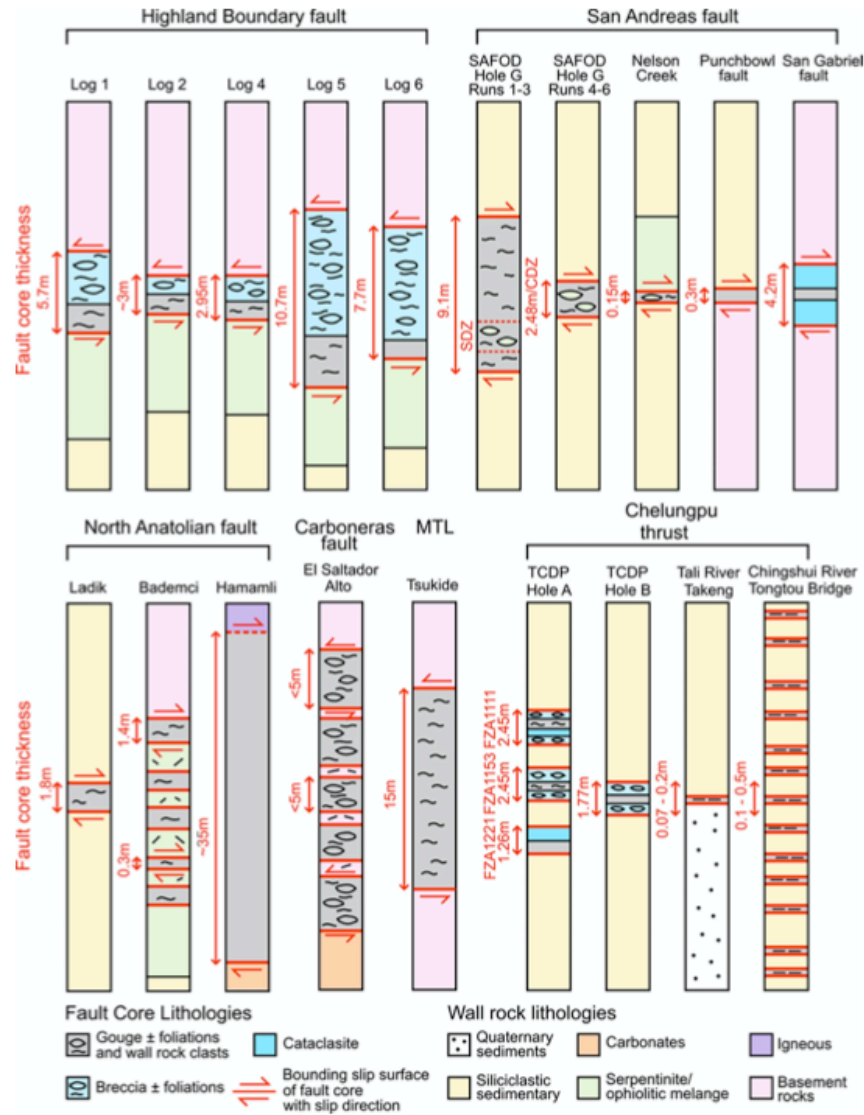
ment has been determined from the frequency spectrum of the recorded displacement (frequency spectrum analyses or moment tensor solutions). Thus, we ensure all measurements are independently derived and prevent a circular argument; no assumptions are made about the fault dimensions in modelling the seismic energy release (seismic moment).

### 3. Results

#### 3.1. Comparing fault core thickness and total displacement for intraplate and plate boundary faults

Like previous compilations (Childs et al., 2009; Shipton et al., 2006b; Torabi et al., 2019; Van Der Zee et al., 2008; Wibberley et al., 2008), we obtain a statistically significant ( $p$  value 0.0004), positive power-law trend between fault core thickness and total displacement for intraplate faults over several orders of magnitude (Fig. 2). In our dataset there is a higher number of lower displacement intraplate faults (between 0.01 m and 24 m), perhaps reflecting the difficulty in identifying a reliable or preserved displacement marker for faults with larger total displacement. For intraplate faults with total displacement values between 0.01 m and 24 m the trendline sits in the middle of the data. Yet when the total displacement of intraplate faults is  $>24$  m the trendline does not plot in the centre of the data and thus underpredicts the thickness of larger displacement intraplate faults (displacement  $>24$  m).

Based on the observed relationship for intraplate faults, plate boundary faults with large total displacement values ( $>1000$  m) would be expected to have wide fault cores. However, we find plate boundary faults are distinct from the trend (Fig. 2). Instead, plate boundary faults are consistently narrow with fault core thicknesses between 0.07 m and  $\sim 35$  m and there is no statistically significant ( $p$  value 0.155) relationship with total displacement. This finding is regardless of either the fault type (strike-slip or convergent, there are no data for divergent boundaries) or the distance along-strike. Interestingly, whilst plate boundary faults are consistently 1-2 orders of magnitude narrower than would be predicted by the trend for intraplate faults, their variability along-



**Fig. 3.** Schematic structural logs illustrating fault core thickness and composition for plate boundary faults. MTL, Median Tectonic Line. See Supplementary Information for the full set of Logs and data.

strike is similar; the thickness of both intraplate and plate boundary faults ranges by 2-3 orders of magnitude for a single value of displacement on an individual fault. Therefore, despite plate boundary faults being consistently narrower, the along-strike variance in fault thickness is similar.

### 3.2. Plate boundary fault structure and composition

Data from intraplate faults show that, in general, low displacement faults are thin but evolve into wide fault zones as they extend in length, link with adjacent faults and develop more complex

structures (Childs et al., 2009, 2017; Fossen and Rotevatn, 2016 and references therein; Fig. 1). Based on this rationale we could hypothesise that plate boundary fault cores are consistently narrower than intraplate faults because they have simple, uniform structures. To test this, we constructed schematic structural logs for each plate boundary exposure and drill core intersection reported in the published scientific literature. Fig. 3 shows a sub-set of these logs: the full set is available in the supplementary information (Fig. S2 and S3). Whilst all these plate boundary faults are narrow, their structures are not the same or simple. For example, the Highland Boundary fault (HBF) is a sinistral strike-slip

fault with  $115 \pm 85$  km total displacement (McKay et al., 2020 and references therein). In all mapped exposures the fault core is a single strand that varies in thickness between 2.95 to 10.7 m (Fig. 3) (McKay et al., 2020). The host rocks remain constant along-strike as the fault separates serpentinite from basement rocks at all exposures. In contrast, the fault core of the dextral strike-slip North Anatolian fault (NAF) remains narrow despite juxtaposing different host rock lithologies along-strike (Fig. 3) (Dor et al., 2008). Unlike the HBF and NAF, the Chelungpu thrust is a convergent boundary with a minimum of 14 km total displacement (Heermance and Evans, 2006). The fault principally slips within siliciclastic sedimentary rocks. At some exposures the fault core is composed of a single strand that varies in thickness between 0.07 to 1.77 m (Heermance et al., 2003; Yeh et al., 2007). At other exposures the fault core consists of multiple strands each ranging in thickness from 0.1 to 2.45 m (Fig. 3 and S2 and S3) (Heermance et al., 2003; Yeh et al., 2007). Thus, the fact that plate boundaries are narrow appears not to be related to the host rock, slip directions, plate boundary type (strike-slip or convergent), distance along-strike or the number of fault strands. These all vary, but the plate boundaries remain comparatively narrow.

Based on this small dataset it may be the case that the fault core is narrowest when wall rocks of contrasting competencies juxtapose the fault, i.e., mechanically weak serpentinite against basement or sedimentary rock, compared to basement against basement or sedimentary against sedimentary with similar competencies. For example, the San Andreas fault is narrowest (0.15 m) when serpentinite juxtaposes sedimentary rocks (Moore and Rymer, 2012) and widest (9.1 m) when sedimentary rock juxtaposes sedimentary rock (Holdsworth et al., 2011) (Fig. 3). This suggests the strength contrast between the faulted layers (mechanical stratigraphy) may, in part, control the variations in fault core thickness along-strike, but it clearly does not control the average thickness.

### 3.3. Comparing intraplate and plate boundary fault earthquake events

To examine whether there is any evidence in the seismological literature for a difference in the energy emitted by intraplate and plate boundary faults we examined the scaling relations between seismic moment, average displacement and surface rupture length. Seismic moment ( $M_0$ ) is a measure of the "size" or "work" of an earthquake (Bormann et al., 2013). It can be calculated from fault slip dimensions measured in the field or from aftershock distributions using the formula (equation (2)):

$$M_0 = \mu AD \quad (2)$$

where,  $\mu$  is the shear modulus,  $A$  is the event rupture area and  $D$  is the average displacement on the fault during coseismic rupture i.e. the average displacement caused by the individual seismic event (Fig. 1; Kanamori and Anderson, 1975; Kanamori and Brodsky, 2001). The approach for the calculation of the area depends to a degree on the source (kinematic) model (circular, rectangular, elliptical), for example for small faults and earthquakes, Brune's circular model is considered adequate. The rectangular plane is considered adequate for large earthquakes. Alternatively,  $M_0$  can be measured from the source spectra of body or surface waves (from the integral of the far-field displacement, or from the amplitude of the near-field displacement) or is derived from a moment tensor solution (Bormann et al., 2013). As such, calculating the seismic moment from spectral analyses is independent from average displacement. Whilst  $M_0$  is not a direct measure of energy, it is linearly related to the radiated seismic energy ( $E_R$ ) by the formula (equation (3)):

$$E_R \approx \eta_R \frac{\Delta\sigma_S}{2\mu} M_0 \quad (3)$$

where,  $\eta_R = E_R/(E_R + E_G)$  is radiated efficiency and  $\Delta\sigma_S$  is the static stress drop, i.e., the difference between shear stresses on the fault before and after the earthquake (Bormann et al., 2013; Venkataraman and Kanamori, 2004 and references therein). As stated by Kanamori and Brodsky (2004),  $M_0$  is also linearly related to the magnitude ( $M_w$ ) by the formula (equation (4)):

$$M_w = (\log M_0 - 9.1)/1.5 \quad (4)$$

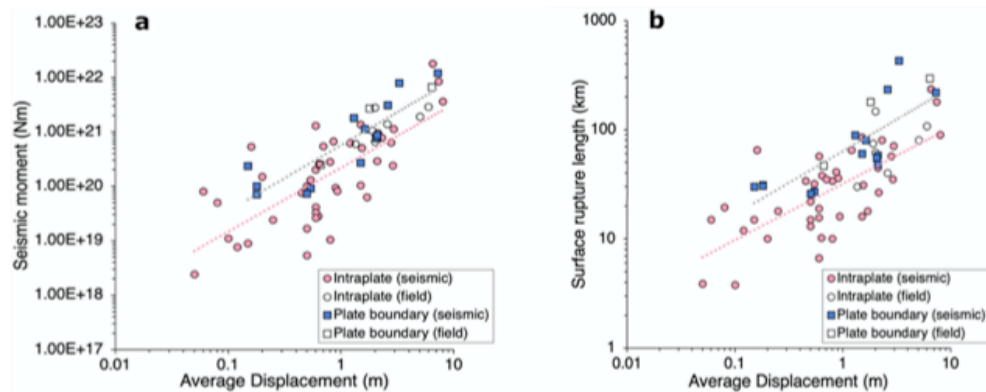
Thus, the higher the seismic moment, the higher the radiated seismic energy and the higher the magnitude of the resulting earthquake.

We find that for a given value of average displacement, plate boundary fault earthquakes typically have a greater seismic moment (Fig. 4a) and rupture a longer length at the surface (Fig. 4b) compared to intraplate faults. Values for seismic moment in Fig. 4a are taken from Wells and Coppersmith (1994) and only where such values have been derived from spectral analysis of the seismic data (i.e. are independent of measured displacement). Our analyses show the best-fit line derived only from those events for which seismic moment has been derived from spectral analyses (as explained previously); however, for information, seismic events with field-derived seismic moments are also included on (Fig. 4) (unfilled symbols) and clearly show the same trends. These findings imply that plate boundary faults do not dissipate as much energy as intraplate faults during earthquakes meaning that for a given value of average displacement, more energy is radiated to the surface resulting in a greater seismic moment and hence a higher magnitude earthquake.

## 4. Discussion

For the first time fault core thickness and total displacement data have been compared for plate boundary and intraplate faults. We observe that plate boundary faults are anomalous when compared to the global population of intraplate faults; they have narrower fault cores and the fault core thickness does not increase with increasing displacement. Keren and Kirkpatrick (2016) previously observed that the damage zone thickness of the Japan Trench was anomalously narrow and did not follow the damage zone thickness - displacement trend described for intraplate faults (Mayolle et al., 2019 and references therein). It may be possible that a similar compilation of damage zone thicknesses may also show that plate boundary faults have anomalously narrow damage zones compared to intraplate faults. This would make sense given that plate boundary fault zones dissipate less energy (Fig. 4), therefore less energy is available to deform the surrounding rock. Data on fault core thickness were only included in Fig. 2 where the difference between the fault core and the fault damage zone was clearly described. Future research could explore whether fault damage zones are also anomalously narrow on plate boundary faults.

Scholz et al. (1986), state that intraplate fault cores are thin (gouge thicknesses 1-10 m), whereas plate boundary faults are wide (gouge thickness 100-1000 m) as a result of increased continuous dynamic wear of the wall rock with increased total displacement. However, no data are provided to back up this statement and our compilation of published data (Fig. 2) contradicts their proposition. From our compilation of plate boundary structures (Fig. 3), we suggest plate boundary fault cores are consistently narrow by comparison to intraplate faults and that this is regardless of the complexity of the plate boundary structure. The fault core composition, host rock, slip direction, fault type, and/or the number of fault core strands all vary, both along an individual plate boundary



**Fig. 4.** Comparing intraplate and plate boundary fault earthquake events. **a)** Log-log plot of average displacement against seismic moment. We separate the data based on fault type (plate boundary fault – squares; intraplate faults – circles) and also the method in which the seismic moment was determined (derived from seismological data – colour, derived from field data – unfilled). We only show the best-fit line where the seismic moment has been derived from seismological data (spectral analysis of displacement data) as the axes are truly independent. The fit line colour matches data points (blue – plate boundary; pink – intraplate events). **b)** Log-log plot of average displacement and surface rupture length of the fault associated with the earthquake event. The average displacement is not available for all events; therefore, the plots do not show exactly the same events.

and on comparison between different plate boundaries, but in all examples the fault core remains consistently narrow.

We suggest plate boundary faults remain narrow as they are not required to grow in the same way as intraplate faults. Intraplate faults get wider with increasing displacement through lateral tip processing and/or linkage with other fault segments via relay formation and breaching (Childs et al., 2009, 2017; Fossen and Rotevatn, 2016 and references therein; Fig. 1). That is, low displacement faults represent a stage of early growth and are thin but evolve into wide fault zones as they extend in length, link with adjacent faults and become more complex in structure. Plate boundary faults start as pre-existing, inherited structures on regional-scale zones of weakness. As such, their tips do not terminate within intact rock – they terminate at triple junctions with other plate boundaries (McKenzie and Morgan, 1969). Tectonic plates are continually rearranging themselves. For instance, the boundary between the North American and Pacific Plate evolved through time from a subduction boundary to the present-day San Andreas transform fault. As a result, while plate boundary faults still grow and evolve through time as triple junctions and plates move apart relative to each other, they are not required to grow in length either by damaging intact rock at their tips or by linking with other pre-existing structures (as shown for intraplate faults in Fig. 1). The lack of linkage zones will tend to produce smoother structures. The lack of a relationship between fault zone thickness and total displacement on plate boundaries tends to support the hypothesis proposed by Delogkos et al. (2020) for growth of intraplate faults. They suggest that fault cores increase in thickness only due to progressive fault linkage, and that once they reach a sufficient thickness they can accommodate slip events without continuous processing of the wall rock – as appears to be the case for plate boundary faults.

Several authors have demonstrated that the more total displacement a fault accumulates, the smoother and straighter its surface geometry (e.g., Brodsky et al., 2011; de Jossineau and Aydin, 2009; Sagy et al., 2007; Stirling et al., 1996; Wesnousky, 1988). Therefore, plate boundary faults with large total displacement values should be expected to have smooth and straight surface geometries as proposed by Wesnousky (1988). Using a combination of rock friction experiments and numerical modelling, Zielke et al. (2017) discuss the role of fault roughness on the stress drop and

earthquake magnitude and postulate that smoother faults generate larger earthquakes compared to rougher faults under the same tectonic loading conditions. That is, faults with smoother surfaces do not need to consume as much energy to slip (i.e. dissipate less energy) compared to faults with rougher surfaces. The observations we present support the hypothesis of Zielke et al. (2017). Fig. 4b demonstrates that for a given value of average displacement, plate boundary faults rupture a longer length at the surface compared to intraplate faults. This implies that it may not be as easy to terminate a rupture on a plate boundary as on a rougher intraplate fault, which makes sense if they are narrow (Fig. 2), smooth (Wesnousky, 1988) and terminate at triple junctions and not within intact rock. Further, as demonstrated by the 1992 Landers earthquake, extra energy is required to hop over segments within faults (Hauksson et al., 1993). Therefore plate boundary faults, which are long structures not formed via fault linkage, will absorb less energy through segment hopping, allowing more energy to be radiated to the surface, manifested as higher magnitude earthquakes. By contrast, intraplate faults dissipate energy and get wider as cumulative fault slip increases, generating complex zones of damage in the surrounding rock and propagating through linkage with neighbouring structures (Fig. 1). The more complex the final fault geometry, the more energy has to be consumed at depth and the less energy reaches the surface (Ross et al., 2018).

## 5. Conclusions

Fault cores are well documented as getting wider and developing more complex geometries with increasing total displacement, albeit with a wide range in thicknesses at a single value of displacement. This increase in thickness occurs through the linkage of fault segments with increasing total displacement and/or repeated rupture events that comminute fault slip surfaces and progressively fracture the surrounding intact rock at the fault tips and in a zone of damage that surrounds the fault. We have compiled data from the peer-reviewed literature to show that this relationship between fault core thickness and increasing displacement does not hold for plate boundary faults, which are anomalously narrow by comparison to intraplate faults and do not show the same trend of increasing average thickness with increasing displacement. From a compilation of plate boundary structures, we find plate boundary

faults remain narrow regardless of how many earthquake events they have experienced or their local fault structure (fault core composition, host rock juxtaposition, slip direction, fault type, and/or the number of fault core strands). By examining the scaling relations between seismic moment, average displacement and surface rupture length for plate boundary and intraplate fault ruptures, we confirm that plate boundary faults display a greater seismic moment than intraplate faults for a given displacement and show that they also rupture a longer length. We propose that this occurs because plate boundary faults are anomalously narrow, they are comparatively smooth and terminate at triple junctions and not intact rock, and since our data show they do not increase in thickness with increasing displacement, they are not processing intact rock as much during seismic events. Thus, plate boundary faults do not dissipate as much energy as intraplate faults during earthquakes meaning that for a given value of average displacement, more energy is radiated to the surface resulting in higher magnitude earthquakes.

#### CRedit authorship contribution statement

**L. McKay:** Conceptualization, Data curation, Formal analysis, Funding acquisition, Investigation, Visualization, Writing – original draft. **R.J. Lunn:** Conceptualization, Supervision, Visualization, Writing – review & editing. **Z.K. Shipton:** Conceptualization, Funding acquisition, Supervision, Writing – review & editing. **S. Pytharoulis:** Conceptualization, Investigation, Writing – review & editing. **J.J. Roberts:** Conceptualization, Writing – review & editing.

#### Declaration of competing interest

The authors declare that they have no known competing financial interests or personal relationships that could have appeared to influence the work reported in this paper.

#### Supplementary material/data statement

Data compiled in this study can be found in the supplementary information and is available from the University of Strathclyde KnowledgeBase at <https://doi.org/10.15129/21271686-f115-4f9d-bf9a-ac681fd6f15b>.

#### Acknowledgements

This work is funded by an Environmental and Physical Science Research Council (EPSRC) Doctoral Training Partnership (DTP) grant awarded to LM (EP/N509760/1). The paper benefited from reviews by two anonymous reviewers.

#### Appendix A. Supplementary material

Supplementary material related to this article can be found online at <https://doi.org/10.1016/j.epsl.2021.116757>.

#### References

- Barth, N.C., Boulton, C., Carpenter, B.M., Batt, G.E., Toy, V.G., 2013. Slip localization on the southern Alpine Fault New Zealand. *Tectonics* 32, 620–640. <https://doi.org/10.1002/tect.20041>.
- Bormann, P., Wendt, S., Di Giacomo, D., 2013. Seismic sources and source parameters. In: Bormann, P. (Ed.), *New Manual of Seismological Observatory Practice 2 (NMSOP2)*. Deutsches GeoForschungsZentrum GFZ, Potsdam, pp. 1–259.
- Brodsky, E.E., Gilchrist, J.J., Saay, A., Collettini, C., 2011. Faults smooth gradually as a function of slip. *Earth Planet. Sci. Lett.* 302, 185–193. <https://doi.org/10.1016/j.epsl.2010.12.010>.
- Caine, J.S., Evans, J.P., Forster, C.B., 1996. Fault zone architecture and permeability structure. *Geology* 24, 1025–1028. [https://doi.org/10.1130/0091-7613\(1996\)024<1025](https://doi.org/10.1130/0091-7613(1996)024<1025).
- Childs, C., Holdsworth, R.E., Jackson, C.A.-L., Manzocchi, T., Walsh, J.J., Yielding, G., 2017. Introduction to the geometry and growth of normal faults. In: Childs, C., Holdsworth, R.E., Jackson, C.A.-L., Manzocchi, T., Walsh, J.J., Yielding, G. (Eds.), *The Geometry and Growth of Normal Faults*. Geological Society, London. In: *Special Publications*, vol. 439, pp. 1–9.
- Childs, C., Manzocchi, T., Walsh, J.J., Bonson, C.G., Nicol, A., Schöpfer, M.P.J., 2009. A geometric model of fault zone and fault rock thickness variations. *J. Struct. Geol.* 31, 117–127. <https://doi.org/10.1016/j.jsg.2008.08.009>.
- de Jossineau, G., Aydin, A., 2009. Segmentation along strike-slip faults revisited. *Pure Appl. Geophys.* 166, 1575–1594. <https://doi.org/10.1007/s00024-009-0511-4>.
- Delogkos, E., Manzocchi, T., Childs, C., Camanni, G., Roche, V., 2020. The 3D structure of a normal fault from multiple outcrop observations. *J. Struct. Geol.* 136, 1–18. <https://doi.org/10.1016/j.jsg.2020.104009>.
- Dor, O., Yildirim, C., Rockwell, T.K., Ben-Zion, Y., Emre, O., Sisk, M., Duman, T.Y., 2008. Geological and geomorphologic asymmetry across the rupture zones of the 1943 and 1944 earthquakes on the North Anatolian Fault: possible signals for preferred earthquake propagation direction. *Geophys. J. Int.* 173, 483–504. <https://doi.org/10.1111/j.1365-246X.2008.03709.x>.
- Faulkner, D.R., Lewis, A.C., Rutter, E.H., 2003. On the internal structure and mechanics of large strike-slip fault zones: field observations of the Carboneras fault in southeastern Spain. *Tectonophysics* 367, 235–251. [https://doi.org/10.1016/S0040-1951\(03\)00134-3](https://doi.org/10.1016/S0040-1951(03)00134-3).
- Fossen, H., Rotevatn, A., 2016. Fault linkage and relay structures in extensional settings—a review. *Earth-Sci. Rev.* 154, 14–28. <https://doi.org/10.1016/j.earscirev.2015.11.014>.
- Hauksson, E., Jones, L.M., Hutton, K., Eberhart-Phillips, D., 1993. The 1992 Landers earthquake sequence: seismological observations. *J. Geophys. Res.* <https://doi.org/10.1029/93jB02384>.
- Heermance, R., Shipton, Z.K., Evans, J.P., 2003. Fault structure control on fault slip and ground motion during the 1999 rupture of the Chelungpu fault, Taiwan. *Bull. Seismol. Soc. Am.* 93, 1034–1050. <https://doi.org/10.1785/0120010230>.
- Heermance, R.V., Evans, J.P., 2006. Geometric evolution of the Chelungpu fault, Taiwan: the mechanics of shallow frontal ramps and fault imbrication. *J. Struct. Geol.* 28, 929–938. <https://doi.org/10.1016/j.jsg.2006.01.015>.
- Holdsworth, R.E., Van Diggelen, E.W.E., Spiers, C.J., De Bresser, J.H.P., Walker, R.J., Bowen, L., 2011. Fault rocks from the SAFOD core samples: implications for weakening at shallow depths along the San Andreas Fault, California. *J. Struct. Geol.* 33, 132–144. <https://doi.org/10.1016/j.jsg.2010.11.010>.
- Kanamori, H., Anderson, D.L., 1975. Theoretical basis of some empirical relations in seismology. *Bull. Seismol. Soc. Am.* 65, 1073–1095.
- Kanamori, H., Brodsky, E.E., 2004. The physics of earthquakes. *Rep. Prog. Phys.* 67, 1429–1496. <https://doi.org/10.1088/0034-4885/67/8/R03>.
- Kanamori, H., Brodsky, E.E., 2001. The physics of earthquakes. *Phys. Today* 54, 34–40. <https://doi.org/10.1063/1.1387590>.
- Keren, T.T., Kirkpatrick, J.D., 2016. The damage is done: low fault friction recorded in the damage zone of the shallow Japan Trench decollement. *J. Geophys. Res., Solid Earth* 121, 3804–3824. <https://doi.org/10.1002/2015JB012311>.
- Kirkpatrick, J.D., Rowe, C.D., Ujiie, K., Moore, J.C., Regalla, C., Remitti, F., Toy, V., Wolfson-schwehr, M., Kameda, J., Bose, S., Chester, F.M., 2015. Structure and lithology of the Japan Trench subduction plate boundary fault. *Tectonics* 34, 53–69. <https://doi.org/10.1002/2014TC003695>.
- Kirkpatrick, J.D., Shipton, Z.K., 2009. Geologic evidence for multiple slip weakening mechanisms during seismic slip in crystalline rock. *J. Geophys. Res.* 114, 1–14. <https://doi.org/10.1029/2008JB006037>.
- Li, H., Wang, H., Xu, Z., Si, J., Pei, J., Li, T., Huang, Y., Song, S.R., Kuo, L.W., Sun, Z., Chevalier, M.L., Liu, D., 2013. Characteristics of the fault-related rocks, fault zones and the principal slip zone in the Wenchuan Earthquake Fault Scientific Drilling Project Hole-1 (WFSD-1). *Tectonophysics* 584, 23–42. <https://doi.org/10.1016/j.tecto.2012.08.021>.
- Mayolle, S., Soliva, R., Caniven, Y., Wibberley, C., Ballas, G., Milesi, G., Dominguez, S., 2019. Scaling of fault damage zones in carbonate rocks. *J. Struct. Geol.* 124, 35–50. <https://doi.org/10.1016/j.jsg.2019.03.007>.
- McKay, L., Shipton, Z.K., Lunn, R.J., Andrews, B., Raub, T.D., Boyce, A.J., 2020. Detailed internal structure and along-strike variability of the core of a plate boundary fault: The Highland Boundary fault, Scotland. *J. Geol. Soc. (Lond.)* 177, 283–296. <https://doi.org/10.1144/jgs2018-226>.
- McKenzie, D.P., Morgan, W.J., 1969. Evolution of triple junctions. *Nature* 224, 125–133.
- Moore, D.E., Rymer, M.J., 2012. Correlation of clayey gouge in a surface exposure of serpentinite in the San Andreas Fault with gouge from the San Andreas Fault Observatory at Depth (SAFOD). *J. Struct. Geol.* 38, 51–60. <https://doi.org/10.1016/j.jsg.2011.11.014>.
- Ross, Z.E., Kanamori, H., Hauksson, E., Aso, N., 2018. Dissipative intraplate faulting during the 2016 Mw 6.2 Tottori, Japan earthquake. *J. Geophys. Res., Solid Earth* 123, 1631–1642. <https://doi.org/10.1002/2017JB015077>.
- Rowe, C.D., Moore, J.C., Remitti, F., 2013. The thickness of subduction plate boundary faults from the seafloor into the seismogenic zone. *Geology* 41, 991–994. <https://doi.org/10.1130/G34556.1>.
- Sagy, A., Brodsky, E.E., Axen, G.J., 2007. Evolution of fault-surface roughness with slip. *Geology* 35, 283–286. <https://doi.org/10.1130/G23235A.1>.

- Savage, H.M., Brodsky, E.E., 2011. Collateral damage: evolution with displacement of fracture distribution and secondary fault strands in fault damage zones. *J. Geophys. Res.* 116, 1–14. <https://doi.org/10.1029/2010JB007665>.
- Scholz, C.H., Aviles, C.A., Wesnousky, S.G., 1986. Scaling differences between large interplate and intraplate earthquakes. *Bull. Seismol. Soc. Am.* 76, 65–70.
- Shearer, P.M., 2009. *Introduction to Seismology*, 2nd ed. Cambridge University Press, Cambridge.
- Shipton, Z.K., Evans, J.P., Abercrombie, R.E., Brodsky, E.E., 2006a. The missing sinks: slip localization in faults, damage zones, and the seismic energy budget. In: Abercrombie, R., McGarr, A., Di Toro, G., Kanamori, H. (Eds.), *Earthquakes: Radiated Energy and the Physics of Faulting*. American Geophysical Union, Washington D.C., pp. 193–198. [http://refhub.elsevier.com/S0012-821X\(21\)00016-9/bib1DD56AFAA762224B807FD9D49430088A51](http://refhub.elsevier.com/S0012-821X(21)00016-9/bib1DD56AFAA762224B807FD9D49430088A51)
- Shipton, Z.K., Roberts, J.J., Collettini, C., 2006b. Fault damage zones: cognitive biases and implications for seismic hazard analysis. *J. Geophys. Res.* 111, B08301. <https://doi.org/10.1029/2005JB004001>.
- Urai, J.L., Dee, S., Wilson, D., 2006. The influence of layering and pre-existing joints on the development of internal structure in normal fault zones: the Lodève basin, France. In: Wibberley, C.A.J., Kurz, W., Imber, J., Holdsworth, R.E., Collettini, C. (Eds.), *The Internal Structure of Fault Zones: Implications for Mechanical and Fluid-Flow Properties*. In: Special Publications, vol. 299. Geological Society, London, pp. 57–74.
- Venkataraman, A., Kanamori, H., 2004. Observational constraints on the fracture energy of subduction zone earthquakes. *J. Geophys. Res., Solid Earth* 109, 1–20. <https://doi.org/10.1029/2003JB002549>.
- Wells, D.L., Coppersmith, K.J., 1994. New empirical relationships among magnitude, rupture length, rupture width, rupture area, and surface displacement. *Bull. Seismol. Soc. Am.* 84, 974–1002. <https://doi.org/10.1029/B08406>.
- Wesnousky, S.G., 2008. Displacement and geometrical characteristics of earthquake surface ruptures: issues and implications for seismic-hazard analysis and the process of earthquake rupture. *Bull. Geol. Soc. Am.* 98, 1609–1632. <https://doi.org/10.1785/B0120070111>.
- Wesnousky, S.G., 2006. Predicting the endpoints of earthquake ruptures. *Nature* 444, 358–360. <https://doi.org/10.1038/nature05275>.
- Wesnousky, S.G., 1988. Seismological and structural evolution of strike-slip faults. *Nature* 335, 340–343. <https://doi.org/10.1038/335340a0>.
- Wibberley, C.A.J., Shimamoto, T., 2003. Internal structure and permeability of major strike-slip fault zones: The Median Tectonic Line in Mie Prefecture, Southwest Japan. *J. Struct. Geol.* 25, 59–78. [https://doi.org/10.1016/S0191-8141\(02\)00014-7](https://doi.org/10.1016/S0191-8141(02)00014-7).
- Wibberley, C.A.J., Yielding, G., Di Toro, G., 2008. Recent advances in the understanding of fault zone internal structure: a review. In: Wibberley, C.A.J., Kurz, W., Imber, J., Holdsworth, R.E., Collettini, C. (Eds.), *Special Publications*. Geological Society, London, pp. 5–33.
- Yeh, E.C., Sone, H., Nakaya, T., Ian, K.H., Song, S.R., Hung, J.H., Lin, W., Hirono, T., Wang, C.Y., Ma, K.F., Soh, W., Kinoshita, M., 2007. Core description and characteristics of fault zones from Hole-A of the Taiwan Chelungpu-Fault Drilling Project. *Terr. Atmos. Ocean. Sci.* 18, 327–357. [https://doi.org/10.3319/TAO.2007.18.2.327\(TCDP\)](https://doi.org/10.3319/TAO.2007.18.2.327(TCDP)).
- Zielke, O., Galis, M., Mai, P.M., 2017. Fault roughness and strength heterogeneity control earthquake size and stress drop. *Geophys. Res. Lett.* 44, 777–783. <https://doi.org/10.1002/2016GL071700>.



# Appendix 4 – Details of the Compiled Fault Core Thickness – Displacement Dataset in Chapter 4

This Appendix gives a detailed description of how the compiled dataset in **Fig. 4.2** was established. Except from my own field data from the Highland Boundary fault (Chapter 3), all other data was compiled from the peer-reviewed scientific literature. In total we found data for 75 sites on 13 plate boundary faults. These are described in more detail below.

## *San Andreas fault*

The San Andreas fault (SAF) is a major, steeply dipping, dextral strike-slip boundary that accommodates the majority of relative motion between the Pacific and North American Plates. Rocks to the east of the SAF on the North American Plate consist of folded and faulted Tertiary through Jurassic siliciclastic rocks, mélange of the Jurassic Franciscan Formation, and sheared serpentinite tectonically emplaced from the Coastal Range Ophiolite. The Pacific Plate assemblage west of the SAF consists of Tertiary sedimentary rocks and Mesozoic granitoids (Bradbury et al., 2011 and references therein). The remarkably straight surface trace extends for >1000 km NW to SE along the west coast of California and is associated with a complex zone of smaller, linked faults such as the San Jacinto and Garlock faults, that help accommodate some of the strain of relative plate motion (Wesnousky 2005). The total displacement of the SAF has been reported as ~250 km (Wesnousky 1988) based on the separation of the correlative Neenach and Pinnacles volcanic rocks (Matthews 1976). but this may not include 50–60 km of slip on the San Gabriel fault (Dor *et al.* 2006). However, these volcanics are younger than most of the fault strands that are part of the fault system so ~250 km must be a minimum estimate. Others have reported total displacements of 315 km based on the separation of Pelona schist and other basement units (Dibblee 1989).

The plate boundary fault structure was revealed by Phase 2 and 3 of the \$25M San Andreas Fault Observatory at Depth (SAFOD) drilling project that intersected the fault at ~3 km depth near Parkfield, California (e.g., Bradbury *et al.* 2011, 2014; Holdsworth *et al.* 2011 and references therein). The drill site was located within a transitional zone between the central, actively creeping segment of the SAF and segments that produce large earthquakes (Bradbury *et al.* 2011). The three drill cores sampled both host and fault rocks. Hole G (core runs 4-6) sampled the 2.48 m thick, actively creeping Central Deforming Zone (CDZ) composed of foliated, smectite(saponite)-rich, serpentinite-bearing, grey gouge (Bradbury *et al.* 2011; Holdsworth *et al.* 2011). Hole G (core runs 1-3) sampled the 1.6 m thick, less active, southwest deforming zone (SDZ) composed of the same foliated, smectite-rich, serpentinite-bearing, grey gouge as the CDZ (Bradbury *et al.* 2011; Holdsworth *et al.* 2011). The SDZ is set within a ~9.1 m thick zone of grey, foliated gouge (see Fig. 1 in Holdsworth *et al.* 2011). For the purpose of data collation, using our criteria for defining the fault core thickness, 9.1 m was taken as the total thickness of the fault core for Hole G (core runs 1-3). Both the CDZ and SDZ gouges display highly-sheared, scaly fabrics wrapping around isolated, cm-scale serpentinite and sedimentary clasts that are elongate parallel to foliation (Bradbury *et al.* 2011).

Surface exposures of the core of the SAF are exposed at Nelson Creek, ~2.4 km NNE of the SAFOD drill site (Moore & Rymer, 2012). Here, a ~3 km thick tectonic sliver of serpentinite, that extends for several kilometres along-strike of the surface trace, is faulted against Tertiary sandstones and siltstones on both sides. Smectite(saponite)-rich gouge, similar to that observed in the active SDZ and CDZ was observed in a fault core zone measuring 0.15 m thick (Moore & Rymer, 2012). It is inferred the surface exposure of gouge at Nelson Creek correlates to one or both of the gouge zones in the SAFOD core at depth. All three gouges (surface exposures, CDZ and SDZ) are interpreted as the product of shear-enhanced, fluid-assisted, metasomatic reaction between the serpentinite and quartzo-feldspathic crustal wall rocks of contrasting chemistry (Moore and Rymer, 2012 and references therein).

### ***Punchbowl and San Gabriel***

The Punchbowl and San Gabriel faults are ancient, dextral strike-slip faults of the SAF system with large total displacement values. These faults are included in the dataset as both faults likely represented the main trace of the SAF during the Miocene and Pliocene epochs before being abandoned in favour of displacement along the present-day SAF (Chester & Logan 1986; Chester *et al.* 1993). Based on the separation of rock units, the total displacement of the Punchbowl is 44 km (Chester *et al.* 1993; Schulz & Evans 2000). Total displacement of the San Gabriel fault was initially reported as 22 km in Chester *et al.* (1993) but was subsequently updated to 50-60 km as reported in Dor *et al.* (2006). The Punchbowl fault consists of a single, continuous gouge zone typically 30 cm thick on average surrounded by an approximate 15 m thick damage zone (Chester & Logan 1986; Chester *et al.* 2005). The San Gabriel fault consists of a narrow layer (less than tens of centimetres) of gouge within a zone of foliated cataclasite several metres thick (Chester *et al.* 1993). Based on the schematic provided in Chester *et al.* (1993), where the fault core is symmetrical about the fault, we take the fault core thickness to be ~4.2 m.

### ***Alpine fault***

The Alpine fault (New Zealand) is a major dextral transpressive boundary that accommodates most of the relative displacement between the Pacific and Australian Plates. The remarkably straight surface trace extends for 800 km (~660 km onshore) from Milford Sound in the SW to Hokitika in the NE, where it transfers displacement onto four main strands of the Marlborough Fault System (the Wairau, Awatere, Clarence and Hope Faults) (Schuck *et al.* 2020 and references therein). The minimum total displacement of the Alpine fault is 470 km based on the right-lateral offset of the Dun Mountain Ophiolite Belt (Sutherland *et al.* 2007). The fault typically separates Pacific Plate amphibolite-greenschist facies, quartzo-feldspathic Alpine Schist in the hangingwall from basement, granitic and gneissic Australian Plate (plutonic) rocks in the footwall (Toy *et al.* 2015). The Australian Plate footwall assemblage is mostly overlain by Quaternary fluvio-glacial sediments and are thus poorly exposed at the surface (Toy *et al.* 2015).

The plate boundary fault structure was revealed by the first phase of the Deep Fault Drilling Project (DFDP-1) that drilled through the central section of the Alpine fault at Gaunt Creek. Phase 1 drilled two 96.6 m (DFDP-1A) and 150.4 m (DFDP-1B) deep vertical pilot holes in 2011 (Sutherland *et al.* 2012; Toy *et al.* 2015). These DFDP-1 boreholes provide a continuous section of fault rocks from hanging wall ultramylonites to footwall gravels enabling lithological (Toy *et al.* 2015), mineralogical (Schleicher *et al.* 2015), geomechanical (Boulton *et al.* 2014; Carpenter *et al.* 2014) and geophysical analysis (Sutherland *et al.* 2012). These analyses reveal a 10-30-m-thick package of gouge and cataclasite (including the principal slip zone) that forms the fault core (units 3-6 of Toy *et al.*, 2015) with material derived from both wall rocks (Toy *et al.* 2015). The total width of the fault core units in DFDP-1A is 11 m and 28 m in DFDP-1B (see Figure 2 in Toy *et al.* 2015), although there is some ambiguity in defining the thickness of the fault core. Sutherland *et al.* (2012) narrow it down to the 2 m surrounding the principal slip zone and Schuck *et al.* (2020) narrows it down further to exclusively consider the fault gouge forming the principal slip zone as core of the Alpine Fault's central segment (approximately 20 cm). Distinct fault core gouges were observed in each borehole. DFDP-1A's gouge consists of a quartzo-feldspathic, chlorite and muscovite-bearing blue gouge, whereas, DFDP-1B's gouge consists of a smectite-rich brown gouge with random, scaly fabrics that wrap around sub-rounded clasts (Boulton *et al.* 2014). The surrounding damage zone is composed of fractured ultramylonites and breccias (units 1, 2 and 7 of Toy *et al.*, 2015). There is no evidence these breccias are fault-related so they are not included as part of the fault core description in Toy *et al.* (2015). Another two boreholes were drilled in DFDP phase 2 (DFDP-2A: 212.6m MD – measured depth; DFDP-2B: 893.1 m MD) but these boreholes were not able to sample the fault core due to scientific and technical difficulties (Toy *et al.* 2017).

Barth *et al.* (2013) also conducted the first detailed field study of the well-exposed, along-strike, southern onshore section of the Alpine fault at three localities (Martyr River, McKenzie Creek and Hokuri Creek). At all three localities, the fault core is a

single, well-defined, >1 m thick tabular zone containing only Australian Plate-derived materials (Barth *et al.* 2013). At Martyr River, the fault core is a minimum 1.5 m thick. The core is composed of blue-grey and white foliated, chlorite-illite gouge where the foliations are sub-parallel to the fault core margins wrapping around cm-scale clasts of quartz and calcite, and chlorite-quartz cataclasite (Barth *et al.* 2013). At McKenzie Creek, a ~2 m thick serpentinite outcrop on the Australian Plate juxtaposes the fault. The fault core is 1.1 m thick and composed of foliated, smectite (saponite)-rich gouge with cm-scale serpentinite clasts (Barth *et al.* 2013). At Hokuri Creek, Australian Plate basement rocks with localised pods of serpentinite, pegmatite and limestone/marble juxtapose the fault. Similar to McKenzie Creek, the fault core consists of foliated, smectite (saponite)-rich gouge but is 12 m thick and contains larger clasts/pods of serpentinite (sometimes > 5 m across) (Barth *et al.* 2013). The serpentinite clasts at McKenzie and Hokuri Creek are elongate parallel to the fault margins and the foliations wrap around the footwall-derived clasts.

### ***Carboneras fault***

The Carboneras fault (Iberian Peninsula, Spain) is an ancient, sinistral strike-slip fault that formed part of the African-Iberian plate boundary 5 to 18 Mya. The fault forms part of a 450 km long, segmented sinistral strike-slip fault system interpreted to have acted as a lateral detachment or stretching transform (Rutter *et al.* 2012). It separates metamorphic basement rocks of the Betic Cordilleras against Miocene calc-alkaline volcanic rocks during upper Miocene time as a result of subducted slab rollback. The total displacement is not precisely known. The model presented in Rutter *et al.* (2012) and Faulkner *et al.* (2003) suggests 40 km of lateral offset has accumulated in the vicinity of Carboneras, although there is direct geological evidence for only about 15 km of this. For the purpose of data collation a total displacement of 15-40 km has been assumed.

Detailed field mapping along a 5 km section near the village of El Salvador Alto revealed the internal structure of the fault. The Carboneras fault is composed of multiple strands of phyllosilicate-rich fault gouge (each strand a few metres thick,

typically ~5 m thick; see Fig. 3 in Faulkner *et al.* 2003) bound by lenses of variably damaged phyllosilicate-rich host rock (Faulkner *et al.* 2003; Rutter *et al.* 2012). The strands of fault gouge are continuous along the length of the fault and structurally foliated with the foliations wrapping around clasts of quartz. ‘Blocks’ of dolomite are almost present within the phyllosilicate matrix, allowing a ‘mixed mode’ seismicity. The phyllosilicate-rich gouge is conducive with fault creep, whereas, the dolomite blocks are conducive to earthquake rupture nucleation (Faulkner *et al.* 2003).

### ***North Anatolian fault***

The North Anatolian fault (NAF) is a ~1500 km long, active, dextral strike-slip fault that extends from eastern Turkey to northern Greece and accommodates displacement between the Eurasian and Anatolian Plates. Almost all of the fault has failed during the last century as a westward migrating sequence of large, destructive earthquakes (e.g., 1999 Mw7.6 Izmit and 1999 Mw7.2 Düzce). The fault is analogous in length, geometry and slip rate to the SAF, although is younger (activated ~5 Ma compared to 17-30 Ma for the SAF) and has a lower total displacement. The total displacement of the NAF still remains a matter of debate. Based on structural and morphological markers, Armijo *et al.* (1999) and Hubert-Ferrari *et al.* (2002) report values of ~30 to ~80 km with no systematic variation. In contrast, based on different geological and geomorphological markers, Sengör *et al.* (2005) suggest the total displacement varies from 25-40 km in the west up to ~90 km in the eastern section of the fault. For the purpose of data collation, we take the total displacement to be between 25 and 90 km ( $57.5 \pm 32.5$  km) to incorporate all studies.

The Geophysical borehole Observatory at the North Anatolian Fault (GONAF) project has drilled into the NAF in the Istanbul/eastern Sea of Marmara region where a major (Mw>7) earthquake is pending. However, results from this project have not yet been released. Instead, field exposures at Ladik, Bademci and Hamamli, described in Dor *et al.* (2008), reveal the internal structure of the plate boundary fault. At Ladik, the NAF juxtaposes late Cretaceous limestone–sandstone–shale rocks from Jurassic sandstone and shale. The active fault core is 1.8 m thick and composed of a dark bluish-

grey to black, foliated gouge (Dor et al., 2008). At Bademci, the NAF juxtaposes ophiolitic mélange against a basement complex of schist marble and metabasalt. The fault core includes five individual dark grey, foliated gouge zones ranging from 0.3 to 1.4 m thick, separated by slivers of damaged and foliated host rock (Dor et al., 2008). Some or all of the gouge layers may merge at depth. At Hamali, the NAF juxtaposes Eocene basaltic and andesitic rocks from Jurassic and Cretaceous limestone. A thick fault core zone of gouge was observed. The northern boundary of the gouge zone is obscured by a river so the minimum thickness is stated between 30-40 m, although some of the gouge exposed at the surface may have arrived there as a result of sliding from the top of the hill (Dor et al., 2008). We therefore take the total thickness of the Hamamli gouge as  $35 \pm 5$  m.

Uysal et al. (2016), also briefly describe illite-rich fault gouge zones in the middle and eastern sections (Gerede–Mudurnu, and Niksar–Erzincan) of the NAF. Two localities along the Gerede-Mudurnu section reveal gouge zones 0.2 to 0.3 m and 1 to 1.5 m thick. Two localities along the Niksar-Erzincan section reveal gouge zones 10 to 15 cm and 40 to 50 cm thick. We plot the minimum and maximum values for each of these zones.

### ***Median Tectonic Line***

The Median Tectonic Line (MTL) is an active, ~800 km long fault that crosses Shikoku Island, SW Japan and helps accommodate displacement between the Philippine Sea Plate and Eurasian plate. The fault is a result of the oblique subduction of the Philippine Sea Plate and Eurasian Plate as the oblique subduction of a plate forms a strike-slip fault parallel to the trench on the continental plate side. The MTL separates the low-P/high-T Ryoke metamorphic terrain from the high-P/low-T Sanbagawa terrain (Wibberley & Shimamoto 2003). Total displacement of the MTL is difficult to estimate and poorly constrained (Wibberley & Shimamoto 2003). Okada (1980) state a minimum dextral strike-slip total displacement across the fault of ~5 km (Okada 1980). Whereas, Wibberley & Shimamoto (2003) state the total displacement

is constrained in the order of around 200-1000 km, however there is no evidence where this estimate comes from.

Detailed field mapping of the Tsukide outcrop revealed the internal structure of the fault (Wibberley & Shimamoto 2003). Here, the fault core of the MTL consists of a black and orange, foliated quartz/phyllsilicate gouge ~15 m thick (Wibberley & Shimamoto 2003).

### ***Japan Trench***

The Japan Trench is a convergent margin where the Pacific Plate subducts beneath the North American Plate. The subduction interface was sampled during the Integrated Ocean Drilling Program (IODP) Expedition 343/343T known as the Japan Trench Fast Earthquake Drilling Project (JFAST). The JFAST study site (IODP site C0019) is located at the frontal prism of the margin, ~7 km landward of the Japan Trench and ~100 km ESE of the 2011 Tohoku-oki earthquake epicenter in a shallow dipping (~8°) décollement (Chester *et al.* 2013; Kirkpatrick *et al.* 2015; Keren & Kirkpatrick 2016). The décollement separates Neogene prism marine sediments (hemipelagic mudstone) in the hangingwall from flat-lying subducting footwall sediments (mudstones, clay and chert) of the subducting Pacific Plate (Chester *et al.* 2013; Kirkpatrick *et al.* 2015). Based on an area-balanced reconstruction of a plate convergence seismic section through the JFAST site, Chester *et al.* (2013) estimate the total displacement to be at least 3.2 km.

JFAST recovered 21 cores from targeted intervals with an overall recovery of 43% (Chester *et al.* 2013). Core section 17R-1 was recovered from the depth of the décollement seismic reflector and is composed of deformed, smectite-rich (60–80 wt %) clay interpreted to be the fault core of the plate boundary fault (821.5 to 822.5 mbsf) (Chester *et al.* 2013; Kirkpatrick *et al.* 2015; Keren & Kirkpatrick 2016). The reported maximum thickness of the fault core is 4.87 m, accounting for unrecovered intervals above and below core section 17R-1 (Chester *et al.* 2013; Kirkpatrick *et al.*



2015). Note that only 1 m of core was sampled from this 4.87 m thick interval so the fault core could be 1 m wide only.

### ***Nankai Trough***

The Nankai Trough, offshore Japan, is the result of the Phillipean Sea Plate subducting beneath the Eurasian Plate and is one of the most extensively studied subduction zones. The trough consists of two major thrust faults: the plate boundary décollement (the shallow region of the plate-boundary fault) and a major out-of-sequence thrust, termed the megasplay, that branches from the plate boundary. The megasplay is an important component of the plate boundary system extending for > 100 km along-strike and is implicated in coseismic slip and tsunami generation.

The Nankai Trough Seismogenic Zone Experiment (NanTroSEIZE), conducted during Integrated Ocean Drilling Program (IODP) Expeditions 314–316, targeted the rupture area (Kumano Basin) of the 1944 Tonankai earthquake and sampled fault rocks in the shallow portions of both the plate boundary décollement (site C0007) and the megasplay fault (site C0004). The plate boundary separates Pliocene hemipelagic mudstones with volcanic ash layers in the hangingwall from subducted Pleistocene sand-rich turbidites in the footwall (Ujiie & Kimura 2014). Moore et al. (2009) estimated the total displacement along the megasplay to be a minimum of 1.45 km. It is unclear what this number is based on, however, for the purpose of data collation we use this number as it is the only estimate available in the literature that we could find. This estimate is a minimum and the total displacement may be larger on the plate boundary décollement.

Both the plate boundary décollement and megasplay fault zones are characterised by multiple fault core strands of breccias with an anastomosing network of clay foliations and thin, ~10 mm thick layers of dark gouge displaying a preferred orientated of clay fabrics parallel to the gouge boundaries (Ujiie & Kimura 2014). The fault core strands are separated by ‘fractured’ rocks, which we assume represent fractured host rock between the fault core strands, and drilling-induced breccias (Ujiie & Kimura 2014).

We do not include the ‘fractured’ rocks or drilling-induced measurements in the fault core thickness measurement. Each fault core strand in the décollement is < 2 m thick, and < 3 m thick in the megasplay, although these are minimum estimates as some of the core was unrecovered (see Fig. 2 and 3 in Ujiie & Kimura 2014).

The Ocean Drilling Project (ODP) also sampled the fault core of the décollement at 897 m (ODP Leg 196, Site 808, Hole 808C). Logging of the décollement at depth revealed a thicker, more complicated décollement structure, consisting of three intensely sheared faults 5-7 m thick composed of breccia and gouge (Shipboard Scientific Party 2002).

### ***Chelungpu Thrust***

The oblique convergent boundary between the Eurasian and Philippine Sea Plates was sampled in 2004-2005 during the Taiwan Chelungpu-fault Drilling Project (TCDP) following the 1999 Mw7.6 Chi-Chi earthquake. The purpose of the project was to observe and sample the fault zone structure of the Chelungpu thrust in Taiwan in order to understand the earthquake mechanisms involved in the Chi-Chi rupture. The seismic behaviour and consequently surface severity and damage of the Chi-Chi earthquake is considerably different between the northern and southern sections of the fault (e.g., Heermance et al., 2003). The northern section saw large displacements of ~8 m, while displacement in the south was only ~1m. The Chelungpu thrust is a major structure that extends for 90 km N-S across central Taiwan. The fault principally slips within, and parallel to, bedding of the Pliocene Chinshui shale with the total displacement estimated to be a minimum of 14 km (Heermance and Evans, 2006 and references therein).

Two vertical boreholes were drilled 40 m apart to a depth of 2 km (TCDP-Hole A) and 1.3 km (TCDP-Hole B). The observations from Hole A reveal the Chelungpu fault system comprises of a series of smaller fault zones observed at 1111 m depth (TCDP Hole A FZA1111), 1153 m depth (TCDP Hole A FZA1153) and 1221 m depth (TCDP Hole A FZA1221) (Yeh *et al.* 2007). The fault core of FZA1111 is 2.45 m thick and

comprises of a sequence of breccia, light-grey gouge, thin black gouge, foliated gouge, black gouge, ultracataclasite and breccia (Yeh *et al.* 2007). The fault core of FZA1153 is 2.45 m thick and consists of breccia and gouge with sand-rich clasts (Yeh *et al.* 2007). The fault core of FZA1221 is 1.26 m thick and consists of multiple gouge and ultracataclasite layers (Yeh *et al.* 2007). Hirono *et al.* (2007), describe the observations from Hole B. A smaller fault zone was observed at 1136 m depth (TCDP Hole B FZB1136). This fault zone has a fault core thickness of 1.77 m and consists of a sequence of gouge and breccia layers.

Heermance *et al.*, (2003) also studied field exposures of the northern and southern section of the Chelungpu thrust. The outcrop in the northern section at Tali River, near Takeng has a narrow fault core consisting of dark grey, sheared gouge that varies in thickness along-strike from 7-20 cm. The outcrop in the southern section at Chingshui River near the Tongtuo Bridge, consists of a thick 20–70 m zone of sheared gouge with numerous ( $n > 20$ ) individual gouge zones 10-50 cm thick. We take the thickness of the gouge zone as the thickness of the fault core strands and plot the minimum and maximum thickness. This difference in along-strike fault core thickness has been used to explain the difference in surface severity and damage experienced between the northern and southern section of fault (Heermance *et al.*, 2003).

### ***Longmenshan Thrust***

The Longmenshan thrust fault zone is a tectonic boundary between the eastern margin of the Tibetan Plateau and the Sichuan Basin of the South China Block. As a strike-slip thrust fault zone, it is characterized by thrust-sinistral strike-slip motion from late Triassic to Paleogene and by thrust-dextral strike-slip motion since the Meso-Cenozoic (Li *et al.* 2013). We take the maximum total displacement to be  $15.5 \pm 1.5$  km as stated in Li *et al.* (2009).

The Longmenshan fault was sampled during the Wenchuan earthquake Fault Scientific Drilling project (WFSD), following the 2008 Mw 8.0 Wenchuan earthquake. A total of five boreholes are expected to be drilled in the fault zone. The fault core thicknesses

and compositions of the first borehole (WFSD-1), which are drilled through mainly sedimentary rocks, are reported in Li et al. (2013). The observations from Hole 1 reveal the Longmenshan fault system comprises of a series of twelve smaller fault zones observed at 333m depth (WFSD-1 FZ333), 590m depth (WFSD-1 FZ590), 608m depth (WFSD-1 FZ608), 621m depth (WFSD-1 FZ621), 628m depth (WFSD-1 FZ628), 639m depth (WFSD-1 FZ639), 646m depth (WFSD-1 FZ646), 655m depth (WFSD-1 FZ655), 669m depth (WFSD-1 FZ669), 678m depth (WFSD-1 FZ678), 759m depth (WFSD-1 FZ759) and 970m depth (WFSD-1 FZ970). The fault cores range from 1.7 m to 19.8 m thick and are composed of gouge, breccia and cataclasite. Refer to Li et al. (2013) for a more detailed description of each fault zone.

#### ***Northern Barbados Accretionary Prism***

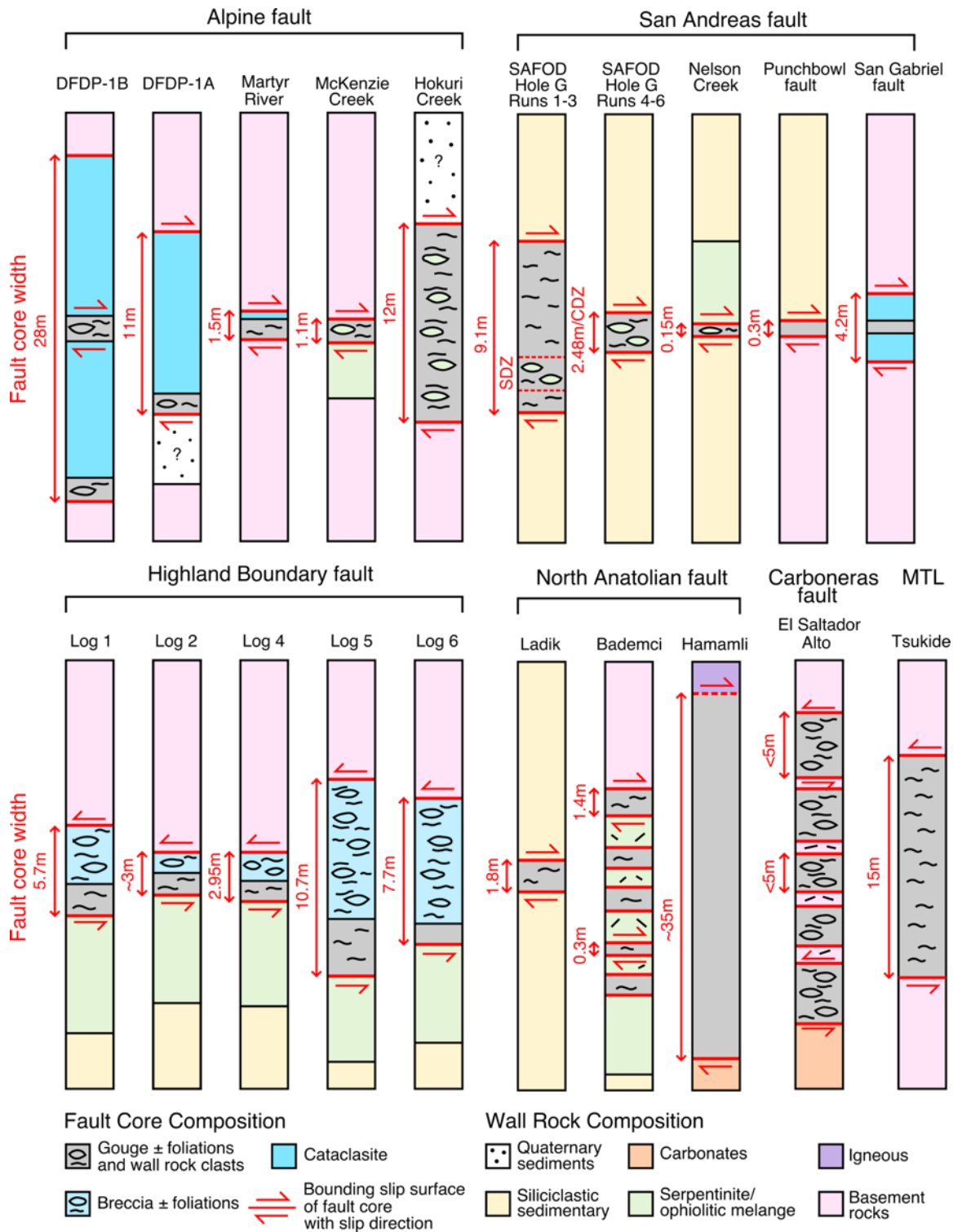
The subduction interface between the North America and Caribbean Plate was sampled at the Northern Barbados Accretionary Prism (Site 1047) during ODP Leg 171. Two measurements were made of the plate boundary décollement, which comprises of a single fault core strand in both holes, 10 and 26 m thick consisting of gouge and breccia (Shipboard Scientific Party 1998). The total displacement is unknown due to a lack of reliable/preserved displacement markers. Refer to the compilation of Rowe et al. (2013) for further details.

#### ***Shimanto Accretionary Complex***

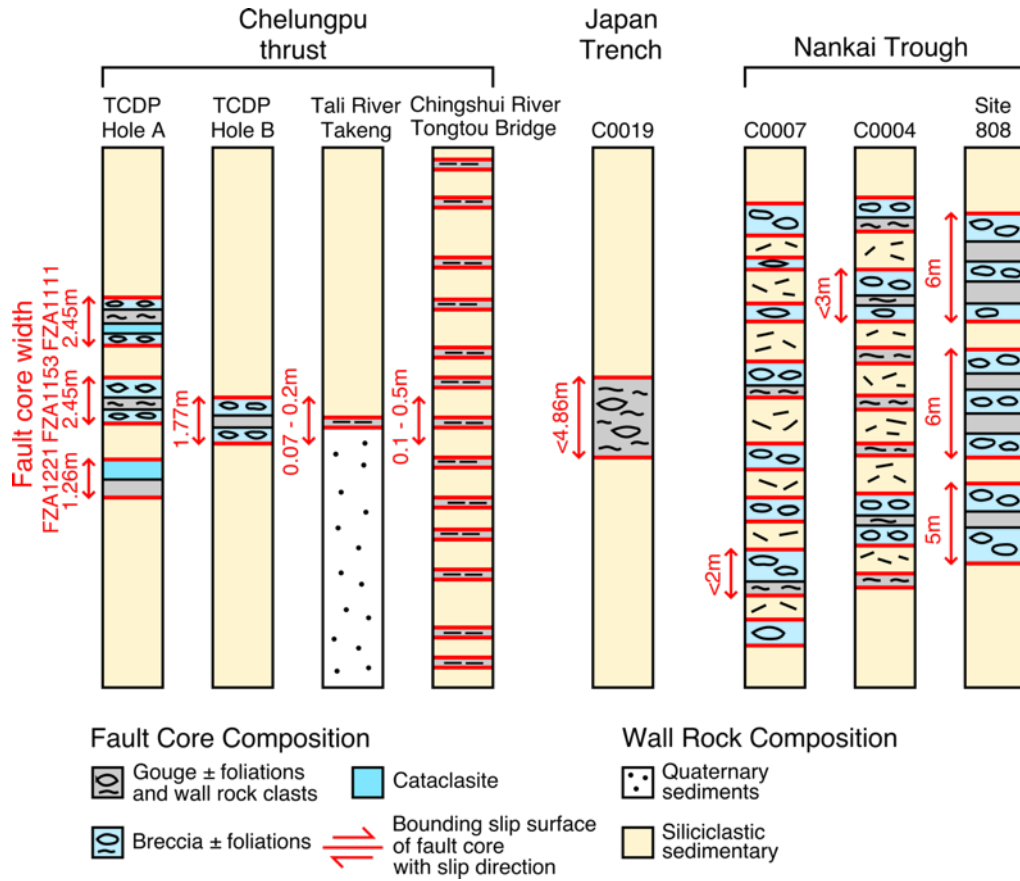
The Shimanto Accretionary Complex exposed in Shikoku, Japan is an ancient subduction décollement active during the late Cretaceous (Ikesawa et al., 2003 and references therein) consisting of several mélange zones. The Okistu mélange consists of a single fault core 2 to 5 m thick consisting predominantly of cataclasites with thin (few millimetres thick) pseudotachylyte layers observed along the S-C fabric (Ikesawa et al. 2003). A similar pseudotachylyte-bearing fault core is observed in the Mugi mélange ~1-2 m thick (Ujiie, et al., 2007a). A thicker fault core, consisting only of foliated cataclasites 19 m thick is described in Ujiie et al. (2007b). The total displacement is unknown due to a lack of reliable/preserved displacement markers. Refer to the compilation of Rowe et al. (2013) for further details.

***Pasagshak Point Thrust***

The Pasagshak Point Thrust, exposed on Kodiak Island, Alaska, is an ancient subduction décollement active in the earliest Palaeocene (Rowe *et al.* 2011). The preserved plate boundary consists of anastomosing strands of cataclastic fault rock 7-31 m thick with thin layers of pseudotachylyte. The total displacement is unknown due to a lack of reliable/preserved displacement markers. Refer to the compilation of Rowe *et al.* (2013) for further details.



**Fig. S1.** Schematic structural logs illustrating fault core thickness and composition for strike-slip plate boundaries used in this study in order of decreasing total displacement (not to scale).



**Fig. S2.** Schematic structural logs illustrating fault core thickness and composition for convergent plate boundaries used in this study in order of decreasing total displacement (not to scale).